ELUCIDATION OF THE EFFECT OF CANNABINOIDS ON ER STRESS TO DETERMINE THEIR MOLECULAR MECHANISM OF ACTION IN BREAST CANCER CELLS.

A.L. DE LA HARPE

2020

ELUCIDATION OF THE EFFECT OF CANNABINOIDS ON ER STRESS TO DETERMINE THEIR MOLECULAR MECHANISM OF ACTION IN BREAST CANCER CELLS.

By

Amy de la Harpe

Submitted in fulfilment of the requirement of the degree of Magister Scientiae in Biochemistry in the Department of Biochemistry and Microbiology in the Faculty of Science at the Nelson Mandela University, Port Elizabeth, South Africa

April 2020

Supervisor: Prof. C L Frost

Co-supervisor: Dr N Beukes

Declaration

I, Amy Lynne de la Harpe 214150658, hereby declare that the treatise for Magister Scientiae is my own work and that it has not previously been submitted for assessment or completion of any postgraduate qualification to another university or for another qualification.

Amy de la Harpe

31/03/2020

Date

Contents

i. List of figures vii

ii. List of tables xii

iii. Abbreviations list xiii

iv. Acknowledgements xviii

v. Abstract xix

Chapter 1 – General introduction and literature review 1

1. The endoplasmic reticulum 1

1.1. Structure 1

1.2. Functions 2

1.2.1. Protein synthesis and folding 3

1.2.2. Protein export 3

1.2.3. Retro-translocation and ERAD 4

1.2.4. Ca^{2+} homeostasis 4

1.3. ER stress and the unfolded protein response 4

1.3.1. Branches of the UPR 6

1.3.1.1. PERK 7

1.3.1.2. IRE-1 7

1.3.1.3. ATF6 8

1.3.2. Life and death decisions 9

1.4. The role of ER stress and the UPR in disease 11

1.4.1. Diseases in which ER stress and the UPR have been implicated 11

1.4.2. The role of ER stress and the UPR in cancer and malignancy 15

1.4.3. The therapeutic possibilities of targeting endoplasmic reticulum stress and components of the unfolded protein response to treat cancer 17

1.5. Cannabinoids and the endocannabinoid system 20

1.5.1. Cannabinoids 20
1.5.2. The endocannabinoid system 22
Chapter 2 – Problem statement, aims & objectives and chapter summary 24
2.1. Problem statement 24
2.2. Aims 25
2.3. Objectives 25
2.4. Chapter summary 26
2.5. Research Outputs 27
Chapter 3 – Thioflavin T optimization 28
3.1. Introduction 28
3.1.1. Current ER stress detection methods 28
3.1.2. Thioflavin T 29
3.2. Materials and methods 31
3.2.1. Cell culture and maintenance 31
3.2.2. Positive controls for ER stress induction 32
3.2.3. xCelligence electrical impedance assay 34
3.2.4. Optimization of Thioflavin T staining and fluorescence normalization 36
3.2.4.1. Thioflavin T staining 36
3.2.4.2. DAPI staining 36
3.2.4.3. SRB assay 37
3.2.5. SDS-PAGE and western blotting 37
3.2.5.1. Preparation of cell lysates 37
3.2.5.2. Bradford protein assay 37
3.2.5.3. Protein concentration 38
3.2.5.4. SDS-PAGE 40
3.2.5.5. Western blotting 40
3.2.6. Biolog Redox Dyes 41

3.2.7. Statistical analysis 43
3.3. Results and discussion 44
3.3.1. Real-time changes in viability 44
3.3.2. ThT staining and data normalization 49
3.3.3. Distinguishing between ER stress and mitochondrial dysfunction 67
Chapter 4 – Screening and Mechanism(s) of ER stress induction 73
4.1. Introduction 73
4.2. Materials and methods 77
4.2.1. Cannabinoid treatments 77
4.2.1.1. Cannabinoid degradation 77
4.2.1.2. Treatments 78
4.2.1.3. MTT cell viability assay 78
4.2.2. Enzyme Assays 79
4.2.2.1. Lactate dehydrogenase 79
4.2.2.2. Succinate dehydrogenase 80
4.2.3. Fluorescent staining for confocal microscopy 80
4.2.3.1. ER Tracker 80
4.2.3.2. MitoTracker 80
4.2.3.3. LipidTox 80
4.2.3.4. LysoTracker 81
4.2.4. Detecting the induction of ER stress 81
4.2.4.1. Griess reagent for Nitric Oxide 81
4.2.5. Detecting increases in reactive oxygen species 82
4.2.6. Detecting changes in the intracellular calcium concentration 83
4.3. Results and discussion 83
4.3.1. Viability screening 84
4.3.2. Inflammatory pathways 87

4.3.3. ER stress induction and UPR activation 90
4.3.4. Mitochondrial function 97
4.3.5. Changes in intracellular ROS and Calcium 115
4.3.6. Antioxidant co-treatment 125
4.3.7. TRPV1 Agonist/Antagonist studies 130
4.3.8. Differential activation of branches of the UPR 136
Chapter 5 – Conclusions and future recommendations 140
Chapter 6 – References 150
Appendices 161
i. Appendix i – Reagents and consumables 161
ii. Appendix ii – Buffer components 163
iii. Appendix iii – Equipment and software information 165
iv. Appendix iv – Supplementary data 166

i. List of figures

Figure 1: Summary of the major functions of the ER. 2

Figure 2: The various branches of the unfolded protein response and their role in pro-survival and pro-death signalling. 6

Figure 3: Proposed model for the pro-survival to pro-death switch of the UPR. 11

Figure 4: Summary of the role of ER stress and the UPR in various diseases 12

Figure 5: Chemical structures of selected phytocannabinoids found in *C. sativa* 21

Figure 6: Structures of the two major endocannabinoids. 22

Figure 7: Structure of ThT and proposed model of ThT binding 30

Figure 8: Simplified illustration of the principle of the xCelligence RTCA for measuring cell adhesion based on electrical impedance 35

Figure 9: Optimization of TCA, TFA, ethanol and acetone concentration methods on cell lysates. 39

Figure 10: Example of how the area under the curve was calculated using the trapezoid method. 42

Figure 11: Redox dye reduction by the MCF7 cell line. 43

Figure 12: Overview of the experimental design followed in Chapter 3 44

Figure 13: xCelligence curves of various cell lines showing real-time changes in the cell index over 24 hours after treatment with the positive controls. 45

Figure 14: Cell index relative to untreated control (%) of the various cell lines at the respective time intervals after treatment with the controls. 48

Figure 15: Representative fluorescent images of MCF7 cells stained with ThT. 50

Figure 16: Fold change in the ThT/cell of MCF7 cells treated with the various controls when normalized to cell number obtained using DAPI staining. 52

Figure 17: Representative images of MCF7 cells stained with DAPI after treatment for various time intervals. 54

Figure 18: Cell number determined using DAPI staining in the MCF7 cell line after extrapolation from a cell density standard curve..... 55

Figure 19: Cell number determined using SRB assay and extrapolation from a cell density standard curve in the MCF7 cell line 56

Figure 20: The correlation between ThT per cell and UPR activation for the detection of ER stress in the MCF7 cell line. 58

Figure 21: Representative fluorescent images of MDA-MB-231 cells stained with ThT. 59

Figure 22: The correlation between ThT per cell and UPR activation for the detection of ER stress in the MDA-MB-231 cell line. 61

Figure 23: Representative fluorescent images of MCF10A cells stained with ThT..... 63

Figure 24: The correlation between ThT per cell and UPR activation for the detection of ER stress in the MCF10A cell line. 64

Figure 25: Doubling time of the MCF7, MDA-MB-231 and MCF10A cell lines, calculated using the xCelligence RTCA software 65

Figure 26: The correlation between ThT per cell and UPR activation after treatment with FCCP in the MCF7 cell line. 68

Figure 27: The correlation between ThT per cell and UPR activation after treatment with FCCP in the MDA-MB-231 cell line. 70

Figure 28: The correlation between ThT per cell and UPR activation after treatment with FCCP in the MCF10A cell line..... 71

Figure 29: Effect of THC binding to CB receptors..... 75

Figure 30: Proposed mechanism of ER stress induction by TRPV1 activation 76

Figure 31: TLC of various cannabinoid standards, visualized using Fast Blue B stain. 77

Figure 32: Principle of the MTT cell viability assay. 78

Figure 33: Principle of the Griess reagent 82

Figure 34: Principle of DCFH-DA staining for the detection of ROS 82

Figure 35: Overview of the experimental design for the determination of the effect of cannabinoid treatment on the induction of endoplasmic reticulum stress and activation of the unfolded protein response. 84

Figure 36: Change in the viability of MCF7, MDA-MB-231 and MCF10A cell lines after treatment with various cannabinoids. 86

Figure 37: Nitrate concentration in spent media of treated cells. 89

Figure 38: Representative fluorescent images (200x magnification) of MCF7, MDA-MB-231 and MCF10A cells treated with various cannabinoids for 48 hours and stained with ThT and DAPI 91

Figure 39: Fold change in the ThT staining normalized to cell number after treatment with the various positive controls and cannabinoids for 48 hours. 92

Figure 40: Fold change in GRP78 expression in MCF7 cells after treatment with the various positive controls and cannabinoids for 48 hours. 93

Figure 41: Fold change in GRP78 expression in MDA-MB-231 cells after treatment with the various positive controls and cannabinoids for 48 hours. 95

Figure 42: Fold change in GRP78 expression in MCF10A cells after treatment with the various positive controls and cannabinoids for 48 hours. 97

Figure 43: Effect of cannabinoid treatment of reduction of the Biolog redox dye. 98

Figure 44: Overview of how supra-physiological levels of pyruvate can regenerate NAD^+ which increases glycolytic flux to generate ATP. 101

Figure 45: The effect of CBN treatment on the specific activity of various enzymes. 102

Figure 46: Change in the viability of MCF7 cells after treatment with CBN for 24 hours, determined using MTT and SRB cell viability assay. 103

Figure 47: Representative phase-contrast micrographs of MCF7 cells treated with various cannabinoids for 24 hours. 104

Figure 48: Representative images of MCF7 cells stained with LysoTracker (green) and Hoechst (blue)..... 105

Figure 49: Representative images of MCF7 cells stained with LipidTox (green) and Hoechst (blue). 106

Figure 50: Representative images of MCF7 cells stained with ER Tracker (Red) and Hoechst (blue). 107

Figure 51: Representative image of MCF7 cells stained with ER Tracker (red) and Hoechst (blue) after CBN treatment for 24 hours. 108

Figure 52: Representative images of MCF7 cells stained with MitoTracker (red) and Hoechst (blue). 109

Figure 53: Representative images of MCF7 cells stained with ER Tracker (Red) and LipidTox (green) and Hoechst (blue). 112

Figure 54: Overview of the experimental design for the determination of the molecular mechanism(s) associated with cannabinoid-induced ER stress 114

Figure 55: Effect of cannabinoid treatment on ROS production in the MCF7, MDA-MB-231 and MCF10A cell lines. 115

Figure 56: Concentration-dependent effect of CBD treatment on ROS production in the MCF7, MDA-MB-231 and MCF10A cell lines. 117

Figure 57: Concentration-dependent effect of CBD treatment on intracellular calcium in the MCF7, MDA-MB-231 and MCF10A cell lines. 119

Figure 58: Maintenance of calcium homeostasis in a generalized cell..... 120

Figure 59: Calcium exchange between the ER and mitochondria during early ER stress. 124

Figure 60: Effect of concomitant treatment of CBD with ascorbic acid on ROS accumulation in the MCF7 cell line..... 125

Figure 61: Effect of concomitant treatment with CBD and ascorbic acid on ROS production in the MCF7, MDA-MB-231 and MCF10A cell lines. 126

Figure 62: Effect of concomitant treatment with CBD and ascorbic acid on cell viability in the MCF7, MDA-MB-231 and MCF10A cell lines. 128

Figure 63: Effect of concomitant treatment with CBD and ascorbic acid on ER stress induction in the MCF7, MDA-MB-231 and MCF10A cell lines..... 130

Figure 64: Effect of concomitant treatment with a TRPV1 agonist and antagonist on cell viability in the MCF7, MDA-MB-231 and MCF10A cell lines 132

Figure 65: Effect of CBD treatment on the differential activation of the UPR in the MCF7 cell line. 136

Figure 66: xCelligence curves showing real-time changes in the cell index over 24 hours showing attachment of various cell lines. 166

Figure 67: Cell density standard curve of the MCF7 cell line (0 – 80 000 cells/well) obtained using DAPI staining, n=1..... 167

Figure 68: Protein standard curve (0-1mg/mL) obtained using BSA as a reference protein and the Bradford Reagent, n=3. 167

Figure 69: Cell density standard curves of various cell lines (0 – 80 000 cells/well), obtained using the SRB cell viability assay. 168

Figure 70: Screenshot of ImageJ software showing the outline of a region of interest (ROI) to generate 3D overlay of individual cells. 169

Figure 71: Nitrate standard curve (0 – 100 μM) obtained using a nitrate standard and the Griess reagent, n=3. 169

Figure 72: Cell density standard curves of various cell lines (0 – 80 000 cells/well), obtained using the MTT cell viability assay 170

Figure 73: A typical set of progress curves illustrating concentration-dependence of (A) LDH and (B) SDH enzyme assays in the MCF7 cell line and the corresponding slopes. 171

Figure 74: Representative progress curves of (A) LDH and (B) SDH activity for the various treatments in the MCF7, MDA-MB-231 and MCF10A cell lines 172

Figure 75: IC_{50} curves of capsaicin and curcumin in (A & B) MCF7, (C & D) MDA-MB-231 and (E & F) MCF10A cell lines after treatment for 48h, n=3 173

ii. List of tables

Table 1: Differences in receptor expression between the various breast cancer cell lines. . 31

Table 2: Concentrations of the various ER stress-inducing controls used throughout this project. 33

Table 3: Manufacturer details of antibodies used in this study 161

Table 4: Manufacturer details of reagents and consumables used in this study 161

Table 5: Manufacturer details of equipment used in this study 165

Table 6: Information of software used in this study 165

Table 7: IC_{50} values of capsaicin and curcumin in the MCF7, MDA-MB-231 and MCF10A cell lines. 173

iii. Abbreviations list

2-AG	-	2-Arachidonoylglycerol
AA	-	Ascorbic Acid
AD	-	Alzheimer's disease
ADP	-	Adenosine diphosphate
AEA	-	Anandamide
Akt-mTOR	-	Protein kinase B-mammalian target of rapamycin
ALD	-	Alcoholic liver disease
ALS	-	Amyotrophic lateral sclerosis
ANOVA	-	Analysis of variance
AP1	-	Transcription factor activating protein
ARF	-	Adenosine diphosphate ribosylation factor
ASK1	-	Apoptosis signal-regulated kinase 1
ATF4	-	Activating transcription factor 4
ATF6	-	Activating transcription factor 6
ATP	-	Adenosine triphosphate
Bad	-	Bcl-2-associated death promoter
Bak	-	Bcl-2 antagonist/killer-1
Bax	-	Bcl-2-associated X protein
Bcl	-	B-cell lymphoma
BFA	-	Brefeldin A
BH3	-	Bcl-2 homology
Bid	-	BH3-interacting-domain death agonist
Bim	-	Bcl-2-interacting mediator of cell death
bZIP	-	Basic leucine zipper
CB	-	Cannabinoid
CB1/2	-	Cannabinoid receptor 1/2
CBD	-	Cannabidiol
CBG	-	Cannabigerol
CBN	-	Cannabinol
CHOP	-	CCAAT/enhancer-binding protein (C/EBP) homologous protein
CI	-	Cell Index

COPII	-	Coat protein complex II
CSC	-	Cancer stem cell
CTLA	-	Cytotoxic T-lymphocyte-associated antigen
DAPI	-	4,6-Diamidino-2-phenylindole
DCFH-DA	-	2', 7'-Dichlorofluorescein-diacetate
DMEM	-	Dulbecco's modified essential medium
DMSO	-	Dimethyl sulfoxide
DNA	-	Deoxyribonucleic acid
ECM	-	Extracellular matrix
ECS	-	Endocannabinoid system
EDTA	-	Ethylenediaminetetraacetic acid
EGF	-	Epidermal Growth Factor
eIF2α	-	Eukaryotic initiation factor 2 alpha
Em	-	Emission
EMT	-	Epithelial-to-mesenchymal
eNOS	-	Endothelial nitric oxide synthase
ER	-	Endoplasmic reticulum
ERAD	-	Endoplasmic reticulum associated degradation
ERO1α	-	Endoplasmic reticulum oxidoreductase 1 alpha
ETC	-	Electron transport chain
Ex	-	Excitation
FBS	-	Fetal bovine serum
FCCP	-	Carbonyl cyanide 4-trifluoromethoxyphenyl hydrazine
FFA	-	Free fatty acid
GADD34	-	Growth arrest and DNA-damage-inducible protein 34
GPR55	-	G protein-coupled receptor 55
GRP78	-	Glucose-regulated protein 78
HEPES	-	4-(2-hydroxyethyl)-1-piperazineethanesulfonic acid
HER2	-	Human epidermal growth factor-receptor 2
HGF/c-Met	-	Hepatocyte growth factor/c-mesenchymal-epithelial-transition
IKK	-	IκB Kinase
IL-1β	-	Interleukin-1β
iNOS	-	Inducible nitric oxide synthase

INT	-	Iodonitrotetrazolium chloride
IP_3R	-	Inositol 1,4,5-triphosphate (IP_3) receptors
IRE-1α	-	Inositol-requiring enzyme 1 alpha
IκB	-	I kappa B
JNK	-	c-Jun N-terminal kinase
KCN	-	Potassium cyanide
KEAP1	-	Kelch-like Ech associated protein 1
L15	-	Leibovitz 15
LD	-	Lipid droplet
LDH	-	Lactate dehydrogenase
LDL	-	Low-density lipoproteins
LPS	-	Lipopolysaccharide
MAM	-	Mitochondrial-associated membrane
MAPK/ERK	-	Mitogen-activated protein kinase/extracellular signal-regulated kinase
MMP	-	Mitochondrial membrane potential
mRNA	-	Messenger ribonucleic acid
MtCU	-	Mitochondrial Ca^{2+} uniporter
NAD+	-	Nicotinamide adenine dinucleotide
NADH	-	Nicotinamide adenine dinucleotide hydrogen
NAFLD	-	Non-alcoholic fatty liver disease
NCX	-	Na^{+}/Ca^{2+} exchanger
NE	-	Nuclear envelope
NED	-	N-(1-naphthyl) ethylenediamine
NF-κB	-	Nuclear factor kappa B
NO	-	Nitric Oxide
NOS	-	Nitric oxide synthase
Nrf2	-	Nuclear factor-E2-related factor 2
OCR	-	Oxygen consumption rate
OMM	-	Outer mitochondrial membrane
P38MAPK	-	P38 mitogen-activated protein kinase
PARP	-	Poly (ADP-ribose) polymerase
PBS	-	Phosphate buffered saline
PBS-EDTA	-	Phosphate buffered saline-ethylenediaminetetraacetic acid

PD	-	Parkinson's disease
PDI	-	Protein disulfide isomerases
PERK	-	Protein kinase RNA (PKR)-like ER kinase
PI3K	-	Phosphatidylinositol 3-kinase
PMCA	-	Plasma membrane Ca^{2+} transport ATPase
PNPT	-	Polyprenyl-phosphate-N-acetylhexosamine-1-phosphate-transferase
PP1	-	Protein phosphatase 1
PR	-	Progesterone receptor
Puma	-	p53-upregulated modulator of apoptosis
PVDF	-	Polyvinylidene difluoride
qPCR	-	Quantitative polymerase chain reaction
RER	-	Rough endoplasmic reticulum
RIDD	-	Regulated IRE-1-dependent decay
RNA	-	Ribonucleic acid
ROI	-	Region of interest
ROS	-	Reactive oxygen species
RTCA	-	Real-time cell analyser
S1P	-	Site 1 protease
S2P	-	Site 2 protease
SDH	-	Succinate dehydrogenase
SDS	-	Sodium dodecyl sulphate
SDS-PAGE	-	Sodium dodecyl sulphate-polyacrylamide gel electrophoresis
SER	-	Smooth endoplasmic reticulum
SERCA	-	Sarco- endoplasmic reticulum Ca^{2+} ATPases
SRB	-	Sulforhodamine B
SREBP	-	Sterol regulatory element-binding protein
TAG	-	Triacylglycerols
TBS	-	Tris buffered saline
TEM	-	Transmission electron microscopy
TG	-	Thapsigargin
THC	-	Δ^9-Tetrahydrocannabinol
ThT	-	Thioflavin T
TLC	-	Thin layer chromatography

TNC	-	Tunicamycin
TNFα	-	Tumour-necrosis factor-α
TP53	-	Tumour protein 53
TRAF2	-	Tumour necrosis factor-receptor associated factor 2
TRB3	-	Pseudo-kinase tribbles homologue 3
TRPV1	-	Transient receptor potential cation channel subfamily V, member 1
UDP	-	Uridine diphosphate
UDP-GlcNac	-	Uridine diphosphate-N-acetylglucosamine
UGGT	-	Uridine diphosphate-glucose: glycoprotein glucosyltransferase
UPR	-	Unfolded protein response
VDAC	-	Voltage-dependent anion channel
VEGF	-	Vascular endothelial growth factor
XBP1	-	X-Box binding protein 1
XBP1s	-	X-Box binding protein 1 spliced

iv. Acknowledgements

I would like to extend my deepest gratitude to the following individuals and institutions for the role they played in the completion of this project:

First and foremost, Professor C.L. Frost for her constant guidance, motivation and willingness to always go the extra mile for her students.

Secondly, Dr N. Beukes for her input and time, and willingness to answer my many questions.

Dr R.A. Levendal for her constant input and enthusiasm throughout this study.

Mr W. van Losenoord for being my on-hand calculator and textbook, and for his assistance with enzyme assays.

Professor E. Prinsloo (Biotechnology Innovation Centre – Rhodes University) for his assistance and guidance with the use of the xCelligence RTCA.

Professor A. Edkins (Biochemistry Department – Rhodes University) for her assistance and guidance with the use of the confocal microscope.

My family who always support me unconditionally, and to my grandmothers, Laura de la Harpe (21/06/1950 – 15/10/2018) and Lillian Sparkman (22/06/1948 – 04/09/2019) for their constant enthusiasm and encouragement about my studies.

The National Research Foundation (NRF) for funding received for the duration of this project.

Nelson Mandela University (NMU) for funding received for the duration of this project and the provision of research facilities.

v. Abstract

Endoplasmic reticulum (ER) stress is defined as an imbalance between the ER's protein-folding load and folding capacity. ER stress is induced by various physiological conditions and subsequently triggers the activation of the unfolded protein response (UPR) to re-establish homeostasis and promote cell survival. However, under severe or chronic stress, apoptosis is induced. Normal cells generally do not experience ER stress; however, stressful conditions in the tumour micro-environment facilitates chronic ER stress and UPR activation, which plays a pivotal role in tumour survival. Exacerbation of pre-existing ER stress can trigger cancer cell death, with a minimal effect on normal cells. Currently, no high-throughput method exists to detect and quantify ER stress in cell lines. This study showed that Thioflavin T, a fluorescent dye that binds to misfolded protein aggregates, can be used for the high-throughput detection of ER stress, and provides several advantages over currently used methods. Current literature suggests that cannabinoid treatment may induce cancer cell death via ER stress, however little is known about the mechanism of induction. This study proposed a mechanism that occurs via the influx of Ca^{2+} via the vanilloid receptor 1 (TRPV1), and subsequent ROS production, which affects protein folding. ER stress was induced using various cannabinoids and measured using Thioflavin T and western blot analysis. The effect of cannabinoid treatment on ROS production and the intracellular Ca^{2+} concentration was measured. Cannabidiol (CBD) was the most potent ER stress inducer, significantly increasing Ca^{2+} and ROS accumulation; however, the level of accumulated Ca^{2+} across cell lines varied, which may be due to the differences in the TRPV1 expression and localization. Concomitant treatment of CBD with an antioxidant significantly increased cell viability and decreased ER stress induction in the MCF7 cell line. Concomitant treatment with a TRPV1 antagonist increased viability in this cell line. In conclusion, the results suggested that CBD may induce ER stress via Ca^{2+} influx through the TRPV1 receptor, thereby elevating intracellular ROS levels and disrupting protein folding.

Chapter 1 – General introduction and literature review

1. The endoplasmic reticulum

1.1. Structure

In 1945, the endoplasmic reticulum (ER) was first detected by transmission electron microscopy (TEM) when Porter *et al.* (1945) noted the presence of a "lace-like" reticulum in the cytoplasm of cultured cells. Due to its structure and localization, it became known as the endoplasmic reticulum and became recognized as a distinct organelle in 1954 (Palade and Porter, 1954). The ER is the largest cellular organelle and can be divided into the nuclear ER or nuclear envelope (NE), and the peripheral ER. The NE surrounds the nucleus, with the inner and outer membranes connecting at the nuclear pores (Voeltz *et al.*, 2002). The peripheral ER, on the other hand, is a network of interconnected tubules with a shared lumen, and membranes that interact with the cytoskeleton to spread throughout the cytoplasm (English *et al.*, 2009, Voeltz *et al.*, 2002). The lumen of the peripheral ER is also continuous with that of the nuclear envelope (Voeltz *et al.*, 2002). The wide distribution of the peripheral ER allows for the association with other membrane-bound compartments, making the ER a remarkably dynamic organelle (English *et al.*, 2009).

The ER can also be divided into the rough ER (RER) and smooth ER (SER). RER has a granular appearance due to association with ribosomes on the cytosolic side of the ER membrane, while SER does not associate with ribosomes and has a smooth appearance (Berridge, 2002, van Anken and Sitia, 2016). The ratio of RER relative to SER between cell types depends largely on their functions, *i.e.* highly secretory cells primarily contain RER (Voeltz *et al.*, 2002), which is responsible for protein synthesis, folding and secretion, while the SER is responsible for fatty acid and phospholipid synthesis, carbohydrate metabolism and the regulation of calcium homeostasis (Schönthal, 2012).

1.2. Functions

The ER has four major functions: (1) protein synthesis, (2) protein folding and post-translational modifications, (3) intracellular Ca^{2+} storage and (4) lipid and sterol biosynthesis (Schröder, 2008). **Figure 1** summarizes these functions with focus on the major aspects of protein synthesis and folding.

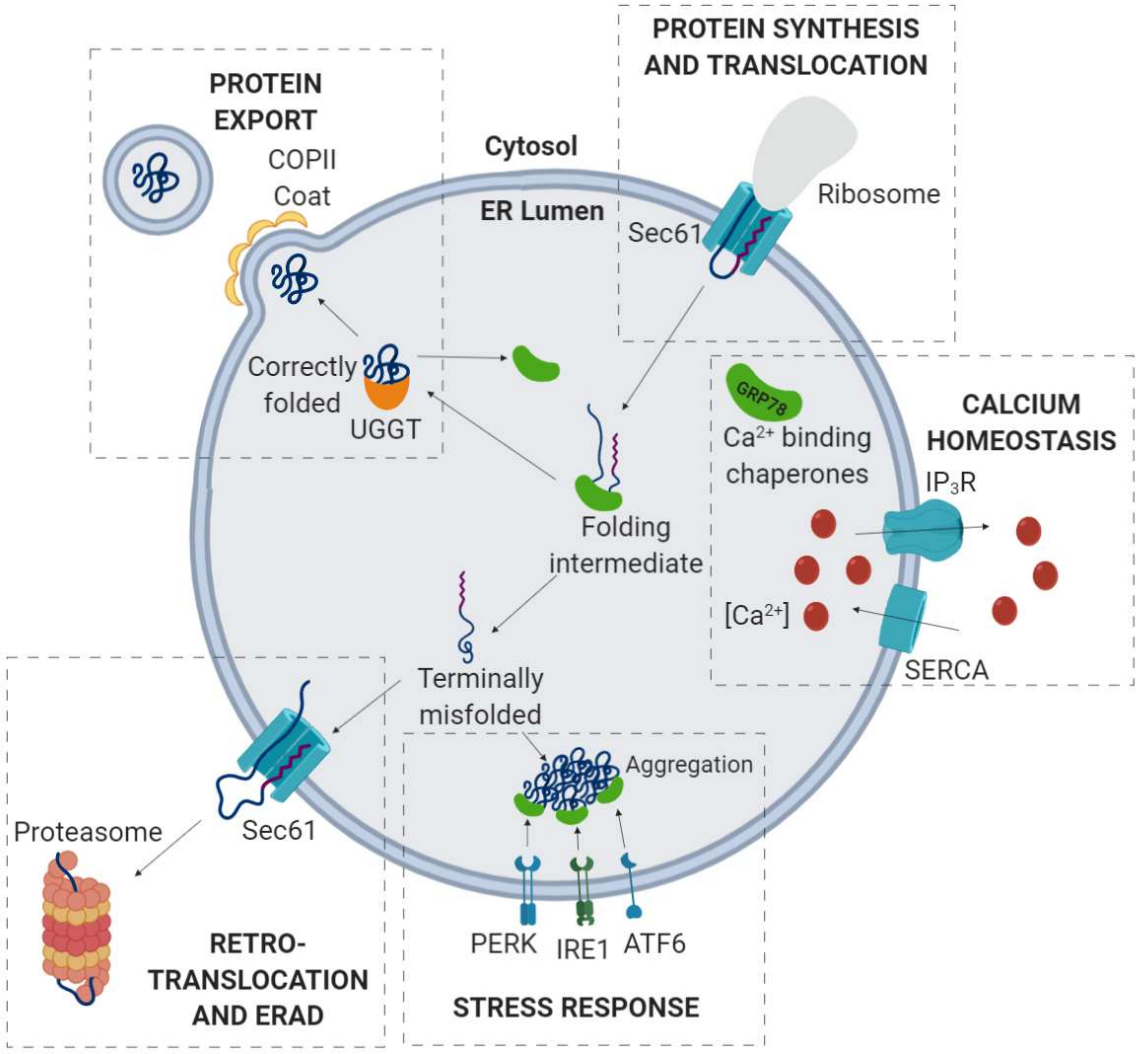

Figure 1: Summary of the major functions of the ER.
Figure was created using the BioRender online tool and adapted from Chen et al. (2010) and Sitia and Braakman (2004). Proteins are translated by ribosomes on the ER membrane and enter the ER lumen through the Sec61 channel, where they are bound to molecular chaperones that assist with protein folding. The UDP-glucose: glycoprotein glucosyltransferase (UGGT) folding sensor then ensures that the nascent proteins are correctly folded before export of the protein via COPII-dependent transport. Critically misfolded proteins exit the ER via the Sec61 channel and are degraded by the proteasome system. Accumulation of misfolded proteins results in the activation of the ER stress response. The ER is also responsible for maintaining ER Ca^{2+} homeostasis. Ca^{2+} enters the ER via the SERCA pump and exits via the IP_3R channel. The high Ca^{2+} concentration in the ER is required for chaperone function. IP3R – Inositol 1, 4, 5-triphosphate receptor, COPII – coat protein complex II, UGGT - UDP-glucose: glycoprotein glucosyltransferase, SERCA – sarco-/endoplasmic reticulum calcium ATPase.

1.2.1. Protein synthesis and folding

Secretory proteins are synthesized on bound ribosomes on the ER membrane (Chen *et al.*, 2010). These nascent, unfolded proteins enter the ER (Schröder, 2008, Schröder and Kaufman, 2005), for folding and post-translational modification(s) to enable the delivery of these proteins to their target sites (Schröder and Kaufman, 2005).

Translation of proteins begins in the cytosol. Ribosomes containing the messenger RNA (mRNA) are then recruited to the ER membrane where translation continues. Once translation is complete, the ribosomes are either released back into the cytosol or may remain bound to the ER membrane. The nascent, unfolded protein enters the ER lumen via the Sec61 translocation channel (**Figure 1**) to undergo proper folding and modifications, which may include N-linked glycosylation, disulphide bond formation and oligomerization (Schwarz and Blower, 2016). The ER lumen is also an oxidizing environment, which favours disulfide bond formation via protein disulfide isomerases (PDIs) (Malhotra and Kaufman, 2007, Schröder and Kaufman, 2005). Unfolded protein conformations are characterized by an increased number of hydrophobic patches on the protein surface relative to the native protein conformation, increasing their susceptibility to interaction and aggregation with other unfolded proteins (Schröder, 2008). Therefore, the high concentration of partially folded and/or unfolded proteins in the ER means that these folding intermediates are susceptible to aggregation. Molecular chaperones, such as glucose-regulated proteins 78 and 94 (GRP78 and GRP94) in the ER lumen interact with these hydrophobic patches to slow down the protein folding process by shielding the unfolded proteins and creating an isolated folding environment to prevent undesirable interactions and aggregation (Malhotra and Kaufman, 2007, Schröder, 2008, Schröder and Kaufman, 2005).

1.2.2. Protein export

After folding and modification, secretory proteins are released by the molecular chaperones (e.g. GRP78) and packaged for transport to the Golgi apparatus (Schwarz and Blower, 2016). Properly folded proteins exit the ER by coat protein complex II (COPII)-dependent vesicular transport (Chen *et al.*, 2010, Sitia and Braakman, 2004) (**Figure 1**). In order to ensure that misfolded proteins do not enter the secretory

pathway, the ER contains a quality control system that distinguishes between properly folded proteins and irreversibly misfolded proteins (Kostova and Wolf, 2003). UDP-glucose: glycoprotein glucosyltransferase (UGGT) acts as a folding sensor to monitor any aberrations from a proteins native state and allows partially folded proteins to re-associate with chaperones to undergo a further folding cycle (Chen *et al.*, 2010, Kostova and Wolf, 2003, Ruddock and Molinari, 2006).

1.2.3. Retro-translocation and ERAD

Critically misfolded proteins are retro-translocated across the ER membrane to the cytosol, where they are ubiquitinated and degraded by the 26S proteasome system in a process termed ER-associated degradation (ERAD). Retro-translocation is believed to occur through Sec61, which is the same translocation channel through which unfolded proteins enter the ER (Chen *et al.*, 2010, Sitia and Braakman, 2004, Tsai *et al.*, 2002).

1.2.4. Ca^{2+} homeostasis

The ER is the primary site of intracellular Ca^{2+} storage, with the concentration ranging from 100 – 800 µM, whereas the concentration in the cytosol is approximately 100 nM. The ER contains numerous calcium channels, ryanodine receptors and inositol 1,4,5-triphosphate (IP_3) receptors (IP_3R) that are responsible for the release of Ca^{2+} into the cytosol when the concentration is low (Schwarz and Blower, 2016). Ca^{2+} can also be pumped from the cytosol into the ER via sarco-/endoplasmic reticulum Ca^{2+} ATPases (SERCA) (Schwarz and Blower, 2016). A high Ca^{2+} concentration in the ER is also required for both protein folding and protein chaperone functions, as several of the molecular chaperones in the ER are Ca^{2+}-binding proteins (Malhotra and Kaufman, 2007, Schröder and Kaufman, 2005).

1.3. ER stress and the unfolded protein response

Protein flux into the ER is variable, as it changes in response to cell differentiation, environmental conditions and the cells physiological state. To cope with this dynamic situation, cells adjust their folding capacity according to demand, ensuring that only correctly folded proteins are secreted, regardless of increases in protein demand (Ron

and Walter, 2007), thereby maintaining ER homoeostasis. ER homeostasis is defined as the balance between the ER's protein load and its capacity to fold proteins (Beukes *et al.*, 2014). Various physiological conditions such as hypoxia, Ca^{2+} depletion in the ER, oxidative stress, and hypoglycaemia disrupt protein folding, interfering with ER homoeostasis. This causes an imbalance between protein-folding load and capacity, ultimately leading to an accumulation of unfolded and/or misfolded proteins in the ER (Verfaillie *et al.*, 2013), a cellular state generally known as ER stress (Giampietri *et al.*, 2015, Merksamer and Papa, 2010).

To maintain ER homeostasis, there are multiple sensors facing the ER lumen and effectors that transmit the message to other subcellular compartments (Ron and Walter, 2007). In response to protein accumulation, coordinated signal transduction pathways, collectively known as the unfolded protein response (UPR), are activated (Wang *et al.*, 2010). The UPR consists of three parallel pathways, each activated by different ER transmembrane sensors, namely PERK (protein kinase RNA (PKR)-like ER kinase), IRE-1 (inositol-requiring enzyme 1) and ATF6 (activating transcription factor 6). These sensors are transmembrane proteins with their N-terminus in the ER lumen and their C-terminus in the cytosol (Xu *et al.*, 2005). They are kept in an inactive state by direct association with the GRP78 chaperone on their N-terminus. However, GRP78 has a higher affinity for misfolded proteins, and an increase in misfolded protein triggers the titration of the chaperone away from the UPR sensors in order to refold the proteins, thus activating the signalling pathways (Corazzari *et al.*, 2017, Verfaillie *et al.*, 2013).

The main goal of the UPR pathway is to re-establish ER homoeostasis. Two mechanisms are employed to return the ER to its normal physiological state: (1) increasing the folding capacity of the ER and (2) decreasing the unfolded protein burden. To increase the folding capacity, the increased expression of molecular chaperones (*e.g.* GRP78) is induced, and the size of the ER is increased. In order to decrease the protein folding load, general protein synthesis is inhibited on a transcriptional and translational level, and the degradation of misfolded proteins via ERAD is increased (Corazzari *et al.*, 2017, Schröder and Kaufman, 2005). When these mechanisms fail to alleviate ER stress, apoptosis is induced in order to remove the stressed cells (Schröder and Kaufman, 2005).

1.3.1. Branches of the UPR

As mentioned previously, the UPR consists of three parallel pathways (**Figure 2**), each activated by a receptor in the ER membrane.

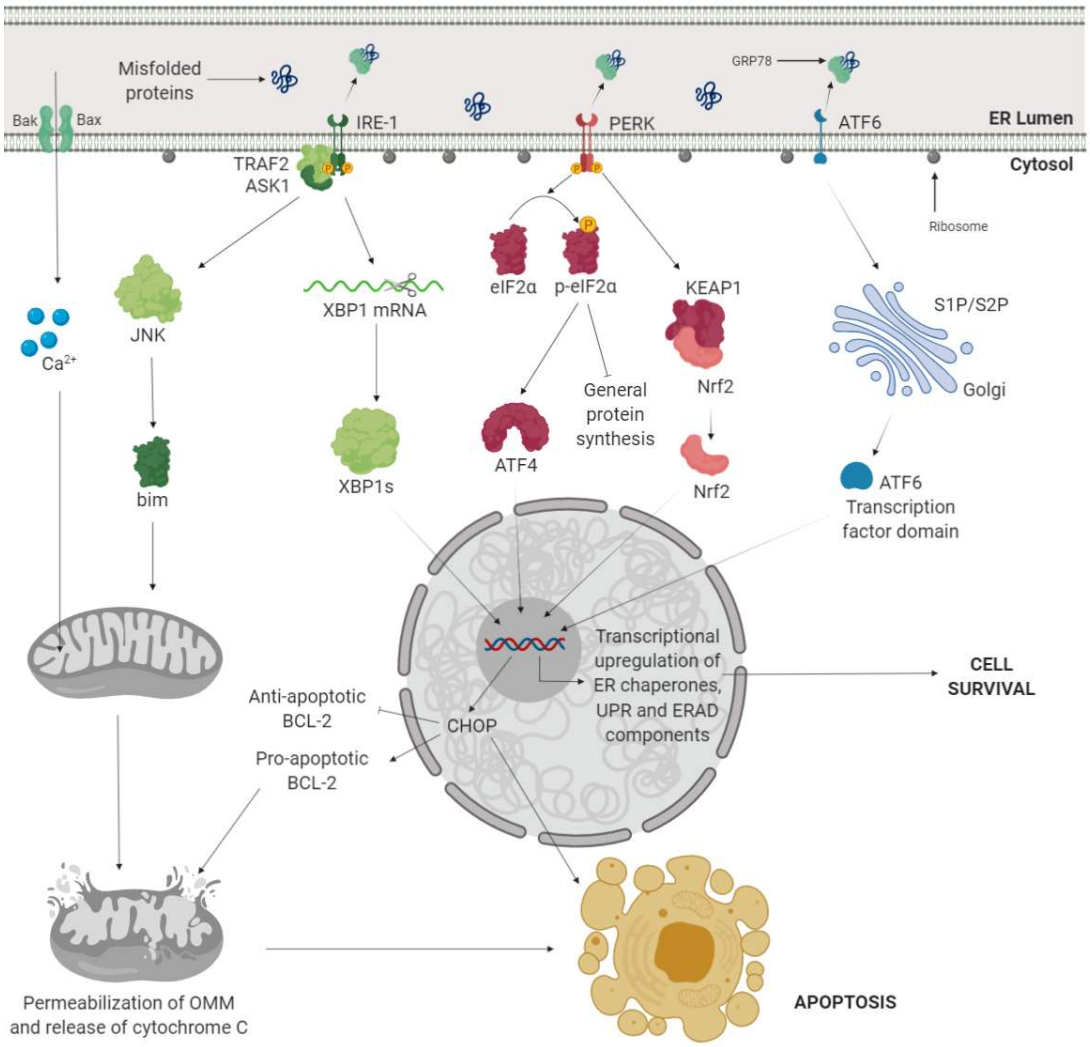

Figure 2: The various branches of the unfolded protein response and their role in pro-survival and pro-death signalling.

Figure was created using the BioRender online tool and adapted from Verfaillie et al. (2013). Active IRE-1α splices XBP1, which then codes for a transcription factor that upregulates UPR/ERAD genes and CHOP. IRE-1 also recruits TRAF2, which forms a complex with ASK1 and activates Bim, to induce apoptosis via mitochondrial dysfunction. Activated PERK phosphorylates eIF2α, suppressing general mRNA translation, however selectively translating certain genes including ATF4. Active PERK triggers the dissociation of Nrf2 from its cytosolic repressor, allowing translocation to the nucleus, where it upregulates genes for antioxidant enzymes. Activated ATF6 translocates to the Golgi apparatus where it is cleaved, releasing the N-terminal portion. Cleaved ATF6, ATF4 and XBP1s all translocate to the nucleus where they upregulate genes that code for CHOP and ERAD/UPR components. CHOP then results in apoptosis through various mechanisms including an increase in the expression of pro-apoptotic Bcl-2 members (Bax and Bak).

IRE-1α – Inositol-requiring enzyme 1; PERK – Pancreatic Endoplasmic Reticulum kinase (PKR)-like ER kinase; ATF6 – Activating transcription factor 6; TRAF2 – Tumour necrosis factor-receptor associated factor 2; ASK1 – Apoptosis-signal-regulating kinase; JNK – c-Jun N-terminal kinase; XBP1 – X-box Binding Protein 1; eIF2α – Eukaryotic initiation factor 2; ATF4 – Activating transcription factor 4; Keap1 – Kelch-like Ech associated protein 1; Nrf2 – Nuclear factor-E2-related factor 2; CHOP – C/EBP (ccaat/enhancer-binding protein) homologous protein; UPR – Unfolded protein response; ERAD – ER-associated degradation; OMM- outer mitochondrial membrane.

1.3.1.1. PERK

The PERK branch of the UPR consists of two pathways (**Figure 2**) that favour cell survival (Verfaillie *et al.*, 2013). PERK is a type I transmembrane serine/threonine kinase with two substrates, namely eukaryotic initiation factor 2 (eIF2α) and nuclear factor-E2-related factor 2 (Nrf2) (Schröder and Kaufman, 2005, Verfaillie *et al.*, 2013). In stressed cells, GRP78 dissociates from PERK and allows oligomerization in the membrane, triggering the trans-autophosphorylation of the kinase domains (Ron and Walter, 2007). Once activated, PERK phosphorylates the α-subunit of eIF2α, inhibiting cap-dependent translation and subsequently decreasing the protein load in the ER (Verfaillie *et al.*, 2013). Phosphorylation of eIF2α favours cap-independent translation, resulting in the selective translation of activating transcription factor 4 (ATF4), which regulates the expression of several genes, including chaperones (GRP78 and GRP94), antioxidant stress response genes and apoptosis-associated genes. When PERK's second substrate, Nrf2, is phosphorylated it separates from its cytosolic repressor, Kelch-like Ech associated protein 1 (KEAP1), translocates to the nucleus and upregulates the expression of genes involved in the antioxidant stress response (Verfaillie *et al.*, 2013).

1.3.1.2. IRE-1

Similarly to PERK (**Figure 2**), IRE-1 oligomerizes upon GRP78 dissociation from the sensor, allowing for trans-autophosphorylation of the kinase domains (Ron and Walter, 2007). IRE-1 oligomerization can be triggered by both the release of GRP78 or the direct binding of misfolded proteins to the luminal domain (Ron and Walter, 2007). IRE-1 is a bifunctional enzyme with protein kinase and endoribonuclease activity. It splices XBP1 mRNA to remove a 26 nucleotide intron and ligates the 5' and 3' ends, generating a translational frameshift to produce XPB1s (Ron and Walter, 2007, Verfaillie *et al.*, 2013, Wang *et al.*, 2010). XBP1s codes for a transcription factor that increases the expression of genes involved in ER quality control (Verfaillie *et al.*, 2013), such as ER chaperones (e.g. GRP78), enzymes that assist with protein maturation and secretion (Wang *et al.*, 2010), ERAD components and genes associated with the oxidative stress response (Verfaillie *et al.*, 2013).

The autophosphorylation of IRE-1 also results in a conformational change in its cytosolic domain. This initiates the binding to tumour necrosis factor-receptor associated factor 2 (TRAF2), which activates apoptosis signal-regulated kinase 1 (ASK1) and c-Jun N-terminal kinase (JNK) (**Figure 2**). This signalling pathway results in the permeabilization of the outer mitochondrial membrane (OMM) and the execution of the intrinsic apoptotic pathway (Schönthal, 2012). This intrinsic apoptotic pathway is regulated by the B-cell lymphoma 2 (Bcl-2) protein family by controlling the permeabilization of the OMM. The Bcl-2 family is divided into 3 groups: (1) pro-apoptotic proteins such as Bcl-2-associated X protein (Bax) and Bcl-2 antagonist/killer-1 (Bak), (2) anti-apoptotic proteins such Bcl-2 and Bcl-2-like 1 (Bcl-XL), and (3) pro-apoptotic BH3-only proteins such as BH3-interacting-domain death agonist (Bid), Bcl-2-associated death promoter (Bad), Bcl-2-interacting mediator of cell death (Bim), Noxa and p53-upregulated modulator of apoptosis (Puma) (Brunelle and Letai, 2009). JNK phosphorylation activates pro-apoptotic BH3-only proteins such as Bid and Bim, which leads to the oligomerization of Bax and Bak in the ER membrane (Zong *et al.*, 2003). This results in a release of Ca^{2+} from the ER into the cytosol, which is then taken up by the mitochondria, depolarizing the inner mitochondrial membrane and releasing cytochrome C (Crompton, 1999).

The IRE-1 branch of the UPR is also essential for the integration of ER stress signalling with inflammatory response signalling. The IRE-1α-TRAF2 complex recruits IκB Kinase (IKK), which phosphorylates IκB, leading to its degradation and the subsequent translocation of NF-κB to the nucleus (Hu *et al.*, 2006), inducing the expression of inflammatory genes. Activated JNK can also induce the expression of inflammatory genes by phosphorylating the transcription factor activating protein (AP1) (Davis, 2000).

1.3.1.3. ATF6

Upon GRP78 dissociation, ATF6 translocates to the Golgi apparatus and is cleaved in the luminal domain by site-1 protease (S1P, serine protease), and the site-2 protease (S2P, metalloprotease) cleaves the membrane-anchored N-terminal of ATF6 (**Figure 2**). This releases the cytosolic, DNA-binding, N-terminal portion of ATF6, which encodes a basic leucine zipper (bZIP) transcription factor (Ron and Walter, 2007, Schröder and Kaufman, 2005), which moves to the nucleus and upregulates genes

that code for ER chaperones, CHOP, ERAD components (Verfaillie *et al.*, 2013) and increases the transcription of XBP1 (Yoshida *et al.*, 2001) (**Figure 2**).

1.3.2. Life and death decisions

When cells experience mild or tolerable ER stress, the UPR can restore homeostasis, allowing cells to resist ER stress and promote cell survival. If homeostasis cannot be restored, the UPR induces cell death. Cells experiencing severe or prolonged ER stress commit to apoptosis through both mitochondrial-dependent and -independent pathways. CCAAT/enhancer-binding protein (C/EBP) homologous protein (CHOP), JNK signalling and various caspases have been implicated in ER stress-induced apoptosis (Lai *et al.*, 2007).

CHOP is the main mediator of ER stress-induced apoptosis (Sano and Reed, 2013). It is a pro-apoptotic transcription factor that is upregulated by all three branches of the UPR and regulates the expression of various genes that result in cell death (Wang *et al.*, 2014). CHOP upregulates the expression of growth arrest and DNA-damage-inducible protein (GADD34), which has been documented to induce apoptosis. GADD34 is a regulatory subunit of protein phosphatase 1 (PP1), which dephosphorylates eIF2α, allowing protein synthesis to continue, increasing the protein load in the ER. Persistent protein synthesis would result in chronic activation of the UPR and promote death signalling pathways (Malhotra and Kaufman, 2007). CHOP upregulates endoplasmic reticulum oxidoreductase 1 alpha (ERO1α), which encodes an ER oxidase that increases the oxidizing potential of the ER, creating a hyper-oxidizing environment (Malhotra and Kaufman, 2007, Verfaillie *et al.*, 2013), which is detrimental to protein folding (Verfaillie *et al.*, 2013) and further commits the cell to apoptosis (Wang *et al.*, 2014). CHOP has also been shown to regulate the balance between pro-survival and pro-apoptotic Bcl-2 members (Healy *et al.*, 2009). It reduces the expression of the anti-apoptotic Bcl-2 protein (Wang *et al.*, 2014) and increases the expression of pro-apoptotic Bcl-2 members (Bax and Bak) (Verfaillie *et al.*, 2013). CHOP induces the expression of death receptor 5 (DR5), a cell surface death receptor that may activate caspase cascades, further committing cells to apoptosis (Schönthal, 2012). The ability of CHOP to induce apoptosis has been shown to be dependent on the duration and/or severity of ER stress. Chronic exposure to mild stress can lead to adaptation by selectively decreasing CHOP expression, facilitated by the degradation

of both CHOP mRNA and protein, while the expression of pro-survival downstream targets is persistent due to long-lived mRNAs and proteins (Malhotra and Kaufman, 2007, Rutkowski *et al.*, 2006).

Caspases -2, -3, -4, -7, -9 and -12 have been reported to be involved in ER stress-induced cell death (Cheung *et al.*, 2006, Dahmer, 2005, Di Sano *et al.*, 2006, Hitomi *et al.*, 2004). Pro-caspase 12 is associated with the ER membrane and is cleaved and activated by ER stress. Active caspase-12 activates caspase-9, which subsequently activates caspase-3 and leads to cell death. Studies have shown that calpains, a family of Ca^{2+}-dependent cysteine proteases (Nakagawa and Yuan, 2000), as well as caspase-7, which moves to the ER surface upon ER stress (Rao *et al.*, 2004), can cleave and activate caspase-12. However, active caspase-7 cleaves caspase-12 at different sites to that of calpain (Nakagawa and Yuan, 2000, Rao *et al.*, 2004).

As discussed previously, ER stress and the activation of the UPR upregulates both pro-survival and pro-death factors. How the UPR switches from a pro-survival to a pro-death signalling pathway, as well as how cells can selectively utilize the adaptive response of the UPR to avoid cell death is poorly understood. It is generally accepted that the adaptive response to stress is not a result of selective activation of the various sensors, but a result of the selective stabilities of mRNAs and proteins that enable adaptation as opposed to those that result in cell death, more specifically – the selective instability of pro-apoptotic mRNAs and proteins (Rutkowski *et al.*, 2006). Rutkowski *et al.* (2006) showed that upon pharmacological induction of ER stress, the induction of GRP78 and CHOP mRNA were comparable; however, they found that the GRP78 mRNA and protein were significantly more stable than the CHOP mRNA and protein. They found that the CHOP mRNA was rapidly degraded, with a half-life of approximately 2 to 3 hours, while GRP78 mRNA showed little degradation over the same time period. The half-life of the GRP78 protein is approximately 46 hours, and approximately 4 hours for the CHOP protein (Rutkowski *et al.*, 2006). This would mean that cells require either an increase in the severity and/or the duration of ER stress, resulting in sustained UPR activation, in order to pass the hypothetical threshold that would commit the cells to apoptosis (**Figure 3**).

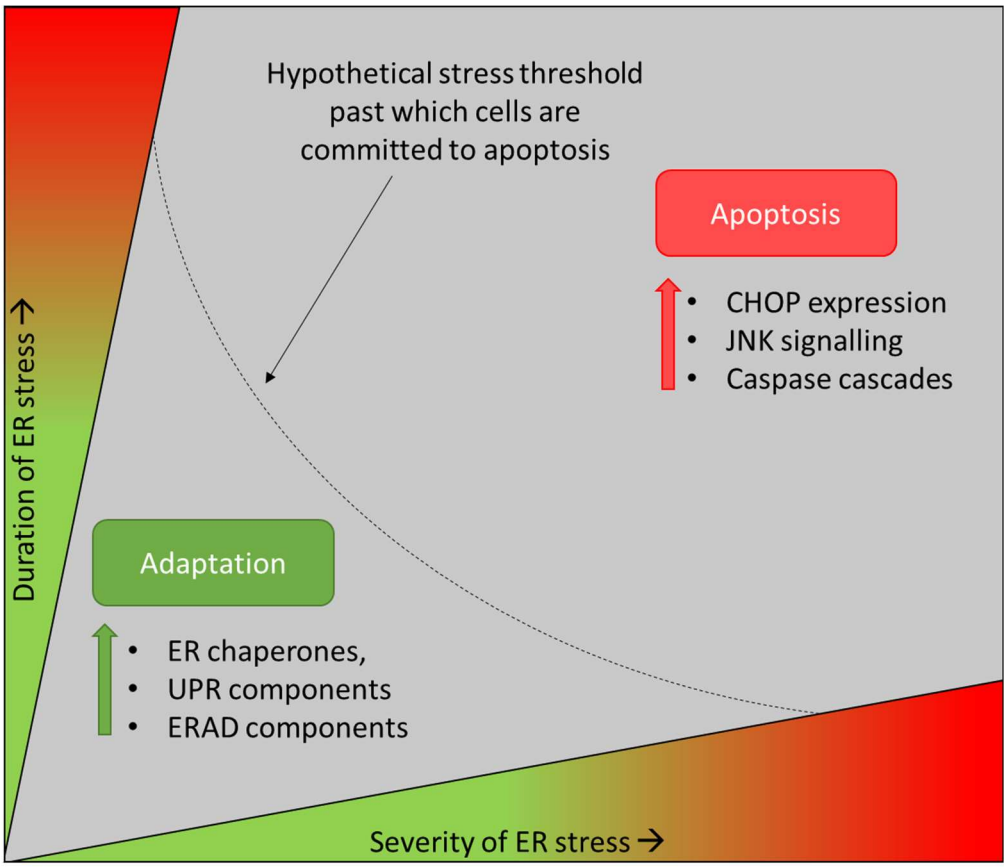

Figure 3: Proposed model for the pro-survival to pro-death switch of the UPR.
Figure adapted from Merksamer and Papa (2010).

1.4. The role of ER stress and the UPR in disease

1.4.1. Diseases in which ER stress and the UPR have been implicated

Diseases caused by the misfolding of cellular proteins are collectively known as 'conformational' or 'folding' diseases (Yoshida, 2007). It has been hypothesized that ER stress plays a role in the majority of conformational diseases, such as neurodegenerative diseases, diabetes mellitus, atherosclerosis, ischemia, inflammation, heart, liver, and kidney diseases, certain viral infections and cancer (Ozcan and Tabas, 2012, Yoshida, 2007). **Figure 4** summarizes the role of ER stress in these diseases.

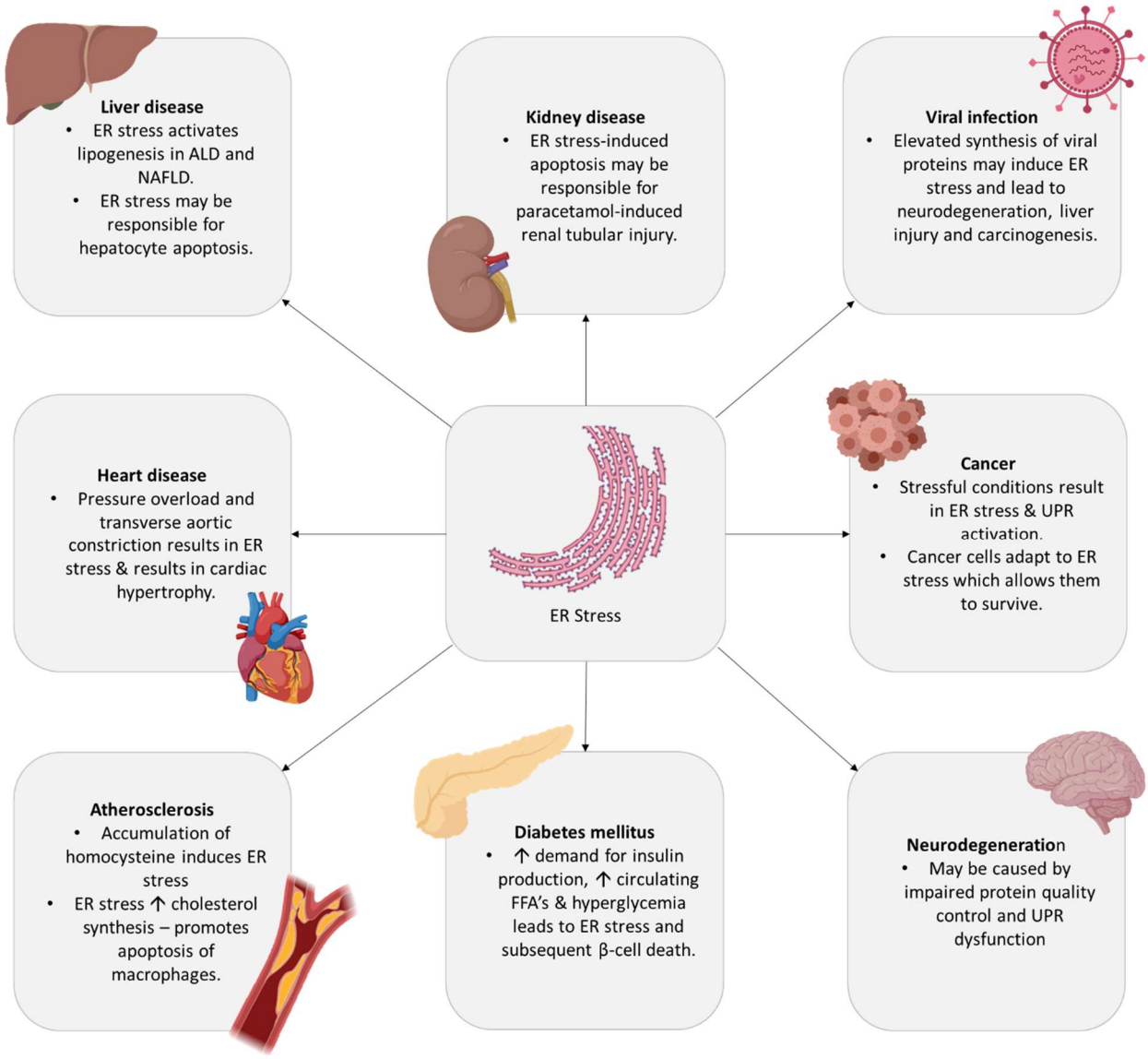

Figure 4: Summary of the role of ER stress and the UPR in various diseases.
Figure was created using the BioRender online tool and adapted from Navid and Colbert (2017). ER stress and the UPR have been implicated in playing a role in various diseases including heart, liver, and kidney disease, atherosclerosis, diabetes, neurodegeneration, cancer, and viral infection.

Alzheimer's disease is a neurodegenerative disease characterized by an accumulation of extracellular β-amyloid peptides and intracellular aggregates of phosphorylated tau proteins, as well as a disruption in calcium homeostasis and neuronal death (Ittner and Götz, 2010). Recent research has shown that the UPR is activated in the brains of people affected by Alzheimer's disease, based on the increased expression of GRP78 when compared to controls (Hoozemans *et al.*, 2005). Other neurodegenerative diseases associated with ER stress and the UPR are Parkinson's disease (PD) and amyotrophic lateral sclerosis (ALS). PD is characterized

by the death of dopaminergic neurons and the accumulation of protein aggregates, known as Lewy bodies (Healy *et al.*, 2004). Studies have indicated that impaired protein quality control and UPR dysfunction have crucial roles in the development of this disease. ALS is characterized by selective degradation of the brain and spinal cord motoneurons. Markers of ER stress have been found to be upregulated in the spinal cords of patients with ALS (Atkin *et al.*, 2008).

Type 2 diabetes is characterized by insulin resistance in peripheral tissues (**Figure 4**), impaired glucose production in the liver and insufficient insulin secretion by pancreatic beta cells. The progression of type 2 diabetes results in an increased demand on pancreatic beta cells to produce insulin to compensate for increasing insulin resistance. The processing of proinsulin to produce insulin occurs in the ER. The increased demand for insulin, in combination with an increase in circulating free fatty acids (FFA's) and hyperglycaemia results in ER stress in the beta cells (Cnop *et al.*, 2005). Chronic ER stress leads to beta-cell death and further exacerbates hyperglycaemia.

Atherosclerosis is caused by the accumulation of lipids and proteins derived from circulating low-density lipoproteins (LDL) in cells and the extracellular space of the large arteries (Ursini *et al.*, 2002). Research has suggested that ER stress and the UPR can mediate the development of atherosclerosis (Zhang and Kaufman, 2008). Important lipid biosynthetic pathways occur in the ER (Gregor and Hotamisligil, 2007) and ER stress has been found to be a driver of free cholesterol-induced apoptosis (Tabas, 2009). The accumulation of homocysteine, an intermediate produced during the metabolism of sulfur amino acids, is considered a risk factor for the development of atherosclerosis (Lawrence de Koning *et al.*, 2003). Homocysteine induces ER stress via an unknown mechanism, increasing the expression of various chaperones and CHOP (Outinen *et al.*, 1998). The induction of ER stress then increases the synthesis of cholesterol. Both CHOP induction and accumulation of cholesterol promotes apoptosis of macrophages and leads to macrophage debris being deposited in blood vessels, contributing to the development of atherosclerosis (DeVries-Seimon *et al.*, 2005, Feng *et al.*, 2003, Han *et al.*, 2006).

Research has found that the ER stress response is essential for the homeostasis of cardiomyocytes (**Figure 4**). The expression of ER chaperones, as well as ER stress-

induced apoptosis, is induced in cardiac myocytes by pressure overload caused by transverse aortic constriction, which leads to cardiac hypertrophy (Okada *et al.*, 2004). Upregulation of ER chaperones was found to protect cardiomyocytes from ER stress-induced apoptosis (Martindale *et al.*, 2006).

The liver is a major secretory organ, and hepatocytes have a well-developed ER, which is essential for the vigorous synthesis of secretory proteins. It has been reported that ER stress is associated with various liver diseases (Ji and Kaplowitz, 2006). Hepatic lipogenesis is activated upon uptake of excess carbohydrates and is controlled at a transcriptional level by sterol regulatory element-binding protein-1c (SREBP-1c) (Ozcan and Tabas, 2012, Wang *et al.*, 2015). Non-alcoholic fatty liver disease (NAFLD) is characterized by the abnormal storage of lipids in hepatocytes. Studies have highlighted the role of *de novo* lipogenesis in excessive lipid accumulation in the livers of patients with NAFLD (Ozcan and Tabas, 2012). Research has also shown that the induction of ER stress activates lipogenesis through the induction of SREBP-1c (Kammoun *et al.*, 2009). ER stress has been shown to play a role in alcoholic liver disease (ALD). ER stress-related genes, such as GRP78 and CHOP, were found to be upregulated in mice fed with ethanol (Ji and Kaplowitz, 2006). CHOP knockout mice exhibited a minimal amount of hepatocyte apoptosis, which further supports the role of ER stress in ALD (Ji *et al.*, 2005). The induction of ER stress by alcohol may be due to the inhibition of key enzymes for sulfur-based amino acid metabolism, which leads to an accumulation of the ER stress inducer, homocysteine (Ji and Kaplowitz, 2003). ER stress activates SREBP, which increases fatty acid synthesis and leads to lipid-induced apoptosis (Ji and Kaplowitz, 2004, Ji *et al.*, 2005).

Various factors have been documented to result in renal injury through the induction of ER stress. One of the mechanisms involved in paracetamol-induced renal tubular injury is ER stress-induced apoptosis via the induction of CHOP (Lorz *et al.*, 2004). ER stress is also induced by complement attack, activating the PERK branch of the UPR, leading to glomerular epithelial cell injury (Cybulsky *et al.*, 2005). Excessive accumulation of secretory proteins induces podocyte injury through the induction of ER stress (Inagi *et al.*, 2005). Finally, the overexpression of a kidney-specific protease inhibitor, megsin, induces ER stress and renal injury (Miyata *et al.*, 2005). Prior

induction of GRP78 protects renal epithelial cells from chemical-induced renal injury (Asmellash *et al.*, 2005), suggesting that ER stress is one of the major causes of chemical-induced renal injury.

Infections caused by various viruses have been documented to induce ER stress, due to the elevated synthesis of viral proteins. Upon infection, the ER stress response is activated to protect against ER stress-induced apoptosis (Yoshida, 2007). ER stress induced by viral infection is thought to cause various pathogenic effects such as neurodegeneration, liver injury and carcinogenesis, depending on the types of cells affected (Ji and Kaplowitz, 2006).

1.4.2. The role of ER stress and the UPR in cancer and malignancy

The role of the UPR in oncogenic processes was first proposed in 2004 (Ma and Hendershot, 2004). UPR activation can contribute to both increased survival and apoptosis in cancer cells (Wang and Kaufman, 2014), and it has recently been shown that *in vivo* UPR activation is vital to cancer development (Wang and Kaufman, 2014).

UPR activation in cancer cells can be attributed to both intrinsic and extrinsic factors. Certain types of cancer cells are highly secretory and are thus prone to UPR activation (Wang and Kaufman, 2014). Intrinsic factors that result in UPR activation include: (1) the activation of oncogenes or mutations that result in a loss of function of tumour-suppressor genes, which increases protein synthesis and translocation into the ER (Wang and Kaufman, 2014), (2) gene mutations that result in protein misfolding (Marada *et al.*, 2013, Wang and Kaufman, 2014), (3) expansion of the ER for cell division and transmission to daughter cells during mitosis (Babour *et al.*, 2010), (4) the activation of pathways that activate other cells in the tumour microenvironment, such as immune and endothelial cells to support tumour growth which may require UPR activation to increase folding and secretion of cytokines, metalloproteinases, angiogenic factors and components of the extracellular matrix (ECM) (Wang and Kaufman, 2014).

Besides the intrinsic factors that activate the UPR, several extrinsic factors can result in ER stress. The rapid proliferation of cancer cells results in the development of a hostile microenvironment, which disrupts protein folding and activates the UPR (Wang and Kaufman, 2014). Cancer cells metabolize glucose at a high rate. Due to the fast

glucose metabolism, coupled with their uncontrolled growth, tumours are often poorly vascularized and experience a limited supply of oxygen, nutrient deprivation and changes in cellular pH (Wang *et al.*, 2010). Glucose deprivation disrupts protein folding in the ER due to improper glycosylation (Wang and Kaufman, 2014), as glucose functions as a donor for asparagine (N)-linked glycosylation. Glucose deprivation indirectly disrupts Ca^{2+} homeostasis by decreasing SERCA activity as a result of decreased energy supply (Moore *et al.*, 2011) to tumour cells in the form of ATP. Hypoxia experienced by cancer cells affects protein folding through interruption of disulphide bond formation, a post-translational modification catalysed by disulphide isomerases. Disulphide bond formation during protein synthesis is oxygen-independent; however, when the bonds are formed as a post-translational modification during folding in the ER, they are oxygen-dependent (Koritzinsky *et al.*, 2013).

Several types of cancer adapt to hypoxia and nutrient depletion by initiating angiogenesis (Clarke *et al.*, 2012); however, this may be insufficient to provide enough oxygen and nutrients to the cancer cells. The stressful conditions in the tumour microenvironment results in the activation of the UPR (Healy *et al.*, 2009), which plays a vital role in oncogenic transformation, tumour survival and progression (Verfaillie *et al.*, 2013, Wang *et al.*, 2010, Wang and Kaufman, 2014).

Cancer cells have unique alterations that enable them to use ER stress responses to promote survival and growth (Giampietri *et al.*, 2015). Cancer cells may adapt to ER stress and evade stress-induced apoptotic pathways by differentially activating the branches of the UPR (Wang *et al.*, 2010). It is currently unclear whether the protective mechanisms of the UPR are increased, or if the destructive mechanisms are blocked in tumour cells in order to adjust to long-term ER stress. Upregulation of the UPR in cancer may be advantageous, as the protein folding capacity is increased, prolonging life. However, up-regulation may also increase the expression of the pro-apoptotic components of the UPR; therefore, down-regulation of the UPR may allow cells to evade ER stress-induced apoptotic pathways (Healy *et al.*, 2009). The overexpression of GRP78 is related to the survival response of cancer cells to environmental stress (Giampietri *et al.*, 2015). The evidence that highlighted the prominent role of GRP78 in cell survival came from the observation that suppression of GRP78 in fibrosarcoma cells inhibited their ability to form tumours *in vivo* (Jamora *et al.*, 1996). Dong *et al.*

(2008) suggested that GRP78 regulates cancer progression through three mechanisms: enhancement of tumour cell proliferation, protection against apoptosis, and promotion of tumour angiogenesis.

1.4.3. The therapeutic possibilities of targeting endoplasmic reticulum stress and components of the unfolded protein response to treat cancer

The importance of the UPR in maintaining malignancy has encouraged research into the therapeutic possibilities of targeting the UPR (Giampietri *et al.*, 2015, Verfaillie *et al.*, 2013). Normal cells typically do not experience chronic ER stress; therefore, they express limited amounts of GRP78 and CHOP. *In vitro*, normal cells require deliberate exposure to ER stress-inducing treatments to trigger GRP78 and CHOP expression, while cancer cells display an elevated basal ER stress level. Although the chronic ER stress experienced by cancer cells provides them with a survival advantage, it also presents a difference between normal and tumour cells, that can be exploited for therapeutic intervention (Schonthal, 2011). Recent research has shown that the controlled exacerbation of pre-existing ER stress in cancer cells can overload the ER stress system. This results in the incapacitation of the protective UPR components and activates pro-apoptotic components of the UPR. In contrast, normal cells have larger reserves to accommodate the increased stress levels by activating pro-survival functions (Schonthal, 2011).

Two approaches can be taken to target the UPR for potential cancer treatments. The first is to inhibit the components of the UPR (e.g. PERK, IRE-1α, ER chaperones, PDIs) in tumours where the cells are dependent on the UPR to survive. The second approach is to exasperate the UPR in cells that had already activated the UPR pathways to survive the harsh microenvironment, overloading the ER stress system and triggering cell death (Healy et al., 2009). However, the life and death decisions that occur during ER stress are not completely understood; therefore, there is the risk that potential treatments block ER stress-induced apoptosis and subsequently promote tumour progression (Verfaillie et al., 2013).

There are various signatures or hallmarks that define cancer. Approximately 10 classes of cancer therapeutics have been proposed which specifically target these hallmarks. These are epidermal growth factor-receptor inhibitors, cyclin-dependent

kinase inhibitors, immune-activating anti-cytotoxic T-lymphocyte-associated antigen (CTLA4) antibodies, telomerase inhibitors, selective anti-inflammatory drugs, inhibitors of hepatocyte growth factor/c-mesenchymal-epithelial-transition (HGF/c-MET), inhibitors of vascular endothelial growth factor (VEGF) signalling, poly (ADP-ribose) polymerase (PARP) inhibitors, pro-apoptotic BH3 mimetics and aerobic glycolysis inhibitors (Garg *et al.*, 2015).

Therapeutic induction of ER stress as a strategy to target various hallmarks of cancer has shown promise in cancer patients (Garg *et al.*, 2015). Several well-established cancer therapeutics have been shown to induce ER stress with positive outcomes. Therapy-induced ER stress differs from basal ER stress in which basal ER stress experienced by cancer cells is considered chronic and is induced by various physiological stressors and is largely pro-tumourigenic (Garg *et al.*, 2015).

UPR signalling drives the different hallmarks of cancer (Urra *et al.*, 2016). One of the hallmarks of cancer is proliferative signalling and resistance to growth suppression. Chronic proliferation is an intrinsic property of tumour cells. Cancer cells tend to deregulate the normally rigorously controlled growth-promoting pathways (Garg *et al.*, 2015). Research has shown that therapy-induced ER stress can suppress various growth-promoting signalling pathways, including the P38 mitogen-activated protein kinase (P38MAPK), phosphatidylinositol 3-kinase (PI3K), protein kinase B – mammalian target of rapamycin (Akt-mTOR) and mitogen-activated protein kinase/extracellular signal-regulated kinase (MAPK/ERK) pathways (Garg *et al.*, 2015).

Another hallmark of cancer is tumour-associated angiogenesis. Studies have shown that the UPR can promote angiogenesis by regulating the transcription of several pro-angiogenic factors in cancer cells *in vitro*. Therapy-induced ER stress has been shown to have antiangiogenic effects in endothelial cells *in vitro.* However, with the treatment of tumours with certain ER stressors *in vivo*, the antiangiogenic effect of the endothelial cells appeared to override the proangiogenic effect mediated by the cancer cells (Garg *et al.*, 2015).

Another hallmark of cancer is resistance to cell death. Therapy-induced ER stress that triggers cell death pathways has several advantages regarding the activation of certain cell death resistance mechanisms. The most common mechanisms of cell death

resistance by cancer cells include the loss of tumour-suppressor genes (e.g. TP53), increased levels of anti-apoptotic proteins (Bcl-2 proteins), decreased levels of pro-apoptotic proteins (Bax, Bim), deregulation of caspase signalling, or deregulation of the extrinsic death receptor-based pathways (Hanahan and Weinberg, 2011). Several ER stressors induce apoptosis independent of TP53 (tumour-suppressor) activity, which is advantageous since cancers typically show a loss of function of this protein. Therapy-induced ER stress also tends to occur through the intrinsic apoptotic pathway rendering caspase 8 and the extrinsic death receptor-based signalling unnecessary for cancer cell death in this regard, which is advantageous due to the deregulation of these pathways in cancers. However, the ability of therapy-induced ER stress to preferentially induce intrinsic apoptosis is a weakness, because cancer-associated defects that deregulate intrinsic apoptosis (*e.g.* loss of function of Bax and increased expression of Bcl-2 proteins) also deregulate ER stress-induced apoptosis (Garg *et al.*, 2015, Schröder, 2008, Verfaillie *et al.*, 2013).

Invasion and metastasis are hallmarks of cancer cells. The flexibility exhibited by cancer cells in switching between two differentiation-related programs of epithelial-to-mesenchymal transition (EMT) and mesenchymal-to-epithelial transition (MET) contributes towards increased invasion and metastasis (Hanahan and Weinberg, 2011). At the stage of invasion and metastasis, cancer cells undergo EMT-based dedifferentiation, during which time the cancer cell shape is altered, and they produce extracellular matrix (ECM) degrading enzymes and lose their attachment to neighbouring cells and the ECM. When these cells reach a site of metastatic seeding, reverse MET-based re-differentiation occurs, which facilitates the formation of additional cancer colonies (Garg *et al.*, 2015, Hanahan and Weinberg, 2011). During the EMT transition, the cancer cells have a highly secretory phenotype that activates the UPR. The increased secretion of ECM-degrading enzymes by EMT cells results in an increased sensitivity to ER stress (Feng et al., 2014). Recent research suggests that therapy-induced ER stress may be promising to selectively target the EMT phenotype in cancer cells compared to any other available therapy (Garg et al., 2015).

1.5. Cannabinoids and the endocannabinoid system

1.5.1. Cannabinoids

Extracts from *Cannabis sativa* have been used for centuries for both medicinal and recreational purposes; however, the chemical structures of the major active components, the cannabinoids, were not elucidated until the 1960s (Velasco *et al.*, 2016a). Cannabinoids are diverse lipophilic compounds that interact with cannabinoid receptors found in the body (Śledziński *et al.*, 2016). They exert their effects primarily through the tissue-specific G protein-coupled receptors, CB1 and CB2 (Śledziński *et al.*, 2016); however, it has been reported that some effects of cannabinoids are not CB1/CB2 mediated (Pyszniak *et al.*, 2016). Other receptors such as the transient receptor potential cation channel subfamily V, member 1 (TRPV1) and the orphan G protein-coupled receptor 55 (GPR55) have been proposed to act as endocannabinoid receptors (Velasco et al., 2016).

Cannabinoids can be divided into 3 main classes, namely phytocannabinoids, endocannabinoids and synthetic cannabinoids. Phytocannabinoids occur naturally in plants of the *Cannabis* genus (Śledziński et al., 2016). It is widely accepted that Δ^9-tetrahydrocannabinol (THC) is the most potent and abundant cannabinoid in *C. sativa* (Velasco et al., 2016) and is the main psychoactive component (Śledziński et al., 2016). The recreational use of THC induces a euphoric state. Due to these psychoactive/intoxicating effects, there has been limited research on its potential as a pharmaceutical compound (Ligresti et al., 2006). Other abundant phytocannabinoids include cannabidiol (CBD), cannabinol (CBN), cannabigerol (CBG) and cannabidivarin (CBDV) (Śledziński et al., 2016) (**Figure 5**).

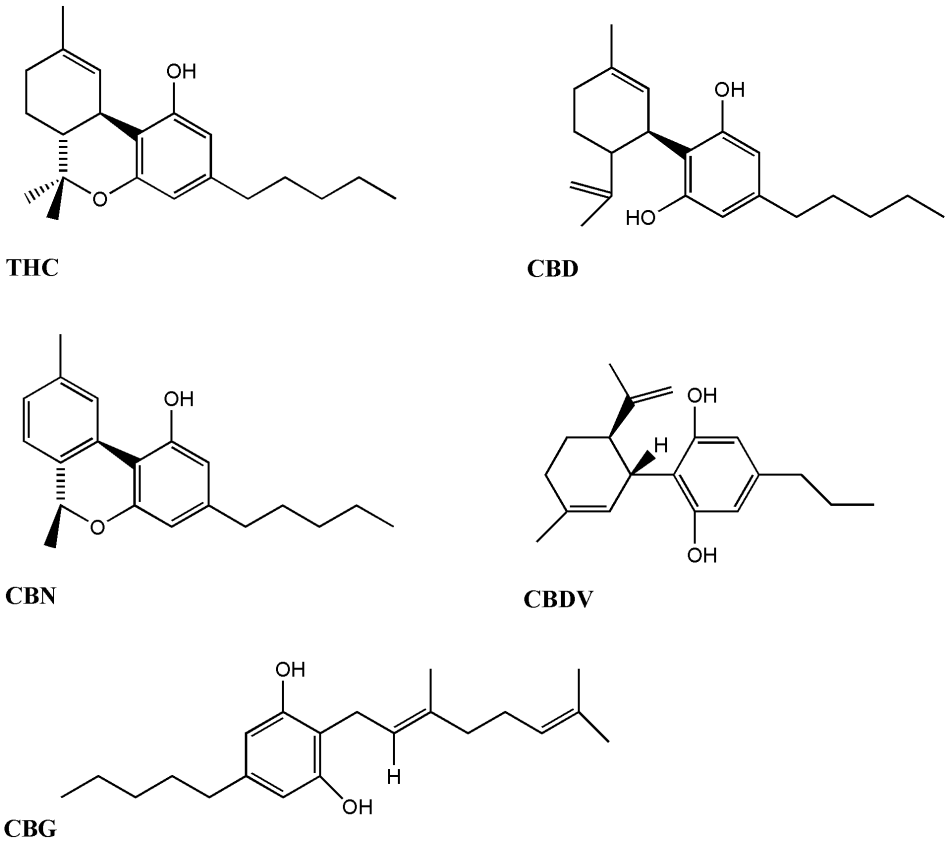

Figure 5: Chemical structures of selected phytocannabinoids found in *C. sativa*
(Chakravarti et al., 2014, Ligresti et al., 2006, Pacher et al., 2006).
(THC – tetrahydrocannabinol; CBD – cannabidiol; CBN – cannabinol; CBDV – cannabidivarin; CBG – cannabigerol)

Endocannabinoids include the endogenous ligands of CB receptors that are part of the endocannabinoid system (Śledziński et al., 2016). The two major endocannabinoids (**Figure 6**) are 2-arachidonoylglycerol (2-AG) and anandamide (AEA) (Pyszniak et al., 2016). Endocannabinoids are rapidly synthesized following an increase in the intracellular calcium level and are released from depolarized postsynaptic neurons and act as retrograde messengers to bind and activate the CB1 receptors at presynaptic terminals. They inhibit the release of neurotransmitters, such as glutamate and *γ*-aminobutyric acid. Apart from its neuromodulatory activity, the endocannabinoid system exerts other regulatory functions in the body such as control of cardiovascular tone, energy metabolism and reproduction (Velasco et al., 2016).

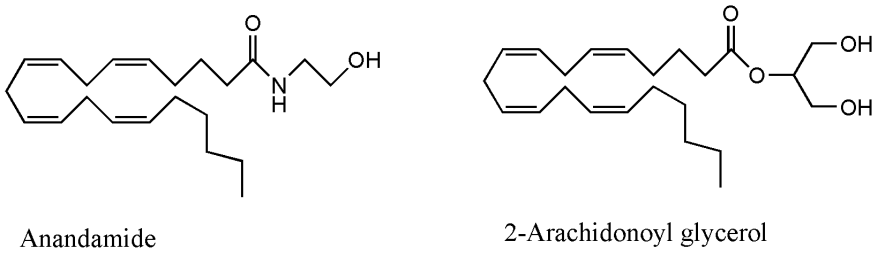

Anandamide 2-Arachidonoyl glycerol

Figure 6: Structures of the two major endocannabinoids.
(Chakravarti et al., 2014, Śledziński et al., 2016).

The third group consists of synthetic cannabinoids, which are compounds that have been chemically synthesized to mimic the properties of natural cannabinoids (E.g. JWH-133 and WIN 55) (Śledziński et al., 2016).

1.5.2. The endocannabinoid system

The endocannabinoid system (ECS) constitutes the endocannabinoids, their receptors and the proteins responsible for their synthesis, transport and degradation (Velasco et al., 2016). The ECS is present throughout the human body and functions by maintaining homeostasis of the body (Sallaberry and Astern, 2018).

At first, it was believed that cannabinoids exerted their effect by non-specifically disrupting cell membranes, due to the lipophilic nature of these compounds. However, the discovery of Δ^9-tetrahydrocannabinol (THC) led to the successful mapping and characterization of cannabinoid binding sites (Zou and Kumar, 2018). Cannabinoid receptor 1 (CB1) was the first receptor in the ECS to be identified and successfully cloned (Devane *et al.*, 1988, Matsuda *et al.*, 1990), and cannabinoid receptor 2 was discovered shortly thereafter (Munro *et al.*, 1993). Both these receptors are G protein-coupled receptors (GPCRs); however, at the protein level, CB1 and CB2 share only a 44% sequence similarity (Zou and Kumar, 2018). CB1 consists of 472 amino acids in humans; however, two additional isoforms with a shorter N-terminus have been reported (hCB1a and hCB1b) both a result of alternative splicing (Ryberg *et al.*, 2005, Shire *et al.*, 1995). CB2 consists of 360 amino acids in humans and two isoforms, (hCB2a and hCB2b) have also been identified (Liu *et al.*, 2009).

The CB1 receptor was first discovered in the brain and was later shown to be the most widely expressed GPCR in the brain, with the highest expression levels in olfactory bulb, cerebellum, hippocampus and basal ganglia, and moderate expression in the

cerebral cortex, septum, amygdala, hypothalamus and parts of the brainstem and dorsal horn of the spinal cord (Kano *et al.*, 2009, Mackie, 2005, Zou and Kumar, 2018). CB1 is also abundantly expressed in the peripheral nervous system, mostly in sympathetic nerve terminals (Tam *et al.*, 2008) and in peripheral tissues in a region-specific manner (Mackie, 2005, Zou and Kumar, 2018). The CB2 receptor was first discovered in the spleen and macrophages (Munro *et al.*, 1993), and has subsequently been found to be expressed in immune cells and is moderately expressed in other peripheral tissues such as the cardiovascular system, gastrointestinal tract, liver adipose tissue, bone and reproductive system (Howlett *et al.*, 2002, Zou and Kumar, 2018).

Due to the promise of utilizing ER stress to selectively target cancer cells, and the possibility that cannabinoids may induce ER stress (as discussed later in Section 4.1), the following chapter summarizes the gap of knowledge in the literature and provides the aims and objectives of the study.

Chapter 2 – Problem statement, aims & objectives and chapter summary

2.1. Problem statement

The importance of ER stress and activation of the UPR in maintaining the malignancy of cancer cells has encouraged research to pursue possible therapies that target ER stress and/or the UPR. One limitation of studying ER stress in cell lines is the absence of a high-throughput method to detect and quantify ER stress. ER stress is usually detected as an endpoint measurement using western blotting and/or quantitative PCR (qPCR), which are time-consuming and expensive, and does not allow for the high-throughput screening of ER stress-inducing compounds. Another limitation of current methods is the ability to distinguish between true ER stress induction and mitochondrial dysfunction-induced ER stress. Due to the crosstalk between the ER and mitochondria, mitochondrial dysfunction may result in ER stress and is indistinguishable from true ER stress induction when measured as an endpoint.

Therapy-induced ER stress that facilitates cell death has several advantages in the treatment of cancer, such as targeting multiple hallmarks of cancer simultaneously without having an effect on normal cells. Several different pharmacological agents have been shown to induce ER stress in the treatment of cancer. Phytocannabinoids from *Cannabis sativa* have been shown to induce ER stress in cancer cells, highlighting their potential as therapeutic compounds. However, there are several limitations with previously conducted research: the molecular mechanisms by which ER stress is induced by cannabinoids has not been fully elucidated. Studies conducted are limited to only a few cancer cell lines and most research was conducted using THC, and occasionally CBD, and as such, the effect of the other cannabinoids on ER stress remains relatively unknown.

2.2. Aims

The aims of this study, therefore, included:

1. To optimize a high-throughput method for the detection and quantification of ER stress.
2. To demonstrate the effect of four cannabinoids (THC, CBD, CBG and CBN) on cell viability, mitochondrial function, the induction of ER stress and the activation of the various branches of the UPR in breast cancer cell lines (MCF7 and MDA-MB-231) and in a non-tumourigenic cell line (MCF10A).
3. To investigate the possible molecular mechanism(s) through which the various cannabinoids induce ER stress in breast cancer cells.

2.3. Objectives

In order to optimize a high-throughput method for the detection and quantification of ER stress (aim 1), the following objectives were completed:

1. Induce ER stress using various controls with distinct mechanisms of induction and measure cell proliferation using the xCelligence real-time cell analyser.
2. At various exposure times, stain cells with a non-conventional fluorescent dye, thioflavin T, and normalize fluorescence to cell number, obtained using the SRB cell viability assay.
3. Perform western blots for GRP78 and CHOP after various exposure times with the positive controls to determine UPR activation and correlate it with the ThT fluorescence per cell.

In order to demonstrate the effect of various cannabinoids on cell viability, the induction of ER stress and UPR activation (aim 2), and to investigate the possible molecular mechanism(s) of action of ER stress induction (aim 3), the following objectives were completed:

1. Treat different breast cell lines (MCF7, MDA-MB-231 and MCF10A) with a concentration range of THC, CBD, CBN and CBG.
2. Monitor changes in cell viability using the MTT cell viability assay

3. Detect the induction of ER stress using ThT staining and determine the NO levels using the Griess reagent.
4. Determine the effect of cannabinoid treatment on mitochondrial inhibition using a tetrazolium redox dye.
5. Confocal microscopy to investigate the origin of cytoplasmic vacuoles.
6. Determine the level of activation within the UPR using western blotting analysis for various UPR components.
7. Detect changes in intracellular Ca^{2+} and ROS using fluorescent stains.
8. Inhibit ROS accumulation using an antioxidant and determine the subsequent effect on ER stress induction.
9. Perform agonist/antagonist studies using capsaicin and curcumin to confirm if the mechanism of action of the cannabinoids occurs via the activation of the TRPV1 receptor.

2.4. Chapter summary

The data for this research was divided into two chapters which correspond to the three aims of the project. The first data chapter (Chapter 3) corresponds to the first aim – to optimize a high-throughput method for the detection and quantification of ER stress. The second data chapter (Chapter 4) corresponds to the second and third aims – to demonstrate the effect of cannabinoids on cell viability, the induction of ER stress and the activation of the UPR, and to investigate the possible molecular mechanism(s) through which the cannabinoids induce ER stress.

Each data chapter contains three sections: an introduction with a brief literature review, materials and methods, and results and discussion. For the methods section, only methods that were new to that chapter were described. The final conclusions and future recommendations are discussed in chapter 5 to provide an overview of the significance of the study. All buffer reagent details, components, equipment and software information, and supplementary data can be found in Appendices i, ii, iii and iv respectively.

2.5. Research Outputs

1. Conference attendances

1.1. Poster presentation

A. de la Harpe, N. Beukes, C. Frost, 2019, 'The molecular mechanisms of endoplasmic reticulum stress induction and subsequent cell death by cannabinoids in different breast cancer cell lines', The 44th FEBS Congress: From molecules to living systems, Krakow, Poland, 6-11 July.

1.2. Oral presentation

A. de la Harpe, N. Beukes, C. Frost, 2019, 'ER stress and mitochondrial dysfunction: a chicken and egg situation, SA Medical Research Council: Advancing Research in the Eastern Cape Province, East London, South Africa, 29-30 August.

2. Proposed article titles for publication in peer-reviewed journals:

2.1. A. de la Harpe, N. Beukes, C. Frost (2020). The use of Thioflavin T for the detection and quantification of ER stress in cancer cell lines (In preparation).

2.2. A. de la Harpe, N. Beukes, C. Frost (2020). CBD induces ER stress through the activation of TRPV1 receptors and ROS production in breast cancer cell lines (In preparation).

Chapter 3 – Thioflavin T optimization

3.1. Introduction

3.1.1. Current ER stress detection methods

Current methods that are utilized to monitor ER stress are indirect methods that detect responses downstream of ER stress. Direct measurements of ER stress include the detection of ER dilation upon ER stress induction (Oslowski and Urano, 2011), or real-time redox measurements. As mentioned previously (section 1.2.1), the ER lumen maintains an oxidizing environment to favour disulphide bond formation via protein disulphide isomerases (PDIs) (Malhotra and Kaufman, 2007, Schröder and Kaufman, 2005). When cells experience ER stress, the UPR enhances disulphide bond formation and promotes oxidative protein folding (Travers *et al.*, 2000). A sustained increase in the protein folding load would ultimately saturate the ER's oxidative folding machinery, hindering disulphide bond formation and protein folding. Therefore, the ER's redox state may deviate in either direction in response to an accumulation of unfolded or misfolded proteins (Merksamer *et al.*, 2008). Merksamer *et al.* (2008) developed the method to measure the redox state of green fluorescent protein (GFP) to measure ER stress. The reporter, ER-targeted redox-sensitive GFP (eroGFP) changes fluorescence upon disulphide bond formation. The fluorescence emission at 490nm increases and decreases at 400nm with the reduction of eroGFP. The fluorescence ratio based on these two wavelengths is a reflection of the ER redox status in cells (Merksamer *et al.*, 2008, Oslowski and Urano, 2011).

Commonly used approaches for detecting ER stress are indirect measurements and include the detection of UPR components using western blotting and qPCR. The ideal method to detect UPR activation would be to measure IRE-1α and PERK phosphorylation, as well as ATF6 cleavage; however, these receptors are expressed at very low levels within cells, increasing the difficulty of detection. Therefore the expression levels of downstream components regulated by these receptors (IRE-1, PERK and ATF6) are more commonly detected (Oslowski and Urano, 2011). These biomarkers may include XBP1s, eIF2α, ATF4, CHOP, GRP78 and PDI. There are several disadvantages to indirectly measuring ER stress, for example, cells are said

to be experiencing ER stress if the expression of downstream UPR components have been induced, such as the molecular chaperone, GRP78. However, this definition is not applicable when the UPR machinery is absent or inactivated (Merksamer *et al.*, 2008). An additional disadvantage of using the UPR to indirectly measure ER stress is that UPR activation indicates that a response had been initiated, but does not indicate if ER homeostasis has been restored (Merksamer *et al.*, 2008).

3.1.2. Thioflavin T

As mentioned previously (Section 1.3), ER stress is defined as an imbalance between protein-folding load and capacity that results in an accumulation of unfolded and/or misfolded proteins in the ER lumen (Giampietri *et al.*, 2015, Merksamer and Papa, 2010, Verfaillie *et al.*, 2013). The most frequent fate of misfolded proteins is self-aggregation, due to the exposure of hydrophobic fragments that are usually buried within the protein (Moreno-Gonzalez and Soto, 2011). The β-sheet conformation is the most common secondary structure identified in misfolded protein aggregates and can accommodate an almost unlimited number of polypeptide chains (Moreno-Gonzalez and Soto, 2011).

The benzothiazole dye, Thioflavin T (4-(3,6-dimethyl-1,3-benzothiazole-3-ium-2-yl)-N, N-dimethylaniline chloride) binds to proteins rich in β-sheet structures (Vassar and Culling, 1959). Thioflavin T (ThT) has commonly been used to monitor amyloid fibril formation *in vitro* (Xue *et al.*, 2017). Amyloid fibrils share a cross-linking β structure, consisting of β-sheets organized in an orientation where the strands run perpendicular to the fibril axis (Nelson and Eisenberg, 2006).

It has been suggested that ThT behaves like a molecular rotor. In solution, the benzylamine and benzothiazole ring rotate freely about their shared C-C bond (**Figure 7A**). This rotation causes a low fluorescence emission for unbound ThT; however, when bound, ThT is immobilized (**Figure 7B**), preserving the excited state and leading to an enhancement of ThT fluorescence (Biancalana and Koide, 2010). The proposed mechanism for ThT binding to amyloid fibrils (**Figure 7C**) involves an alignment of ThT along the fibril axis, allowing the dye to be inserted into hydrophobic grooves (Noël *et al.*, 2013), which does not allow for free rotation around the shared C-C bond, increasing ThT fluorescence (Biancalana and Koide, 2010). Therefore, the tendency

of misfolded proteins to aggregate and preferentially form a β-sheet structure, and the selectivity of ThT binding to this structure suggests that ThT can be used to detect and quantify ER stress in cells.

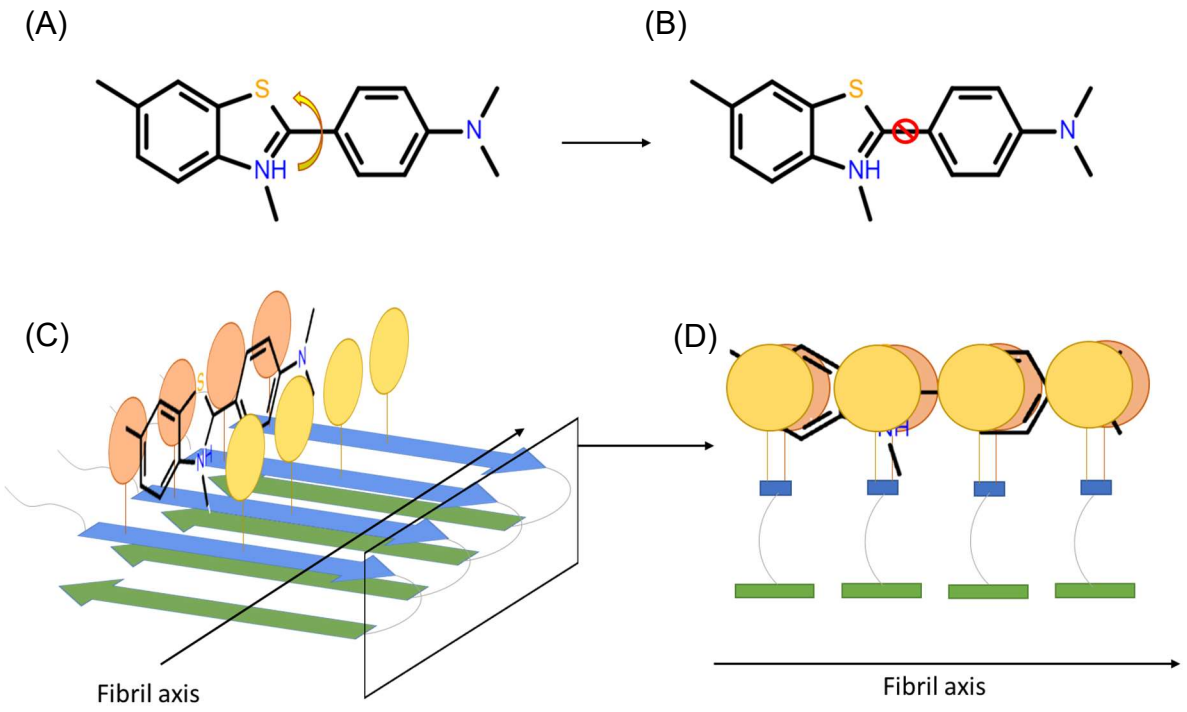

Figure 7: Structure of ThT and proposed model of ThT binding
(A) Structure of ThT in solution showing free rotation around the shared C-C bond between the benzylamine and benzothiazole rings, (B) structure of ThT when bound indicating the immobilization of the shared C-C bond that leads to enhanced fluorescence, (C & D) proposed model of ThT binding to β-sheets parallel to the fibril axis. Red and yellow circles represent hydrophobic residues that interact with the aromatic rings of ThT. Figure adapted from (Noël et al., 2013).
ThT – Thioflavin T.

The use of ThT would provide a more direct method of measuring ER stress by detecting the presence of misfolded proteins within the cell, as opposed to quantifying the activation of downstream responses. Theoretically, the use of ThT would also provide an indication of whether homeostasis had been restored, as seen by decreases in the ThT fluorescence, which would suggest a decrease in the percentage of misfolded proteins in the ER lumen. This chapter discusses the development & optimisation of a high-throughput screening method for the detection and quantification of ER stress via the binding and quantification of misfolded proteins using Thioflavin T.

3.2. Materials and methods

3.2.1. Cell culture and maintenance

The cell lines used in this research were the non-metastatic MCF-7 (ECACC No. 86012803) and metastatic MDA-MB-231 (kind donation from Prof A. Edkins) breast cancer cell lines, as well as the non-tumourigenic MCF10A (kind donation from Prof A. Edkins) breast cell line. Breast cancer is classified into 5 subtypes based on gene expression profiling and immunohistochemical expression of the oestrogen receptor, the progesterone receptor (PR) and human epidermal growth factor-receptor 2 (HER2) (Holliday and Speirs, 2011). These include the luminal A, luminal B, HER2, basal and normal subtypes. Each subtype differs in its prognosis and response to treatment (Sørlie *et al.*, 2001). The MCF7 cell line is a luminal A breast cancer subtype, which is characterized by the presence of the oestrogen and progesterone receptors, and the absence of HER2 (Table 1). Due to the presence of the oestrogen receptor, this subtype is susceptible to hormone therapy (Holliday and Speirs, 2011). The MDA-MB-231 was initially classified as a basal subtype, which is characterized by the absence of oestrogen receptor, PR and HER2 (Table 1). However, it has been re-classified as the claudin-low subtype (Herschkowitz *et al.*, 2007). In addition to the absence of the 3 main cancer cell receptors, the claudin-low subtype is also characterized by down-regulation of genes involved in tight junctions and cell-cell adhesion (claudin-3, -4 and -7), low expression of the proliferation marker Ki67, and high expression levels of markers associated with the epithelial-to-mesenchymal transition (EMT) and cancer stem cell (CSC)-like features (Prat *et al.*, 2010).

Table 1: Differences in receptor expression between the various breast cancer cell lines.
(Holliday and Speirs, 2011, Jhaveri et al., 2004, Meier et al., 2010, Qu et al., 2015, Soule et al., 1990, Subik et al., 2010).

Receptor	MCF-7 (Luminal A)	MDA-MB-231 (Claudin-low)	MCF10A (Basal)
FR	Present	Present	Present
ER	Present	Absent	Absent
PR	Present	Absent	Absent
HER2	Absent	Absent	Absent

FR – folate receptor; ER – oestrogen receptor; PR – progesterone receptor; HER2 – human epidermal growth factor-receptor 2

All the cell lines were cryopreserved and stored at -80°C or in a Dewar canister with liquid nitrogen vapour. The MCF-7 and MDA-MB-231 cell lines were maintained, split and treated in high glucose Dulbecco's modified essential medium (DMEM) and Leibovitz (L-15) media respectively, both supplemented with 10% (v/v) fetal bovine serum (FBS). The MCF10A cell line was maintained, split and treated in DMEM:Nutrient mixture F12 (1:1 v/v) supplemented with 10 µg/mL (1.7 µM) human insulin, 0.5 µg/mL (1.4 µM) hydrocortisone, 20 ng/mL (3.2 nM) human epidermal growth factor (EGF) and 5% (v/v) donor horse serum. MCF7 and MDA-MB-231 cells were kept in a humidified incubator at 37°C with 5% CO_2. MDA-MB-231 cells were incubated in an airtight container to prevent the entry of CO_2, as L-15 is formulated for use in a CO_2 free environment.

At approximately 80% confluency the spent media was removed, and cells were washed with PBS-EDTA (pH 7.4) and subsequently trypsinized using 0.25 % (v/v) trypsin. The cells were split or seeded for the various treatments in their respective medium. Cells were seeded at a density of 10 000 cells/well in 96-well plates and incubated for 24 hours for the MCF7 and MDA-MB-231 cell line, and for 72 hours for the MCF10A cell line.

3.2.2. Positive controls for ER stress induction

The positive controls used to induce ER stress, brefeldin A (BFA), tunicamycin (TNC) and thapsigargin (TG), were selected as they induce ER stress and UPR activation via different mechanisms.

BFA is a macrocyclic lactone produced by a variety of fungi (Härri *et al.*, 1963). Upon BFA treatment, ER stress is induced by the inhibition of adenosine diphosphate (ADP) ribosylation factor (ARF), which reduces coatomer protein assembly and disrupts vesicular transport from the ER to the Golgi apparatus (Donaldson *et al.*, 1992, Klausner *et al.*, 1992). This results in the inhibition of protein secretion from the ER. BFA has also been documented to trigger the collapse and redistribute the Golgi apparatus into the ER (Chardin and McCormick, 1999).

TNC is an antibiotic produced by *Streptomyces lysosuperificus* (Takatsuki *et al.*, 1971). It is a nucleoside analogue inhibitor of the multiple polyprenyl-phosphate-N-acetylhexosamine-1-phosphate-transferase (PNPT) enzymes superfamily (Yoo *et al.*, 2018). TNC blocks N-linked glycosylation by acting as a high-affinity competitive inhibitor of UDP-N-acetylglucosamine (UDP-GlcNAc) in the mammalian enzyme UDP-N-Acetylglucosamine: dolichyl-phosphate N-acetylglucosamine-phosphotransferase (GlcNAc-1-P-transferase, GPT), which catalyses the first and committed step of N-linked glycosylation (Wu *et al.*, 2018, Yoo *et al.*, 2018).

TG is a sesquiterpene lactone that blocks the activity of sarco-endoplasmic reticulum Ca^{2+} ATPases (SERCA), resulting in a rapid depletion of the calcium stores in the ER (Sehgal *et al.*, 2017). This leads to a loss of activity of the calcium-dependent chaperones and ultimately leads to an accumulation of misfolded proteins in the ER lumen (Oslowski and Urano, 2011).

The various cell lines were treated with all three positive controls at concentrations that induce ER stress within a few hours (Table 2).

Table 2: Concentrations of the various ER stress-inducing controls used throughout this project.

Control	Mass/volume concentration	Molar concentration
Brefeldin A	1 µg/mL	3.6 µM
Tunicamycin	1 µg/mL	1.16 – 1.22 µM
Thapsigargin	65 ng/µL	100 nM

The molar concentration of TNC is represented as a range, as the product is a mixture of homologous antibiotics, which differ in their fatty acid components and the fatty acid chain length. The cells were consistently treated at a concentration of 1 µg/mL.

3.2.3. xCelligence electrical impedance assay

The xCelligence real-time cell analyser (RTCA) monitors cell proliferation, morphological changes and changes in viability in adherent cell cultures in real-time. The system utilizes a 96-well microtiter E-plate with a gold microelectrode sensor incorporated into the bottom of each well (**Figure 8B**). When a low voltage is applied, an electric field is generated between the electrodes. The electrical field is impeded by the presence of adhered cells, which is measured as changes in impedance (**Figure 8C**). The level of this change is proportional to the number of attached cells (Atmaca *et al.*, 2016). The impedance values are converted by the RTCA software into the cell index (CI) and recorded as a measurement of adhesion. The greater the CI, the greater the level of cell adhesion (Kho *et al.*, 2015b).

All experimental work completed using the xCelligence RTCA was done at Rhodes University with the assistance of Prof E Prinsloo. Complete media was added to each well and incubated for 30 minutes in the RTCA cradle to coat the microelectrodes and to obtain a baseline reading. The media was removed, and all cell lines used (MCF7, MDA-MB-231 and MCF10A) in the study were seeded at a density of 10 000 cells/well in their respective media. The plate was returned to the RTCA cradle and incubated for 24 hours with readings recorded in 5-minute intervals between sweeps (total of 289 sweeps). After 24 hours, the media was removed, and the various treatments were added. The plate was returned to the RTCA cradle for a further 24 hours with readings recorded with a 1-minute interval between sweeps (total of 1441 sweeps). The corresponding CI curves were plotted and the corresponding growth rates (doubling time) were calculated using the xCelligence RTCA software (Appendix iii – Equipment and software information).

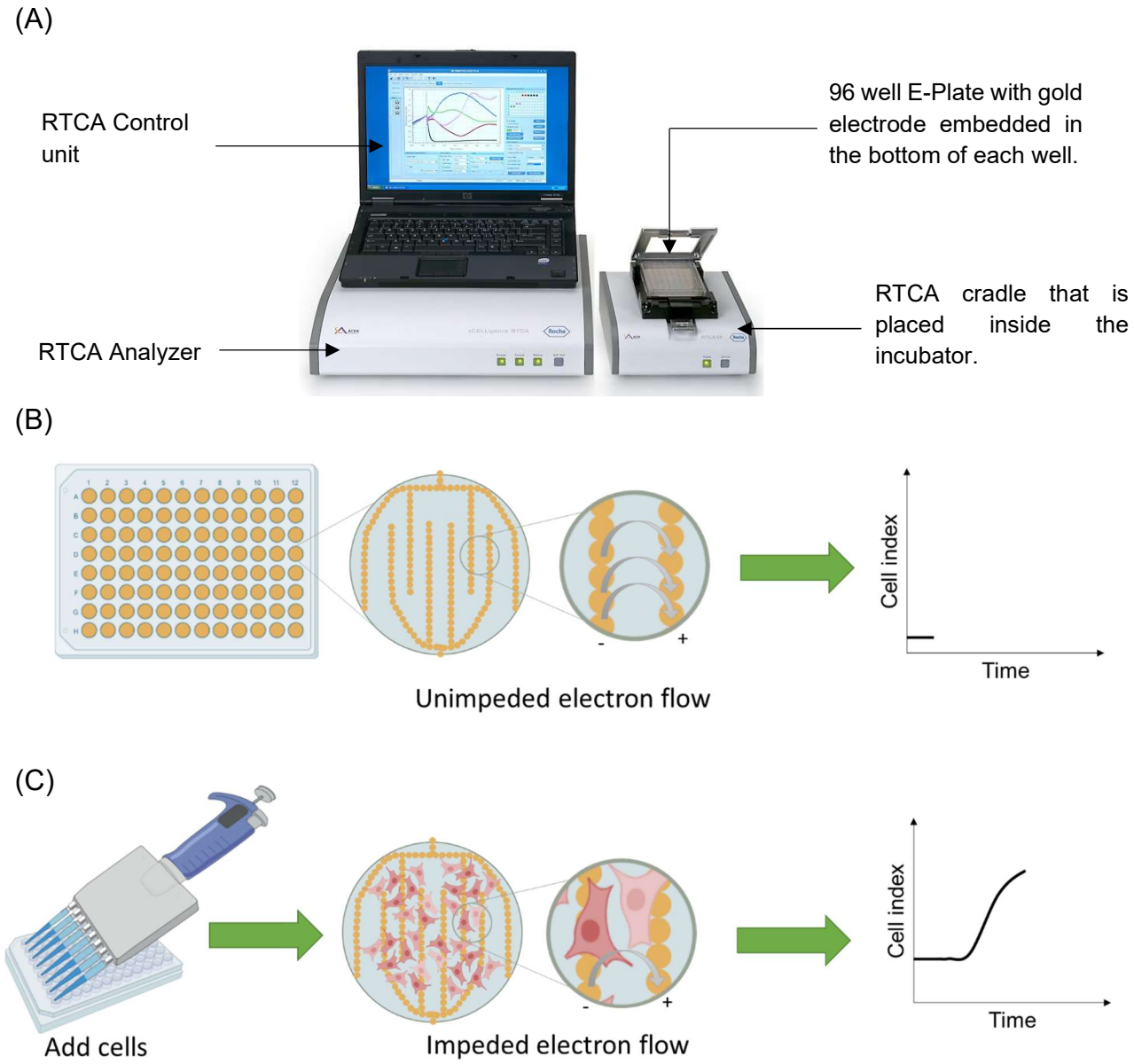

Figure 8: Simplified illustration of the principle of the xCelligence RTCA for measuring cell adhesion based on electrical impedance.
Figure was created using the BioRender online tool and adapted from Hamidi et al. (2017). (A) Overview of the xCelligence RTCA setup, (B) Simplified illustration of the gold microelectrode embedded in the bottom of each well of the 96 well plate. In wells with no cells, electron flow from the negative to the positive terminal is unimpeded and results in a flat baseline reading. (B) Cells are added and attach to the base of the well, resulting in increased impedance of electron flow is and results in an increase in the measured impedance and therefore the cell index.

3.2.4. Optimization of Thioflavin T staining and fluorescence normalization

3.2.4.1. Thioflavin T staining

In order to detect and quantify ER stress, cells were seeded in black, optical bottom 96-well plates. After treatment, they were stained with 5 µM ThT. A 5 mM stock solution was prepared by dissolving the ThT in 70 % (v/v) ethanol and diluting it to 5 mM in ddH_20. The stock solution was diluted in ddH_20 to prepare a 5 µM working solution.

After the various treatments, the spent media was removed, and the cells were fixed with 100 % cold methanol for 10 minutes. The methanol was removed, and cells were permeabilized with 0.1 % (v/v) Triton X-100 in ddH_20 for 10 minutes. The cells were washed 3 times with ddH_20 and stained with the 5 µM working solution for 10 minutes in the dark, after which excess stain was removed by washing 5 times with ddH_20. The fluorescence was measured using a BioTek® SynergyMx microplate reader (E_x/E_m 450/500 nm).

In order to image the cells, they were re-stained with 5 mM ThT and washed 5 times with ddH_20. Images were acquired using the Zeiss Axio Observer fluorescent microscope with the FITC filter (467 – 556 nm). For the duration of image acquisition, the light intensity and exposure were kept consistent for the specific cell line that was being imaged.

3.2.4.2. DAPI staining

A fluorescent DNA-specific fluorescent probe, 4,6-Diamidino-2-phenylindole (DAPI), was used to stain the nuclei of cells. DAPI forms a complex by attaching to the minor groove of adenine-thymine rich sequences of DNA (Kapuscinski, 1995).

After fixation and permeabilization of the cells, they were stained with DAPI. The DAPI staining solution (5 µg/mL) was prepared in ddH_20 and the cells were stained for 10 minutes in the dark, after which they were washed 5 x with ddH_20. The fluorescence was then measured using a BioTek® synergyMx microplate reader (E_x/E_m 358/461 nm).

In order to quantify the number of cells, a cell density standard curve (0 – 80 000 cells/well) was prepared using DAPI staining (Appendix iv – Supplementary data, **Figure 67**).

Images were acquired using the Zeiss Axio Observer fluorescent microscope with the DAPI filter (352 – 447nm). For the duration of image acquisition, the light intensity and exposure were kept consistent for each cell line.

3.2.4.3. SRB assay

Sulforhodamine B (SRB) is a pink aminoxanthene dye with two sulfonic groups. Under mildly acidic conditions, it binds to basic amino acid residues in fixed cells to provide an indication of the cellular protein content (Skehan *et al.*, 1990).

After staining and imaging, the SRB cell viability assay was performed in order to quantify the number of cells present, based on protein content. Fixed cells were stained with 0.4 % (w/v) SRB in 1 % (v/v) acetic acid in ddH_20 for 30 minutes at room temperature. They were washed 5 times with 1 % (v/v) acetic acid and the cell-bound stain was solubilized in 100 µL 10 mM Tris buffer (pH 10.5). The absorbance was read using the BioTek Epoch 2 microplate reader (540 nm).

In order to quantify the number of cells, a cell density standard curve (0 – 80 000 cells/well) was prepared using the SRB cell viability assay (Appendix iv – Supplementary data, **Figure 69**).

3.2.5. SDS-PAGE and western blotting

3.2.5.1. Preparation of cell lysates

Cells were seeded in 6-well plates and grown to ~ 80% confluency. The cells were then treated for various time intervals. Cold lysis buffer was added to the cells and they were incubated for 10 minutes at 4°C. A cell scraper was used to lift the cells and prepare the lysates, which were subsequently aliquoted and stored at -20°C until use.

3.2.5.2. Bradford protein assay

The Bradford protein assay was used to quantify the protein content in the cell lysates. This assay utilizes Coomassie brilliant blue R250, which binds to protein and

undergoes an absorption maximum shift from 465 nm to 595 nm (Bradford, 1976). Bradford reagent (200 µL) is added to the protein sample/standard (10 µL) and incubated for 10 minutes at room temperature. The absorbance was read (595 nm) using the BioTek Epoch 2 microplate reader.

A protein standard curve (0-1 mg/mL) was prepared using the Bradford protein assay and bovine serum albumin (BSA) as a reference protein (Appendix iv – Supplementary data, **Figure 68**).

3.2.5.3. Protein concentration

Cell lysates were diluted to the same protein concentration prior to concentrating the solution using various commonly used methods. Conventionally, isopropanol precipitation is used, however, the resulting protein pellet was largely insoluble in sample buffer and resulted in unequal masses of protein being loaded, due to partial solubilization of the pellet. Various alternative precipitation methods were tested, including alcohol precipitation (ethanol), acid precipitation, namely trifluoracetic acid (TFA) and trichloroacetic acid (TCA), as well as acetone precipitation.

Four cell lysate samples were thawed on ice and the Bradford protein assay was used to determine the concentration of protein. The samples were diluted in lysis buffer to the same concentration and each divided into 4 to test the different concentration methods.

For TCA and TFA precipitation, the respective acid was added to the cell lysates to a final concentration of 10 % (v/v) and samples were incubated at -20°C for 30 minutes. For ethanol precipitation, 9 volumes of cold ethanol were added to 1 volume of sample. For acetone precipitation, 4 volumes cold acetone was added to 1 volume of sample. Samples were then incubated at -20°C for 1 hour. All samples were then centrifuged at 12 045 *xg* for 10 minutes. The organic phase was removed, and the pellet was dried and resuspended in sample buffer. The samples were electrophoresed and separated on a 4 % (v/v) stacking and 10 % (v/v) resolving gel. Gels were stained with Coomassie R250 staining solution and unbound stain was removed using destain solution. Images of the gels were acquired, and ImageJ software (Appendix iii – Equipment and software information) was used for densitometric analysis of the band indicated (**Figure 9A**), as is visible both pre- and post-concentration (**Figure 9A**). The fold

change in the density before and after precipitation of the respective band was calculated (**Figure 9B**).

(A)

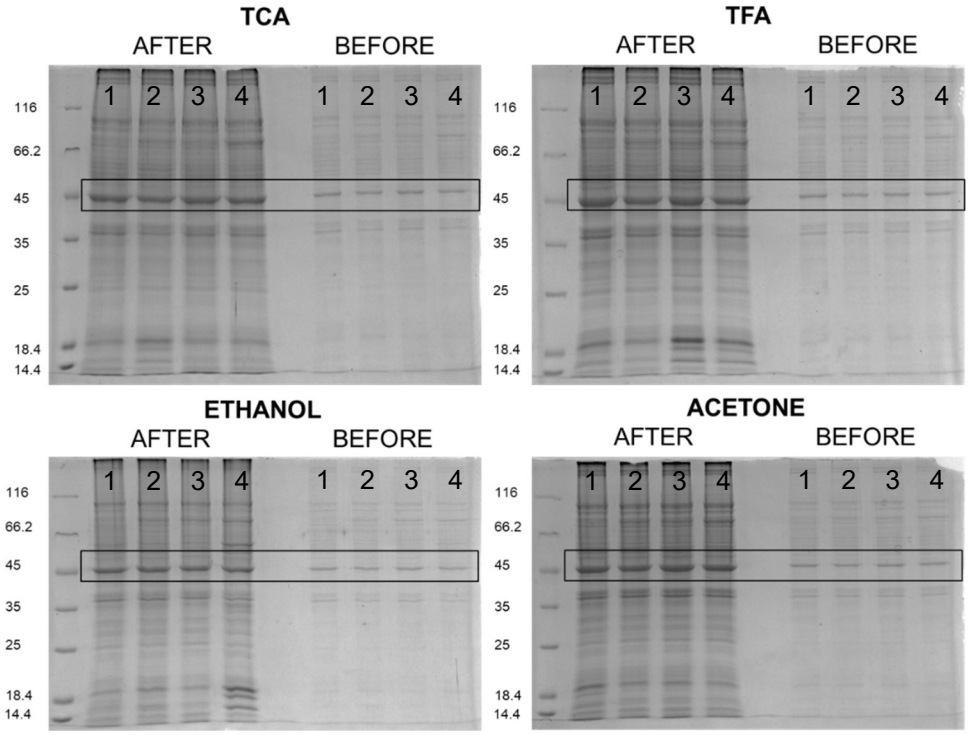

(B)

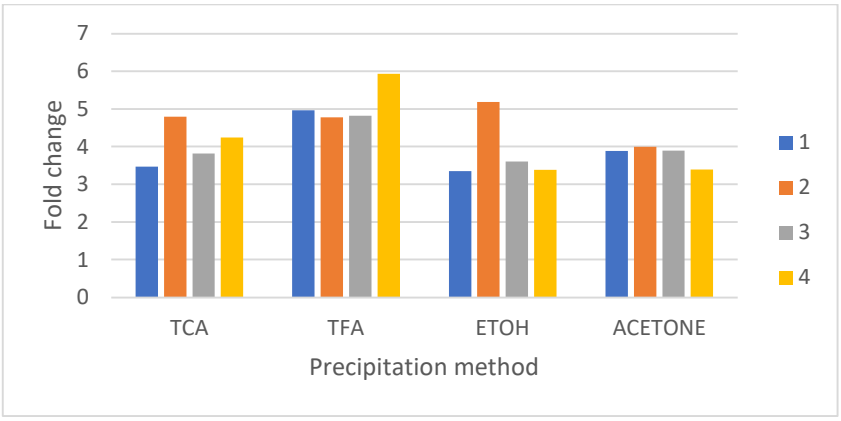

Figure 9: Optimization of TCA, TFA, ethanol and acetone concentration methods on cell lysates.
(A) Stained protein in 10% SDS-PAGE gels before and after concentration using various precipitation methods and (B) fold change in density after each precipitation method relative to the density before precipitation, n=1.

The pellet formed from acetone precipitation proved to be the easiest to resuspend and showed the most consistent fold change before and after precipitation. Overall, this method proved to be the most effective and was used for subsequent experiments.

The protein in the lysates was concentrated using ice-cold acetone by mixing with the lysate in a ratio of 4:1 (v/v) and incubated for 1 hour at -20°C. The protein was then pelleted by centrifuging the samples at 12 045 *xg* using the Eppendorf benchtop mini spin centrifuge. The supernatant was discarded, and the dried protein pellet was resuspended in sample buffer and heated to 95°C for 5 minutes prior to electrophoresis.

3.2.5.4. SDS-PAGE

Sodium dodecyl sulphate-polyacrylamide gel electrophoresis (SDS-PAGE) was used to separate the proteins. The proteins were electrophoresed and separated on a 4 % (v/v) stacking gel and 10 % (v/v) resolving gel. The prepared samples were run alongside a pre-stained molecular weight marker at 100 v until the dye front entered the resolving gel, after which the voltage was increased to 150 v until the dye front reached the bottom of the gel. After separation, the proteins were transferred to a polyvinylidene difluoride (PVDF) membrane using transfer buffer (Appendix ii – Buffer components) and the Semi-dry BioRad Trans-Blot Turbo transfer system (Appendix iii – Equipment and software information) at 20 volts for 20 minutes.

3.2.5.5. Western blotting

The PVDF membranes containing the protein were blocked overnight at 4°C with gentle agitation in blocking solution (Appendix ii – Buffer components). The membranes were washed 3 times for 15 minutes in TBS-Tween20. All primary antibodies were diluted 1:1000 in TBS-Tween20, except histone H3 which was diluted 1:2000 in TBS-Tween20 and added to the membrane. The membranes were incubated with the primary antibody for 2-3 hours at 4°C with gentle agitation. The membrane was washed 3 times with TBS-Tween20 for 15 minutes to remove unbound primary antibody. The appropriate alkaline phosphatase-conjugated secondary antibody was diluted 1:20 000 in TBS-Tween20 and added to the membrane for 3 hours with gentle agitation. The membrane was washed 3 times for 15 minutes with

TBS-Tween20 to remove unbound secondary antibody and the bands were then developed using the BioRad alkaline phosphatase conjugate substrate kit. All antibodies used and the relevant manufacturer information is listed in Appendix i – Reagents and consumables.

Changes in protein expression were measured using ImageJ software (Appendix iii – Equipment and software information) for densitometric analysis. Two methods were used to normalize the western blots in this study. The first was normalization to total protein which was completed for time-dependent studies, due to variations in the expression of housekeeping proteins. The prepared samples were analysed on a 10% SDS-PAGE gel and stained. Densitometric analysis was then performed on the entire lane and used to normalize the target protein. The second normalization method was to a house-keeping antibody, namely Histone H3 or β-Actin. Antibodies for these loading controls were completed alongside the antibody for the target protein and used to normalize the target protein (**Equation 1**, Appendix iv – Supplementary data).

3.2.6. Biolog Redox Dyes

To measure changes in mitochondrial activity associated with mitochondrial dysfunction/inhibition, Biolog redox dye mixes (MA or MB) were used. The dyes contain the same water-soluble tetrazolium, but differ in the electron transfer reagent that transports electrons from intracellular NADH to the extracellular tetrazolium for reduction.

Both dyes can be used for all cell lines, however, one may give a faster reduction rate and the Biolog company reported that dye MB was the preferred dye mix for the MCF7 cell line. MDA-MB-231 cells were seeded for 24 hours prior to treatment with Carbonyl cyanide 4-trifluoromethoxyphenyl hydrazine (FCCP), which was used as a positive control for mitochondrial dysfunction. FCCP is an uncoupler of oxidative phosphorylation. It is a protonophore capable of transferring H^+ into the matrix space across the inner mitochondrial membrane and disrupts the membrane potential, which inhibits ATP synthesis by allowing H^+ to bypass ATP synthesis. In the presence of an uncoupler, respiration proceeds until virtually all of the available oxygen is reduced, and rapid oxidation of substrates proceeds with little to no phosphorylation of ADP *i.e.* it uncouples oxidation from phosphorylation (Kuruvilla *et al.*, 2003).

The MDA-MB-231 cells were then treated with 20 μM FCCP and 20 μL of each dye was added to the respective wells. The cells were immediately incubated at 37°C and the absorbance was read every 30 minutes for 24 hours (**Figure 11**). The absorbances at 590 and 750 nm were read and the absorbance at 750 nm was subtracted from the absorbance at 590 nm (590-750nm) in order to remove non-specific absorbance at 590 nm. The area under the curve (AUC) was calculated using the trapezoidal method, which is a numerical integration method that allows for the calculation of AUC by dividing the total area into trapezoid shapes between 2 consecutive points. The area of a trapezoid is calculated by the following formula:

$$Area = \frac{b1 + b2}{2} \times h$$

where b1 and b2 represent the base and h represents the height of the trapezoid.

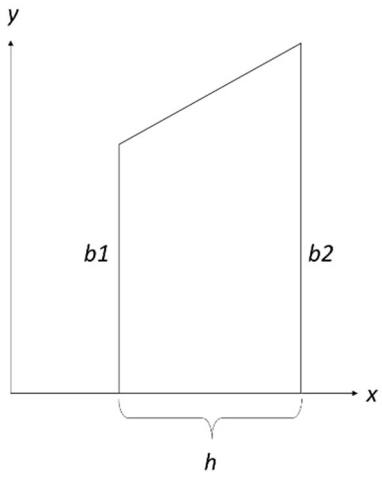

Figure 10: Example of how the area under the curve was calculated using the trapezoid method.

The area of the trapezoid between each consecutive point was calculated, and the total area was calculated by adding up the areas of each trapezoid.

(A)

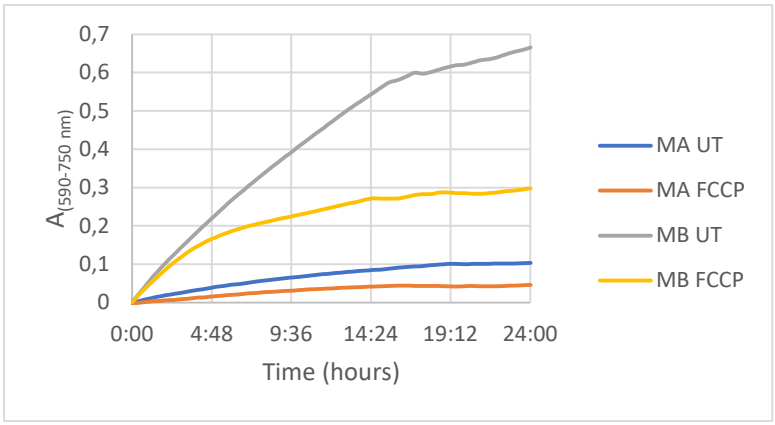

(B)

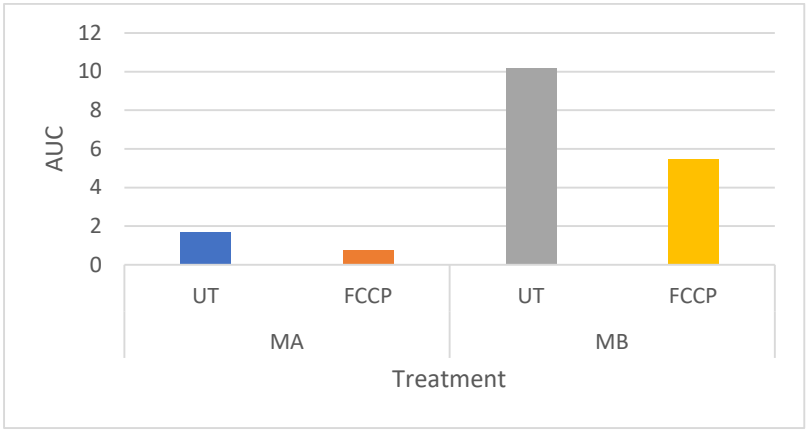

Figure 11: Redox dye reduction by the MCF7 cell line.
(A) Progress curves of redox dye reduction for dyes MA and MB and (B) area under the curve of the progress curves.
UT (untreated), FCCP (carbonyl cyanide 4-trifluoromethoxyphenyl hydrazine) – 20 µM, n=1.

The redox dye MB showed the greatest increase in reduction, as indicated by the large increase in absorbance and area under the curve (AUC) and was therefore used for subsequent experiments for all cell lines.

3.2.7. Statistical analysis

All statistical analysis was completed using the Real Statistics add-in for Microsoft Excel. Significance was determined using single-factor analysis of variance (ANOVA), followed by a post hoc Tukey test and Bonferroni alpha correction for contrasts. Error bars represent the standard deviation of three experiments that were prepared using three different passage numbers for each respective cell line (n=3).

3.3. Results and discussion

Figure 12 provides an overview of the experimental design followed in chapter 3 for the optimization of Thioflavin T (ThT) staining as an alternative method for the detection and quantification of ER stress.

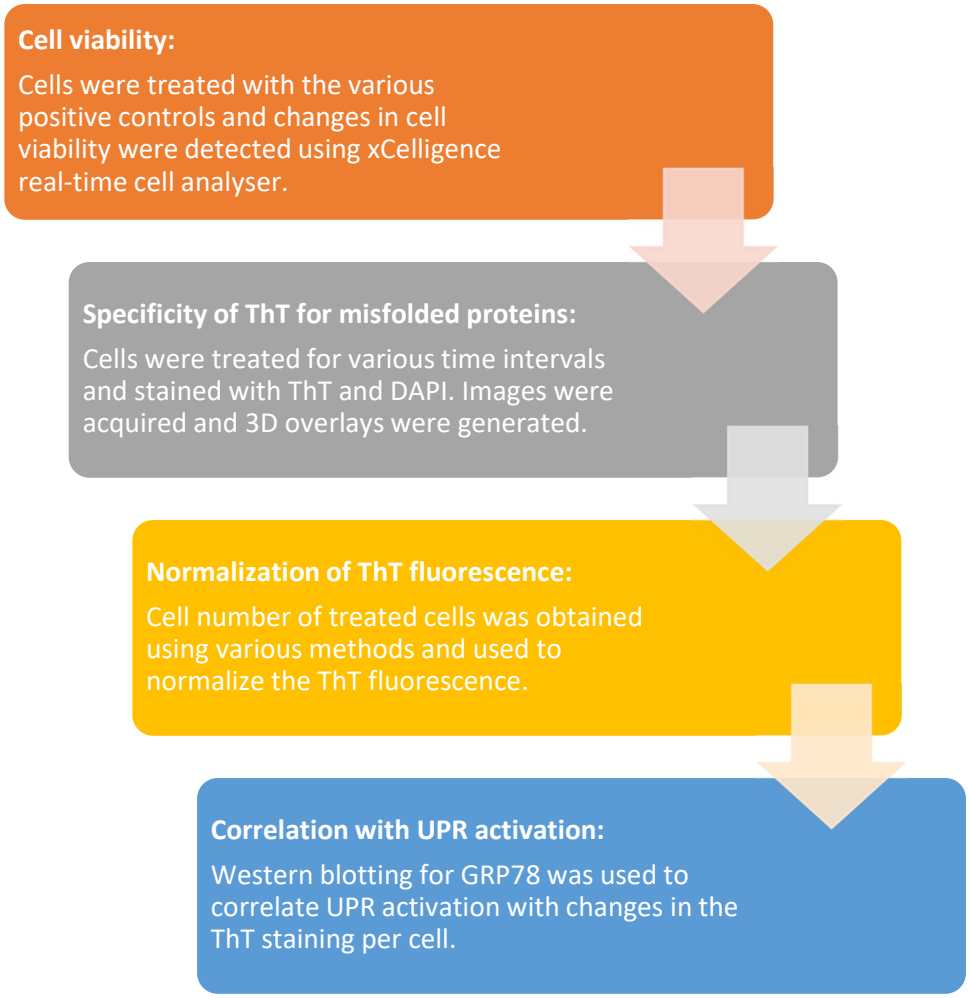

Figure 12: Overview of the experimental design followed in Chapter 3.

3.3.1. Real-time changes in viability

The xCelligence RTCA measured real-time changes in cell viability after treatment with the various ER stress-inducing controls over a 24 period (**Figure 13**). The curves for the 24-hour attachment period are shown in Appendix iv – Supplementary data (Appendix iv – Supplementary data, **Figure 66**).

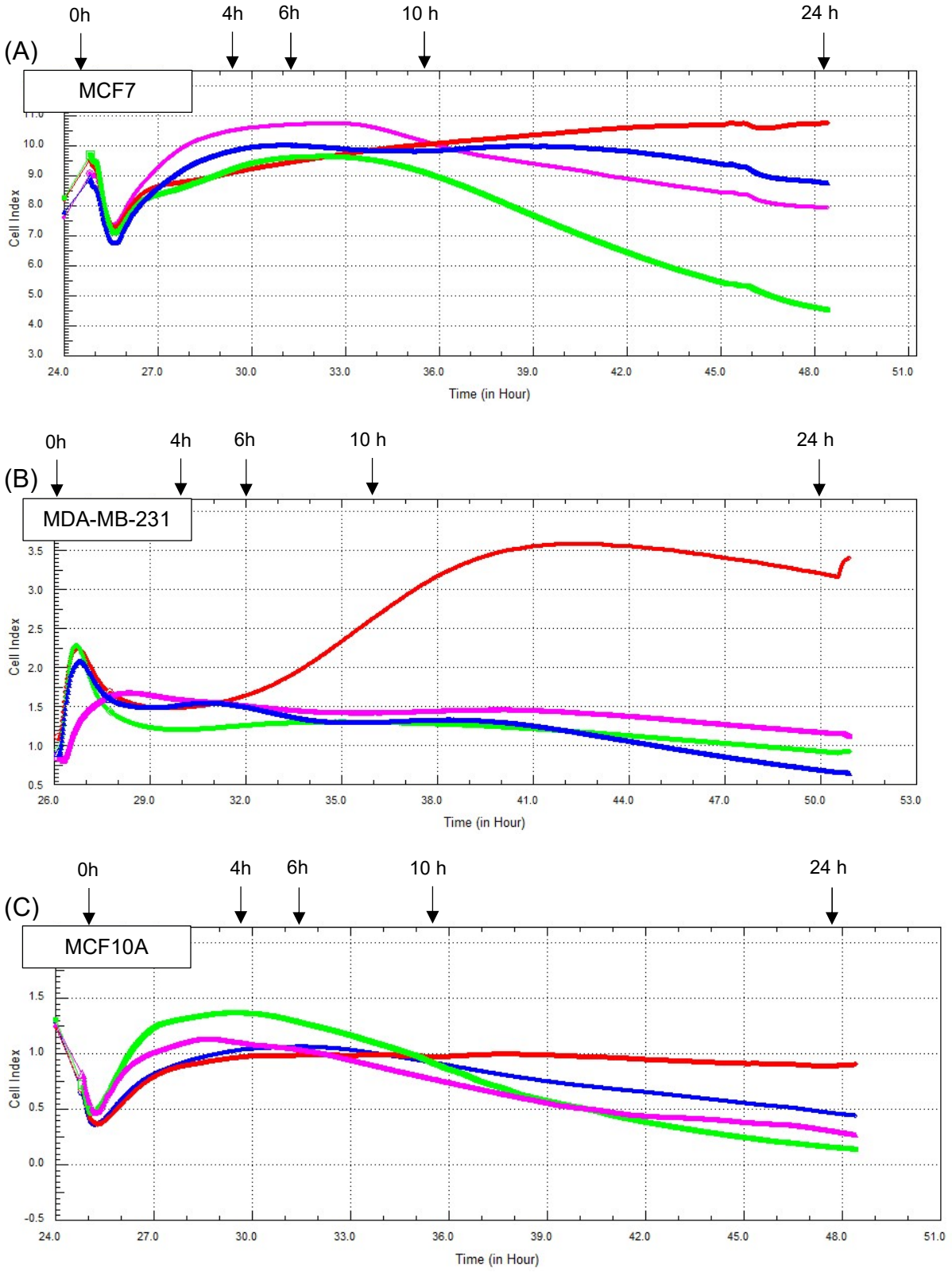

Figure 13: xCelligence curves of various cell lines showing real-time changes in the cell index over 24 hours after treatment with the positive controls.
Untreated (Red), Brefeldin A – 3.6 µM (green), Tunicamycin – 1µg/mL (blue) and Thapsigargin – 100nM (purple), in the (A) MCF7, (B) MDA-MB-231 and (C) MCF10A cell lines, (n=3).

All the ER stress-inducing controls showed a decrease in the CI across the cell lines when compared to the untreated controls. Decreases in the CI are generally due to decreases in viability, causing decreased cell adherence which reduces the electrical impedance and subsequently the CI. However, decreases in the CI can also be due to decreases in the impedance as a result of changes in the cell morphology, such as cell shrinkage that occurs during apoptosis.

BFA treatment showed the greatest decrease in the CI in the MCF7 cell line (**Figure 13A**), followed by TG and then TNC. The CI of cells treated with BFA and TG started to decrease after approximately 10 hours, suggesting that there was a decrease in adherence from this time point. This indicated that ER stress induced by the various positive controls was too severe to restore homeostasis, decreasing cell adhesion and/or triggering an apoptotic pathway. The drastic decrease in the CI of the BFA-treated cells may have been due to a decrease in the expression of Mucin 1 (MUC1) and a collagen type I receptor, the α2β1 integrin (Porowska *et al.*, 2008), which are usually overexpressed in the MCF7 cell line. Porowska *et al.* (2008) found that BFA treatment decreased the cell surface expression of both these receptors in the MCF7 cells, decreasing cell adhesion. This would explain the drastic decrease in the CI in BFA-treated cells, even if cell death had not been induced. TNC treatment showed a slight decrease in the CI at 10 hours, at which point the CI increased slightly until approximately 18 hours. There was then a consistent decrease in the CI. The slight decrease at 10 hours may be due to increased ER stress caused by prolonged exposure to TNC, however, the cells were able to initially recover with minimal proliferation, after which they were unable to recover, and apoptosis was induced. This suggested that the cells are more resistant to TNC-induced ER stress and subsequent cell death than the other controls at the concentrations tested.

In the MDA-MB-231 cell line (**Figure 13B**), all the controls resulted in a lower CI compared to the untreated control starting at approximately 6 hours of exposure; however, they only showed a decrease in their respective CI curves from approximately 15 hours. This suggested that all the controls inhibited cell proliferation between 6 and 15 hours of exposure, after which cell death was induced as indicated by the decrease in the CI value. This suggested that the MDA-MB-231 cell line may be more resistant to ER stress-induced apoptosis, as they are able to modulate ER

stress until a certain point; however, with prolonged stress, homeostasis could not be restored, and apoptosis was induced.

In the MCF10A cell line (**Figure 13C**), all the controls showed a decrease in the CI, after approximately 10 hours of exposure. The difference in the viability between the untreated control and the various controls was less pronounced when compared to what was observed in the MCF7 and MDA-MB-231 cell lines, suggesting that these cells are more resistant to the ER stress inducers at the concentrations tested. This may be due to a slower proliferation rate when compared to the MCF7 and MDA-MB-231 cell lines, as indicated by the CI curve of the untreated cells (**Figure 13**).

To summarize, the MDA-MB-231 cells appeared to be the most sensitive to growth inhibition by the positive controls, but less sensitive to ER stress-induced apoptosis, as they resulted in an inhibition of proliferation from approximately 6 hours of exposure, but only resulted in cell death after a longer exposure time when compared to the MCF7 and MCF10A cell lines. The MCF7 cell line proliferated normally until approximately 10 hours of exposure, after which cell death was induced. This cell line also appeared to be the most susceptible to ER stress-induced apoptosis. The MCF10A cell line exhibited a similar trend to the MCF7 cell line after exposure to the positive controls, however, the cell death that was induced appeared to be less drastic than in the MCF7 cell line.

In order to confirm the decreases in adherence at specific time intervals, the CI value (calculated by the RTCA software based on the electrical impedance) at 0, 4, 6, 10 and 24 hours (indicated by the arrows in **Figure 13**) was calculated as a percentage relative to the untreated control at the respective time of exposure (i.e. the CI at 4 hours for each control was calculated as a percentage of the CI value of the untreated control at 4 hours). These results can be seen in **Figure 14**.

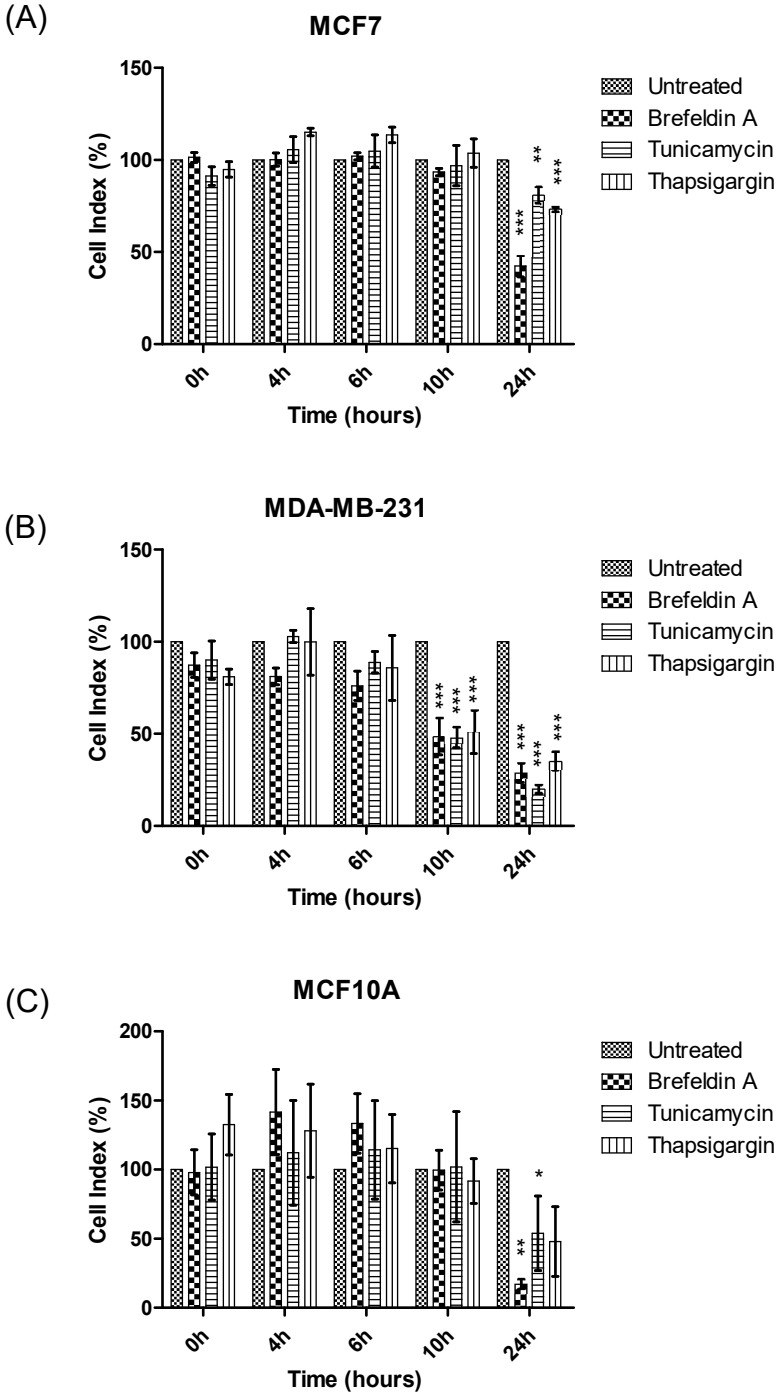

Figure 14: Cell index relative to untreated control (%) of the various cell lines at the respective time intervals after treatment with the controls.
UT – Untreated, BFA – Brefeldin A (3.6 µM), TNC – Tunicamycin (1 µg/mL) and TG – Thapsigargin – (100nM), in the (A) MCF7, (B) MDA-MB-231 and (C) MCF10A cell lines.
*(n=3, * - significant to respective untreated control, * - p < 0.05, ** - p < 0.01, *** - p < 0.001).*

In the MCF7 cell line, the CI of treated cells did not show a significant decrease after 10 hours of exposure; however, this was expected as the xCelligence curves (**Figure**

13A) showed that the CI only started to decrease at approximately 10 hours and would not yet show a significantly decreased CI value when compared to the untreated control at this point. The CI had significantly decreased at the 24-hour time point (**Figure 14A**). BFA treatment resulted in the most significant decrease which, as mentioned previously, may have been due to the inhibition of expression of adherence proteins, causing cells to lose adherence and decrease the CI value.

In the MDA-MB-231 cell line, all controls showed a significantly lower CI than that of the untreated control from 10 hours of exposure (**Figure 14B**). The xCelligence curves (**Figure 13B**) showed that exposure to the various positive controls in the MDA-MB-231 did not result in a decrease in the respective CI curves, but rather indicated that proliferation had been inhibited from 6 hours of exposure. The curves only started to show a decrease in the respective CI values from approximately 15 hours. Therefore, the significantly lower CI at 10 hours was most likely due to a lack of proliferation, rather than the induction of cell death; however, the significantly lower CI at 24 hours was also due to the induction of cell death, as shown by the decrease in the xCelligence curve.

The MCF10A cell line only showed a significant decrease in the CI value after 24 hours of exposure to BFA and TG, with a more significant decrease after BFA treatment (**Figure 14C**). This is consistent with the xCelligence curves that only started to decrease after approximately 10 hours (**Figure 13C**); however, the decrease in the CI was less drastic when compared to the MCF7 cell line. This suggested that the MCF10A cell line was the most resistant to the induction of ER stress and subsequent apoptosis under the conditions tested.

3.3.2. ThT staining and data normalization

After treatment of the various cell lines with the different positive controls for 0, 4, 6, 10 and 24 hours, the cells were fixed and stained with ThT and the fluorescence measured. The cells were then stained with an increased concentration of ThT and DAPI for image acquisition.

ImageJ was used to convert the images of stained cells containing only the FITC channel (ThT staining) into 8-bit images. A region of interest (ROI) containing individual cells was outlined (Appendix iv – Supplementary data, **Figure 70**), and a 3D

plugin was used to generate a 3D surface plot, where the fluorescence intensity emitted by the cell was measured and interpreted as height. A colour scale was also applied, where red indicates areas of increased staining intensity, and blue indicates areas of lower staining intensity. This plot was used to show the localization of ThT staining within the cells (**Figure 15**, **Figure 21** & **Figure 23**).

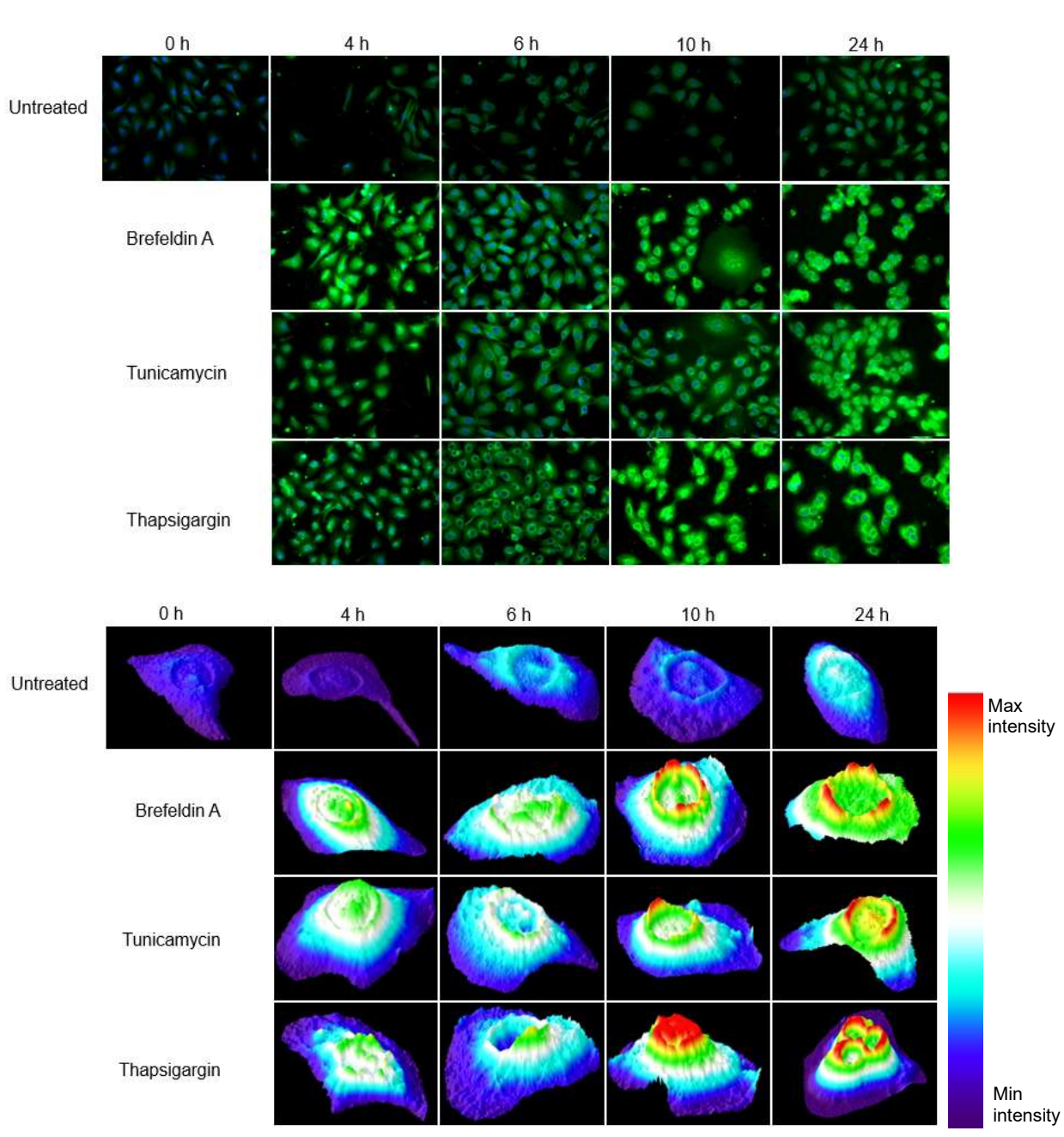

Figure 15: Representative fluorescent images of MCF7 cells stained with ThT.
(A) Representative fluorescent images (200 x magnification) of MCF7 cells treated for various time intervals and stained with ThT and (B) 3D surface plot showing localization of ThT staining within individual cells.
Untreated, Brefeldin A – 3.6 µM, Tunicamycin – 1µg/mL, Thapsigargin – 100nM

The MCF7 cells stained with ThT and DAPI (**Figure 15A**) after treatment with the three positive controls at various time intervals illustrated a dramatic increase in ThT fluorescence relative to the untreated control. Individual treatments also showed an increase in the fluorescence intensity with increasing exposure time, thus indicating that there was an increase in bound ThT and thus misfolded proteins within the cell. The increase in fluorescence intensity appeared to be localized around the nucleus (**Figure 15A**). This was confirmed when the images were represented as 3D surface plots (**Figure 15B**), highlighting that increasing exposure time resulted in increased fluorescence (represented by increased height) around the nucleus, suggesting that there was increased ThT binding. Since the lumen of the peripheral ER is continuous with the nuclear envelope (Voeltz *et al.*, 2002), the increased ThT binding around the nucleus suggested that ThT was preferentially bound to the increased misfolded proteins within the ER lumen. Beriault and Werstuck (2013) also showed that ThT binding within the cell was colocalized with the ER chaperones GRP78/94 (anti-KDEL) in an immunoblot assay.

ThT has been used to stain cells and capture images using a fluorescent microscope for qualitative analysis (King *et al.*, 2019, Mamrosh *et al.*, 2014, Parafati *et al.*, 2018). However, in order to quantify the bound ThT per cell, images were captured and microscope software platforms were used to quantify the ThT intensity per cell (Besio *et al.*, 2019) or ImageJ was used, most commonly for threshold analysis (Beriault and Werstuck, 2013, Huiting *et al.*, 2018). These quantitative analysis methods are not high-throughput and require that individual fluorescent images are captured. Therefore, a high-throughput method was required to quantify the ThT per cell. In order to quantify ER stress using the ThT staining, the fluorescence of stained cells was measured using a fluorimeter and normalized to cell number, which is traditionally determined using metabolism-based assays, such as MTT or resazurin. In order to normalize the ThT fluorescence, a non-metabolic estimation of cell number was required. DAPI staining was initially used to obtain cell number to normalize the ThT fluorescence of the different cell lines (**Figure 16**).

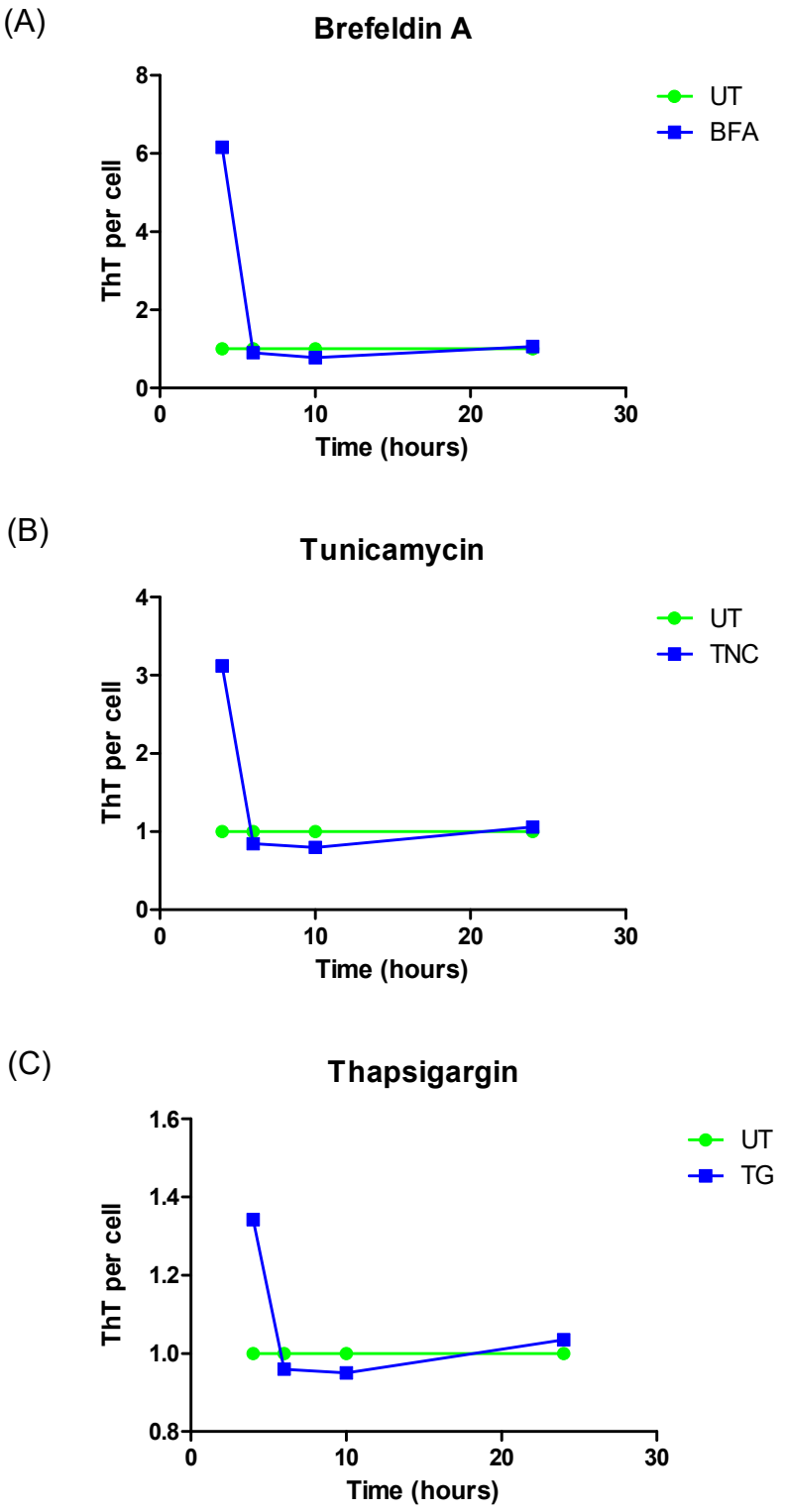

Figure 16: Fold change in the ThT/cell of MCF7 cells treated with the various controls when normalized to cell number obtained using DAPI staining.
Cells were treated with (A) Brefeldin A, (B) Tunicamycin and (C) Thapsigargin for various time intervals. UT (Untreated), BFA (Brefeldin A) – 3.6 µM, TNC (Tunicamycin) – 1 µg/mL, TG (Thapsigargin) – 100 nM, n=1

Regardless of the positive control, bound ThT per cell in the MCF7 cell line increased at 4 hours. Thereafter, the ThT per cell decreased and showed little to no change in the ThT/cell from 6 to 24 hours (**Figure 16**). This was inconsistent with the fluorescent images of MCF7 cells (**Figure 15A**) which highlighted a pronounced increase in fluorescence with increased exposure times. This may have been due to apoptotic chromatin condensation, which is characteristic of cells undergoing apoptosis (Toné *et al.*, 2007). When these cells are stained with nuclear dyes, such as DAPI, the condensed chromatin displays increased levels of fluorescence compared to non-condensed chromatin. Toné *et al.* (2007) demonstrated that cell nuclei undergoing apoptosis *in vitro* appeared to follow three stages of apoptotic chromatin condensation: ring condensation, necklace condensation and nuclear collapse/disassembly. The first stage is characterized by a continuous ring of condensed chromatin at the interior surface of the nuclear envelope. In the second stage, discontinuities are seen in the ring and in the third stage, apoptotic bodies from the nucleus separate into individual fragments. **Figure 17** shows the individual DAPI channel of the images shown in **Figure 15**, in order to demonstrate the changes in the nuclei that were observed.

An increase in the DAPI fluorescence after treatment with the various ER stress-inducing controls was observed (**Figure 17A**); however, the ring structure described by Toné *et al.* (2007) was seen in the nuclei of cells from 6 hours of exposure time, particularly in the cells treated with TG (**Figure 17B**), as indicated by the arrow. BFA and TNC treated cells did not show the ring structure, but showed increased fluorescence compared to the untreated control, suggesting chromatin condensation had occurred. This indicated that the cells were in the early stages of apoptosis, which was consistent with the xCelligence curves for the treated MCF7 cells (**Figure 13A**), where the CI decreased after approximately 10 hours of exposure time. This suggested that after 10 hours of exposure to the positive controls, the treated cells were possibly undergoing apoptosis. The increase in the DAPI fluorescence of apoptotic nuclei after 6 hours of exposure to the controls (**Figure 17A**) resulted in an over-estimation of cell number when extrapolated from the standard curve (**Figure 67** - Appendix iv – Supplementary data) and result in a decrease in the calculated ThT staining per cell once the ThT fluorescence was normalized to cell number (**Figure 16**). To confirm this, the extrapolated cell numbers obtained after treatment and DAPI staining were plotted (**Figure 18**).

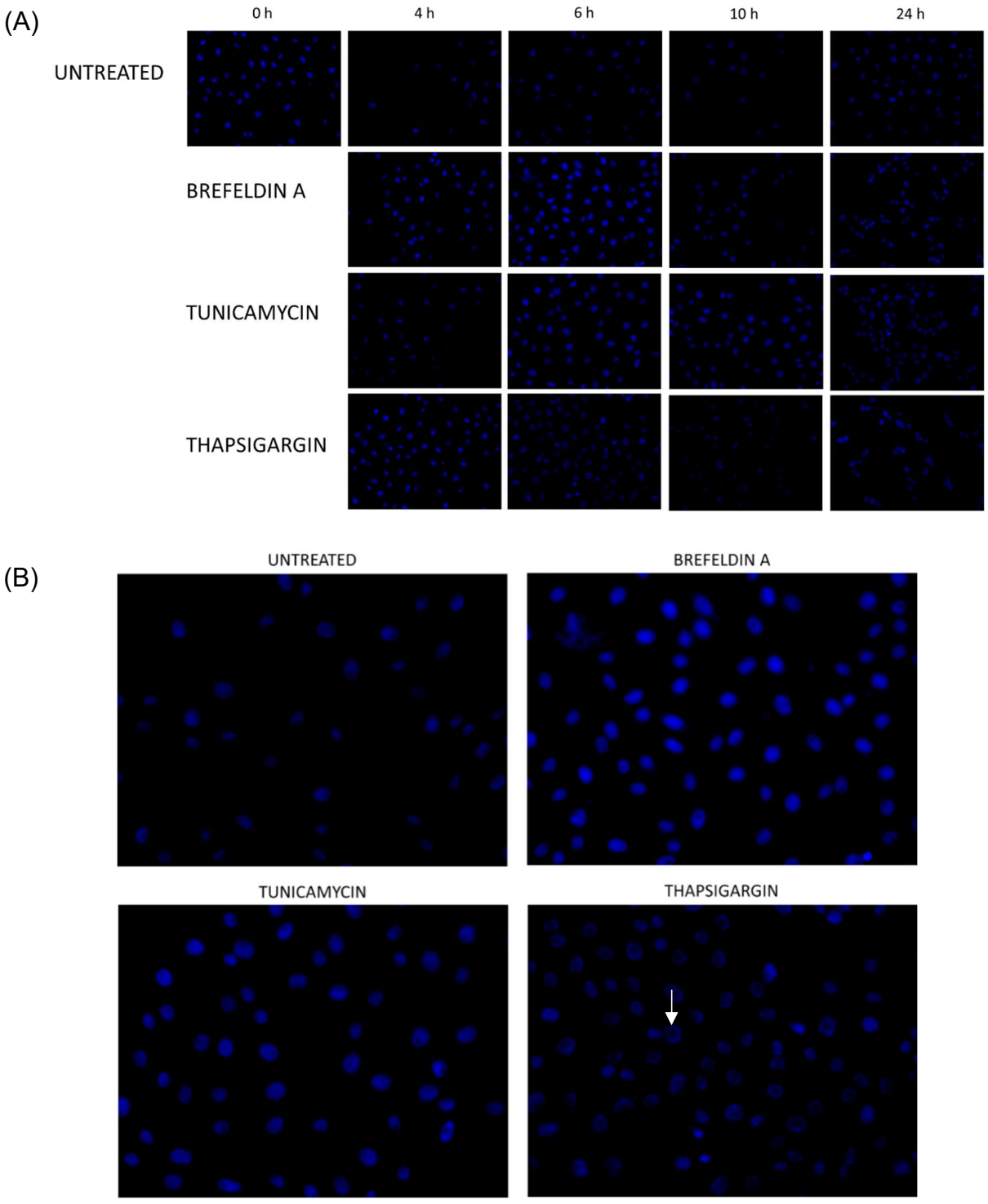

Figure 17: Representative images of MCF7 cells stained with DAPI after treatment for various time intervals.
(A) DAPI staining after treatment for various time periods and (B) DAPI staining at 6 hours of exposure demonstrating increased fluorescence and ring structure characteristic of early apoptosis. Untreated, Brefeldin A – 1 µg/mL, Tunicamycin – 1 µg/mL and Thapsigargin – 100 nM

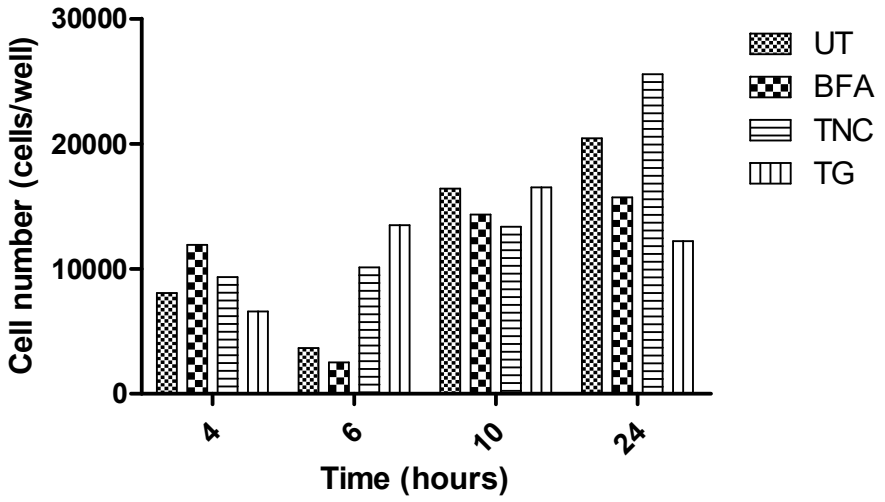

Figure 18: Cell number determined using DAPI staining in the MCF7 cell line after extrapolation from a cell density standard curve.
Untreated, Brefeldin A (BFA) – 3.6 µM, Tunicamycin (TNC) – 1µg/mL and Thapsigargin (TG) – 100nM, (n=1)

Cells were seeded at a density of 10 000 cells per well. At 4 hours, the extrapolated cell number after the various treatments was slightly greater than that of the untreated. At 6 hours, the extrapolated cell number for tunicamycin and thapsigargin treated cells illustrated an increased number of cells when compared to the untreated cells (**Figure 18**). The same trend was observed after 24 hours of treatment, where a much greater cell number was obtained for the TNC treated cells, which did not correlate with the measured decrease in cell viability (**Figure 13A**). As previously mentioned, the increased fluorescence may have been due to apoptotic chromatin condensation, which resulted in an increased DAPI fluorescence and an over-estimation of cell number. Due to the problems faced with normalizing ThT fluorescence to cell number obtained using DAPI staining, this method of normalization was discontinued for subsequent analysis, as the increase in DAPI staining resulted in an over-estimation of cell number.

The SRB cell viability assay was subsequently used to determine the cell number (**Figure 19**) based on protein content to normalize the ThT fluorescence. After fixing, staining and measuring the fluorescence of treated cells, the SRB assay was performed and cell number was extrapolated from a cell density standard curve prepared using the SRB assay (Appendix iv – Supplementary data, **Figure 69**).

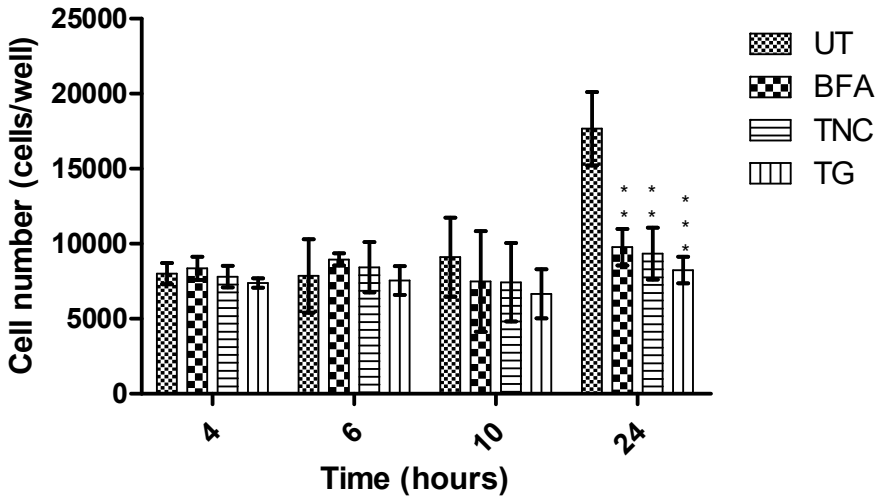

Figure 19: Cell number determined using SRB assay and extrapolation from a cell density standard curve in the MCF7 cell line
Untreated, Brefeldin A (BFA) – 1 µg/mL, Tunicamycin (TNC) – 1µg/mL and Thapsigargin (TG) – 100nM
*(n=3, * - significant to respective untreated control, * - p < 0.05, ** - p < 0.01, *** - p < 0.001).*

Cell number obtained from the SRB assay (**Figure 19**) proved to be more consistent, showing the expected change in cell number based on the xCelligence curves (**Figure 13**), and the changes in the CI value (**Figure 14**). There was little to no difference in cell number between the untreated and treated cells at 4 and 6 hours (**Figure 19**). However, after 10 hours of exposure to the controls, the cells started to show a decrease in cell number (**Figure 19**), which was consistent with the decrease in the CI seen at 10 hours for all treatments (**Figure 14**). A significant decrease in cell number was observed at 24 hours, which was consistent with the significant decrease in the CI observed at 24 hours.

To determine if the changes observed in the normalized ThT fluorescence per cell could be represented as an accurate measurement of ER stress, it had to be correlated with UPR activation. Western blot analysis was used to evaluate changes in GRP78 expression to indicate the activation of the UPR. GRP78 is a chaperone upregulated during early ER stress by all three branches (IRE-1α, PERK and ATF6) and would not be affected by selective activation of individual branches. The expression of GRP78 was measured with densitometric analysis using ImageJ and normalized to total protein. A traditional loading control antibody was not used due to analysis occurring over various time points. Analysis under these conditions has been shown to cause

the levels of traditional loading controls, such as histone H3, to fluctuate (Beukes *et al.*, 2019).

The ThT fluorescence was normalized to cell number obtained using the SRB cell viability assay, after treatment with various ER stress-inducing positive controls. The ThT fluorescence per cell, as well as the normalized GRP78 expression, were calculated as a fold change relative to the untreated cells. Therefore, the data for the untreated cells is represented by an arbitrary unit of 1 (**Figure 20**, **Figure 22** & **Figure 24**).

After 4 hours of exposure, the fold change in the ThT per cell for the MCF7 cell line treated with BFA was comparable to that of the untreated cells (**Figure 20A**). The TNC and TG treated cells showed an increase in the ThT per cell after 4 hours of exposure (~1.5-fold for both treatments, **Figure 20C & E**). This suggested that there was an increase in the accumulation of misfolded proteins in the ER lumen, leading to increased binding of ThT. However, with the increasing exposure time, there was a decrease in the amount of bound ThT per cell at 6 hours of exposure for all treatments, suggesting that there was a decrease in misfolded proteins within the ER lumen. This decrease in the ThT per cell was accompanied by an increase in the GRP78 expression at 6 hours, with significant increases in GRP78 expression in TNC and TG treated cells (**Figure 20D & F**). Treatment with TNC and TG showed the greatest decrease in the bound ThT per cell compared to the BFA-treated cells. The data indicated that ER stress induced after 4 hours of exposure resulted in the activation of the UPR since GRP78 would be titrated away from the UPR sensors to refold the misfolded proteins ultimately resulting in an increase in GRP78 expression in an attempt to refold the proteins to restore the balance between the ER's protein-folding load and capacity, leading to a decrease in the bound ThT at 6 hours. All treatments showed an increase in the ThT per cell at 10 hours with little to no increase in GRP78 expression, suggesting that the GRP78 expression induced at 6 hours was not sufficient to overcome the accumulation of misfolded proteins. The decrease in the ThT per cell at 24 hours, which was most likely due to the significant decrease in cell viability at 24 hours (**Figure 14A**). These results suggested that between 10 and 24 hours of exposure, ER stress was too severe, and homeostasis could not be restored, resulting in the induction of cell death.

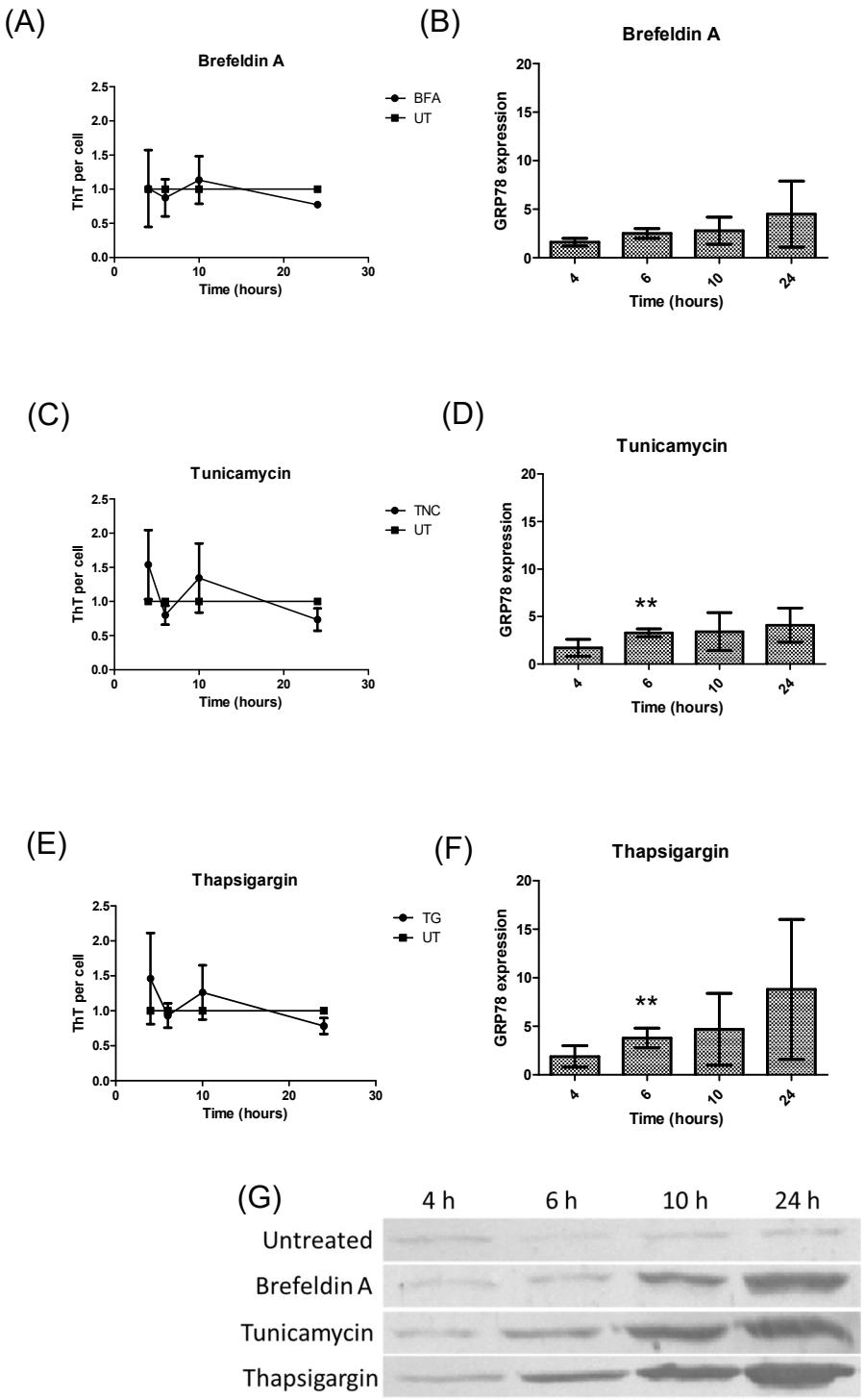

Figure 20: The correlation between ThT per cell and UPR activation for the detection of ER stress in the MCF7 cell line.

Fold change in (A, C, E) ThT per cell and (B, D, F) GRP78 expression after treatment with Brefeldin A, tunicamycin and Thapsigargin for various time intervals in the MCF7 cell line. Changes in GRP78 expression and ThT/Cell were calculated as a fold change of the untreated cells at the respective exposure time. Therefore, untreated is represented by an arbitrary unit of 1.

*Untreated, Brefeldin A – 3.6 μM, Tunicamycin – 1 μg/mL and TG – 100 nM (n=3, * - significant to respective untreated control, * - p < 0.05, ** - p < 0.01, *** - p < 0.001).*

The data obtained for the MCF7 cell line showed a correlation between the fold change in the ThT per cell and UPR activation (GRP78 expression), *i.e.* an increase in GRP78 expression correlated with a decrease in the ThT per cell. Therefore, the use of ThT to measure ER stress appeared to provide the advantage of illustrating that ER homeostasis had been restored at 6 hours, which was not illustrated when solely using UPR activation to measure ER stress.

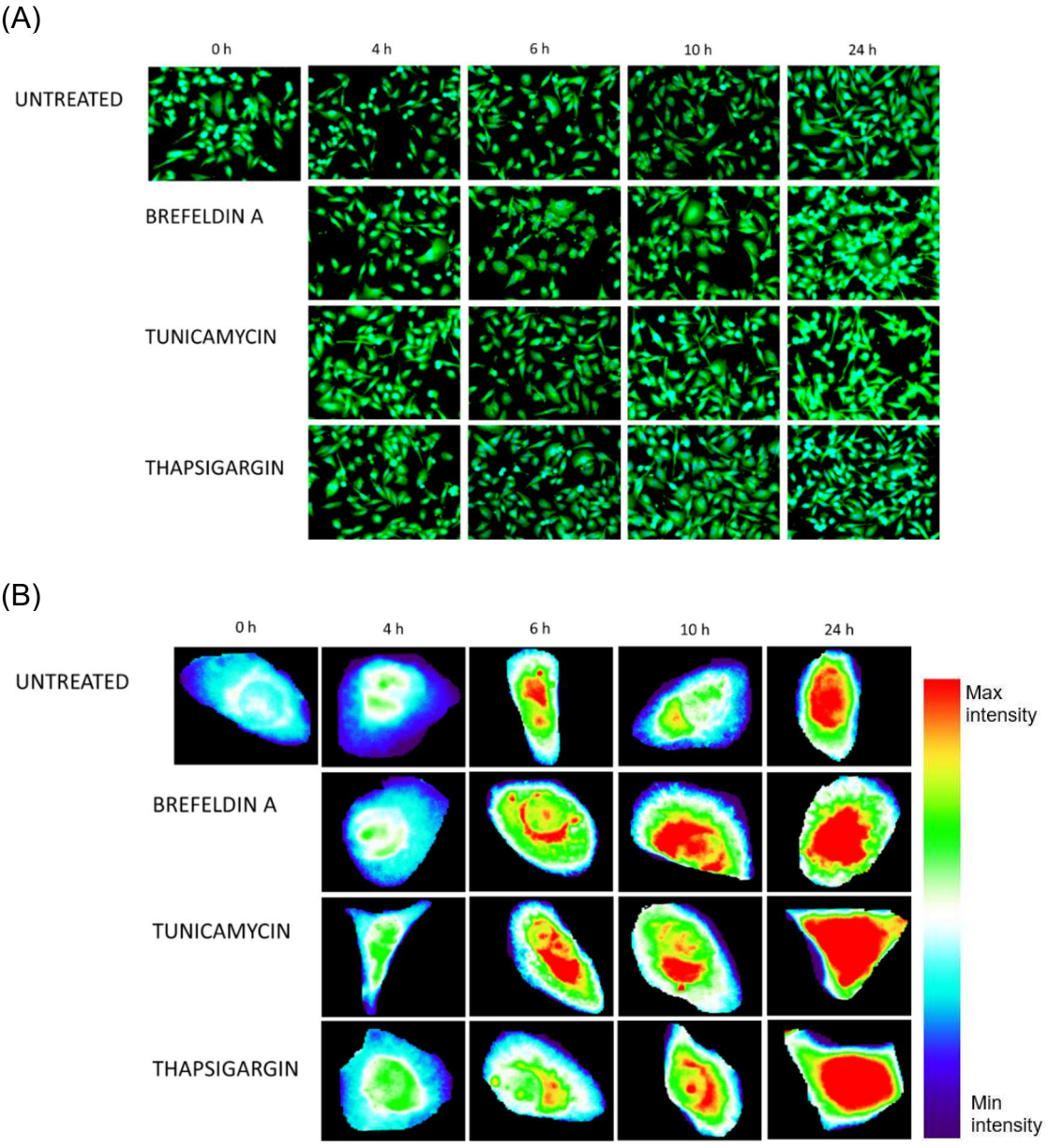

Figure 21: Representative fluorescent images of MDA-MB-231 cells stained with ThT.
(A) Representative fluorescent images (200 x magnification) of MDA-MB-231 cells treated for various time intervals and stained with ThT and (B) 3D surface plot showing localization of ThT staining within individual cells.
Untreated, BFA (Brefeldin A) – 3.6 μM, TNC (Tunicamycin) – 1μg/mL, TG (Thapsigargin) – 100nM

As in the case with the MCF7 cell line, the MDA-MB-231 cells displayed an increase in fluorescence after treatment (**Figure 21A**); however, the variation in fluorescence between the MDA-MB-231 untreated and positive controls was less distinguishable. The MDA-MB-231 untreated control showed a relatively high fluorescence when compared to the MCF7 cell line, suggesting the presence of a higher percentage of misfolded proteins. This indicated that the MDA-MB-231 cell line either had increased protein flux through the ER, and therefore contained an increased unfolded protein load within the ER lumen, or it experiences higher levels of basal ER stress, due to its specific physiological conditions, or a combination thereof. The overall increases in fluorescence across untreated and treated cells made the visual effect of the ER stress-inducing controls less significant, however, an increase was seen after 24 hours of exposure. The 3D overlay for the MDA-MB-231 cell line also illustrated the localization of ThT binding to be primarily around the nucleus, with increased ThT binding with increasing exposure time (**Figure 21B**).

The bound ThT per cell remained relatively constant between 4 and 10 hours of exposure relative to the untreated cells (**Figure 22A, C & E**). This suggested that there was a decrease in the concentration of misfolded protein within the cell. All the controls showed a sharp increase in bound ThT per cell between 10 and 24 hours. The treatments showed minimal change in GRP78 expression between 4 and 6 hours and a larger time-dependent increase between 6 and 10 hours (**Figure 22B, D & F**). The MDA-MB-231 cells showed a higher level of basal GRP78 expression (**Figure 22G**), when compared to the MCF7 cells (**Figure 20G**), suggesting that the MDA-MB-231 cell line had a higher resistance to ER stress induction by the controls used. This highlights why this cell line did not show an increase in misfolded proteins or GRP78 expression in the first 10 hours, as they may have had the capacity to refold the misfolded proteins without requiring additional upregulation of GRP78 expression, or ER stress may have only been induced after 10 hours of exposure. The increased GRP78 expression after 10 hours facilitated the attempt to refold the excess misfolded proteins induced by the positive controls and partially restored ER homeostasis, which may potentially indicate that ThT per cell decreased slightly after 10 hours of exposure. However, due to the prolonged exposure, homeostasis could not be completely restored and cell death was induced between 10 and 24 hours (at ~15 hours, **Figure 13B**), indicating that despite the cell lines increased resistance to ER stress, there was

an accumulation of misfolded proteins, as depicted by the increased bound ThT per cell and GRP78 expression at 24 hours, which ultimately resulted in cell death.

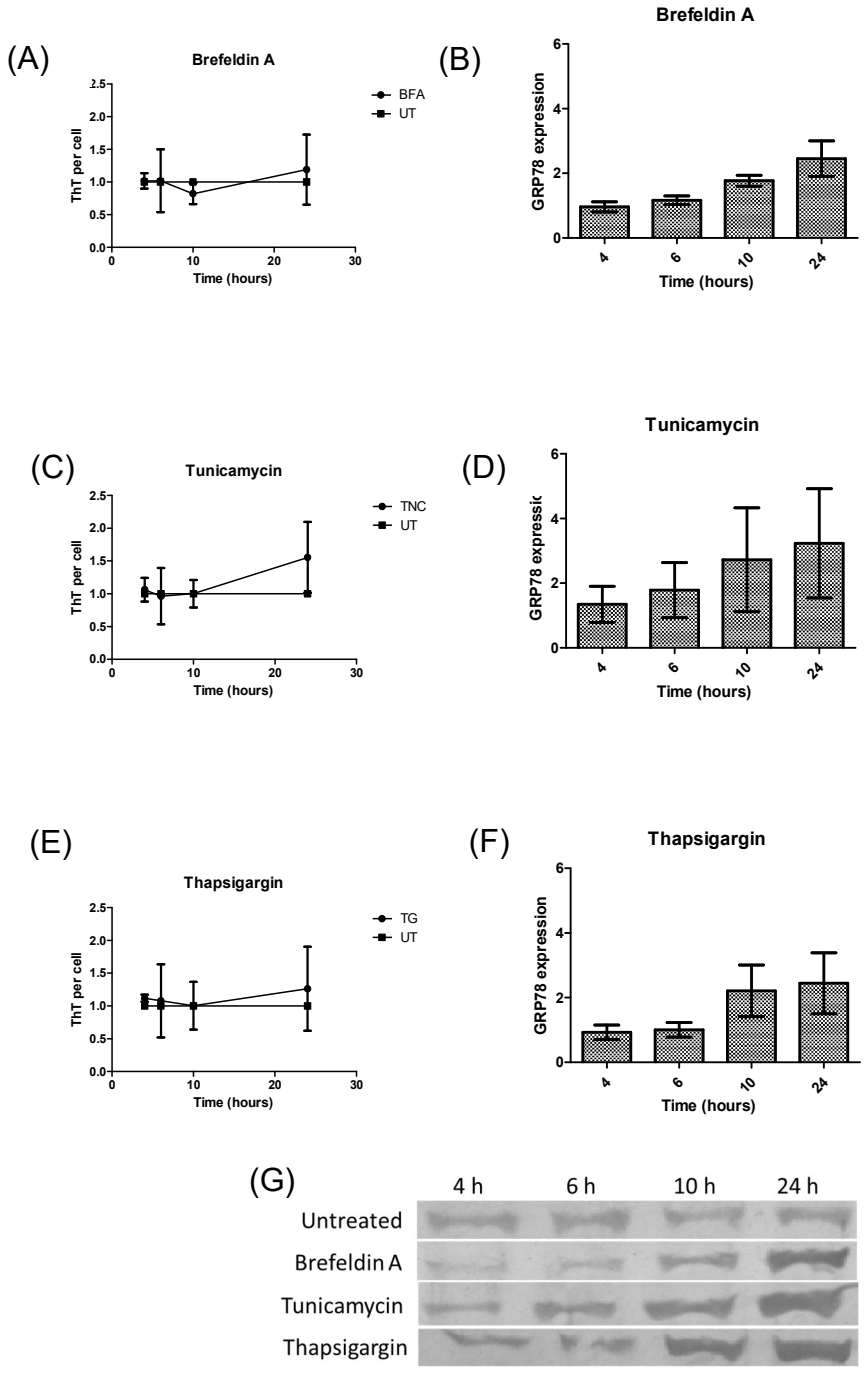

Figure 22: The correlation between ThT per cell and UPR activation for the detection of ER stress in the MDA-MB-231 cell line.
*Fold change in (A, C, E) ThT per cell and (B, D, F) GRP78 expression after treatment with Brefeldin A, tunicamycin and Thapsigargin for various time intervals in the MDA-MB-231 cell line. Changes in GRP78 expression and ThT/Cell were calculated as a fold change of the untreated cells at the respective exposure time. Therefore, untreated is represented by an arbitrary unit of 1. Untreated, Brefeldin A – 3.6 µM, Tunicamycin – 1 µg/mL and TG – 100 nM (n=3, * - significant to respective untreated control, * - p < 0.05, ** - p < 0.01, *** - p < 0.001).*

Similarly, the MDA-MB-231 cell line showed a correlation between the ThT per cell and GRP78 expression. The high level of basal GRP78 expression rendered the cells more resistant to the accumulation of misfolded proteins, which resulted in the ThT per cell being comparable to the untreated for the first 6 hours of exposure and decreased after 10 hours in all positive controls tested. The decrease in ThT per cell correlated with an increase in GRP78 expression, suggesting that ThT could be used to detect the onset of ER stress to indicate when cells may have temporarily re-established ER homeostasis.

With the MCF10A cell line, there was an increase in fluorescence after treatment with the various positive controls (**Figure 23**); however, the change was less drastic when compared to the MCF7 cell line. The 3D overlay did not show a drastic time-dependent increase in the ThT staining around the nucleus until 24 hours of exposure time, at which point increased ThT staining increased around the nucleus, indicating that the positive controls did not induce a significant accumulation of misfolded proteins within the ER lumen until approximately 24 hours of exposure time. Thus the MCF10A cell line had a greater resistance to ER stress, which was consistent with the viability results (**Figure 14C**), where significant cell death occurred at the 24-hour time point, thus the cell line required prolonged exposure to the positive controls to induce ER stress and subsequent cell death.

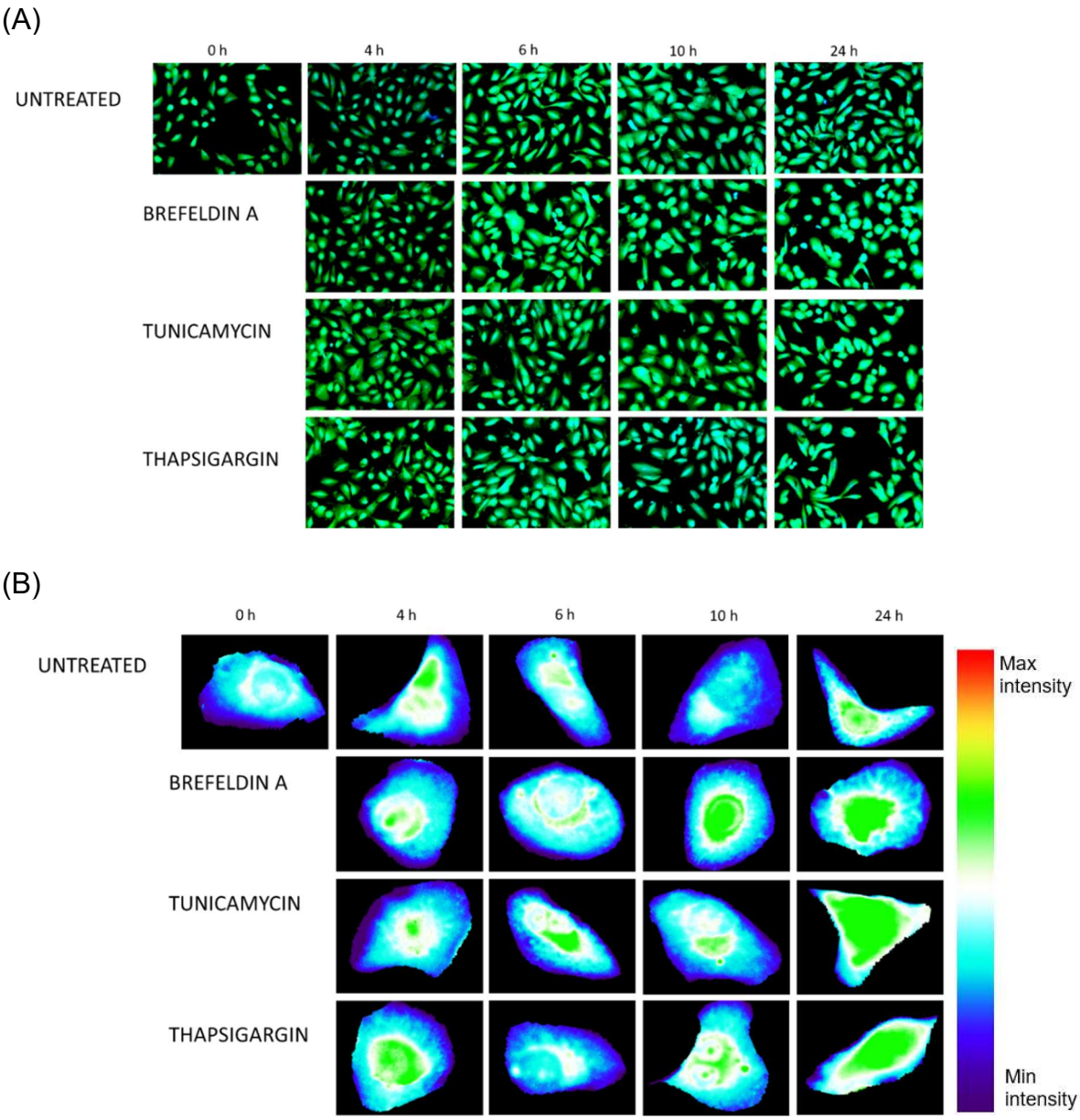

Figure 23: Representative fluorescent images of MCF10A cells stained with ThT.
(A) Representative fluorescent images (20x objective magnification) of MCF10A cells treated for various time intervals and stained with ThT and (B) 3D surface plot showing localization of ThT staining within individual cells.
Untreated, Brefeldin A – 3.6 μM, Tunicamycin – 1 μg/mL and TG – 100 nM

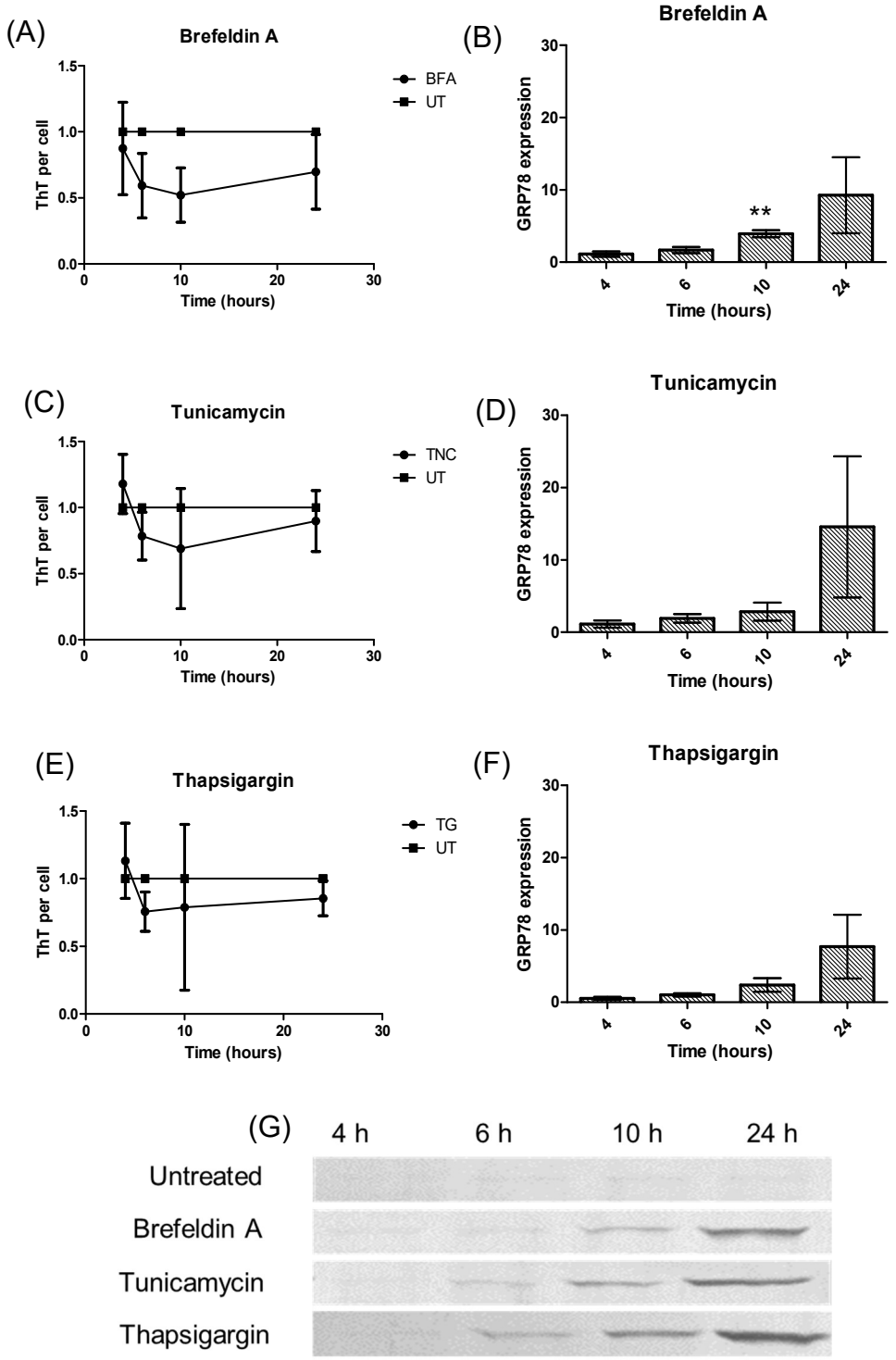

Figure 24: The correlation between ThT per cell and UPR activation for the detection of ER stress in the MCF10A cell line.

Fold change in ThT per cell and GRP78 expression after treatment with Brefeldin A, tunicamycin and Thapsigargin for various time intervals in the MCF10A cell line. Changes in GRP78 expression and ThT/Cell were calculated as a fold change of the untreated cells at the respective exposure time. Therefore, untreated is represented by an arbitrary unit of 1.

*Untreated, BFA (Brefeldin A) – 3.6 μM, TNC (Tunicamycin) – 1μg/mL and TG (Thapsigargin) – 100nM (n=3, * - significant to respective untreated control, * - p < 0.05, ** - p < 0.01, *** - p < 0.001).*

TNC and TG treatment in the MCF10A cell line increased the ThT fluorescence per cell at 4 hours, suggesting that there was an increase in misfolded proteins in the ER lumen. However, the controls showed a general decrease in the ThT per cell at 6 and 10 hours, which increased at 24 hours, suggesting that at 6 and 10 hours of exposure, the misfolded protein load decreased in the ER lumen (**Figure 24A, C & E**). GRP78 expression increased slightly at 6 hours, with a greater increase at 10 hours of exposure (**Figure 24B, D & F**), which correlated with the decrease in ThT per cell data. There was a larger increase in GRP78 expression at 24 hours and decreased viability (**Figure 14C**) at this time point. The results for the MCF10A cell line suggested that the cell line was also more resistant to the induction of ER stress; however, they showed little to no basal GRP78 expression (**Figure 24G**). The growth rate of the MCF10A cell line was much lower when compared to that of the MCF7 and MDA-MB-231 cell line. To confirm the slower growth rate of the MCF10A cell line, the doubling time was calculated from the initial 24-hour seeding period using the xCelligence software (**Figure 25**). The doubling time was calculated between 7 and 24 hours after seeding after the cells had attached and had started proliferating.

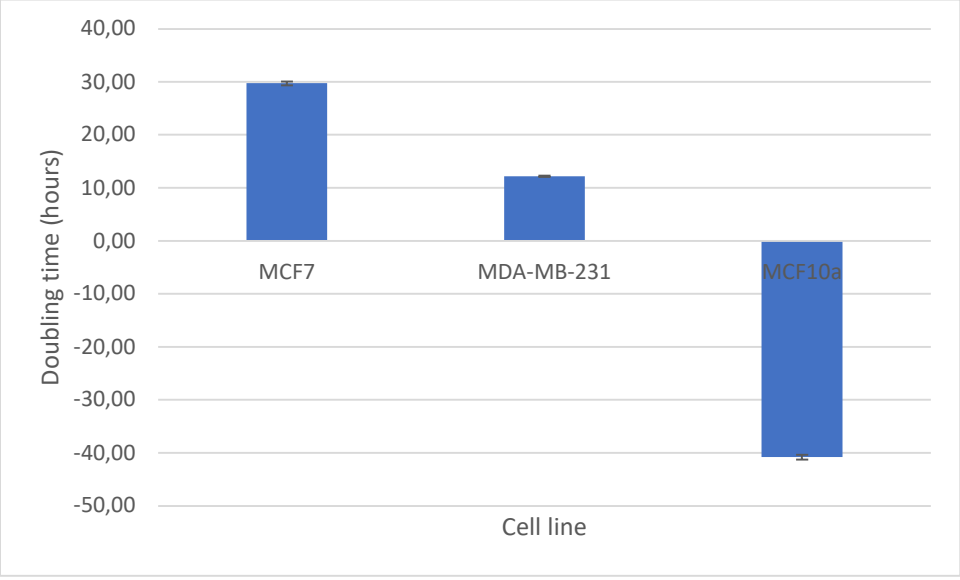

Figure 25: Doubling time of the MCF7, MDA-MB-231 and MCF10A cell lines, calculated using the xCelligence RTCA software

The MCF7 cell line had the longest doubling time, at approximately 30 hours. The MDA-MB-231 cell line displayed a shorter doubling time, with approximately 12 hours.

The MCF10A cell line showed a negative calculated doubling time (**Figure 25**), which is due to the negative slope observed in **Figure 66** (Appendix iv – Supplementary data). The cell index curves obtained from xCelligence correspond to the different phases of cell adhesion. Generally, the curves show an initial increase that corresponds to cell attachment, which generally lasts a few hours depending on the cell line. This is followed by a period of spreading, and a brief plateau phase (Kho *et al.*, 2015a). It is thought that the negative slope observed for the MCF10A cell line was due to the period of spreading, since the cells generally had a rounder and larger morphology during the initial stages of attachment, which changed after an increased attachment time, in which the cells become elongated and narrow. This would cause the cells to cover a smaller area in the base of the plate and decrease the electrical impedance, resulting in a negative slope with increasing time, until the cells started proliferating. In order to obtain the doubling time for the MCF10A cell line, the impedance would have had to be measured over a longer period of time. Generally, when a doubling time is calculated using xCelligence, the impedance is measured over a longer period of time in order to yield a large enough CI; however, the data obtained was used to obtain an indication of the growth rate. The lack of a positive slope in the MCF10A cell line suggested that the MCF10A cell line had not started proliferating in the first 24-hours and therefore had the slowest doubling time. Therefore, at a basal level, the MCF10A cell line would have a decreased rate of protein synthesis and a decreased protein folding load in the ER, rendering them less susceptible to the accumulation of misfolded proteins after treatment with ER stress inducers; therefore, they would only experience ER stress and UPR activation after prolonged exposure, which corresponded to the increase in the ThT per cell and UPR activation after 24 hours of exposure (**Figure 24**).

To summarize, the increase in ThT binding around the nucleus across all the different cell lines suggested that ThT was localized to the ER lumen. This could be confirmed by determining the colocalization of the ThT staining with ER using a stain for the ER. Based on the proposed mechanism of ThT binding (**Figure 7B**), the increased ThT binding indicated that there was an increase in misfolded proteins in the ER lumen. Thus, ThT staining may be utilized as a direct measurement of unfolded/misfolded proteins that are associated with ER stress.

3.3.3. Distinguishing between ER stress and mitochondrial dysfunction

The use of ThT to detect and quantify ER stress in cancer cell lines offers another advantage, namely the ability to distinguish between “true” ER stress and mitochondrial dysfunction-induced ER stress. Due to the crosstalk that exists between the two organelles, mitochondrial dysfunction may result in ER stress, and *vice versa*. If the two organelles are in close proximity, they may physically interact, with up to 20% of the mitochondrial surface in contact with the ER (Kornmann *et al.*, 2009) to produce mitochondrial-associated membranes (MAM) (Vance, 1990), where the membrane and luminal components can intermix and exchange (Bravo *et al.*, 2012). These associations have essential roles in various cellular functions, such as calcium signalling, lipid transport, energy metabolism and cell survival (Malhotra and Kaufman, 2011). As previously described, the activation of the UPR with ER stress induction results in mitochondrial dysfunction through the IRE-1 signalling pathway. However, mitochondrial dysfunction would also result in the induction of ER stress. Lim *et al.* (2009) showed that mitochondrial dysfunction resulted in ER stress in human liver cells due to elevated levels of cytosolic calcium. Lee *et al.* (2010) showed that ER stress is induced by excess NO generated during mitochondrial dysfunction in pancreatic β-cells via the activation of AMP-activated protein kinase (AMPK), which stimulates the production of NO. NO has been documented to decrease the expression of SERCA2b which triggers a decrease in the calcium stores in the ER, inducing ER stress.

Mitochondrial dysfunction was directly induced using FCCP, to determine the overlapping effect on the ER. The cell lines were treated with 20 µM FCCP for various time periods, after which they were stained with ThT and western blotting analysis was completed for GRP78 to determine the activation of the UPR. The Biolog redox dyes were used to detect electron flow in the electron transport chain (ETC) (**Figure 26**).

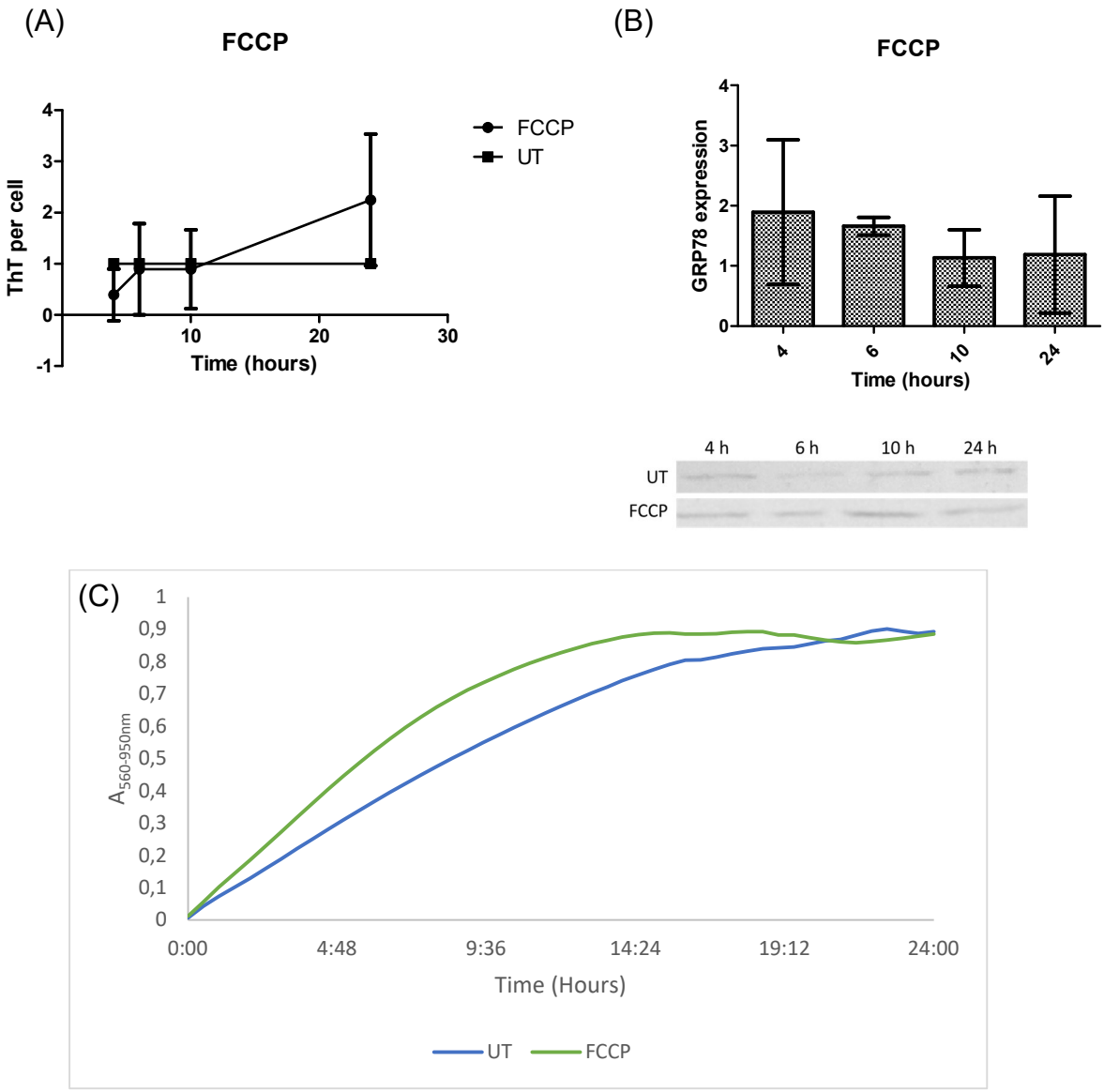

Figure 26: The correlation between ThT per cell and UPR activation after treatment with FCCP in the MCF7 cell line.
(A) Fold change in ThT per cell and (B) GRP78 expression and (C) progress curve of dye reduction after treatment with FCCP for various time intervals in the MCF7 cell line. Changes in GRP78 expression and ThT/Cell were calculated as a fold change of the untreated cells at the respective exposure time. Therefore, untreated is represented by an arbitrary unit of 1 for both A and B. FCCP (carbonyl cyanide 4-trifluoromethoxyphenyl hydrazine) – 20 µM.
*(n=3, * - significant to respective untreated control, * - p < 0.05, ** - p < 0.01, *** - p < 0.001).*

FCCP did not increase the ThT per cell value above 1 (comparable to the untreated) until 24 hours of exposure time (**Figure 26A**), at which point there was a non-significant increase. There was also no significant change in GRP78 expression (**Figure 26B**). The FCCP progress curves started to deviate below the untreated curve

at approximately 20 hours of exposure time, suggesting that at this point, there is a disruption in the electron transport chain (ETC), inducing mitochondrial dysfunction. This may eventually lead to the induction of ER stress due to decreased ATP production and increased ROS. The ThT per cell suggested that ER stress was induced between 10 and 24 hours. It is hypothesized that ER stress was induced closer to 24 hours as the change in GRP78 expression at this time point was not significant, suggesting that, even though there was an increase in misfolded proteins, as shown by the increased ThT per cell, it was not severe or prolonged enough to result in the activation of the UPR under the conditions tested. Increased GRP78 may be detected after a longer exposure time, due to prolonged mitochondrial dysfunction-induced ER stress. Due to the fact that mitochondrial dysfunction was only induced at approximately 20 hours, and ER stress was only detected at 24 hours, we can conclude that mitochondrial dysfunction preceded ER stress induction and that ER stress was most likely induced by mitochondrial dysfunction, rather than true ER stress induction, which is consistent with the mechanism of action of this control.

With the MDA-MB-231 cells, FCCP exposure resulted in a consistent increase in the ThT per cell (**Figure 27A**); however, no significant GRP78 expression was detected (**Figure 27B**). The progress curve of dye reduction (**Figure 27C**) showed that the FCCP curve started to deviate from the untreated curve at approximately 2 hours of exposure time, indicating that mitochondrial dysfunction was induced. As with the MCF7 cells, the induction of mitochondrial dysfunction preceded ER stress induction, suggesting that ER stress was induced by mitochondrial dysfunction. Mitochondrial dysfunction was induced from as early as 2 hours of exposure, whereas a slight increase in misfolded protein was only detected at 6 hours, with a larger increase from 10 hours.

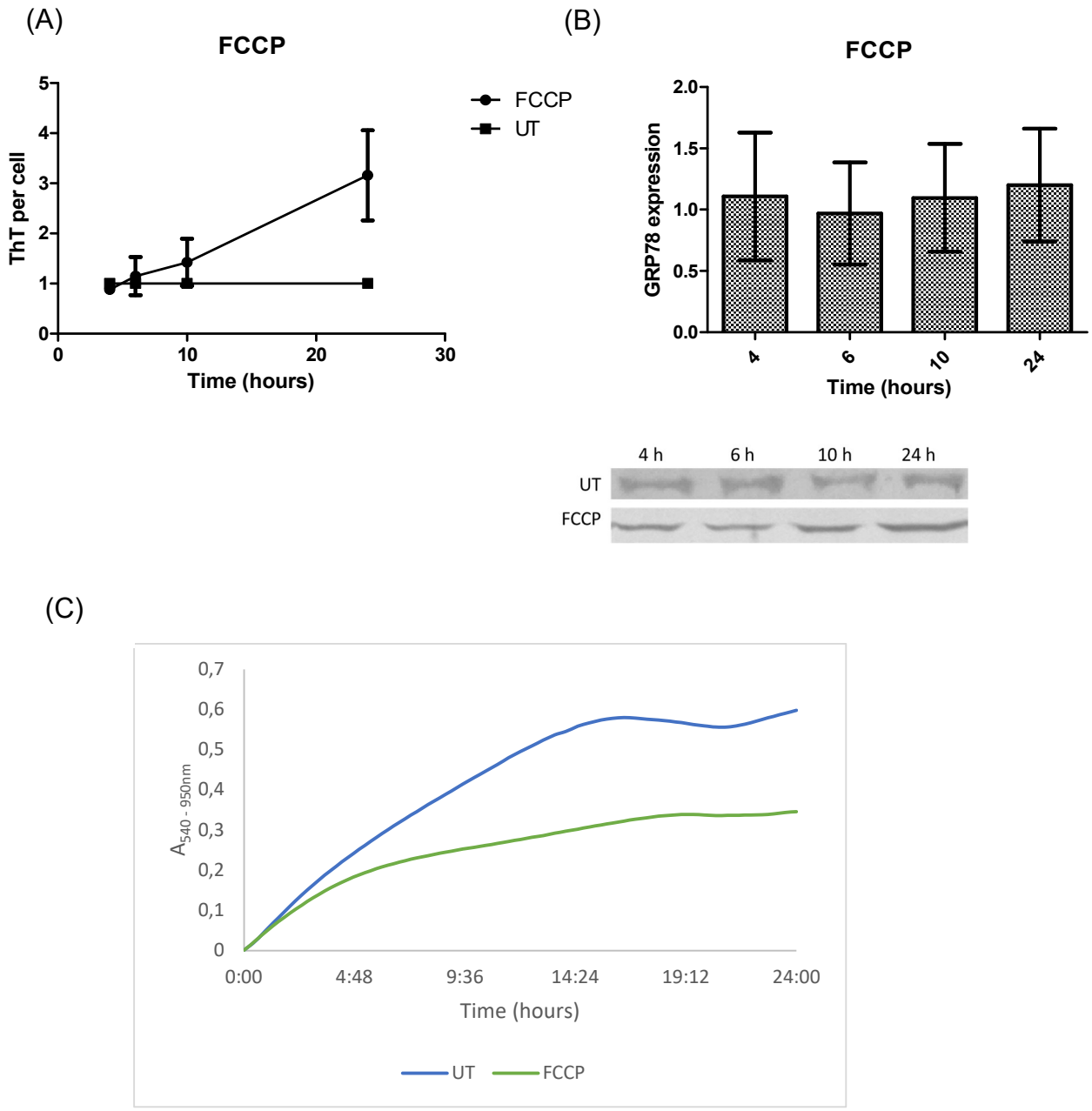

Figure 27: The correlation between ThT per cell and UPR activation after treatment with FCCP in the MDA-MB-231 cell line.
(A) Fold change in ThT per cell and (B) GRP78 expression and (C) progress curve of dye reduction after treatment with FCCP for various time intervals in the MDA-MB-231 cell line. Changes in GRP78 expression and ThT/Cell were calculated as a fold change of the untreated cells at the respective exposure time. Therefore, untreated is represented by an arbitrary unit of 1 for both A and B.
FCCP (carbonyl cyanide 4-trifluoromethoxyphenyl hydrazine) – 20 µM.
*(n=3, * - significant to respective untreated control, * - p < 0.05, ** - p < 0.01, *** - p < 0.001).*

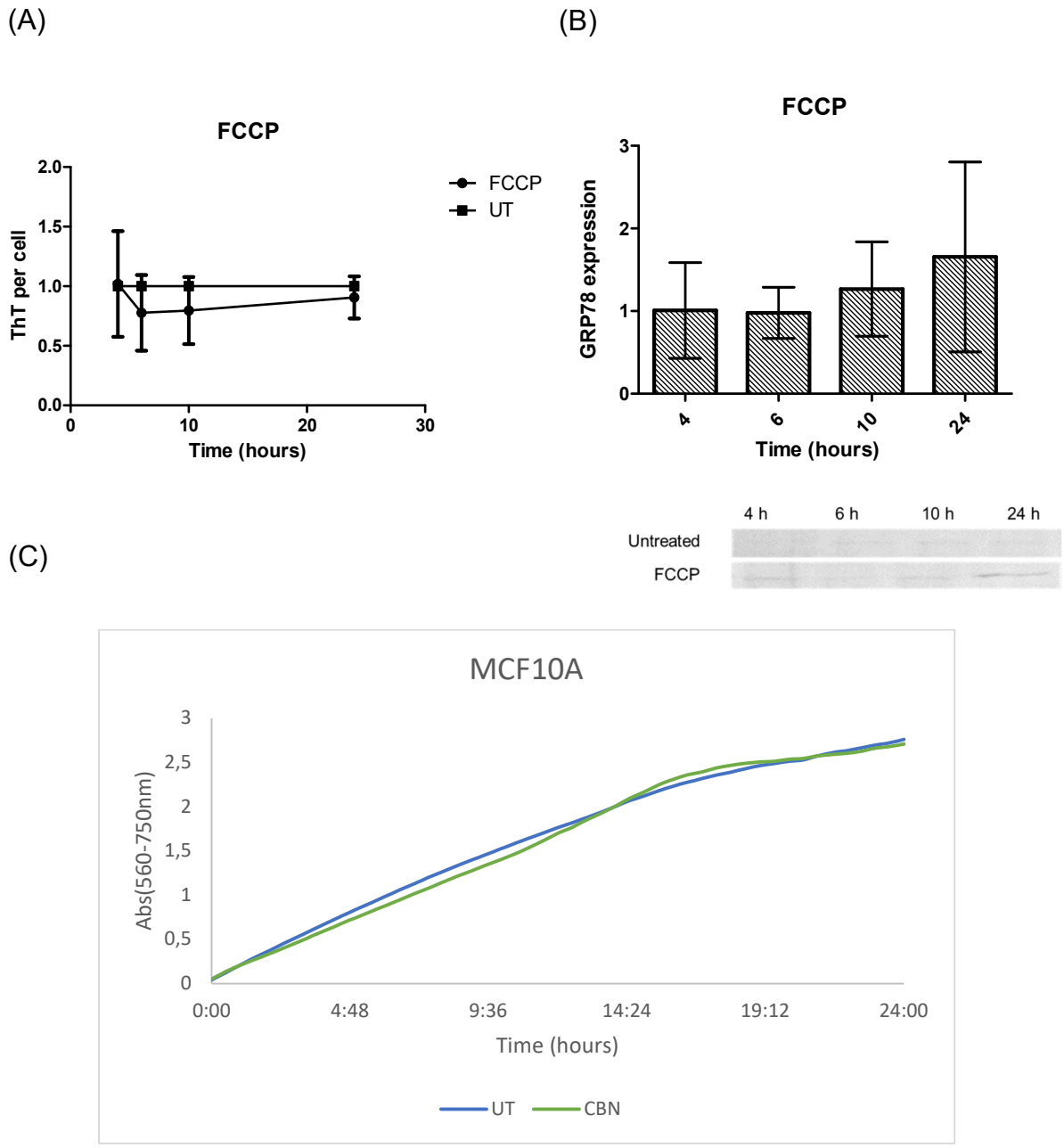

Figure 28: The correlation between ThT per cell and UPR activation after treatment with FCCP in the MCF10A cell line.
(A) Fold change in ThT per cell and (B) GRP78 expression and (C) progress curve of dye reduction after treatment with FCCP for various time intervals in the MCF10A cell line. Changes in GRP78 expression and ThT/Cell were calculated as a fold change of the untreated cells at the respective exposure time. Therefore, untreated is represented by an arbitrary unit of 1 for both A and B.
FCCP (carbonyl cyanide 4-trifluoromethoxyphenyl hydrazine) – 20 µM.
*(n=3, * - significant to respective untreated control, * - $p < 0.05$, ** - $p < 0.01$, *** - $p < 0.001$).*

Treatment with FCCP showed only a slight increase in the ThT per cell at 24 hours (**Figure 28A**) in the MCF10A cell line, which correlated with the slight increase in GRP78 expression (**Figure 28B**). This suggested that ER stress was induced between 10 and 24 hours. Similarly to the MCF7 cell line, it was hypothesized that ER stress was induced closer to 24 hours, as the change in GRP78 expression at 24 hours was not significant, suggesting that, even though there was an increase in misfolded proteins, it was not severe or prolonged enough to result in the significant activation of the UPR. The progress curve of dye reduction showed that the FCCP curve deviated slightly below that of the untreated curve at approximately 20 hours (**Figure 28C**), as in the case with the MCF7 cell line. Therefore, mitochondrial dysfunction most likely preceded ER stress induction with FCCP treatment.

The effect of treatment with individual cannabinoids on ER stress induction in various breast cancer cell lines was then determined, as well as the associated mechanism(s) of induction.

Chapter 4 – Screening and Mechanism(s) of ER stress induction

4.1. Introduction

Current literature describes contradicting views on the role of the endocannabinoid system in cancer. Cannabinoid receptors and the endocannabinoids are typically upregulated in tumour cells. Various studies have associated the increased expression levels of cannabinoid receptors, endocannabinoids or endocannabinoid-metabolizing enzymes with tumour aggressiveness, suggesting that the endocannabinoid system may be upregulated in cancer, promoting a pro-tumourigenic state. Conversely, the upregulation of cannabinoid-degrading enzymes has been observed in aggressive human tumours and cancer cell lines, which suggests that endocannabinoid signalling may be tumour-suppressive (Velasco *et al.*, 2016b).

Cannabinoids are commonly used for their palliative effects in cancer patients. These include appetite stimulation, inhibition of chemotherapy-associated nausea and vomiting, pain relief, mood elevation and insomnia relief (Davis, 2016, Pacher *et al.*, 2006). The first study to show that cannabinoids have anti-tumour effects was reported by Munson *et al.* (1975), who highlighted that Δ^9-THC and Δ^8-THC inhibited the growth of Lewis lung adenocarcinoma cell growth *in vitro* and *in vivo*.

The proposed anti-tumour mechanisms of cannabinoids are complex and may involve the induction of apoptosis, anti-proliferative action, and anti-metastatic effects which are proposed to occur through the inhibition of angiogenesis and tumour cell migration (Alexander *et al.*, 2009, Pacher *et al.*, 2006). Some of these effects have been observed in tumour cells from different origins including gliomas, melanomas, carcinomas of the breast, skin, lungs, liver, pancreas, colon, prostate and lymphomas, confirming that the anti-tumour properties of cannabinoids are non-specific (Velasco *et al.*, 2012). The precise pathways through which these molecules produce an anti-tumour effect has not been fully characterized; however, variations in their mechanism of action may be dependent on the type of tumour being studied (Ligresti *et al.*, 2006). Some studies have shown that, under certain conditions, cannabinoid treatment

stimulates cancer cell proliferation and interferes with the tumour-suppressor role of the immune system (Velasco *et al.*, 2016b), while other studies have shown that cannabinoids may exert their anticancer effects through the induction of ER stress (Carracedo *et al.*, 2006a, Carracedo *et al.*, 2006b, Salazar *et al.*, 2009a, Salazar *et al.*, 2009b).

A significant amount of research has been conducted on the effect of cannabinoids on cancer cells, specifically in glioma cells. The ER is the site for the synthesis of sterols and lipids (Schröder and Kaufman, 2005) and various studies have described how cannabinoids induce apoptotic cell death in glioma cells via the CB1- and CB2-dependent stimulation of the *de novo* synthesis of ceramide in the ER (Blázquez *et al.*, 2004, Galve-Roperh *et al.*, 2000, Gómez del Pulgar *et al.*, 2002, Sánchez *et al.*, 2001). Ceramides are a family of lipids composed of sphingosine and a fatty acid (Guindon and Hohmann, 2011). Further studies provided insight into the signalling events downstream of ceramide. Under certain conditions, THC treatment enhanced the expression of the stress-regulated protein p8. Protein p8, along with several of its downstream targets (ATF4, CHOP and the pseudo-kinase tribbles homologue 3 [TRB3]) have been suggested to control tumourigenesis and tumour progression (Carracedo *et al.*, 2006b). Ohoka *et al.* (2005) showed that TRB3 was involved in the CHOP-dependent induction of cell death. Li *et al.* (2018) indicated that TRB3 had the ability to mediate between ER stress and AKT signalling pathways. The stimulation of the p8-regulated pathway increased the inhibitory interaction of TRB3 with the pro-survival kinase AKT, leading to the inhibition of the mammalian target of rapamycin complex 1 (mTORC1) and the subsequent stimulation of autophagy-mediated cell death (Salazar *et al.*, 2009b) (**Figure 29**).

This mechanism relies on CB1 or CB2 activation; however, cannabinoids with a low affinity for cannabinoid receptors (e.g. CBD) have been proposed to induce apoptosis in cancer cells independently of CB1 and CB2 (Śledziński *et al.*, 2016).

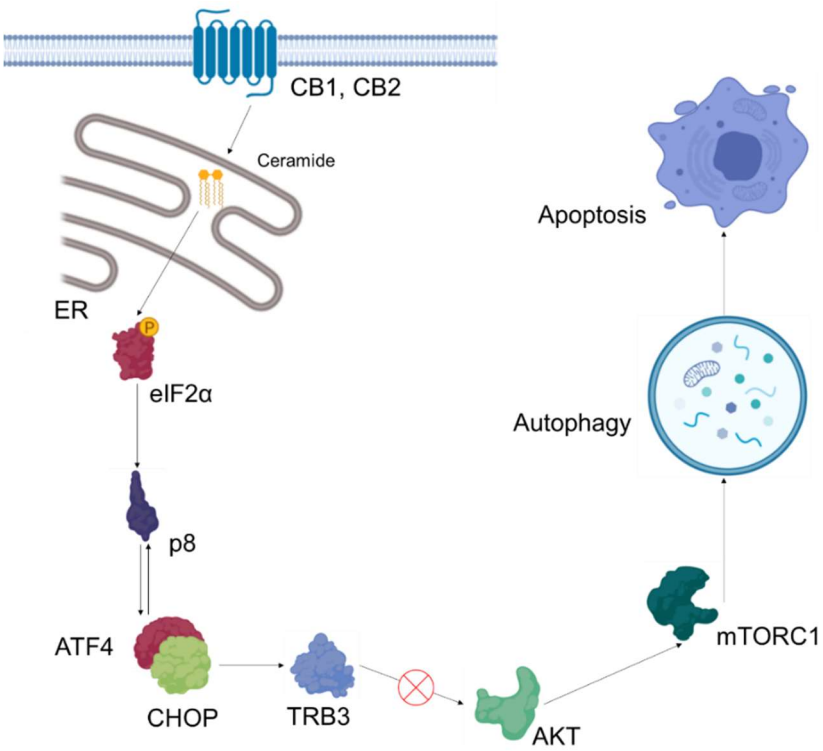

Figure 29: Effect of THC binding to CB receptors.
Figure was created using the BioRender online tool and adapted from (Salazar et al., 2009b, Velasco et al., 2016b). Activation of the CB receptors by THC leads to the de novo synthesis of ceramide, triggering the induction of ER stress and promoting the upregulation of p8 and several of its downstream targets. This ultimately results in autophagy-mediated apoptosis.
(THC – tetrahydrocannabinol, eIF2α – eukaryotic initiation factor 2α, ATF4 – activating transcription factor 4, CHOP – C/EBP (ccaat/enhancer-binding protein) homologous protein, TRB3 – Pseudo-kinase tribbles homologue 3, AKT – Protein kinase B, mTORC1 - Mammalian target of rapamycin complex 1).

Another proposed mechanism of ER stress induction is via the transient receptor potential cation channel (TRP) vanilloid member 1 (TRPV1). TRPV1 is a non-selective cation channel that triggers intracellular signalling via the influx of calcium, thereby increasing the intracellular calcium concentration (Nazıroğlu *et al.*, 2017). Activation of TRPV1 by its conventional agonist, capsaicin, results in apoptosis via the depolarization of the mitochondrial membrane, production of ROS and activation of caspases 9 and 3 (Maccarrone *et al.*, 2000, Nazıroğlu *et al.*, 2017, Nur *et al.*, 2017).

CBD, CBG and CBC directly activate TRPV1 receptors (Bisogno *et al.*, 2001, Ligresti *et al.*, 2006). The proposed mechanism of CBD action *in vitro* is through the increased production of reactive oxygen species (ROS) (Ligresti *et al.*, 2006, Shrivastava *et al.*, 2011). Ligresti *et al.* (2006) suggested that CBD elevates the production of ROS indirectly, i.e. by elevating intracellular Ca^{2+}. They found that CBD treatment resulted in a rapid and sustained elevation of intracellular Ca^{2+}, changing the mitochondrial membrane potential and leading to the production of ROS in MDA-MB-231 cells.

Ligresti *et al.* (2006) also highlighted that antioxidants reduced the apoptotic effects of CBD in MDA-MB-231 cells. They found that there was a significant reversion of the effect of CBD in the presence of a selective antagonist for TRPV1 and CB2 receptors, thus pointing to the partial involvement of these receptors in the anticancer action of CBD in breast carcinoma cells (Ligresti *et al.*, 2006). It is hypothesized that increased ROS production would result in the induction of ER stress due to a disruption of protein folding in the ER (**Figure 30**).

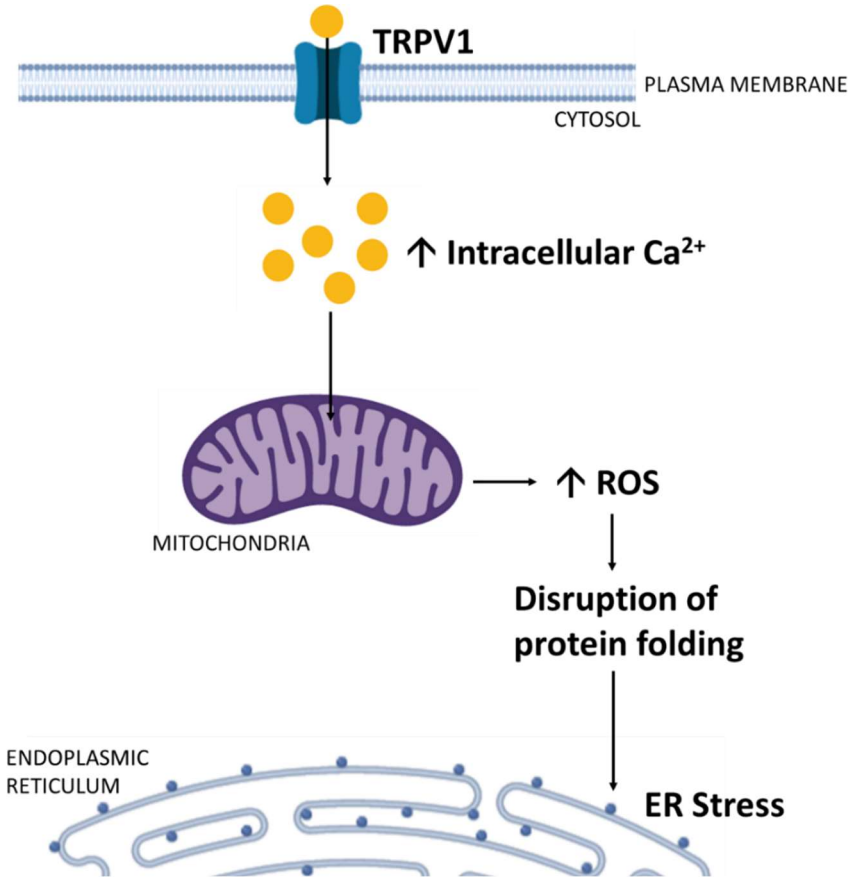

Figure 30: Proposed mechanism of ER stress induction by TRPV1 activation
Figure was created using the BioRender online tool. Activation of the TRPV1 receptor by the cannabinoids results in a rapid influx of Ca^{2+} into the cell, increasing the cytosolic Ca^{2+} concentration. This results in increased calcium uptake into the mitochondria, increasing ATP synthesis and ROS production. The increase in ROS disrupts protein folding and leads to the induction of ER stress.
TRPV1 – Transient receptor potential cation channel vanilloid member 1, ER – endoplasmic reticulum, ROS – reactive oxygen species

The aim of this chapter was to determine the effect of cannabinoid treatment on the induction of endoplasmic reticulum stress and the activation of the unfolded protein response in breast cancer cell lines and to determine the molecular mechanisms of ER stress induction by individual cannabinoids.

4.2. Materials and methods

4.2.1. Cannabinoid treatments

4.2.1.1. Cannabinoid degradation

In order to confirm the integrity of the cannabinoid standards in the study, thin layer chromatography (TLC) was used. The mobile phase (hexane: diethyl ether: acetic acid 80:20:5 v/v/v) was added to the TLC chamber, which was sealed and left for 30 minutes to allow the solvent vapours saturate the air in the chamber. The cannabinoid standards in dimethyl sulfoxide (DMSO) were diluted in 100% methanol to a final concentration of 100 ng/µL. Each cannabinoid (5 µL – 500 ng) was spotted on the plate and allowed to dry. The plate was added to the mobile phase and left to develop until the mobile phase reached the end of the plate. The TLC plate (**Figure 31**) was allowed to dry completely and was then sprayed with 0.5% (w/v) fast blue B solution in distilled water (unpublished optimized protocol).

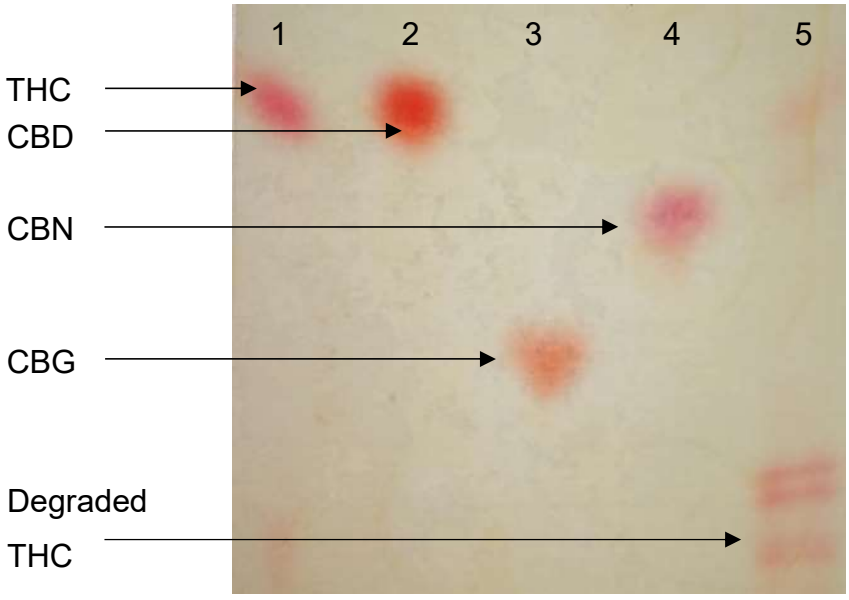

Figure 31: TLC of various cannabinoid standards, visualized using Fast Blue B stain. *1 - THC (Δ^9-tetrahydrocannabinol - 500 ng), 2 - CBD (cannabidiol - 500 ng), 3 - CBG (cannabigerol - 500 ng, 4 - CBN (cannabinol - 500 ng), 5 – Degraded THC*

4.2.1.2. Treatments

For each experiment, the cells were treated with the various positive controls (BFA, TNC and TG) at the concentrations listed in Table 1, as well as with Δ^9-tetrahydrocannabinol (THC), cannabidiol (CBD), cannabigerol (CBG) and cannabinol (CBN) for 48 hours, alongside an untreated and an appropriate DMSO vehicle control. The fold change of each treatment was calculated relative to the respective untreated or vehicle control.

4.2.1.3. MTT cell viability assay

The MTT viability assay is based on the reduction of the yellow tetrazolium salt 3-(4,5-dimethylthiazol-2-yl)-2,5-diphenyl tetrazolium bromide (MTT) to form purple formazan crystals (**Figure 32**) by various dehydrogenase enzymes and reducing agents (*e.g.* NADH) present in metabolically viable cells (Mosmann, 1983).

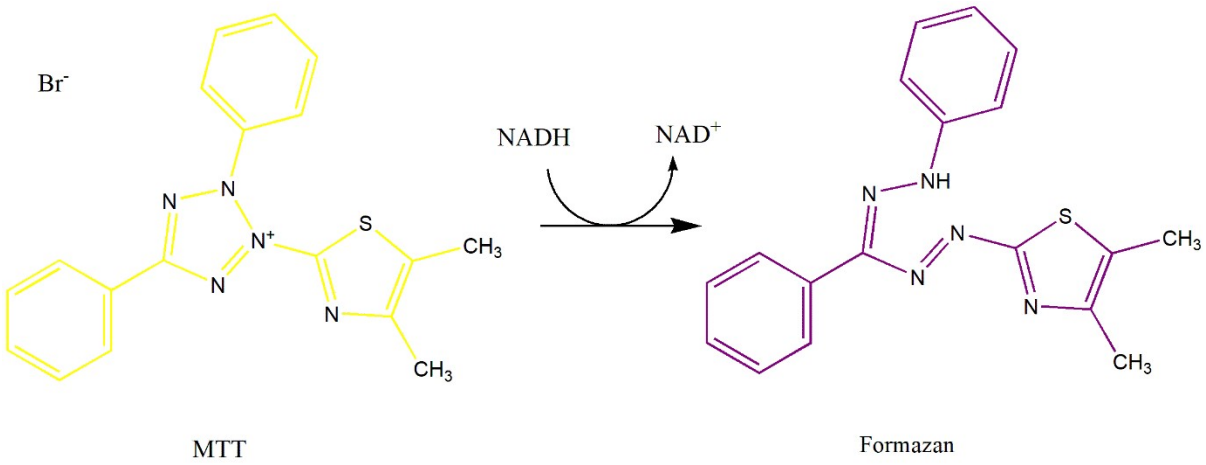

Figure 32: Principle of the MTT cell viability assay.
MTT, a yellow tetrazolium salt, is converted to purple coloured formazan by metabolically viable cells (Riss et al., 2016).
MTT - 3-(4,5-dimethyl thiazolyl-2)-2,5-diphenyltetrazolium bromide; NAD^+ - Nicotinamide adenine dinucleotide; NADH – Nicotinamide adenine dinucleotide hydrogen; Br – Bromide.

After the various treatments, the MTT cell viability assay was performed to detect changes in cell viability. Briefly, the spent media was removed and replaced with 200 µL MTT reagent (0.5 mg/mL MTT in the respective media), and incubated for 2 hours at 37°C. The MTT reagent was removed and the formazan crystals were solubilized

in 200 µL DMSO. The absorbance (540 nm) was read using the BioTek Epoch 2 microplate reader.

In order to quantify the number of cells present after the treatments and calculate the percentage viability, a cell density standard curve for each cell line was prepared using the MTT cell viability assay (Appendix iv – Supplementary data, **Figure 72**).

4.2.2. Enzyme Assays

Cells were seeded in 6 well tissue culture plates and treated with the respective treatments for 24 hours. Trypsin was added to the cells and they were incubated at 37°C until the cells lifted. The cell solution was then collected, and Triton X-100 was added to a final concentration of 1% (v/v). The cells were vortexed and incubated at 4°C for 30 minutes for cell lysis to occur. The solution was centrifuged at 12 045 *xg* for 90 seconds to pellet the cell debris and the supernatant was used for the subsequent enzyme assays.

To confirm that the observed rate was due to the activity of the enzyme, different concentrations of the enzyme were added to evaluate if the amount of activity observed was proportional to the amount of enzyme added. Examples of the progress curves for lactate dehydrogenase and succinate dehydrogenase are shown in Appendix iv – Supplementary data (**Figure 73**).

To determine the specific activity, the protein concentration was determined using the Bradford protein assay and extrapolation from a protein standard curve (Appendix iv – Supplementary data, **Figure 68**). The following calculation was used to calculate the specific activity:

$$Activity\ (mol.min^{-1}.mL^{-1}) = \frac{\Delta Abs/min}{\varepsilon} \times \frac{Total\ assay\ vol\ (mL)}{Enzyme\ vol\ (mL)}$$

$$Specific\ activity\ (mol.min^{-1}.mg^{-1} = \frac{Activity\ (mol.min^{-1}.mL^{-1})}{[Protein](mg/mL)}$$

4.2.2.1. Lactate dehydrogenase

A reaction mixture containing 94 mM 4-(2-hydroxyethyl)-1-piperazineethanesulfonic acid (HEPES) buffer (pH 7.0) and 2 mM pyruvate was prepared and incubated at 37°C

along with the cell lysate for 5 minutes with shaking. The reaction was then initiated with the addition of NADH to a final concentration of 0.2 mM. The absorbance was recorded at 340 nm for 10 minutes at 37°C (Bisswanger, 2019).

4.2.2.2. Succinate dehydrogenase

A reaction mixture containing 94 mM HEPES buffer (pH 8.3), 2 mM potassium cyanide (KCN), 2 mM Iodonitrotetrazolium chloride (INT) and 20 mM succinate was added to the cell lysate. The absorbance at 490 nm was recorded for 15 minutes at 37°C (Adapted from Munujos *et al.* (1993)).

4.2.3. Fluorescent staining for confocal microscopy

Live cells were stained with the various fluorescent dyes and images were acquired using the Zeiss Meta laser scanning confocal microscope (Appendix iii – Equipment and software information). All experimental work completed using the confocal microscope was done at Rhodes University with the assistance of Prof A. Edkins.

4.2.3.1. ER Tracker

The 1 mM ER Tracker stock solution was diluted in 1x binding buffer (Appendix ii – Buffer components) to produce a 1 µM working solution. The cells were incubated with the working solution at 37°C for 30 minutes. The solution was then removed and replaced with media.

4.2.3.2. MitoTracker

The 500x MitoTracker working solution (component A, provided) was diluted 1:500 in the Live Cell Staining Buffer (Component B, provided) to produce a 1x working solution. The cells were incubated with the working solution at 37°C for 30 minutes. The solution was then removed and replaced with media.

4.2.3.3. LipidTox

The 1000x LipidTox working solution was diluted 1:1000 in 1x binding buffer (Appendix ii – Buffer components) to produce a 1x working solution. The cells were incubated

with the working solution at 37°C for 30 minutes. The solution was then removed and replaced with media.

4.2.3.4. LysoTracker

The 1 mM LysoTracker stock solution was diluted 1:20 in 1x binding buffer (Appendix ii – Buffer components) to produce a 50 nM working solution. The cells were incubated with the working solution at 37°C for 30 minutes. The solution was then removed and replaced with media.

4.2.4. Detecting the induction of ER stress

4.2.4.1. Griess reagent for Nitric Oxide

The Griess reagent was used to detect nitric oxide (NO) production in the spent media after treatments (Griess, 1879).

The Griess reaction was used for the indirect determination of NO. The assay involved the measurement of the stable decomposition products of NO, namely NO_3^- and NO_2. NO_3^- is reduced to NO_2^- which, under acidic conditions, reacts with the amino group of sulphanilamide to form the diazonium cation, which couples to N-(1-naphthyl)ethylenediamine (NED) to form the corresponding azo dye (**Figure 33**), which can be measured at 540 nm (Bryan and Grisham, 2007, Tsikas, 2007).

Briefly, Griess reagent (100 µL), warmed to room temperature, was added to 50 µL of the fresh spent media. The solution was incubated in the dark, at room temperature for 20 minutes. Each assay was completed with a 50 µM nitrate standard as an internal assay control. The absorbance (540 nm) was read using the BioTek Epoch 2 microplate reader.

The nitric oxide concentration in the spent media was extrapolated from a nitric oxide standard curve (Appendix iv – Supplementary data, **Figure 71**).

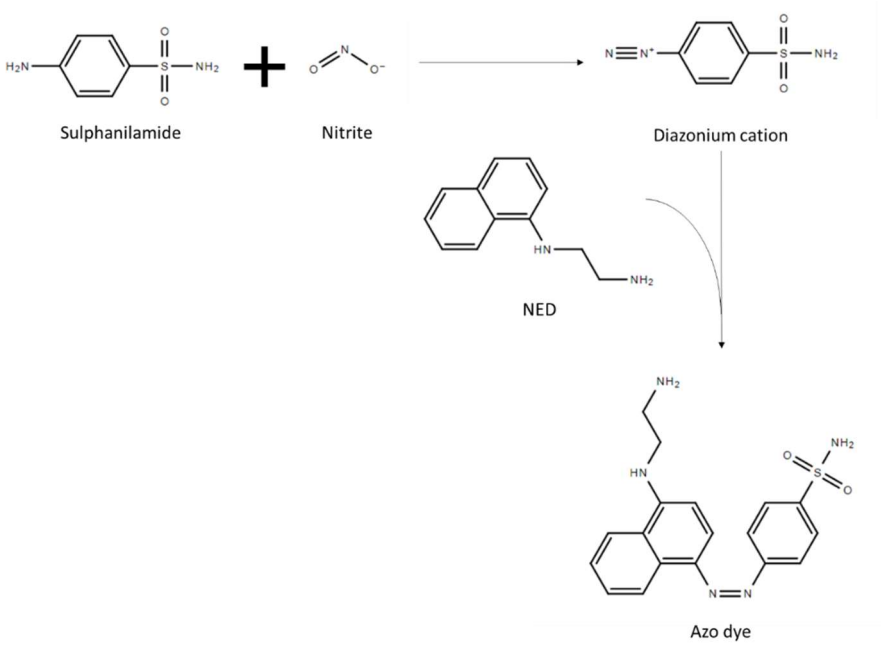

Figure 33: Principle of the Griess reagent
Chemistry of the Griess reaction in which nitrite reacts with sulphanilamide to form a diazonium cation, which subsequently couples to NED to form the corresponding azo dye. Figure adapted from (Tsikas, 2007). (NED - N-(1-naphthyl) ethylenediamine).

4.2.5. Detecting increases in reactive oxygen species

To detect increases in ROS production, 2', 7'-dichlorofluorescein-diacetate (DCFH-DA), a non-fluorescent, cell-permeable probe was utilized. Once the dye enters the cell, it is cleaved by intracellular esterases to form 2', 7'-Dichlorofluorescin (DCFH), which is cell impermeable. DCFH is subsequently oxidized in the presence of ROS to the highly fluorescent molecule, 2', 7'-dichlorofluorescein (DCF) (Dikalov *et al.*, 2007) (**Figure 34**).

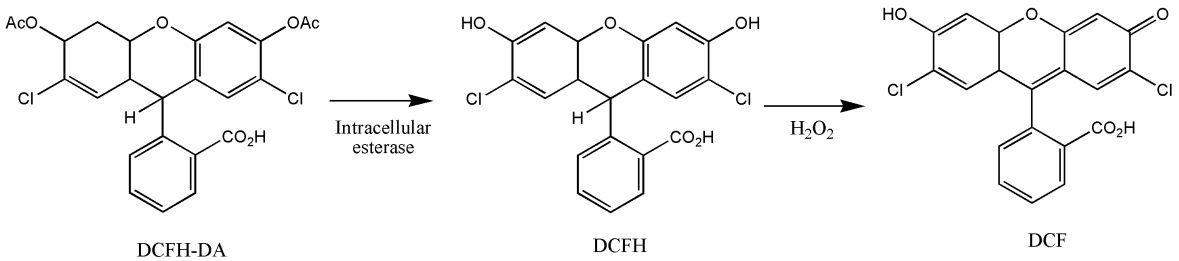

Figure 34: Principle of DCFH-DA staining for the detection of ROS
Figure adapted from (Dikalov et al., 2007).
DCFH-DA – 2',7-dichlorofluorescein-diacetate; DCFH – 2',7'-dichlorofluorescin; DCF – 2',7'-dichlorofluorescein

To detect changes in the production of ROS, spent media was removed and substituted with 10 µM DCFH-DA in PBS (pH 7.4). The cells were incubated at 37°C for 30 minutes. After staining, the cells were washed once with PBS (pH 7.4) to remove excess stain. The fluorescence was read at E_x/E_m of 495/530 nm. To compare ROS levels between treatments, the measured fluorescence was normalized to cell number obtained using the SRB cell viability assay and calculated as a fold change relative to the respective untreated cells or DMSO vehicle control.

4.2.6. Detecting changes in the intracellular calcium concentration

Changes in the intracellular calcium was determined using the fluorescent calcium stain, Calcium Green-1AM, the acetoxymethyl (AM) ester form, which ensures that the dye is cell-permeable.

After the cells were treated with the various cannabinoids as previously described, the spent media was replaced with 50 µL of a 1 µM Calcium Green-1AM staining solution in PBS (pH 7.4) and incubated at ambient room temperature for 20 minutes for de-esterification. The staining solution was then removed, and cells were washed once with PBS (pH 7.4) to remove excess stain and the fluorescence was then read at E_x/E_m of 506/531 nm. To compare Ca^{2+} levels between treatments, the measured fluorescence was normalized to cell number obtained using the SRB cell viability assay and calculated as a fold change relative to the respective untreated cells or DMSO vehicle control.

4.3. Results and discussion

Figure 35 provides an overview of the experimental design followed in chapter 4 for determining the effect of cannabinoid treatment on ER stress induction and UPR activation.

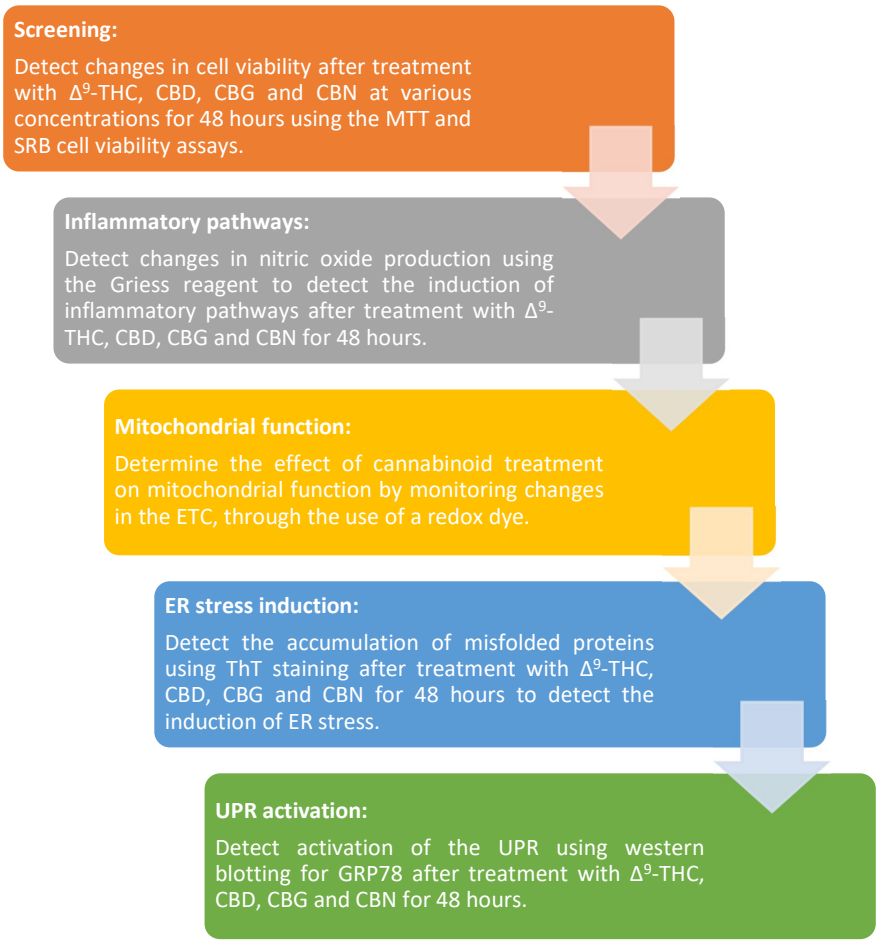

Figure 35: Overview of the experimental design for the determination of the effect of cannabinoid treatment on the induction of endoplasmic reticulum stress and activation of the unfolded protein response.

4.3.1. Viability screening

The MTT cell viability assay is based on changes in the metabolic state of a cell and is therefore used to quantify the metabolic functioning of the cells, as opposed to the overall cell number. The SRB cell viability assay is a measure of the total protein in a cell and would, therefore, provide a better indication of total cell number, regardless of the metabolic state of the cell. The MTT assay (Section 4.2.1.3) was therefore used to determine the effect of various treatments on cell viability, but the SRB assay was used to determine cell number based on protein content to normalize all fluorescent data.

All the positive controls induced a significant decrease in cell viability (**Figure 36A**). This was expected as the cell lines were treated with concentrations that were documented to induce ER stress within a few hours of exposure and would, therefore, result in significant cell death after 48 hours due to sustained UPR activation. The MCF7 cells had the greatest susceptibility to ER stress-induced cell death as depicted by the highly significant decrease in cell viability (**Figure 36A**). The MDA-MB-231 cells were the least susceptible to cell death induced by the controls as they showed the greatest viability after treatment.

Based on the literature, it has become increasingly apparent that low levels of ER stress can be beneficial to cells by eliciting hormesis, which is a cellular response where the activation of protective mechanisms render a cell resistant to additional stressors (Mattson, 2008, Mollereau *et al.*, 2014). This may explain why the MDA-MB-231 cell line exhibited increased resistance to cell death by the various ER stress inducers when compared to the untreated control. The MDA-MB-231 cell line had high levels of basal GRP78 expression (**Figure 22**), suggesting that they experience higher basal levels of ER stress in comparison to the MCF7 and MCF10A cell lines. It was hypothesized that this may be due to the metastatic nature of this cell line. Generally, high GRP78 expression in cancers, including breast cancer, is associated with metastasis and poor prognosis (Limia *et al.*, 2019). This phenomenon may be due to increased protein flux through the highly secretory nature of these cells, as they exhibit increased expression of ECM-degrading enzymes, such as MMPs, that are required for the EMT that occurs upon metastasis (Feng *et al.*, 2003). The high level of basal GRP78 expression means that they would be more resistant to ER stress induction and UPR activation, due to having higher reserves (GRP78) to accommodate increases in misfolded proteins. The higher levels of GRP78 expression in the cell would facilitate the folding of the misfolded proteins, thus the cells would require more severe or prolonged exposure to ER stress inducers to chronically activate the UPR and result in cell death.

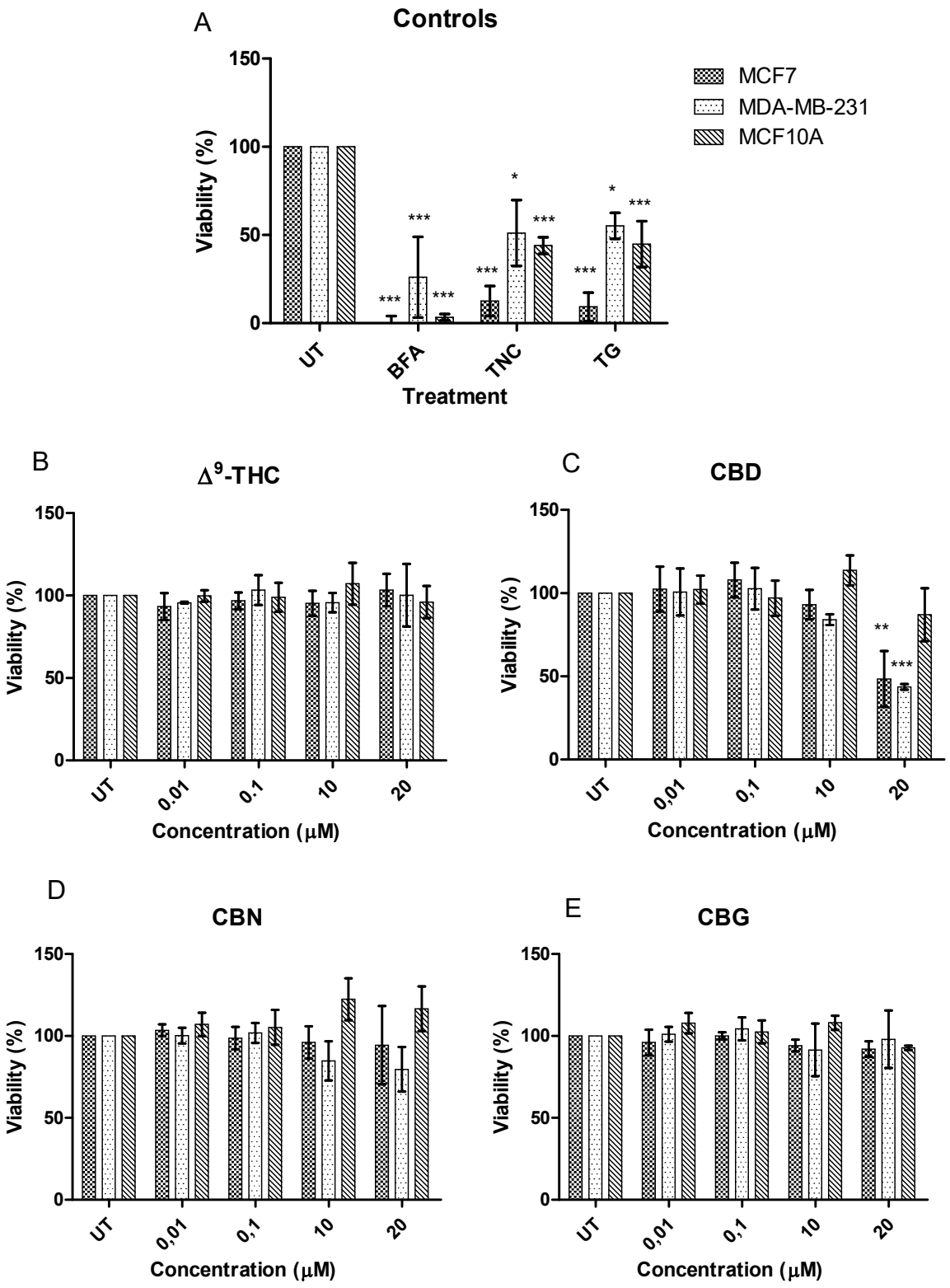

Figure 36: Change in the viability of MCF7, MDA-MB-231 and MCF10A cell lines after treatment with various cannabinoids.

*Cells were treated with (A) positive controls and various concentrations of (B) THC, (C) CBD, (D) CBN and (E) CBG for 48 hours and the change in viability determined using the MTT cell viability assay. Δ⁹-THC – Δ⁹-tetrahydrocannabinol, CBD – cannabidiol, CBG – cannabigerol, CBN – cannabinol, UT – Untreated, BFA – Brefeldin A (1 μg/mL), TNC – Tunicamycin (1μg/mL) and TG - Thapsigargin (100nM). (n=3, * - significant to respective untreated control, * - p < 0.05, ** - p < 0.01, *** - p < 0.001).*

In order to investigate the potential molecular mechanism(s) of cannabinoid-induced ER stress, a cannabinoid concentration that would induce a moderate ER stress response, and not induce complete apoptosis was required. Due to the limited research and contradictions described in existing literature regarding ER stress and cannabinoid treatment, a wide concentration range of the cannabinoids was tested in this study. Each cell line was treated with 0.01 µM, 0.1 µM, 10 µM and 20 µM of each cannabinoid (THC, CBD, CBG and CBN) for 48 hours. The MTT cell viability assay was then performed to determine changes in cell viability at a metabolic level (**Figure 36**).

At the concentrations tested, only CBD (20 µM) induced a significant amount of cell death in the MCF7 and MDA-MB-231 cell lines (**Figure 36C**), with it being highly significant in the MDA-MB-231 cell line after 48 hours of exposure. Significant cell death was not induced in the non-tumourigenic MCF10A cell line under the conditions tested, suggesting that the mechanism of action of CBD that triggered the cell death pathways was more specific to cancer cells than non-tumourigenic cells. CBN also induced minimal cell death in the MCF7 and MDA-MB-231 cell lines at 20 µM (**Figure 36D**), with more death occurring in the MDA-MB-231 cell line; however, it was not significant. The viability of the MCF10A cell line was not affected after treatment with the range of CBN concentrations tested.

Overall, the MDA-MB-231 cell line displayed the highest resistance to the ER stress-inducing positive controls when compared to the MCF7 and MCF10A cell lines, however, they had a higher susceptibility to cell death induced by the cannabinoids, specifically CBD (highly significant) and CBN (not significant) (**Figure 36C & D**).

4.3.2. Inflammatory pathways

The Griess reagent was used to measure changes in NO production, which is a downstream by-product of inflammatory pathways. NO is synthesized from arginine by NO synthase (NOS). There are three isoforms of NOS, namely endothelial NOS (eNOS), neuronal NOS (nNOS) and inducible NOS (iNOS). nNOS and eNOS are constitutively expressed and their activities are dependent on the cytosolic Ca^{2+} concentration. iNOS is not Ca^{2+} dependent (Gotoh and Mori, 2006) and its expression is induced by lipopolysaccharide (LPS) and pro-inflammatory cytokines, such as

interferon-γ (IFN-γ), tumour-necrosis factor-α (TNFα) and interleukin-1β (IL-1β), resulting in the production of much larger amounts of NO compared to the constitutive NOS enzymes (Dimmeler and Zeiher, 1997).

As previously discussed, (Section 1.3.1.2), the IRE-1 branch in the UPR is vital for the integration between ER stress and inflammatory response signalling. The IRE-1α-TRAF2 complex recruits IκB Kinase (IKK), which phosphorylates IκB, leading to its degradation and the subsequent translocation of NF-κB to the nucleus (Hu *et al.*, 2006), inducing the expression of inflammatory genes. JNK is activated by the IRE-1α-TRAF2 complex and induces the expression of inflammatory genes by phosphorylating the transcription factor activating protein (AP1) (Davis, 2000). Therefore, the Griess reagent may be used to detect changes in NO production due to ER stress-induced inflammation.

Changes in the nitrate concentration in the spent media after the various treatments was determined using the Griess reagent and extrapolated from a nitrate standard curve, (Appendix iv – Supplementary data, **Figure 71**) to determine if any of the treatments induced an inflammatory response (**Figure 37**).

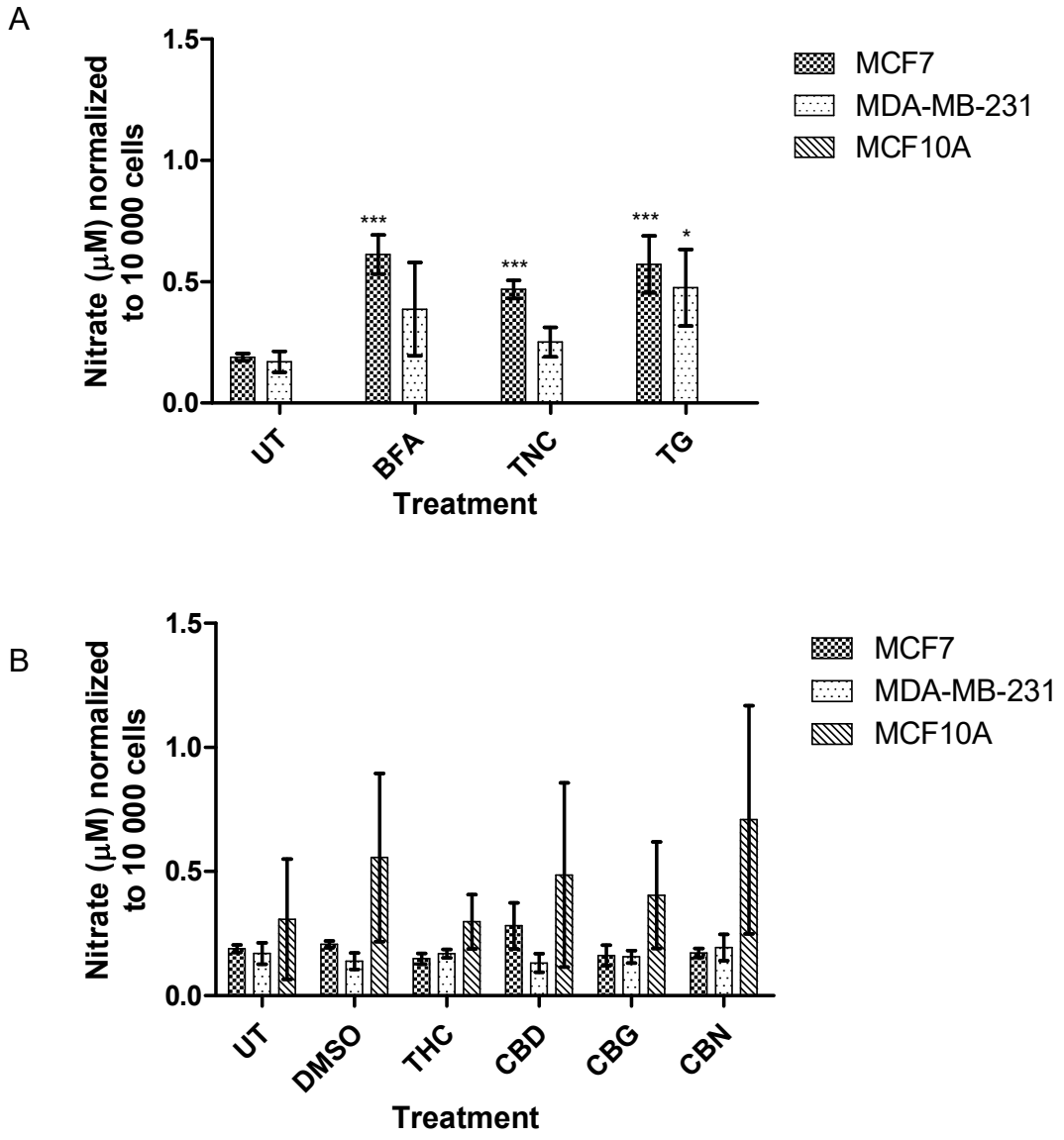

Figure 37: Nitrate concentration in spent media of treated cells.
Cells were treated with (A) various positive controls and (B) the various cannabinoids and the nitrate concentration was determined using the Griess reagent.
UT – Untreated, BFA – Brefeldin A (3.6 μM), TNC – Tunicamycin (1μg/mL) and TG - Thapsigargin (100nM), THC – Δ^9-tetrahydrocannabinol (20 μM), CBD – cannabidiol (20 μM), CBG – cannabigerol (20 μM), CBN – cannabinol (20 μM).
*(n=3, * - significant to respective untreated control, * - p < 0.05, ** - p < 0.01, *** - p < 0.001).*

The MCF7 cell line showed significant increases in the nitrate concentration when treated with the positive controls (**Figure 37A**), suggesting that the positive controls induced an inflammatory response, which correlated with the significant decrease in cell viability that was observed after treatment with the positive controls (**Figure 36A**). The significant decrease in viability and increase in NO production suggested that severe ER stress may have been induced, resulting in the activation of the UPR and

the subsequent induction of inflammation via the IRE-1 branch of the UPR, and ultimately cell death. In the MDA-MB-231 cell line, all positive controls increased NO production; however, only TG resulted in significant NO production, suggesting that TG treatment may result in the most significant activation of the UPR and subsequent induction of inflammatory responses. No nitric oxide production was detected in the MCF10A cell line after treatment with the various positive controls.

No significant changes in NO production were detected after treatment with the various cannabinoids in any of the cell lines (**Figure 37B**). In the MCF7 cell line, CBD treatment was the only cannabinoid that displayed an increase in NO production, suggesting that CBD may have activated the UPR. CBD treatment had no effect in the MDA-MB-231 cells, suggesting that there was no or very little activation of the UPR that resulted in the activation of inflammatory responses.

The Griess reagent has several limitations, namely a low sensitivity due to the high detection limit (100 nM) (Beukes *et al.*, 2019). When used to detect ER stress, the Griess reagent measures responses downstream of both ER stress and the UPR; therefore, the results obtained are not conclusive with regards to detecting the induction ER stress. Another limitation is that this method relies on the activation of inflammatory responses, which may not be activated with all ER stress inducers and may also be induced independently of ER stress.

4.3.3. ER stress induction and UPR activation

Each cell line was treated with the cannabinoids (THC, CBD, CBG and CBN) for 48 hours and subsequently fixed, stained with ThT and normalized to cell number (**Figure 39**) obtained using the SRB assay to determine if there was an increase in the accumulation of misfolded proteins. Images of the stained cells were also acquired using the Zeiss Axio Observer fluorescent microscope (**Figure 38**).

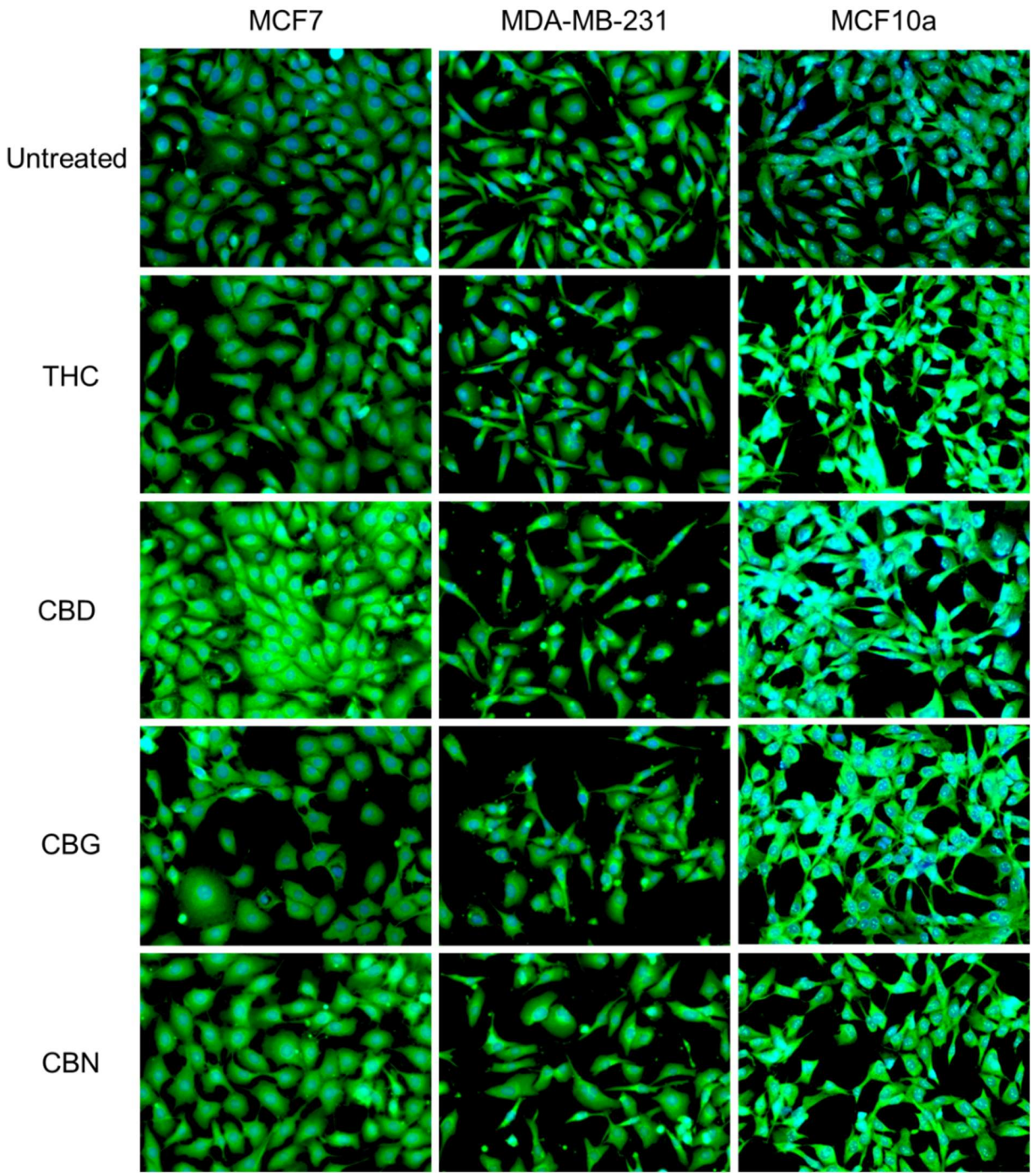

Figure 38: Representative fluorescent images (200x magnification) of MCF7, MDA-MB-231 and MCF10A cells treated with various cannabinoids for 48 hours and stained with ThT and DAPI

UT – Untreated, BFA – Brefeldin A (1 μg/mL), TNC – Tunicamycin (1μg/mL) and TG - Thapsigargin (100nM), THC – Δ^9-tetrahydrocannabinol (20 μM), CBD – cannabidiol (20 μM), CBG – cannabigerol (20 μM), CBN – cannabinol (20 μM).

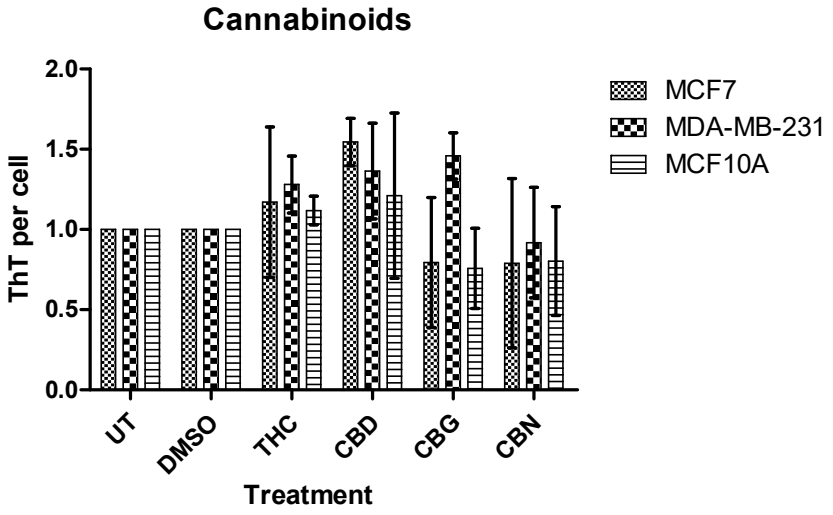

Figure 39: Fold change in the ThT staining normalized to cell number after treatment with the various positive controls and cannabinoids for 48 hours.
UT – Untreated, BFA – Brefeldin A (3.6 μM), TNC – Tunicamycin (1μg/mL) and TG - Thapsigargin (100nM), THC – Δ^9-tetrahydrocannabinol (20 μM), CBD – cannabidiol (20 μM), CBG – cannabigerol (20 μM), CBN – cannabinol (20 μM).
*(n=3, * - significant to respective untreated control, * - p < 0.05, ** - p < 0.01, *** - p < 0.001).*

There were no significant changes in the ThT staining per cell after treatment with the various cannabinoids; however, THC and CBD increased the ThT per cell in all cell lines (**Figure 39**). The MDA-MB-231 showed the largest increase in bound ThT after treatment with THC, whereas the MCF7 cell line showed the greatest increase in bound ThT after treatment with CBD (**Figure 39**), suggesting that these cannabinoids may be increasing the accumulation of misfolded proteins within the ER lumen, inducing ER stress.

With the exception of CBG treatment in the MDA-MB-231 cell line, treatment with CBG and CBN resulted in an overall decrease in the ThT per cell in all cell lines. The decrease in the ThT per cell indicated that CBG and CBN treatment may have decreased the protein-folding load and/or increased the protein folding capacity of the ER. These cannabinoids may be decreasing general protein translation thereby decreasing the folding load within the ER below basal levels; however, it should be noted that none of these treatments were significant.

In summary, the MCF10A cell line displayed the lowest ThT per cell after treatment. There was a slight increase in the bound ThT after treatment with THC and CBD when

compared to the untreated cells; however, it was minimal, suggesting that there was little to no accumulation of misfolded proteins after treatment.

Western blotting analysis was completed to determine changes in GRP78 expression in cells treated with the various cannabinoids, to determine if the cannabinoid-induced ER stress was sufficient to induce UPR activation (**Figure 40**). Histone H3 was used as a loading control to normalize the target protein.

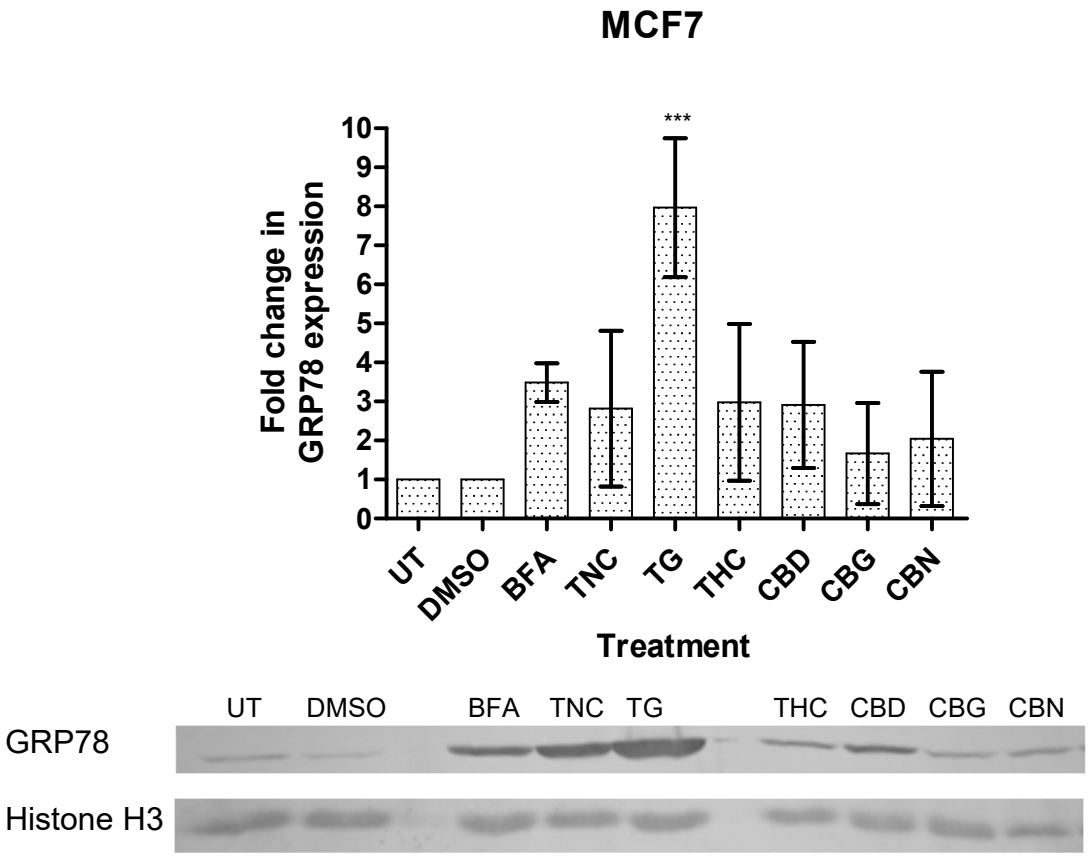

Figure 40: Fold change in GRP78 expression in MCF7 cells after treatment with the various positive controls and cannabinoids for 48 hours.
UT – Untreated, BFA – Brefeldin A (1 μg/mL), TNC – Tunicamycin (1μg/mL) and TG - Thapsigargin (100nM), THC – Δ^9-tetrahydrocannabinol (20 μM), CBD – cannabidiol (20 μM), CBG – cannabigerol (20 μM), CBN – cannabinol (20 μM). Histone H3 was used as a loading control.
*(n=3, * - significant to respective untreated control, * - p < 0.05, ** - p < 0.01, *** - p < 0.001).*

All positive controls showed an increase in GRP78 expression, with significant expression induced by TG treatment (~8 fold). This suggested that, at the concentrations tested, TG was the most potent inducer of ER stress and activator of the UPR. BFA showed the lowest activation of the UPR (~3.5 fold), however, BFA treatment resulted in the greatest decrease in cell viability (**Figure 36**). This

discrepancy may be due to cells becoming less adherent, possibly via the inhibition of MUC1 and α2β1 integrin expression (Porowska *et al.*, 2008), which would decrease the adherence of the cells, giving a false estimation of viability and resemble very low viability based on the MTT viability assay. This loss of adherence in BFA-treated cells was supported by the xCelligence curves (**Figure 13**).

With regards to the cannabinoids, treatment with THC and CBD resulted in the greatest increase in GRP78 expression (~3 fold) (**Figure 40**). This was consistent with the increase in the ThT per cell after treatment with THC and CBD (**Figure 39**) and suggested that there was an increase in the accumulation of misfolded proteins, inducing ER stress and activation of the UPR. Between these two cannabinoids, only CBD resulted in an increase in NO production, with little to no increase in NO after treatment with THC (**Figure 37B**). This could have two possible explanations – firstly, THC did not induce a sufficient amount of ER stress and UPR activation to induce an inflammatory response. The induction of inflammation by ER stress is much further downstream of the initial ER stress trigger, where the ER stress induced may have been modulated and homeostasis restored before inflammatory responses were activated. Secondly, the activation of the UPR by THC may have resulted in the selective activation of the PERK and/or ATF6 branches of the UPR without activating the IRE-1 branch, since the inflammatory response is mainly mediated by the IRE-1 pathway. The former explanation is more likely, due to the lack of cell death that was observed after treatment with THC (**Figure 36B**), which suggested that any ER stress and UPR activation that was induced was not sufficient to induce cell death.

Treatment with CBG and CBN resulted in slight increases in GRP78 expression (~1.6 fold and ~2 fold, respectively) (**Figure 40**), suggesting that there was slight activation of the UPR. The decrease in the ThT per cell, in combination with the increase in GRP78 expression that was observed after treatment with CBG and CBN indicated that there may have been selective activation of the PERK branch of the UPR. As mentioned previously, activated PERK phosphorylates the α-subunit of eIF2α, inhibiting cap-dependent translation and decreasing the protein load in the ER. This branch of the UPR also upregulates the expression of GRP78. Therefore, if PERK signalling was selectively activated, there would be a slight increase in GRP78 expression to facilitate protein folding, as well as a decrease in the ER folding load,

thereby decreasing the bound ThT per cell. However, this theory requires further investigation to confirm.

In the MDA-MB-231 cell line, β-actin was used as a loading control (**Figure 41**), because tunicamycin treatment in this cell line appeared to affect histone H3 expression, as it was not detected in the western blot analysis.

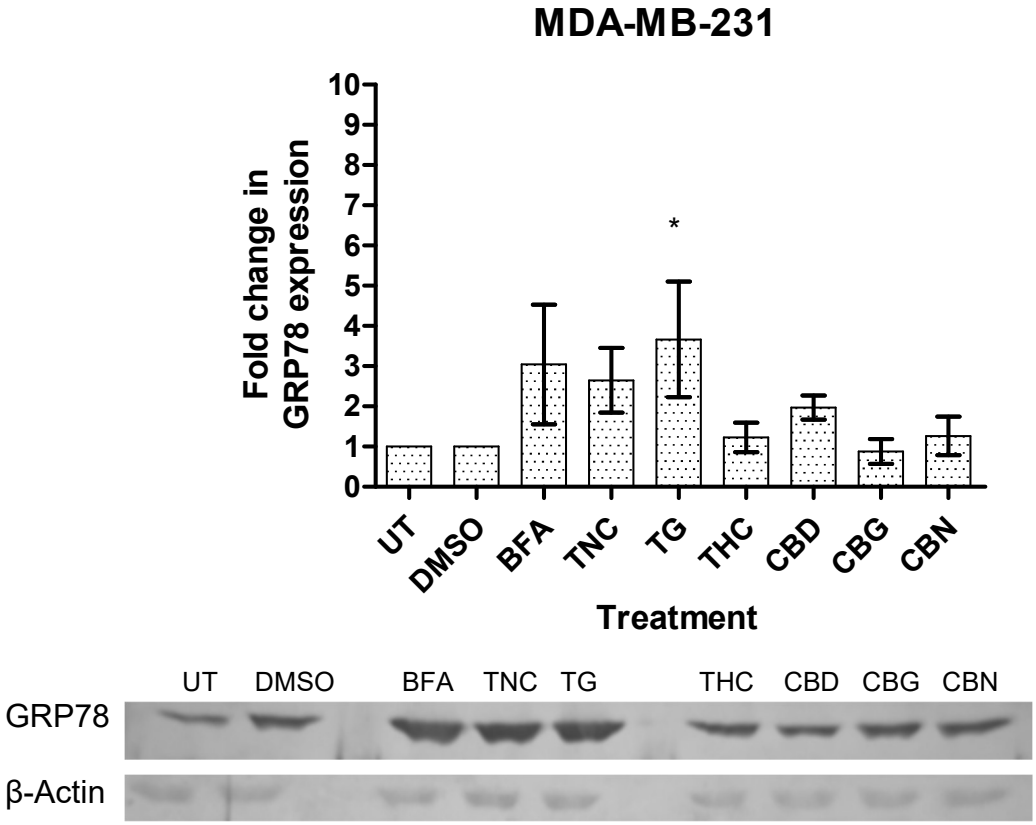

Figure 41: Fold change in GRP78 expression in MDA-MB-231 cells after treatment with the various positive controls and cannabinoids for 48 hours.
UT – Untreated, BFA – Brefeldin A (1 μg/mL), TNC – Tunicamycin (1μg/mL) and TG - Thapsigargin (100nM), THC – Δ^9-tetrahydrocannabinol (20 μM), CBD – cannabidiol (20 μM), CBG – cannabigerol (20 μM), CBN – cannabinol (20 μM). β-actin was used as a loading control.
*(n=3, * - significant to respective untreated control, * - p < 0.05, ** - p < 0.01, *** - p < 0.001).*

Treatment with the positive controls in the MDA-MB-231 cell line resulted in an increase in GRP78 expression, with a significant increase being induced by treatment with TG (**Figure 41**). Similarly, with the MCF7 cells, TG was the most potent ER stress inducer and activator of the UPR. This was consistent with the significant production of NO measured after treatment with TG in this cell line (**Figure 37**). However, the increase in GRP78 expression in the MDA-MB-231 cells (~ 3.6-fold) was lower than in the MCF7 cells (~ 8-fold). This may have been due to the higher basal GRP78

expression in the MDA-MB-231 cells (**Figure 41**), which increased their resistance to UPR activation and subsequent ER stress-induced cell death via the facilitation of an increased protein folding capacity.

CBD showed the greatest increase in GRP78 expression (~2-fold) in the MDA-MB-231 cell line (**Figure 41**); however, the increase was minimal and was consistent with the slight increase in the ThT per cell after treatment with CBD (**Figure 38** & **Figure 39**). Despite the increase in the ThT per cell that was observed with the THC and CBG treatments, there was no increase in GRP78 expression, indicating that there was an accumulation of misfolded proteins, however, it was not sufficient to induce the activation of the UPR, which may have been due to the high basal GRP78 levels. Therefore, it was hypothesized that treatment with a higher cannabinoid concentration or increasing the treatment exposure time would increase the severity of ER stress and trigger UPR activation. CBN did not increase the ThT staining per cell or GRP78 expression, suggesting that, under the specific experimental conditions tested, ER stress was not induced.

No significant increases in GRP78 expression were detected in the MCF10A cell line (**Figure 42**). Treatment with the positive controls resulted in an increase in GRP78 expression, which suggested that the ER stress induced by the controls was sufficient to result in the activation of the UPR. Treatment with the various cannabinoids did not result in a significant change in GRP78 expression in the MCF10A cell line under the conditions tested. This was consistent with the ThT per cell (**Figure 39**), which showed that there was no increase in the percentage of misfolded proteins after treatment; therefore, UPR activation and subsequent increases in GRP78 expression was not expected.

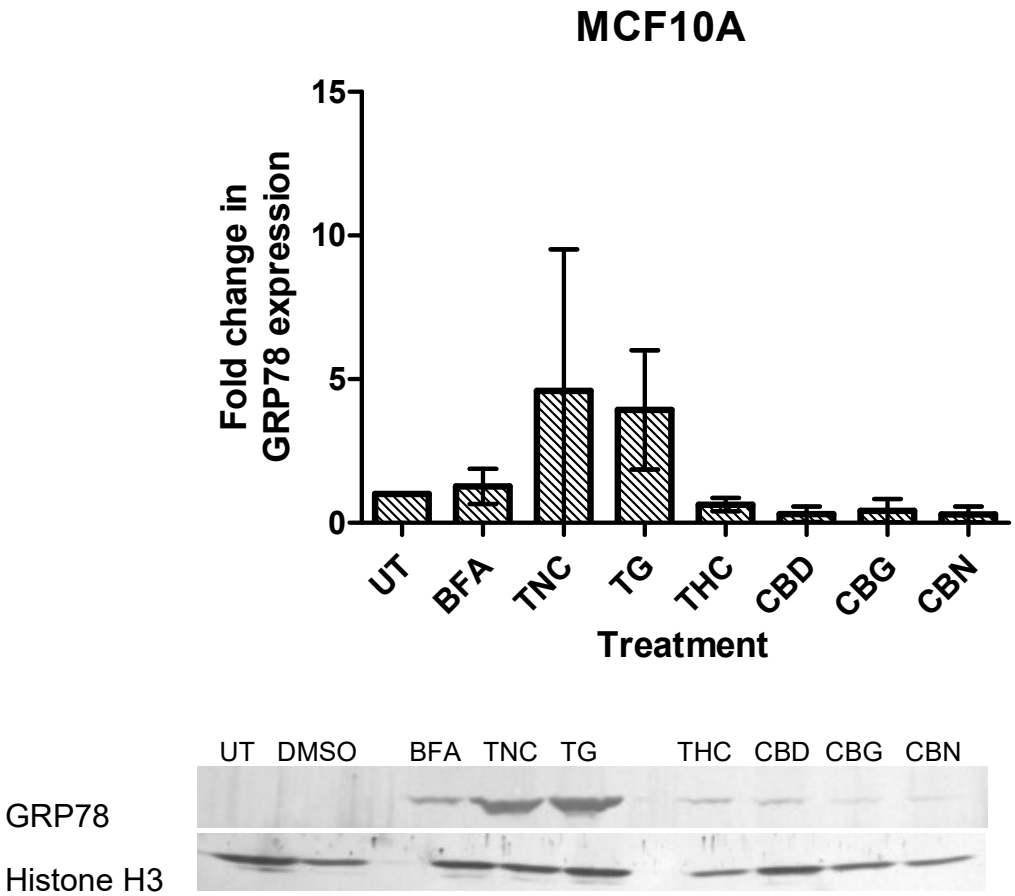

Figure 42: Fold change in GRP78 expression in MCF10A cells after treatment with the various positive controls and cannabinoids for 48 hours.
UT – Untreated, BFA – Brefeldin A (1 μg/mL), TNC – Tunicamycin (1μg/mL) and TG - Thapsigargin (100nM), THC – Δ^9-tetrahydrocannabinol (20 μM), CBD – cannabidiol (20 μM), CBG – cannabigerol (20 μM), CBN – cannabinol (20 μM). Histone H3 was used as a loading control.
*(n=3, * - significant to respective untreated control, * - p < 0.05, ** - p < 0.01, *** - p < 0.001).*

4.3.4. Mitochondrial function

When investigating ER stress it is important to distinguish between true ER stress induction and mitochondrial dysfunction, due to the crosstalk between these organelles (as discussed in section 3.3.3). In order to measure changes in the electron transport chain, the Biolog redox dye (Section 3.2.6) was used (**Figure 43**).

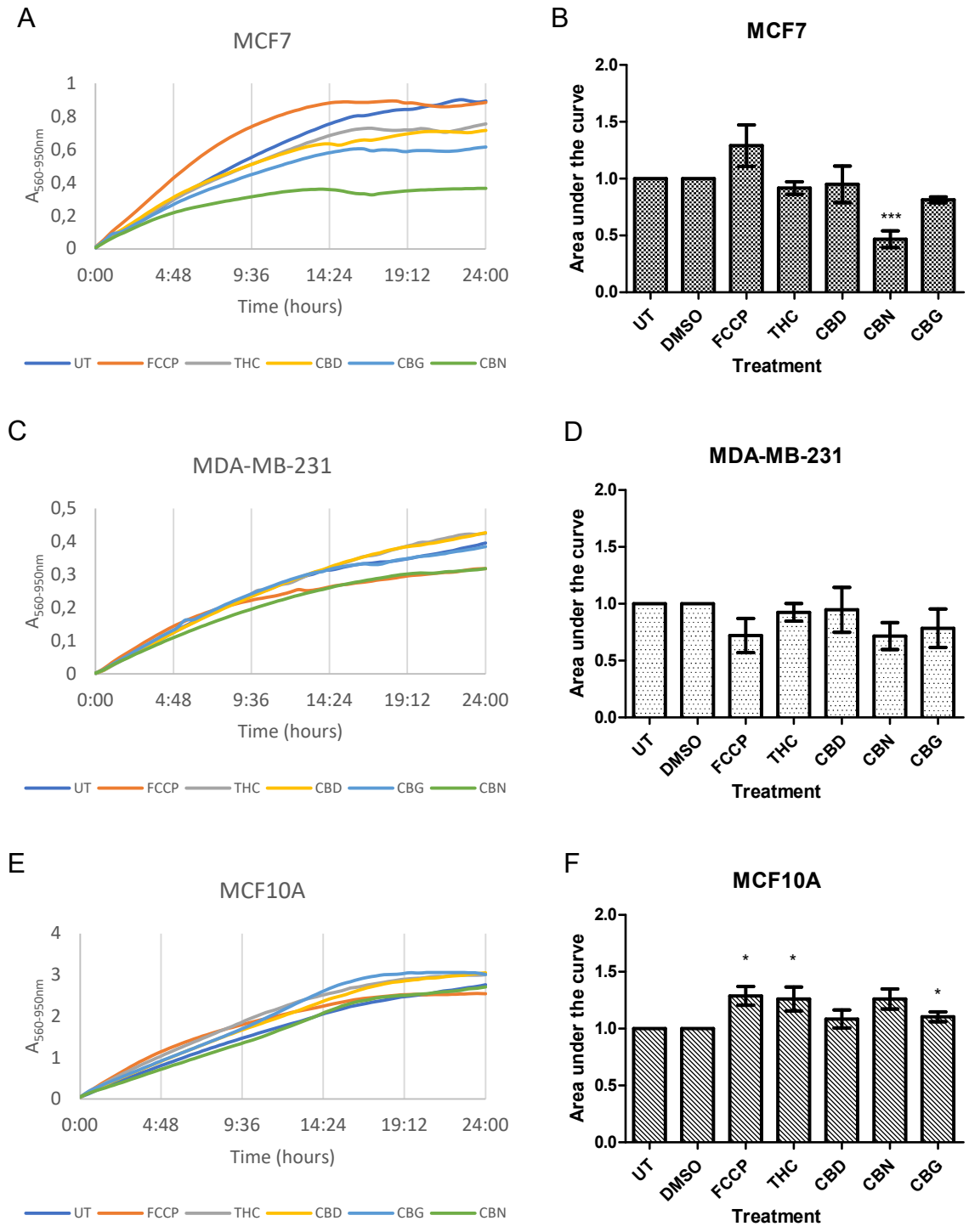

Figure 43: Effect of cannabinoid treatment of reduction of the Biolog redox dye.
(A, C & E) Representative progress curves and (B, D & F) fold change in the area under the curve of redox dye reduction by various cell lines after treatment with THC, CBD, CBG and CBN for 24 hours. UT – untreated, THC – tetrahydrocannabinol (20µM), CBD – cannabidiol (20µM), CBG – cannabigerol (20µM), CBN – cannabinol (20µM)
*(n=3, * - significant to respective untreated control, * - p < 0.05, ** - p < 0.01, *** - p < 0.001).*

FCCP (an uncoupler of oxidative phosphorylation) was used as a mitochondrial control for this assay. In the MCF10A cell line, FCCP showed a significant increase in the

reduction of the tetrazolium dye. In the presence of mitochondrial uncouplers, electron transport from NADH to O_2 proceeds normally; however, the proton-motive force across the inner mitochondrial membrane is dissipated and ATP would not be formed (Berg *et al.*, 2002). The would lead to increased oxygen consumption and the oxidation of NADH to compensate for the decreased ATP levels (Berg *et al.*, 2002), increasing the reduction of the tetrazolium dye. This effect was observed in the MCF7 (**Figure 43A & B**) and MCF10A (**Figure 43E & F**) cell lines, with an increased reduction of the dye in FCCP-treated cells, compared to the untreated cells. However, FCCP treatment in the MDA-MB-231 cell line showed an overall decrease in the reduction of the tetrazolium dye compared to the untreated cells (**Figure 43C & D**). The differences between the cell lines may be due to differences in their energy metabolism. Metabolically, the MCF7 and MCF10A cell lines are similar in that they rely on ATP production from oxidative phosphorylation under normal conditions, however, the MCF7 cells do increase their glycolytic activity under hypoxic conditions (Gatenby and Gillies, 2004, Theodossiou *et al.*, 2019). The MDA-MB-231 cell line are Warburg type cancer cells, and therefore preferentially convert glucose to lactic acid in the presence of oxygen (aerobic glycolysis) (Gatenby and Gillies, 2004), and thus are predominantly dependent on glycolysis for ATP production (Theodossiou *et al.*, 2019). Therefore, the cell lines that have a higher dependency on oxidative phosphorylation for ATP production (MCF7 and MCF10A) would be more susceptible to decreased ATP production by the ETC. This would result in an increase in electron transfer after treatment with an uncoupler in an attempt to compensate for the decreased ATP levels. The MCF7 cell line has been observed to increase their glycolytic activity when required, therefore the increase in electron transfer was less significant than in the MCF10A cell line, which is primarily dependent on the ETC for ATP production, whereas the MCF7 cell line may have upregulated glycolysis to increase ATP production. The MDA-MB-231 cell line is not solely dependent on the ETC for ATP production and would not necessarily increase electron transfer after treatment with an uncoupler.

THC, CBD and CBG showed slight decreases in the reduction of the dye in the MCF7 cell line; however, the change was not significant (**Figure 43B**). There were no significant changes in the MDA-MB-231 cell line after treatment with the various cannabinoids, however THC, CBN and CBG also showed slight decreases in the area

under the curve (**Figure 43D**). Overall, CBN showed the greatest decrease in the reduction of the redox dye in the MDA-MB-231 cell line, however the change not significant.

In the MCF10A cell line, all cannabinoids, showed an increased reduction of the dye when compared to the untreated cells, with a significant increase in cells treated with THC and CBG (**Figure 43F**). Sarafian *et al.* (2003) found that THC treatment in A549 cells resulted in a time- and dose-dependent decrease in ATP levels. A greater than 80% decline in ATP was seen without a significant loss in viability, which suggested an impairment of mitochondrial function may have occurred, as it indicated that the decrease in ATP was not a consequence of the permeability of the mitochondrial membrane caused by cell death. They also found that both FCCP and THC treatment resulted in a decreased mitochondrial membrane potential in a dose-dependent manner. Sarafian *et al.* (2003) compared THC treatment to a variety of mitochondrial inhibitors and demonstrated that THC produced effects similar to that of FCCP, suggesting uncoupling of electron transport. This was consistent with the significant increase in redox dye reduction that was observed after THC treatment (**Figure 43F**), which indicated an increase in electron flow in the ETC. The similarity in redox dye reduction observed in this study after FCCP and THC treatment, combined with the decreased ATP levels and the similarities in the decrease in the MMP after THC and FCCP treatment observed by Sarafian *et al.* (2003), suggested that THC, like FCCP, may act as an uncoupler of oxidative phosphorylation in the MCF10A cell line. This effect was not seen in the MCF7 and MDA-MB-231 cell lines, which show a slight decrease in reduction after THC treatment. This may be due to the MCF7 and MDA-MB-231 cells ability to rely solely on glycolysis for ATP production, and would not result in a decrease in ATP levels after treatment with an uncoupler. The significant increase in reduction in the MCF10A cell line after treatment with CBG (**Figure 43**) suggested that CBG, and possibly CBN, may also be causing uncoupling of oxidative phosphorylation. However, this has not been documented after treatment with these cannabinoids and requires further investigation.

CBN (20 μM) treatment in the MCF7 cell line was the only cannabinoid treatment to significantly decrease the reduction of the redox dye (**Figure 43B**). Based on the principle of the redox dye, in which the tetrazolium salt acts as a terminal electron

acceptor in the ETC, it is possible that CBN treatment significantly inhibited electron flow in the ETC, in turn resulting in a decrease in ATP production, which is required for cell proliferation. However, no significant decreases in cell viability after CBN treatment were detected using the MTT cell viability assay after 48 hours (**Figure 36D**). It is well-established that human cells that lack optimal function of the ETC can proliferate in the presence of supra-physiological concentrations of pyruvate (King and Attardi, 1989), as pyruvate reduction by lactate dehydrogenase (LDH) regenerates the NAD^+ that is lost with ETC inhibition (Harris, 1980, Wilkins *et al.*, 2014). The NAD^+ produced through pyruvate reduction would enable glycolytic flux (**Figure 44**) and therefore ATP would still be produced in cells that lack ETC function (Birsoy *et al.*, 2015).

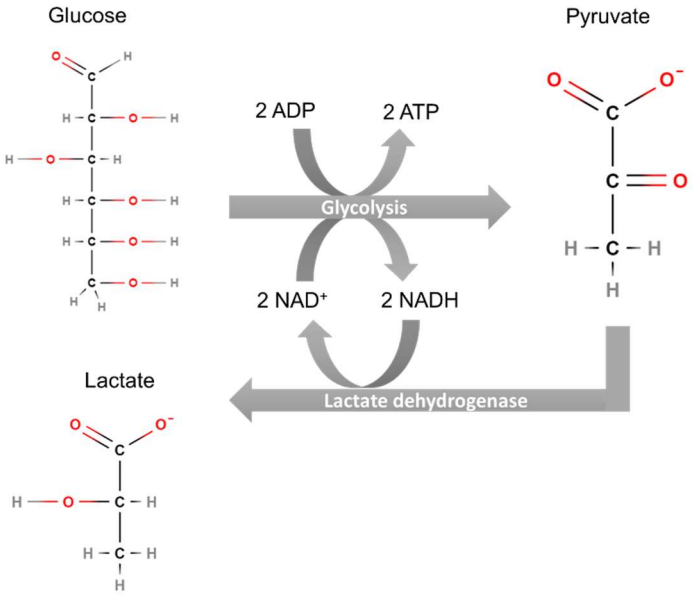

Figure 44: Overview of how supra-physiological levels of pyruvate can regenerate NAD^+ which increases glycolytic flux to generate ATP.
ADP – adenosine diphosphate, ATP – adenosine triphosphate, NAD^+ - nicotinamide adenine dinucleotide.

This may explain why a significant decrease in viability was not observed after 48 hours, despite the significant inhibition of the ETC that was measured at 24 hours. Physiological levels of pyruvate in blood plasma range from 2.6 to 11.4 mg/dL (Phypers and Pierce, 2006). The high glucose DMEM used for the MCF7 cell line contained 110 mg/dL sodium pyruvate, therefore pyruvate was present at a supra-physiological concentration. The pyruvate would be reduced to produce NAD^+, which would be used to drive glycolysis and produce ATP (**Figure 44**) required for cell proliferation. The significant decrease in electron flow after CBN treatment may have

caused significant inhibition of one or more complexes in the ETC, however, due to the limited literature available on CBN, this effect has not been documented.

Enzyme assays for succinate dehydrogenase (SDH) and lactate dehydrogenase (LDH) were performed in order to investigate possible inhibition in the citric acid cycle and/or the ETC (SDH) and an increase in lactate production via LDH activity (**Figure 45A & B** respectively).

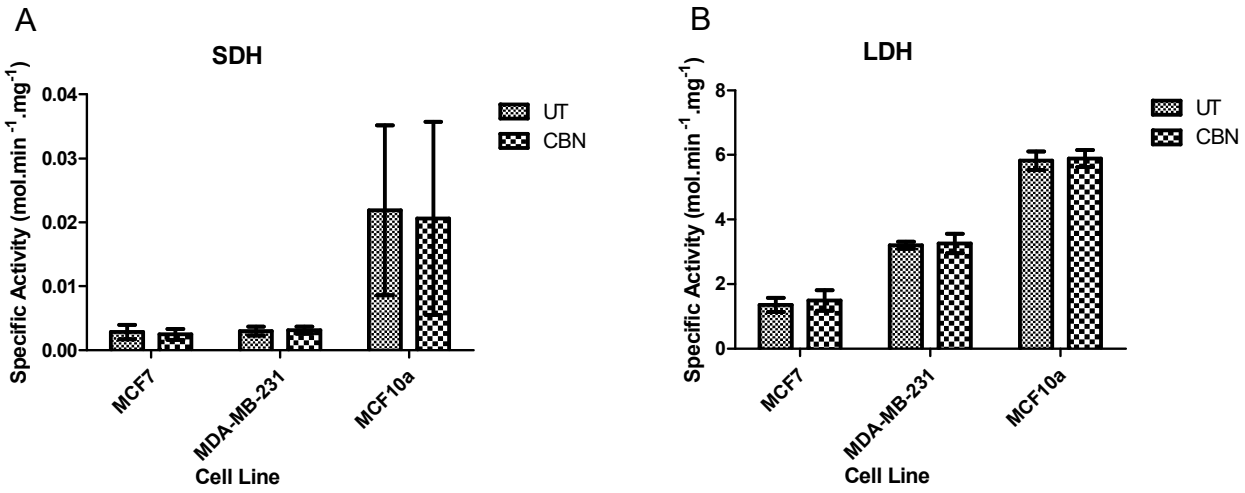

Figure 45: The effect of CBN treatment on the specific activity of various enzymes.
The activity of (A) Succinate Dehydrogenase and (B) Lactate Dehydrogenase was measured in the MCF7, MDA-MB-231 and MCF10A cell lines after treatment with CBN for 24 hours
UT – untreated, CBN – cannabinol (20µM), SDH – succinate dehydrogenase, LDH – Lactate dehydrogenase.
*(n=3, * - significant to respective untreated control, * - p < 0.05, ** - p < 0.01, *** - p < 0.001).*

No significant increases or decreases in the specific activity of SDH or LDH were measured after CBN treatment. This suggested that the expression and/or activities of these enzymes were not increased in response to treatment with CBN, suggesting that the proposed mechanism – inhibition in the ETC after CBN treatment with increased LDH activity to regenerate NAD^+ to allow for cell proliferation – may not have been induced by CBN treatment.

Due to the significant decrease in the reduction of the redox dye in the MCF7 cell line observed with CBN treatment after 24 hours, and the lack of a significant decrease in viability at 48 hours of treatment, the effect of CBN treatment on cell viability at 24 hours was determined. Both the MTT and SRB cell viability assays (**Figure 46**) were performed in order to determine if any changes in viability that were observed were

only due to metabolic inhibition (such as inhibition in the ETC), or due to a decreased cell number (based on protein content).

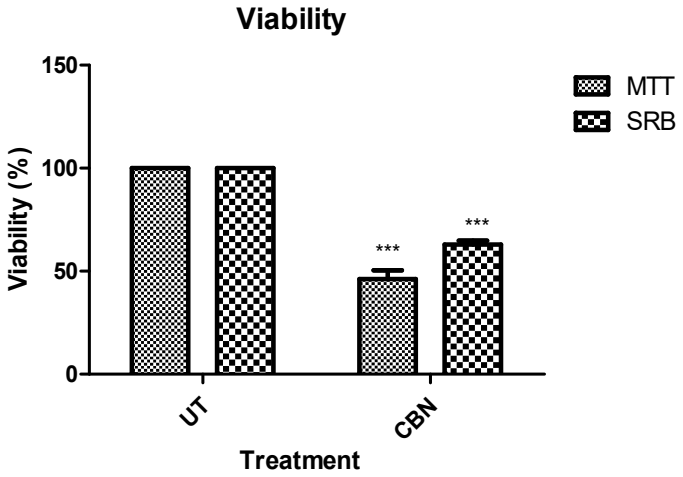

Figure 46: Change in the viability of MCF7 cells after treatment with CBN for 24 hours, determined using MTT and SRB cell viability assay.
UT – untreated, CBN- cannabinol (20μM).
*(n=3, * - significant to respective untreated control, * - p < 0.05, ** - p < 0.01, *** - p < 0.001).*

CBN treatment resulted in a significant decrease in cell viability measured using both the MTT and SRB assays (**Figure 46**). This suggested that CBN treatment significantly decreased metabolic activity (MTT) and cell number (SRB), which may have either been due to an inhibition of cell proliferation or the induction of cell death, or a combination of both. Therefore the significant decrease in the reduction of the redox dye measured after CBN treatment for 24 hours (**Figure 43**) may not have been due to a decrease in electron flow in the ETC with no decrease in cell proliferation as proposed, but rather due to an overall decrease in cell viability. However, the lack of a significant decrease in viability measured after 48 hours of treatment (**Figure 36**) suggested that the concentration of CBN used was low enough that the cells were able to overcome the inhibition caused by CBN treatment and proliferate between 24 and 48 hours of exposure, resulting in a non-significant decrease in viability after 48 hours. The mechanism of cell death by CBN treatment was subsequently investigated. The MCF7 cells were treated with the various cannabinoids (20 μM) and phase-contrast images were acquired after 24 hours (**Figure 47**).

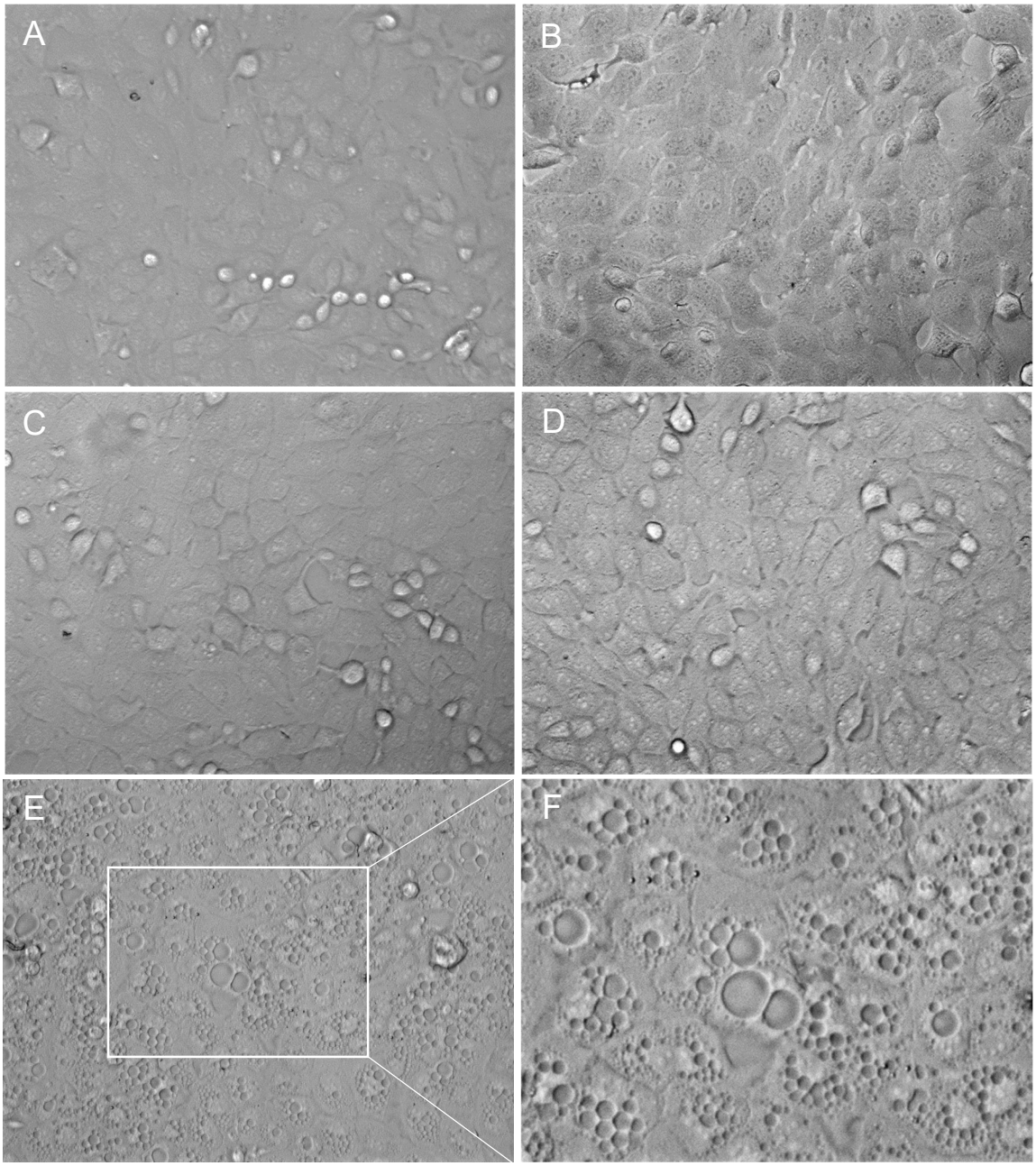

Figure 47: Representative phase-contrast micrographs of MCF7 cells treated with various cannabinoids for 24 hours.
(A-E – 200x magnification, F – 400x magnification). The white block represents the area in which the magnification was increased. (A) Untreated; (B) THC – tetrahydrocannabinol (20 µM); (C) CBD – cannabidiol (20 µM); (D) CBG – cannabigerol (20 µM); (E) CBN – cannabinol (20 µM); (F) CBN – cannabinol (20 µM).

CBN treatment (**Figure 47E & F**) resulted in the formation of vesicle-like structures, which were not observed after treatment with any of the other cannabinoids tested (**Figure 47B – D**). In order to investigate whether the structures observed were due to the formation of lipid droplets, or vacuoles originating from the ER, mitochondria or lysosomes, the cells were treated with CBN for 24 hours and subsequently stained

with LipidTOX, ER tracker, MitoTracker and LysoTracker. Confocal microscopy was then used to acquire images of the cells. In order to capture the images, 5 slices were captured and individually exported using the Zen Blue software (Appendix iii – Equipment and software information). ImageJ software (Appendix iii – Equipment and software information) was then used to stack the slices. The stack was then analysed by applying the maximum intensity Z-projection, in which each of the pixels in the output image contained the maximum value of all the images in the stack at each specific pixel location.

Untreated and CBN-treated cells were stained with LysoTracker™ Green, which stains acidic compartments (Section 4.2.3.4), in order to determine if the vesicles that were observed were due to the increased formation of lysosomes that would be characteristic of autophagy-induced cell death (**Figure 48**).

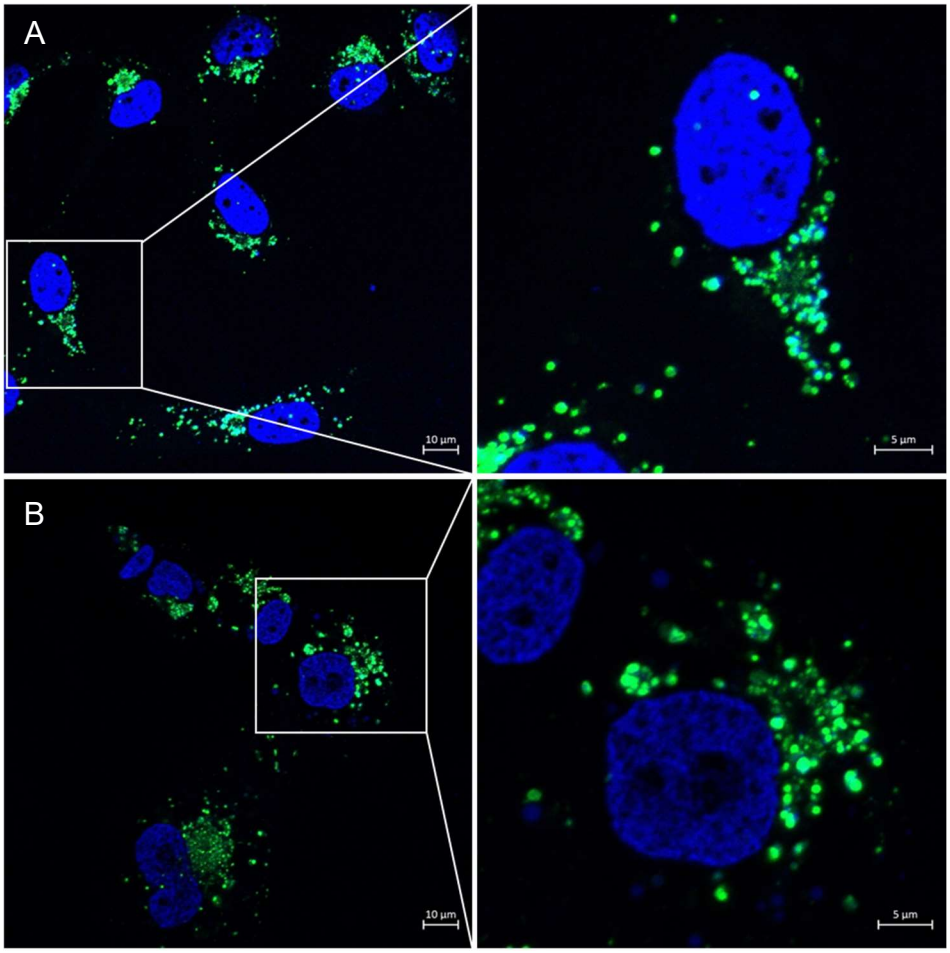

Figure 48: Representative images of MCF7 cells stained with LysoTracker (green) and Hoechst (blue).
Cells were exposed to (A) no treatment and (B) CBN treatment for 24 hours. The white block represents the area in which the magnification was increased. CBN – cannabinol (20 µM).

The large vesicle-like structures observed after CBN treatment did not stain with LysoTracker, suggesting that they were not the result of the formation of lysosomes. CBN treatment did not appear to increase or decrease the size or number of lysosomes in the cell. This suggested that autophagy-mediated cell death may not be induced by CBN treatment, as induction of autophagy would be associated with lysosome accumulation, resulting in an increase in the lysosome size within the cell.

Due to the round, unilocular shape of the vesicle-like structures, it was thought that they may have been the result of lipid accumulation into lipid droplets (LD's). Untreated and CBN-treated cells were also stained with LipidTOX™ Green (Section 4.2.3.3), which has a high affinity for neutral lipids (**Figure 49**).

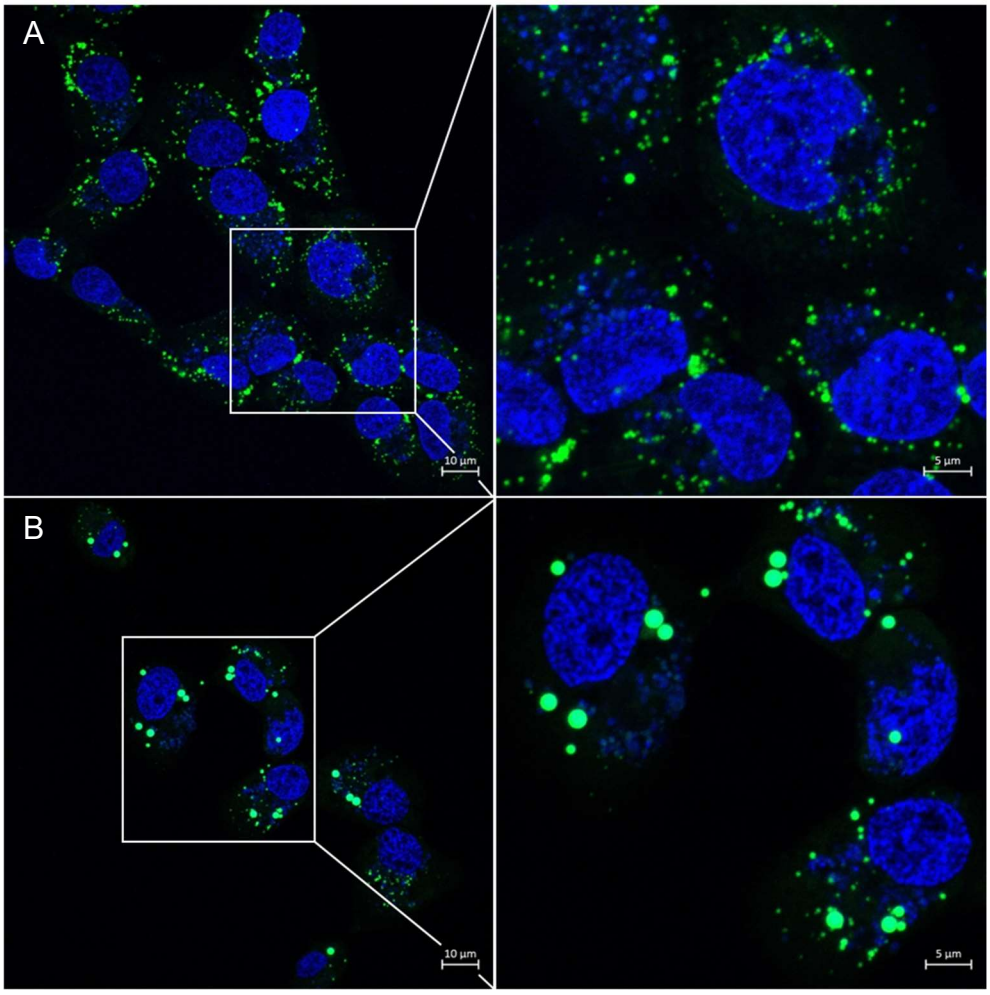

Figure 49: Representative images of MCF7 cells stained with LipidTox (green) and Hoechst (blue).
Cells were exposed to (A) no treatment and (B) CBN treatment for 24 hours. The white block represents the area in which the magnification was increased. CBN – cannabinol (20 µM).

The untreated cells showed small lipid droplets spread uniformly through the cell. This was expected, as eukaryotic cells store neutral lipids, such as triacylglycerols (TAGs), in lipid droplets (Markgraf *et al.*, 2014). The large vesicle-like structures formed after CBN treatment did not stain with the LipidTOX, suggesting that they did not form as a result of neutral lipid accumulation. However, treatment with CBN did appear to dramatically increase the size of the lipid droplets and decrease the average number of droplets in the cell.

The ER Tracker™ dye consists of Glibenclamide, which binds to the sulphonylurea receptors of ATP-sensitive potassium channels, which are prominent on the ER membrane. Untreated and CBN-treated cells were also stained with ER Tracker Red (Section 4.2.3.1) in order to determine if the structures were the result of vacuoles that originated from the ER (**Figure 50**).

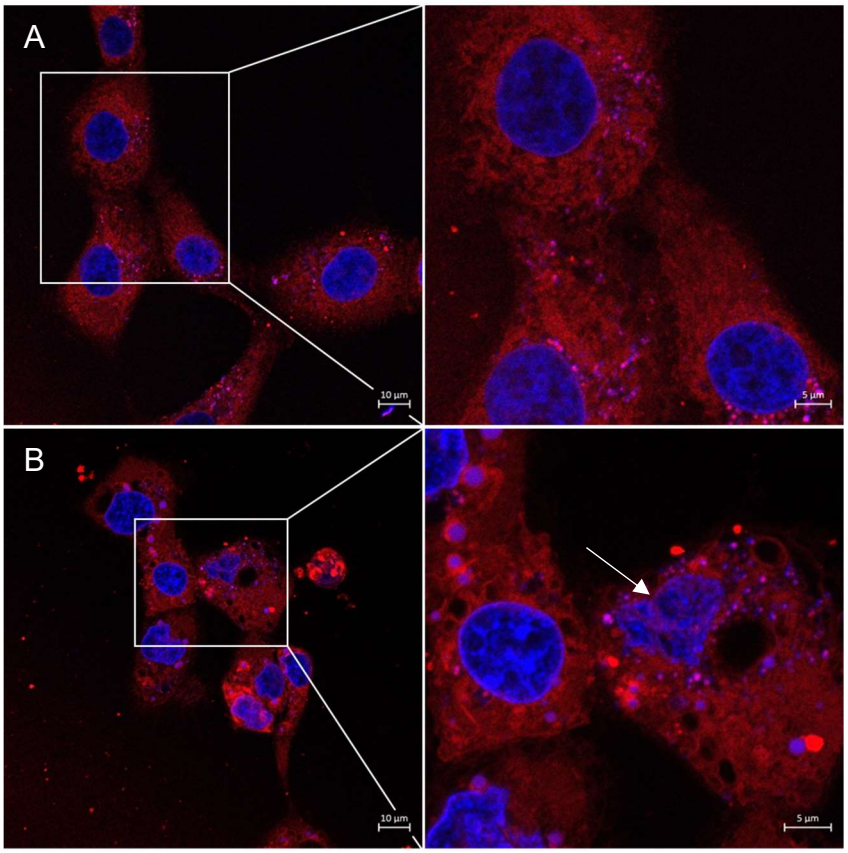

Figure 50: Representative images of MCF7 cells stained with ER Tracker (Red) and Hoechst (blue).
Cells were exposed to (A) no treatment and (B) CBN treatment for 24 hours. The white block represents the area in which the magnification was increased. CBN – cannabinol (20 µM).

The untreated cells showed uniform staining throughout the cell (**Figure 50A**). This was expected because, as described earlier (Section 1), the membrane of the peripheral ER interacts with the cytoskeleton to spread throughout the cytoplasm (English *et al.*, 2009, Voeltz *et al.*, 2002), facilitating the association with other membrane-bound compartments. The staining with the ER tracker highlighted the vacuoles that were formed in CBN-treated cells. While the staining intensity did not appear to specifically increase around the vacuoles formed after CBN treatment, the overall staining was less uniform than in the untreated cells with distinctive areas of increased staining intensity, as indicated by the arrow (**Figure 50B**), suggesting an increase in the ER content in these areas. It can also be seen that CBN treatment appeared to induce some redistribution of the ER into the nucleus with a disruption in the nuclear membrane, as indicated by the arrow (**Figure 50B**). The extensive vacuolation and redistribution into the nucleus were also observed (**Figure 51**).

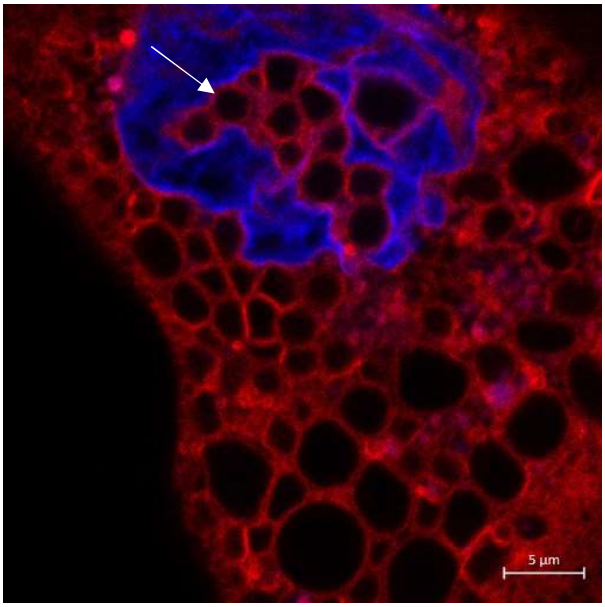

Figure 51: Representative image of MCF7 cells stained with ER Tracker (red) and Hoechst (blue) after CBN treatment for 24 hours.
CBN – cannabinol (20 µM).

The fact that the ER tracker stained around all the vacuoles, and that the vacuoles can be seen in the ER that had redistributed into the nucleus (indicated by the arrow), combined with the disruption of the nuclear membrane, it was hypothesized that the vacuoles were ER-derived. Since the ER is continuous with the nuclear membrane (Section 1.1), the formation of the vacuoles in the ER would have disrupted the ER membrane and by extension, disrupted the nuclear membrane.

Untreated and CBN-treated cells were stained with the Mitochondrial Staining Kit, to determine if any vacuoles formed arose from the mitochondria. The dye selectively accumulates and is retained in mitochondria (Section 4.2.3.1).

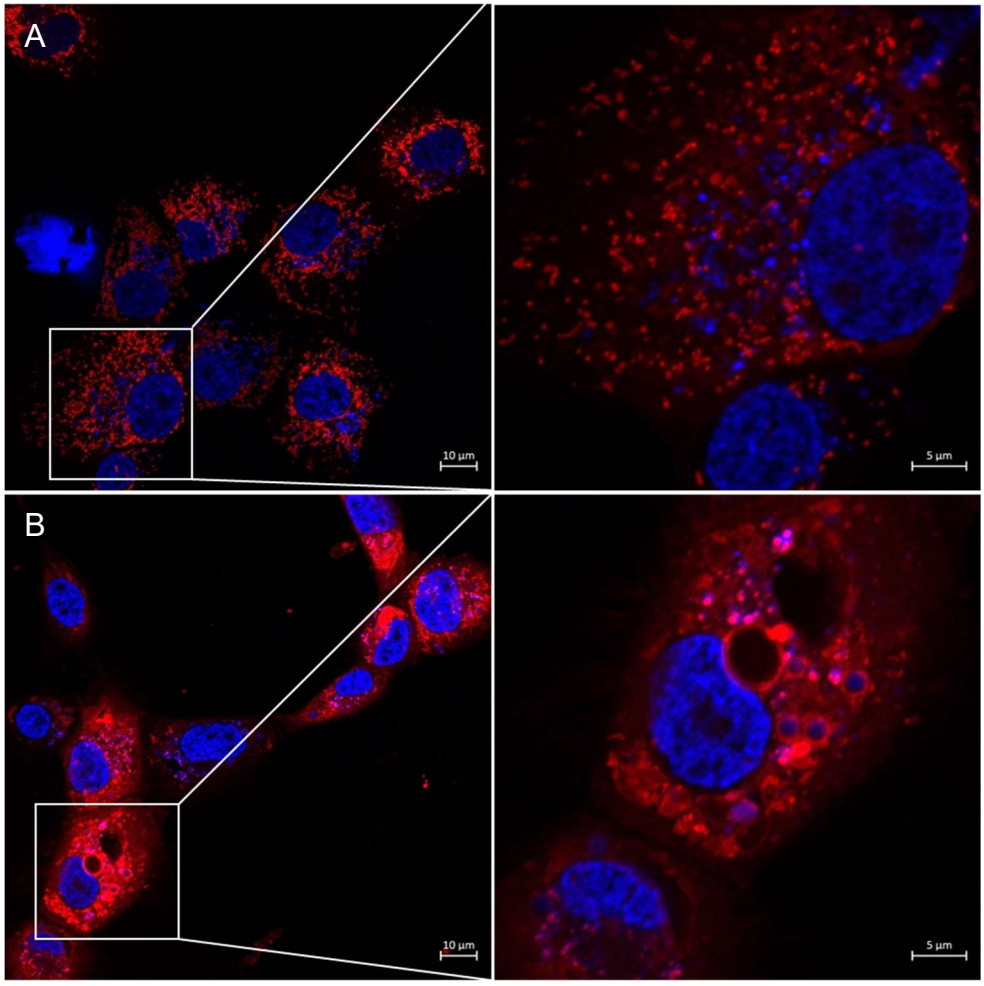

Figure 52: Representative images of MCF7 cells stained with MitoTracker (red) and Hoechst (blue).
Cells were exposed to (A) no treatment and (B) CBN treatment for 24 hours. The white block represents the area in which the magnification was increased. CBN – cannabinol (20 µM).

MitoTracker staining in the untreated cells showed small, defined structures spread throughout the cytoplasm, which would be consistent with mitochondria in a healthy cell. MitoTracker staining in the CBN-treated cells showed a loss of the definition in the mitochondria compared to the untreated cells and resulted in irregular staining throughout the cell.

Due to the morphological changes that were observed after CBN treatment, a possible mechanism that may be induced by CBN is paraptosis, a recently discovered caspase-

independent mechanism of programmed cell death (PCD). Paraptosis is morphologically different from apoptosis and is characterized by cytoplasmic vacuolation that results from the dilation of the ER and mitochondria (Wang *et al.*, 2019). Current research on paraptosis has mostly focused on the associated morphological changes which include: the characteristic cytosolic vacuolation that arises from the ER and mitochondria as well as an increase in the density of the cytoplasm; no destruction of the outer cell membrane and irregular aggregation of chromatin in the nucleus (Wang *et al.*, 2019).

Many of these morphological changes were consistent with what was observed after treatment with CBN, the most extensive being the cytoplasmic vacuolation (**Figure 47E & F**) that appeared to originate from the ER (**Figure 50B**). Cytoplasmic vacuolation is also observed in autophagy, however, autophagic vacuoles are not observed in paraptosis (Sperandio *et al.*, 2000). Therefore, the presence of the cytoplasmic vacuoles (**Figure 50**) but lack of autophagic vacuoles (**Figure 48**) is suggestive of paraptosis, as opposed to autophagy.

Mitochondrial swelling is also characteristic of paraptosis and results in a disruption of mitochondrial structure, and disappearance of the mitochondrial cristae (Thiam and Beller, 2017), which was observed after CBN treatment (**Figure 52B**). This also suggested that the mechanism induced by CBN treatment may be paraptosis. In line with the other morphological changes, none of the treated cells showed a disruption of the outer cell membrane and also showed irregular staining of the nucleus, suggestive of chromatin condensation. The chromatin did not display the characteristic ring structure (described in Section 3.3.2) associated with apoptosis, however many cells, particularly those stained with ER Tracker (**Figure 50**) and MitoTracker (**Figure 52**), showed the formation of what appeared to be micronuclei. The formation of micronuclei has not been recorded as a defining feature of paraptosis and are generally associated with apoptosis. However, it has been reported that apoptosis and paraptosis generally occur simultaneously within a cell (Wang *et al.*, 2019).

Current literature that describes the morphological changes that may occur during paraptosis does not include descriptions of changes in the morphology of lipid droplets, which was observed in the CBN-treated cells. It was hypothesized that the decrease in number but an increase in the size of the lipid droplets after CBN treatment

may be due to the vacuolation of the cytoplasm arising from the ER. Lipid droplet synthesis begins with the synthesis of neutral lipids by enzymes localized at the ER. The newly formed lipids (mostly TAGs) are then transferred into the intermembrane space of the ER. When the concentration of neutral lipids reaches a certain level, it becomes thermodynamically favourable for the molecules to fuse to form a lipid lens (Thiam and Beller, 2017). These lipid lenses can enlarge by 3 mechanisms: (1) by acquiring more TAGs through ongoing lipogenesis, (2) fusion of lipid lenses in the ER bilayer or (3) transfer of lipids between lenses (Thiam and Beller, 2017, Thiam and Forêt, 2016). The growth of lipid lenses subsequently results in the accumulated lipids becoming spherical (budding) and forming a lipid droplet (Thiam and Beller, 2017).

The formation of vacuoles in the ER during paraptosis may favour lipid accumulation due to (1) increased TAGs content in an area and/or (2) disruption in the ER bilayer. Vacuole formation in the ER would result in compression of the ER membrane, increasing the TAG content in a specific area and may also prevent the release of the lipid droplets from the ER membrane, thereby resulting in increased fusion of the smaller lipid droplets to form larger droplets. Disruptions in the ER membrane would also facilitate the formation of lipid droplets due to increased exposure of the hydrophobic regions of the membrane, which induces stress on the membrane. The accumulation of TAGs in these areas is favourable, as it reduces the membrane stress (Thiam and Beller, 2017).

In order to investigate this hypothesis, the cells were stained with both ER tracker and LipidTOX to determine if the areas of increased ER tracker staining, indicating condensed ER, colocalized with the large lipid droplets (**Figure 53**).

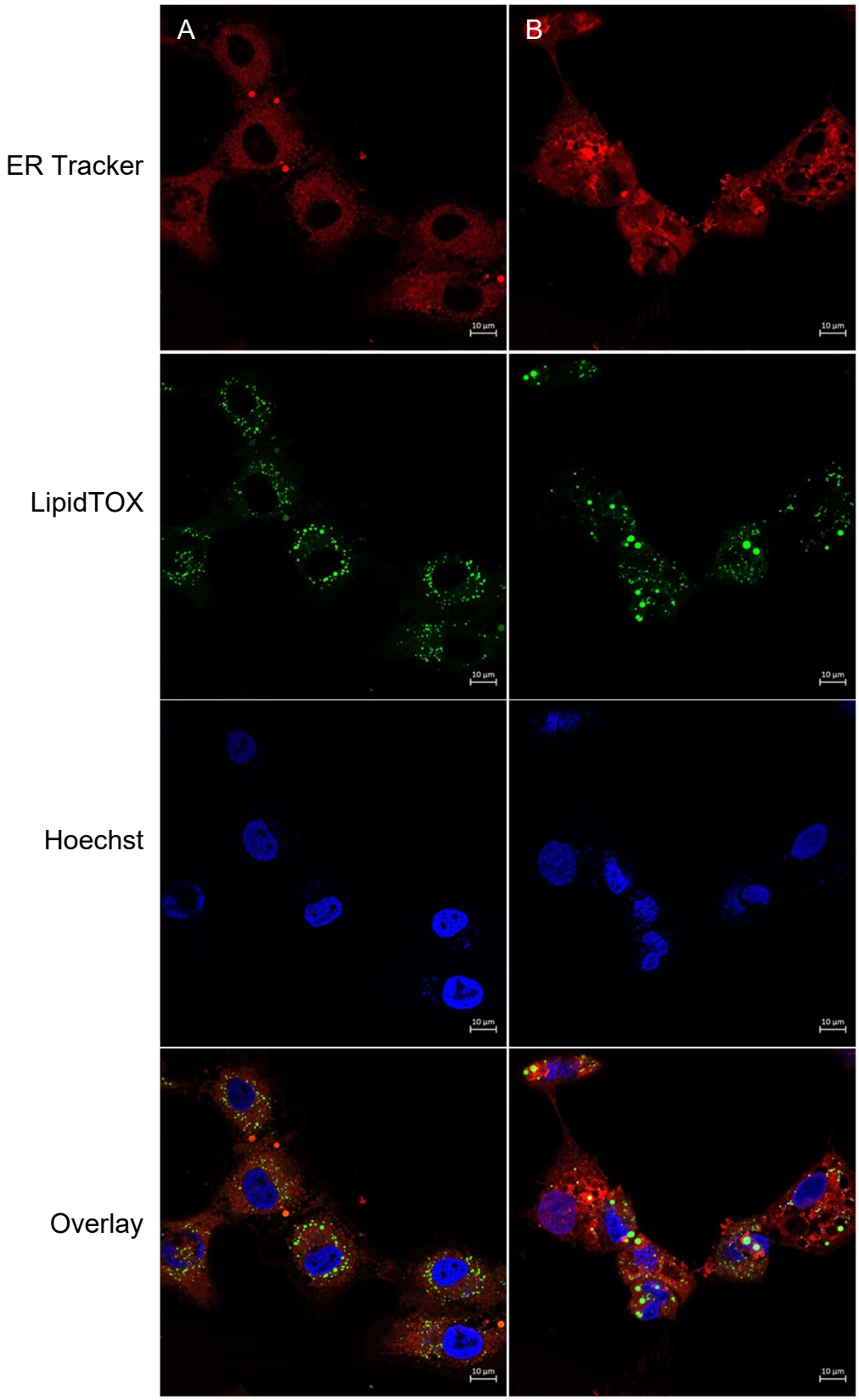

Figure 53: Representative images of MCF7 cells stained with ER Tracker (Red) and LipidTox (green) and Hoechst (blue).
Cells were exposed to (A) no treatment and (B) CBN treatment for 24 hours.
CBN – cannabinol (20 µM).

Many of the larger lipid droplets that formed appeared to colocalize with increased ER Tracker staining intensity, suggesting that the larger lipid droplets may form in areas with increased ER content. This suggested that the lipid droplets may not be a direct result of paraptosis, but rather a consequence of vacuole formation in the ER, which is characteristic of paraptosis.

The proposed mechanism of paraptosis induction was only observed after treatment with CBN in the MCF7 cell line. This may be due to differences in the expression of the IGF1R. Paraptosis was first observed in cell lines that overexpressed the insulin-like growth factor-1 receptor (IGF1R) (Sperandio *et al.*, 2000). Sperandio *et al.* (2004) showed that IGF1R-induced paraptosis is mediated through the activation of MAPK and JNK signalling pathway. Akekawatchai *et al.* (2006) showed that the MCF7 cell line displays high levels of expression of the IGF1R, with 98.85% of positive cells, while the MDA-MB-231 cell line displayed lower levels of expression with 22.65% positive cells. Activation of the IGF1R may, therefore, explain why the induction of paraptosis was only observed in the MCF7 cell line. However, the activation of IGF1R by CBN has not been documented and requires further investigation.

Figure 54 provides an overview of the experimental design followed in chapter 4 for determining the molecular mechanism(s) of ER stress induction.

Figure 54: Overview of the experimental design for the determination of the molecular mechanism(s) associated with cannabinoid-induced ER stress

4.3.5. Changes in intracellular ROS and Calcium

The change in ROS production as a result of cannabinoid treatment was measured using DCFH-DA staining, normalized to cell number obtained using the SRB cell viability assay and the fold change was calculated relative to the respective untreated or vehicle control for the various cell lines (**Figure 55**).

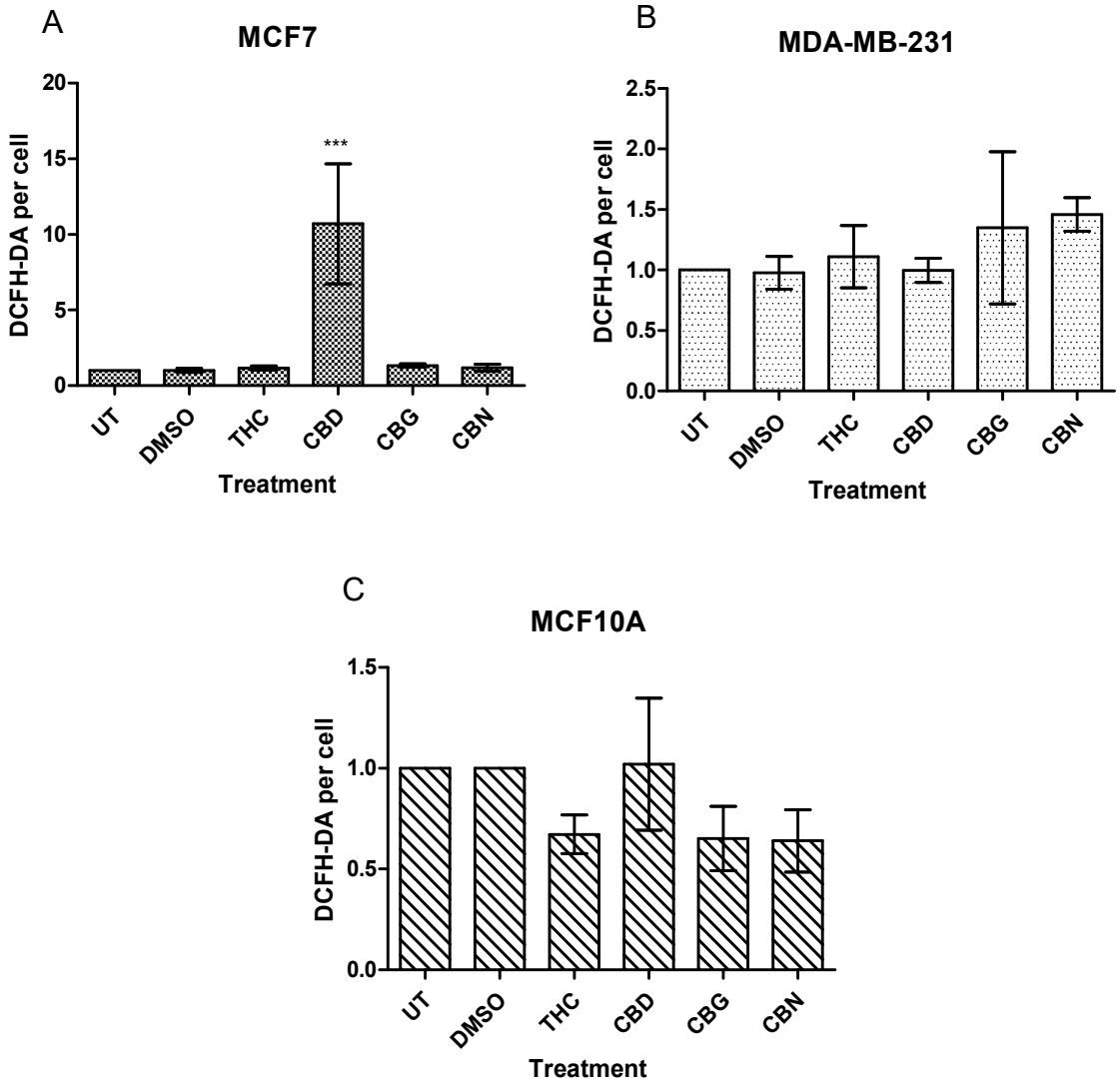

Figure 55: Effect of cannabinoid treatment on ROS production in the MCF7, MDA-MB-231 and MCF10A cell lines.
Fold change in DCFH-DA, normalized to cell number obtained using the SRB assay, relative to the untreated or vehicle control after treatment with the various cannabinoids for 48 hours in the (A) MCF7, (B) MDA-MB-231 and (C) MCF10A cell lines.
UT – untreated, DMSO – dimethyl sulfoxide, THC – tetrahydrocannabinol (20μM), CBD – cannabidiol (20μM), CBG – cannabigerol (20μM), CBN- cannabinol (20μM).
*(n=3, * - significant to respective untreated control, * - $p < 0.05$, ** - $p < 0.01$, *** - $p < 0.001$).*

CBD was the only treatment to significantly increase the production of ROS in the MCF7 cell line (**Figure 55A**). No significant changes were detected after treatment with any of the cannabinoids in the MDA-MB-231 (**Figure 55B**) and MCF10A (**Figure 55C**) cell lines; however, treatment with CBG and CBN in the MCF7 and MDA-MB-231 cell lines displayed a slight increase in ROS production (1.3 and 1.2 fold respectively in the MCF7 cells and 1.3 and 1.5 fold respectively in the MDA-MB-231 cells). Treatment with THC, CBG and CBN decreased ROS production in the MCF10A cell line below basal levels, however, the decrease was not significant. These cannabinoids also showed an increase in electron flow in the ETC in the MCF10A cell line (**Figure 43F**) and it is hypothesized that they may be causing uncoupling of oxidative phosphorylation in the MCF10A cell line. This would result in increased oxygen consumption and would decrease the presence of ROS, which was observed (**Figure 55C**), further supporting the hypothesis that these cannabinoids may be causing uncoupling of oxidative phosphorylation.

Due to the significant increase in ROS production, as well as the increase in ER stress (**Figure 39**) and UPR activation detected after CBD treatment in the MCF7 cell line, the remainder of the study focused on the effect of CBD treatment in all the cell lines.

The cell lines were treated with various CBD concentrations ranging from 0 to 20 μM to determine if the increase in ROS production was concentration-dependent (**Figure 56**). The MCF7 cell line treated with CBD resulted in a concentration-dependent increase in ROS; however, the increase in ROS was only significant at the highest concentration (20 μM). The minimal production of ROS at the lower CBD concentrations may be insufficient to elicit a cellular response and/or may be nullified by the inherent antioxidant mechanisms. Several types of antioxidants play a role in ROS homeostasis, specifically endogenous antioxidant enzymes (e.g. superoxide dismutase, catalase, peroxiredoxins, thioredoxins and heme oxygenase), as well as antioxidant molecules (e.g. glutathione), which are typically upregulated in cancer cells (Marengo *et al.*, 2016).

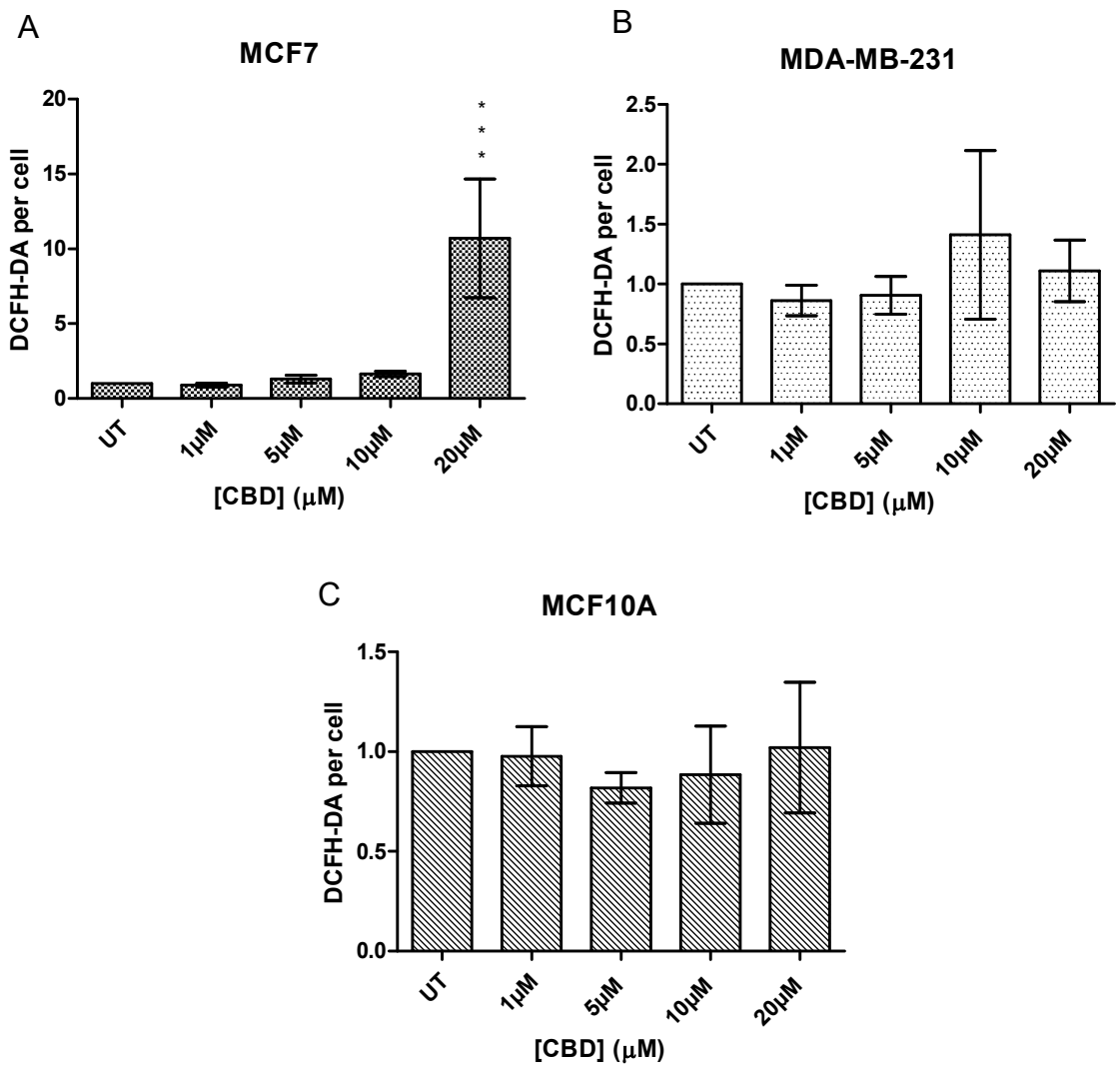

Figure 56: Concentration-dependent effect of CBD treatment on ROS production in the MCF7, MDA-MB-231 and MCF10A cell lines.
Fold change in DCFH-DA, normalized to cell number obtained using the SRB assay, relative to the respective untreated or vehicle control after treatment with the various concentrations of CBD for 48 hours in the (A) MCF7, (B) MDA-MB-231 and (C) MCF10A cell lines.
UT – untreated, CBD – cannabidiol
*(n=3, * - significant to respective untreated control, * - p < 0.05, ** - p < 0.01, *** - p < 0.001).*

No concentration-dependent increase in ROS production was seen in the MDA-MB-231 cell line, however, a significant concentration-dependence was not expected as significant ROS was not detected after treatment with 20 μM CBD (**Figure 55B**).

The MCF10A cell line displayed a non-significant decrease in ROS levels below that that of the untreated cells at 5 μM CBD, after which it showed a concentration-dependent increase in ROS between 5 and 20 μM. However, the fold change in the ROS production of CBD-treated cells did not increase above that of the untreated cells.

There was a slight decrease in ROS production at the lower concentrations (5 and 10 μM) of CBD when compared to the untreated cells, highlighting the antioxidant potential of CBD.

The antioxidant properties of CBD have been documented and CBD was found to have direct, potent antioxidant properties (Hampson *et al.*, 2000). This supported the data obtained (**Figure 56**) in which significant ROS production was only seen at the highest concentration of 20 μM CBD in the MCF7s, and why a decrease was seen in the MCF10A cell line. At the lower CBD concentrations, either the inherent antioxidant systems in the cell or the antioxidant properties of CBD may be sufficient to overcome any ROS produced. However, this is not observed at the highest CBD concentration, as the antioxidant potential may no longer be sufficient to overcome the levels of ROS that were produced.

The cells were then treated with the same concentration range of CBD to determine the effect of CBD treatment of calcium influx into the cells (**Figure 57**), using calcium green staining.

The MCF7 cell line did not show a concentration-dependent increase in the intracellular calcium for the range tested. Between 1 and 10 μM the intracellular Ca^{2+} was comparable to the untreated; however, after treatment with the highest concentration of 20 μM CBD, there was a significant increase in the intracellular calcium (**Figure 57A**). This suggested that treatment with the lower concentrations of CBD (1 – 10 μM) did not affect the influx of calcium, or that the cells were still able to counteract the Ca^{2+} influx and maintain homeostatic levels of cytosolic calcium, or a combination of both these effects.

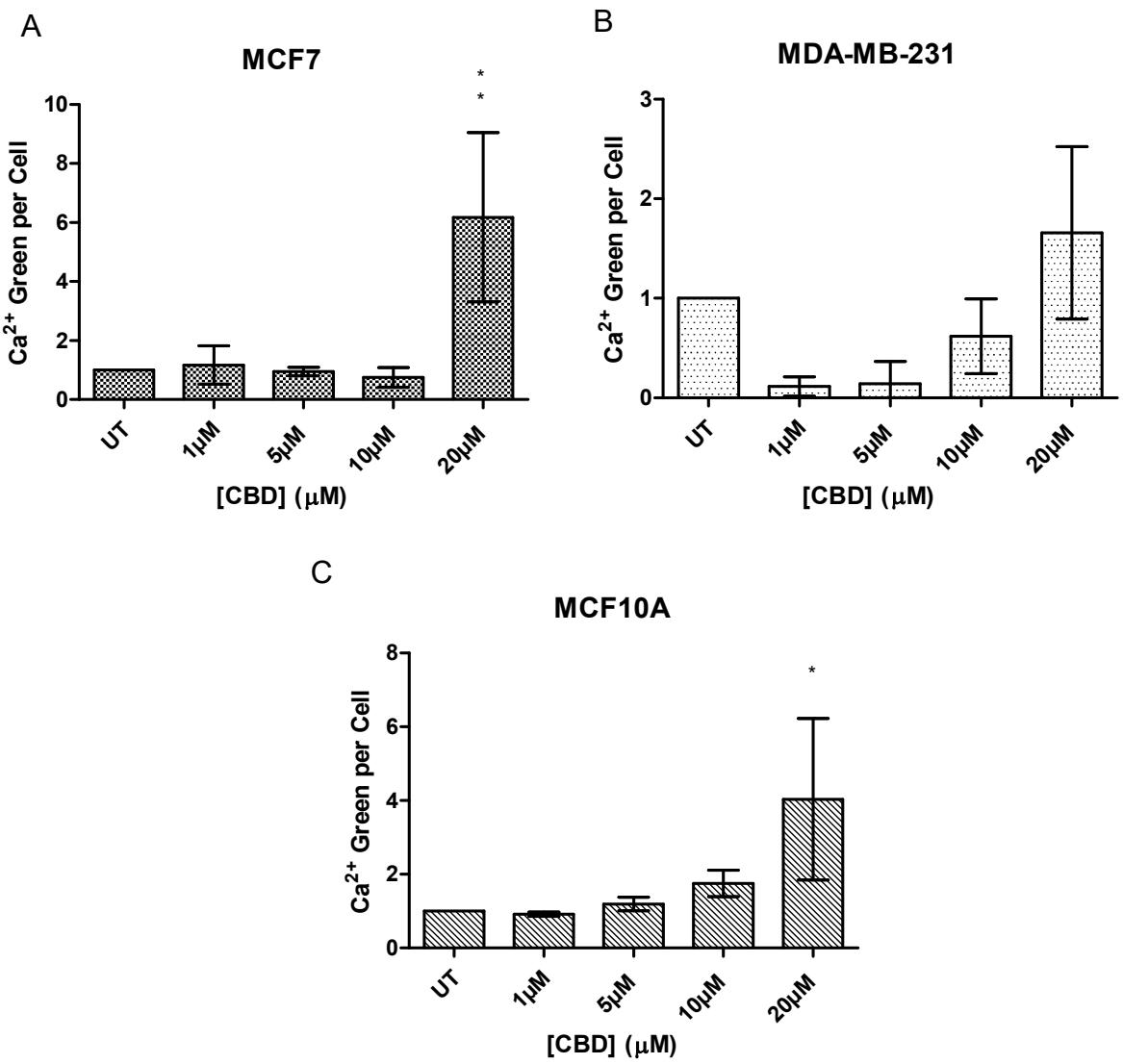

Figure 57: Concentration-dependent effect of CBD treatment on intracellular calcium in the MCF7, MDA-MB-231 and MCF10A cell lines.
Fold change in Ca^{2+} staining, normalized to cell number obtained using the SRB assay, relative to the untreated cells after treatment with the various concentrations of CBD for 48 hours in the (A) MCF7, (B) MDA-MB-231 and (C) MCF10A cell lines.
UT – untreated, CBD – cannabidiol
*(n=3, * - significant to respective untreated control, * - $p < 0.05$, ** - $p < 0.01$, *** - $p < 0.001$).*

The intracellular calcium concentration varies depending on its localization. For example, the calcium levels in the cytoplasm, nuclear and mitochondrial matrix are similar; however, since the ER is the main store of calcium, it accumulates and maintains substantially higher calcium concentrations (**Figure 58**). The low cytosolic calcium concentration is maintained through the action of the plasma membrane Ca^{2+} transport ATPase (PMCA) and Na^{+}/Ca^{2+} exchanger (NCX). Upon elevated cytosolic calcium concentrations, the activity of PMCA and NCX are complemented by SERCA

and, to a lesser extent, by the mitochondrial Ca^{2+} uniporter (mtCU). These proteins sense and are activated by elevated cytosolic calcium concentrations to maintain homeostatic Ca^{2+} levels in the cytosol (Bagur and Hajnóczky, 2017), facilitating calcium uptake into the mitochondria and ER to counteract high cytosolic Ca^{2+} concentrations (**Figure 58**).

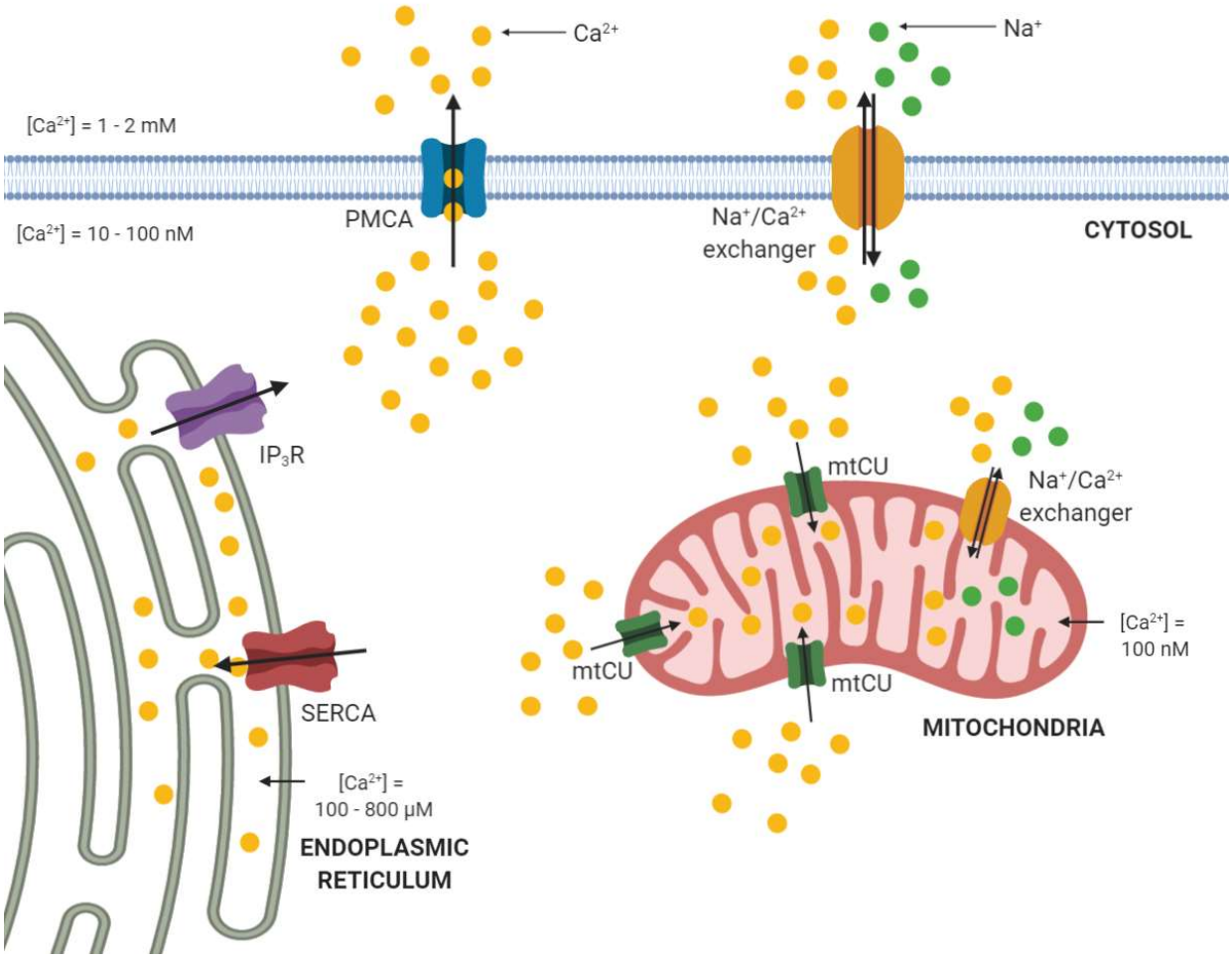

Figure 58: Maintenance of calcium homeostasis in a generalized cell
Figure created using BioRender online tool and adapted from Dong et al. (2006). PMCA – plasma membrane Ca^{2+} transport ATPase, NCX – Na^{+}/Ca^{2+} exchanger, mtCU – mitochondrial Ca^{2+} uniporter, SERCA – sarco-/endoplasmic reticulum Ca^{2+} ATPase

Thomas *et al.* (2000) illustrated that the calcium stain used (Calcium Green-1) displayed uniform cytoplasmic fluorescence with increased fluorescence in the nucleus and minimal compartmentalization in the ER or mitochondria. This suggested that the Calcium Green used predominantly stains cytosolic calcium and does not enter the ER or mitochondria. Therefore, the lack of concentration-dependence in the

MCF7 cells (**Figure 57A**) can be explained by calcium being taken up by the ER and mitochondria to maintain homeostatic calcium levels in the cytosol. At the highest CBD concentration (20 μM), there was a significant influx of calcium into the cytosol, which suggested that the cells were no longer able to regulate the influx of calcium and the homeostatic cytosolic Ca^{2+} concentration could not be restored, which may have triggered a range of signalling pathways.

The MDA-MB-231 cells showed a concentration-dependent increase in intracellular cytosolic Ca^{2+} (**Figure 57B**); however, at the lowest concentration (1 μM), the cytosolic calcium was below basal levels (untreated cells), which increased with increasing CBD concentration. At a concentration of 10 μM CBD, the Ca^{2+} level was comparable to the untreated cells and only increased beyond that of the untreated cells at the highest concentration (20 μM). The MCF10A cell line displayed a concentration-dependent increase in cytosolic Ca^{2+}, with a significant increase detected at 20 μM (**Figure 57C**), however, it was less significant than in the MCF7 cell line.

Based on the variation in the trends observed for changes in the intracellular Ca^{2+} between cell lines, it is hypothesized that the influx of calcium may be occurring via the TRPV1 receptor and that the differences in the influx of Ca^{2+} between the cell lines may be explained by differences in the localization of the TRPV1 channel in the respective cell lines. TRPV1 localization has been described as having both classical and non-classical distribution (Lozano *et al.*, 2018). Classical distribution of the TRPV1 receptor is characterized by localization of TRPV1 expression on the plasma membrane and cytoplasm and is seen in the MCF7 and normal epithelial breast cells (Lozano *et al.*, 2018). Non-classical distribution of the TRPV1 receptor is characterized by localization of the receptor in the ER, Golgi and perinuclear membranes, and is seen in the MDA-MB-231 cell line (Lozano *et al.*, 2018). In the MCF7 and MCF10A cell lines, the activation of the TRPV1 channel on the plasma membrane would result in an influx of calcium into the cytosol. In the MDA-MB-231 cell line, the TRPV1 channel is primarily localized on the ER and Golgi. Therefore, the activation of the TRPV1 channel may not have resulted in a significant influx of extracellular calcium into the cytosol, but rather may have caused an influx of calcium into the ER and Golgi from the cytosol, thereby decreasing the cytosolic Ca^{2+} concentration. This would

explain why there was a decrease in the cytosolic Ca^{2+} below basal levels (untreated) in the MDA-MB-231 cell line at the lower CBD concentrations.

The MCF10A cell line represented normal breast epithelial cells and would theoretically display the classical distribution of TRPV1. As in the case of the MCF7 cell line, activation of the TRPV1 receptor would result in increased cytosolic Ca^{2+} levels. However, TRPV1 is overexpressed in breast cancer cell lines (Weber *et al.*, 2016); therefore, the MCF10A cell line would show decreased expression of the TRPV1 channel. The decreased TRPV1 expression in non-tumourigenic cells (MCF10A) would result in a less significant influx of Ca^{2+}, which confirms what was observed in the MCF10A cell line – treatment with the highest concentration of CBD (20 μM) resulted in a significant influx of calcium (**Figure 57C**), however, it was less significant when compared to the cancerous MCF7 cell line. This theory is supported by a study conducted by Pecze *et al.* (2016), where they illustrated that TRPV1 expression levels are a key factor for TRPV1-mediated cytotoxicity. They observed a threshold phenomenon, where a certain level of TRPV1 expression was required to induce significant accumulation of Ca^{2+} in the mitochondria. This may be the case in the MCF10A cells, where a significant Ca^{2+} influx into the cytosol was detected (**Figure 57C**), without a significant increase in ROS production (**Figure 56C**) and subsequent cell death (**Figure 36**). The different Ca^{2+} sensing proteins have different thresholds for activity; therefore, the level of Ca^{2+} influx in the MCF10A cell line may have been insufficient to induce uptake into the mitochondria. The mtCU has a very low affinity for Ca^{2+} and higher pumping rate compared to SERCA and PMCA (Bagur and Hajnóczky, 2017), which means that the mtCU would require greater Ca^{2+} concentrations prior to activation to facilitate the influx of Ca^{2+} into the mitochondria.

The MCF7 cell line showed a correlation between the ROS production and cytosolic Ca^{2+} influx with CBD treatment in a concentration-dependent manner, with a significant increase both after treatment with 20 μM CBD. This suggested that treatment with 20 μM CBD resulted in the activation of the TRPV1 receptors, inducing the influx of Ca^{2+} into the cytosol at a rate higher than the efflux and subsequently resulted in increased Ca^{2+} uptake into the mitochondria, increasing the rate of ROS production. This theory is supported by a study conducted by Koşar *et al.* (2016), who found that oxidative stress upon Doxorubicin-associated TRPV1 activation in the

MCF7 cell line was linked to the failure of Ca^{2+} extruding mechanisms to cope with excess Ca^{2+} ions entering the cell through activated TRPV1 channels. The mtCU-mediated increase in the Ca^{2+} concentration in the mitochondria activates Ca^{2+}-sensitive dehydrogenases (e.g. pyruvate dehydrogenase, α-ketoglutarate dehydrogenase and isocitrate dehydrogenase, glycerol-3-phosphate dehydrogenase and the ATP synthase), stimulating ATP synthesis (Tarasov *et al.*, 2012) and increased ROS production (Görlach *et al.*, 2015).

No significant changes in intracellular calcium were detected in the MDA-MB-231 cell line after CBD treatment (**Figure 57B**); however, a decrease was detected at the lower concentrations and no changes in the production of ROS were detected. As mentioned earlier, this can be explained by the non-classical distribution of TRPV1, which would not cause a significant influx of calcium into the cytosol, but rather an influx of calcium into the ER and Golgi from the cytosol. Therefore, no significant ROS production would be induced, as the calcium would not be taken up into the mitochondria.

In addition to increased mitochondrial Ca^{2+} uptake from the cytosol and increasing ROS production, there is also significant crosstalk between the mitochondria and ER, which increases during early ER stress and may further induce the production of ROS. Calcium exchange between the ER and mitochondria is a well-established model of communication between these two organelles (Giorgi *et al.*, 2009). IP_3R and the voltage-dependent anion channel (VDAC) are the primary ER-mitochondria Ca^{2+} transfer channels, which are located in the ER and mitochondrial sides of mitochondrial-associated membranes (MAM) respectively (**Figure 59**). These channels form a complex with the GRP75 chaperone to physically connect the two organelles (Szabadkai *et al.*, 2006). Calcium released through IP_3R is taken up by the mitochondria and stimulates ATP production (Bravo *et al.*, 2012). Bravo *et al.* (2011) showed that during stages of early ER stress, the interactions between the mitochondria and ER increase in a microtubule-dependent manner, increasing Ca^{2+} transfer to the mitochondria, subsequently increasing mitochondrial respiration and ATP production (**Figure 59**). This would ultimately result in an increase in ROS production and further induce ER stress.

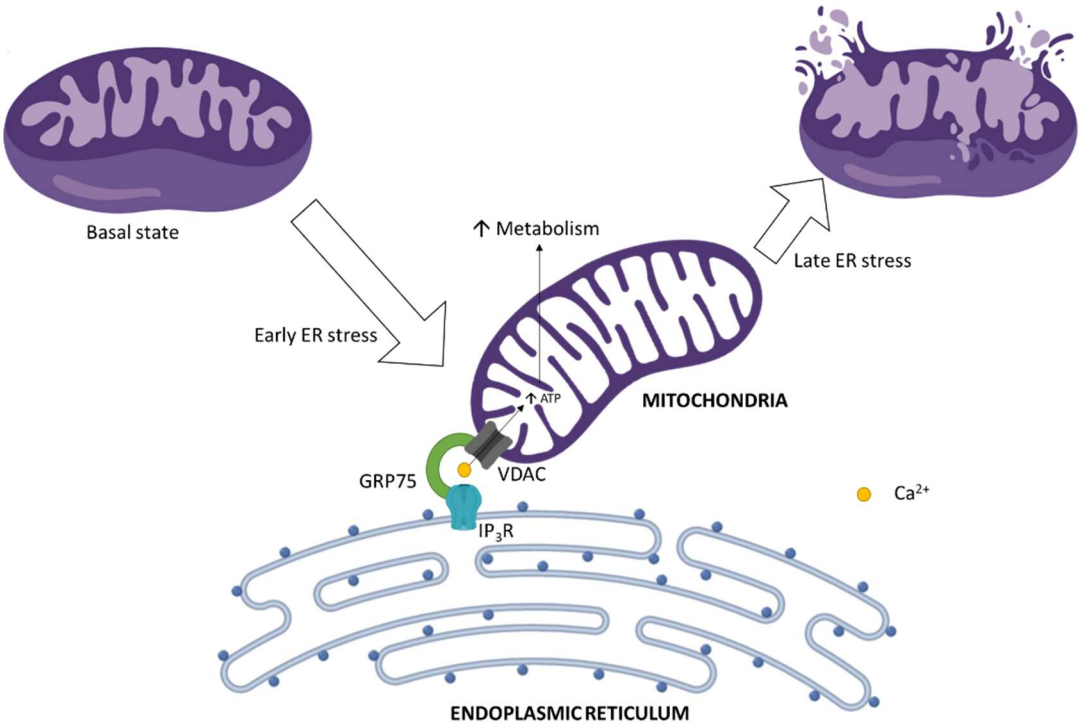

Figure 59: Calcium exchange between the ER and mitochondria during early ER stress.
Figure adapted from Bravo et al. (2012). During early ER stress, interactions between the ER and mitochondria increase, which increases Ca^{2+} transfer into the mitochondria, subsequently increasing ATP synthesis and ROS production
ER – endoplasmic reticulum, ATP – adenosine triphosphate, GRP75 – glucose-regulated protein 75, VDAC – voltage-dependent anion channel, IP3R - Inositol 1,4,5-triphosphate receptors

This suggested that ER stress induced by increased ROS would increase Ca^{2+} transfer from the ER to the mitochondria, further increasing ATP synthesis and ROS production. TRPV1 is also activated by oxidative stress and may be further activated by excessive mitochondrial ROS production (Nur *et al.*, 2017), increasing Ca^{2+} influx via TRPV1 and further contributing to mitochondrial ROS production.

In order to evaluate how much ER stress induction and cell death was due to the production of ROS, cells were concomitantly treated with CBD and ascorbic acid (a known antioxidant), and the subsequent effect on ROS production, cell viability and ER stress induction was measured using DCFH-DA staining, the MTT cell viability assay and ThT staining respectively.

4.3.6. Antioxidant co-treatment

Ascorbic acid is a non-enzymatic antioxidant that scavenges free oxygen radicals (Birben *et al.*, 2012). To test the effect of the CBD treatment both with and without ascorbic acid, each cell line was treated with 20 μM CBD and concomitantly treated with ascorbic acid for a 48-hour period. A concentration of 25 μM is most commonly used in literature; however, to confirm that this concentration was sufficient to decrease ROS production, the MCF7 cell line was treated with CBD alone and concomitantly with various concentrations (0-75 μM) of ascorbic acid. The change in ROS production was then measured using DCFH-DA staining and normalized to cell number obtained using the SRB cell viability assay (**Figure 60**).

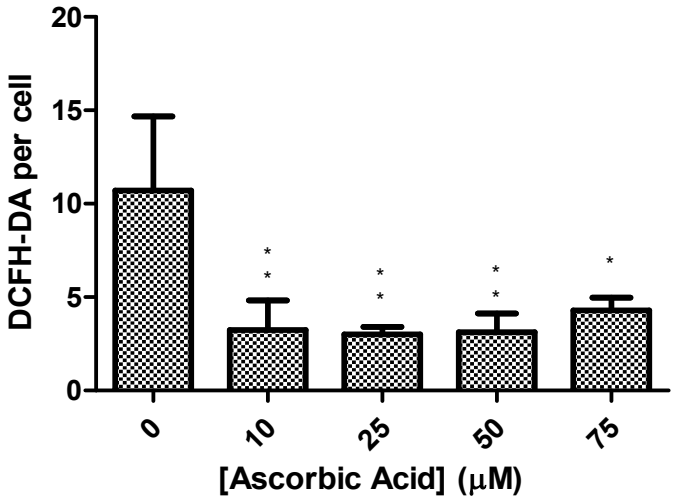

Figure 60: Effect of concomitant treatment of CBD with ascorbic acid on ROS accumulation in the MCF7 cell line.
Fold change in the DCFH-DA, normalized to cell number obtained using the SRB assay, relative to the untreated control after concomitant treatment with 20 μM CBD and various concentrations of ascorbic acid in the MCF7 cell line.
DCFH-DA – 2', 7'-dichlorofluorescein-diacetate
*(n=3, * - significant to CBD treatment (0 μM AA), * - p < 0.05, ** - p < 0.01, *** - p < 0.001).*

There was no concentration-dependent decrease in ROS production with increasing concentrations of ascorbic acid. This suggested that the most commonly used concentration of 25 μM ascorbic acid was sufficient to counteract all possible ROS produced and was used for subsequent concomitant treatments (**Figure 61**).

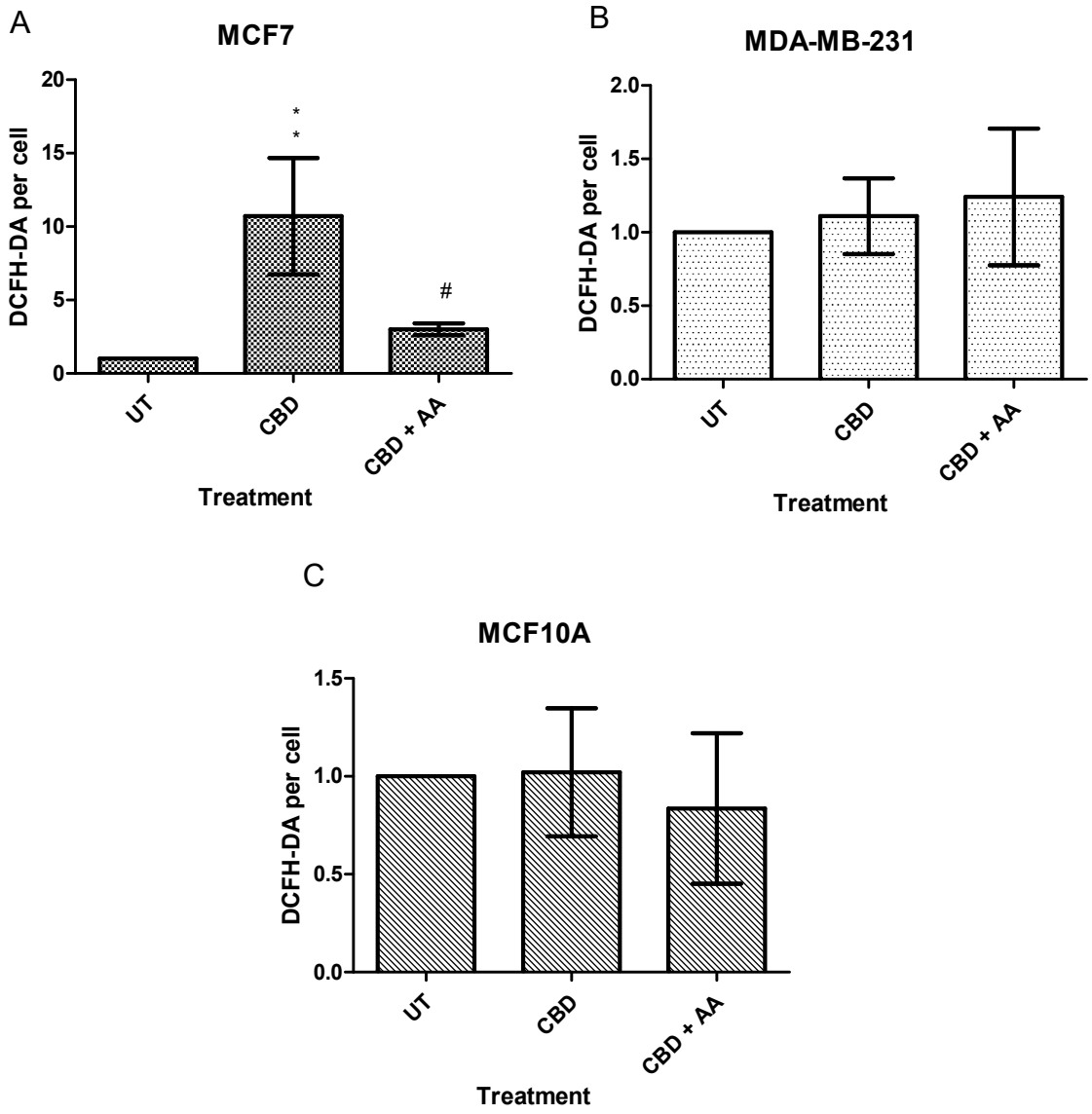

Figure 61: Effect of concomitant treatment with CBD and ascorbic acid on ROS production in the MCF7, MDA-MB-231 and MCF10A cell lines.
Fold change in DCFH-DA, normalized to cell number obtained using the SRB assay, to untreated cells after treatment CBD and concomitant treatment with ascorbic acid for 48 hours in the (A) MCF7, (B) MDA-MB-231 and (C) MCF10A cell lines.
UT – untreated, CBD – cannabidiol (20μM), AA – ascorbic acid (25μM).
*(n=3, * - significant to respective untreated control, * - p < 0.05, ** - p < 0.01, *** - p < 0.001, # - significant to respective treatment with no AA, # - p < 0.05, ## - p < 0.01, ### - p < 0.001)*

Concomitant treatment of the MCF7 cell line with CBD and ascorbic acid resulted in a significant decrease in the intracellular ROS (**Figure 61A**). This was expected since ascorbic acid scavenges free oxygen radicals to decrease intracellular ROS. The fold change in ROS in concomitantly treated cells showed no significant increase in ROS

levels compared to the untreated control, suggesting that the ascorbic acid was able to counteract or inhibit most or all the ROS that was induced after CBD treatment.

The MDA-MB-231 (**Figure 61B**) and MCF10A (**Figure 61C**) cell lines did not show significant changes in ROS production after concomitant treatment with ascorbic acid. This was expected, as these cell lines did not show significant ROS induction after treatment with CBD, therefore concomitant treatment with an antioxidant would not be expected to significantly decrease ROS. The MCF10A cell line showed a slight decrease in the ROS to below basal levels, most likely due to the ascorbic acid scavenging ROS produced as normal by-products of oxidative phosphorylation.

The change in viability after treatment with CBD and concomitant treatment with ascorbic acid was measured using the MTT cell viability assays (**Figure 62**).

The MCF7 cell line showed a significant decrease in viability after treatment with CBD; however, there was a significant increase in viability after concomitant treatment with ascorbic acid (**Figure 62A**), suggesting that a significant proportion of cell death after treatment with CBD was due to the production of ROS. However, the viability of the concomitantly treated cells remained significantly lower when compared to the untreated control, suggesting that ROS production was partially responsible for the cell death after treatment with CBD and that other mechanisms of cell death may have been induced after CBD treatment. The ROS-independent cell death mechanism may be the activation of a caspase cascade upon cytochrome C release from the mitochondria as a result of mitochondrial dysfunction. Nazıroğlu *et al.* (2017) and Nur *et al.* (2017) found that activation of the TRPV1 receptor by MRS1477 and cisplatin respectively, resulted in an increase in the activation of caspase-3 and -9, suggesting the activation of the intrinsic apoptotic pathway.

CBD treatment in the MDA-MB-231 cell line resulted in a significant decrease in viability compared to the untreated control, with a significant increase after concomitant treatment with ascorbic acid compared to CBD treatment alone (**Figure 62B**). However, the increase in viability was relatively small, with an increase from 74 to 85% after concomitant treatment with ascorbic acid. The decrease in viability in concomitantly treated cells relative to the untreated control was significant and suggested that the majority of cell death was not solely due to the production of ROS. However, it suggested that the production of ROS may play some role in cell death.

This is consistent with the slight increase in ROS production that was seen after treatment with 20 μM CBD. Although TRPV1 is predominantly expressed on the Golgi apparatus and ER in this cell line, there is minimal expression on the cell surface, which would facilitate some calcium influx and subsequent ROS production. The MCF10A cell line did not show any significant decreases in viability after treatment with CBD, or significant increases after concomitant treatment with ascorbic acid (**Figure 62**C).

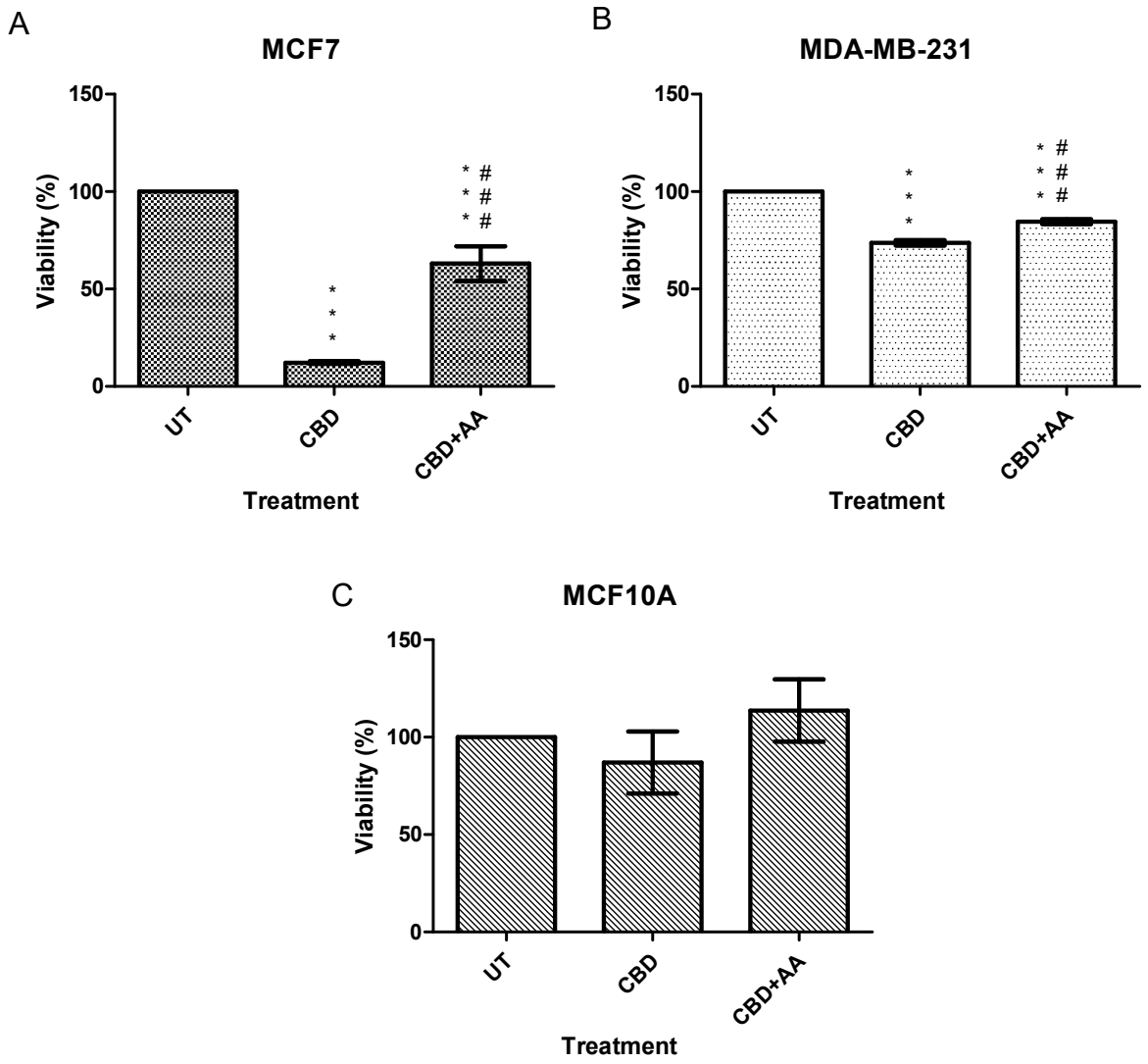

Figure 62: Effect of concomitant treatment with CBD and ascorbic acid on cell viability in the MCF7, MDA-MB-231 and MCF10A cell lines.
Change in viability after treatment CBD and concomitant treatment with ascorbic acid for 48 hours, determined using MTT cell viability assay in the (A) MCF7, (B) MDA-MB-231 and (C) MCF10A cell lines. UT – untreated, CBD – cannabidiol (20μM), AA – ascorbic acid (25μM).
*(n=3, * - significant to respective untreated control, * - p < 0.05, ** - p < 0.01, *** - p < 0.001;*
 # - significant to CBD treatment alone, # - p < 0.05, ## - p < 0.01, ### - p < 0.001).

After determining the effect of the concomitant treatment with ascorbic acid on ROS production and viability, the next step was to determine the effect of concomitant treatment on the induction of ER stress, as the proposed hypothesis was that CBD induces ER stress via the production of ROS, which affected protein folding. This was completed using ThT staining for misfolded protein aggregates and normalization to cell number using the SRB cell viability assay (**Figure 63**).

CBD treatment in the MCF7 cell line significantly increased the ThT binding per cell (**Figure 63A**), suggesting that there was a significant increase in misfolded proteins in the cell. Concomitant treatment with CBD and ascorbic acid significantly decreased the ThT per cell compared to CBD treatment, suggesting that there was a significant decrease in misfolded protein aggregates. The untreated and the concomitantly treated cells were comparable, suggesting that the elevated levels of ROS may have been almost entirely responsible for the accumulation of misfolded proteins in the MCF7 cell line.

CBD treatment in the MDA-MB-231 cell line resulted in a slight increase in the ThT per cell, with a decrease below basal levels after concomitant treatment with ascorbic acid (**Figure 63B**). The slight increase after CBD treatment suggested that it did result in a slight accumulation of misfolded protein aggregates. The decrease after concomitant treatment with ascorbic acid suggested that the accumulation of misfolded protein with CBD treatment was due to the production of ROS, which is consistent with the minimal increase in ROS that was detected. The decrease in ROS below basal levels suggested that the high levels of basal ER stress in the MDA-MB-231 cell line may be due to increased basal ROS levels, which were modulated by concomitant treatment with ascorbic acid.

The MCF10A cell line showed a non-significant increase in the ThT per cell after CBD treatment, with a slight decrease after concomitant treatment with ascorbic acid (**Figure 63C**). This suggested that treatment with CBD caused an accumulation of misfolded proteins, which was most likely due to the production of ROS, as it was alleviated after concomitant treatment with ascorbic acid.

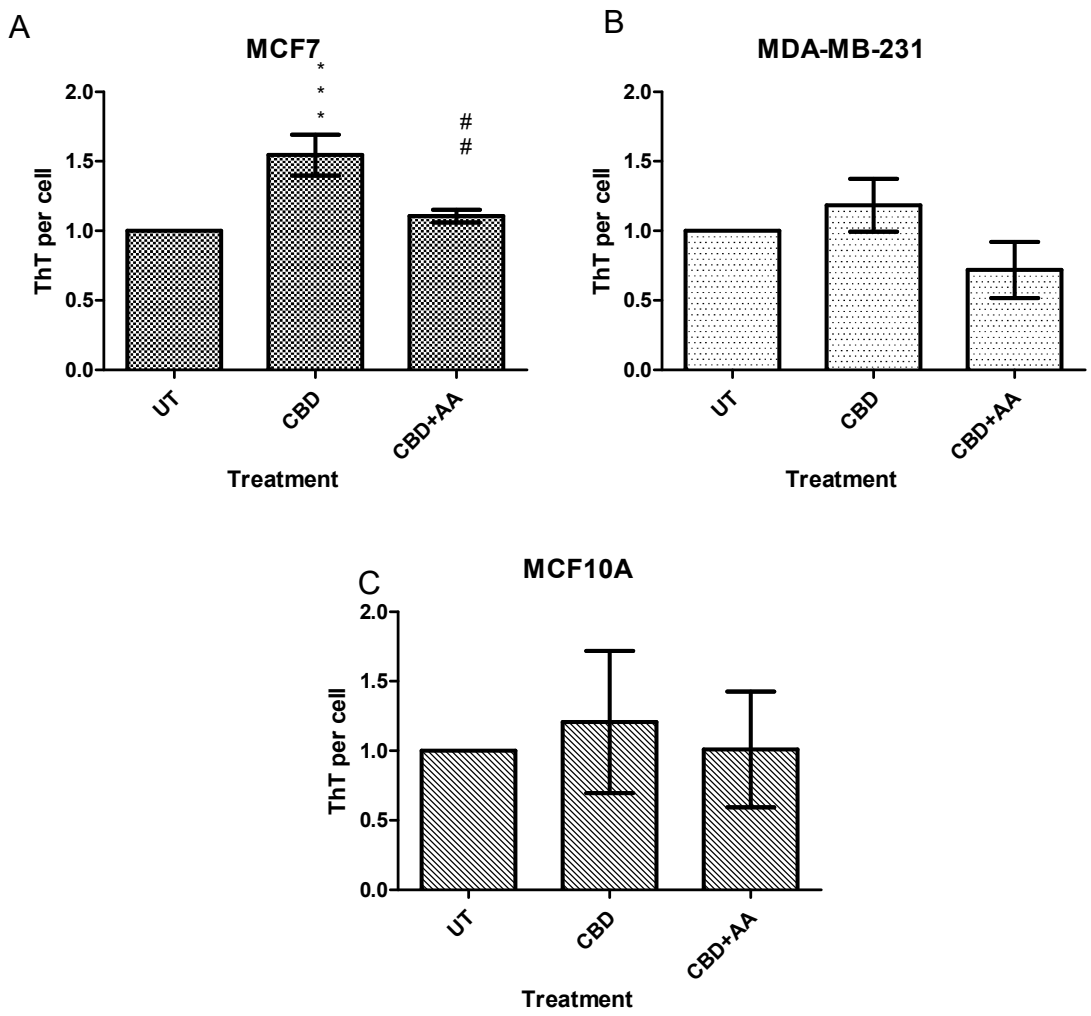

Figure 63: Effect of concomitant treatment with CBD and ascorbic acid on ER stress induction in the MCF7, MDA-MB-231 and MCF10A cell lines.
Fold change in ThT per cell relative to untreated cells after treatment with CBD and co-treatment with ascorbic acid for 48 hours in the (A) MCF7, (B) MDA-MB-231 and (C) MCF10A cell lines.
UT – untreated, CBD – cannabidiol (20μM), AA – ascorbic acid (25μM).
*(n=3, * - significant to respective untreated control, * - p < 0.05, ** - p < 0.01, *** - p < 0.001,*
 # - significant to CBD treatment alone, # - p < 0.05, ## - p < 0.01, ### - p < 0.001).

4.3.7. TRPV1 Agonist/Antagonist studies

To confirm activation of the TRPV1 receptor by CBD, the TRPV1 receptor was blocked using an antagonist (curcumin) and an agonist (capsaicin) as a positive control. Capsaicin is a hydrophobic compound that binds to the TRPV1 receptor (Smutzer and Devassy, 2016). TRPV1 exhibits a high affinity (sub-micromolar) and selectivity for capsaicin (Yang et al., 2015). Yeon et al. (2010) obtained evidence that supported the

antagonistic effect of curcumin in the capsaicin mediated activation of TRPV1. Capsaicin (TRPV1 agonist) and curcumin (TRPV1 antagonist) were used to determine the validity of the agonist/antagonist model. Stock solutions of both the agonist and antagonist were prepared in DMSO and then diluted in the respective complete media. Each cell line was treated with various concentrations of capsaicin (caps) and curcumin (cur), and the MTT cell viability assay was used to construct IC_{50} curves and determine the IC_{50} value of each compound (Appendix iv – Supplementary data, **Figure 75**).

The affinity of the TRPV1 receptor for curcumin is not known; therefore, various concentrations were used that corresponded to the IC_{50} of curcumin (25 µM), as well as selection of a concentration higher (50 µM) and lower (5 µM) than the determined IC_{50} concentration. Each cell line was concomitantly treated with the IC_{50} concentration of capsaicin in the MCF7 cell line (680 µM) or with CBD (20 µM), as well as the respective curcumin concentration for the 48-hour period (**Figure 64**). Changes in cell viability were measured using the MTT cell viability assay. The viability at each concomitant treatment with curcumin was calculated relative to the untreated control with the respective concentration of curcumin, to account for any cell death that was induced by curcumin.

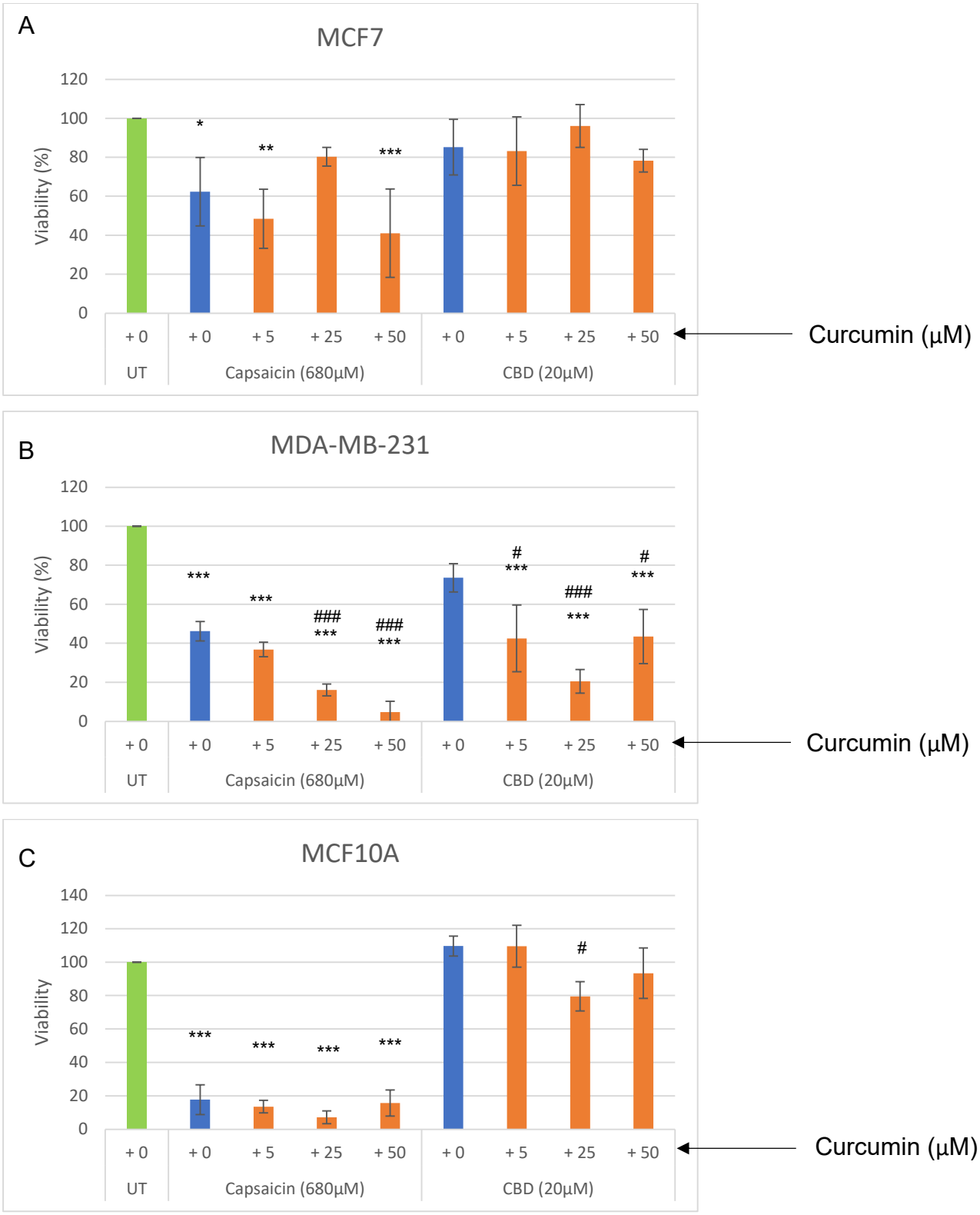

Figure 64: Effect of concomitant treatment with a TRPV1 agonist and antagonist on cell viability in the MCF7, MDA-MB-231 and MCF10A cell lines
Green – UT, Blue – CAPS or CBD alone, Orange – concomitant treatment with CUR
UT – untreated, CBD – cannabidiol (20 µM), caps - capsaicin (680 µM).
*(n=3, * - significant to untreated control, * - p < 0.05, ** - p < 0.01, *** - p < 0.001,*
 # - significant to respective treatment with 0 µM curcumin, # - p < 0.05, ## - p < 0.01, ### - p < 0.001)

In the MCF7 cell line, capsaicin treatment significantly decreased cell viability (**Figure 64A**). Concomitant treatment with capsaicin and curcumin displayed a biphasic effect, in which curcumin concentrations of 5 and 50 µM showed a significant decrease in viability compared to the untreated control, and a slight decrease in viability compared to capsaicin treatment. Concomitant treatment of capsaicin and 25 µM curcumin showed a non-significant increase in viability when compared to capsaicin treatment. While the increase in viability was not significant compared to capsaicin treatment alone, it was no longer significantly lower when compared to the untreated control. This suggested that within the agonist/antagonist model, 25 µM curcumin may have been sufficient to effectively antagonize the TRPV1 receptor and reduce capsaicin-induced cell death. The same trend was observed for concomitant treatment with CBD and the various concentrations of curcumin, however, the changes in viability were not significant. Concomitant treatment with 5 µM and 50 µM curcumin did not affect viability; however, treatment with 25 µM increased viability compared to CBD treatment. As with the concomitant treatment with capsaicin, this suggested that 25 µM curcumin effectively antagonized the TRPV1 receptor and reduced CBD-induced cell death, further suggesting that the cell death induced by CBD treatment was partially due to the activation of the TRPV1 receptor in the MCF7 cell line.

The MDA-MB-231 cell line showed a significant decrease in viability after treatment with capsaicin (**Figure 64B**). It showed a significant concentration-dependent decrease in viability after concomitant treatment with curcumin. All the concentrations of curcumin in combination with capsaicin showed a significant decrease in viability when compared to the untreated control. Concomitant treatment with 25 and 50 µM curcumin showed significantly decreased viability compared to capsaicin treatment. This indicated that the cell death induced by capsaicin treatment was not alleviated after concomitant treatment with a TRPV1 antagonist (curcumin), suggesting that the cell death induced by capsaicin was not due to TRPV1 activation in the MDA-MB-231 cell line. Concomitant treatment with CBD and curcumin also displayed a biphasic effect; however, the 25 µM curcumin concentration showed decreased viability compared to the 5 µM and 50 µM concentrations. Concomitant treatment at all the curcumin concentrations significantly decreased viability compared to both the untreated control and CBD treatment. Since no increase in viability was observed after concomitant treatment with CBD and a TRPV1 antagonist, it can be concluded that

the cell death induced after CBD treatment in the MDA-MB-231 cell line was not due to TRPV1 activation. This correlates with the lack of both ROS production (**Figure 60B**) and the accumulation of intracellular calcium (**Figure 57B**) that was observed in this cell line.

The MCF10A cell line displayed a significantly decreased viability after capsaicin treatment and concomitant treatment with curcumin (**Figure 64C**). The increasing concentrations of curcumin displayed a biphasic effect, with decreased viability after concomitant treatment with 25 µM when compared to treatment with 5 and 50 µM. However, the concomitant treatment with curcumin did not increase viability compared to capsaicin treatment, suggesting that the death induced by capsaicin treatment was not due to the activation of the TRPV1 receptor. The same biphasic trend was observed after concomitant treatment with CBD and curcumin, with a significant decrease in viability after concomitant treatment with 25 µM curcumin. Since no decrease in viability was measured after treatment with CBD, it was not expected that concomitant treatment with curcumin would significantly increase viability.

It is hypothesized that the differences between cell lines observed after concomitant treatment with the antagonist (curcumin) is due to the role that TRPV1 played in the induction of cell death after treatment with either capsaicin or CBD. In the MCF7 cell line, the data collected after CBD treatment (*i.e.* a significant increase in intracellular Ca^{2+} and ROS production) suggested that the TRPV1 receptor was activated. These effects were not seen in the MDA-MB-231 cell line and seen to a lesser extent in the MCF10A cell line. This suggested that activation of the TRPV1 receptor may not have played a role in the cell death that was induced by CBD treatment in the MDA-MB-231 cell line. This theory was confirmed by the agonist/antagonist studies. In the MCF7 cell line, concomitant treatment with the TRPV1 antagonist (25 µM) showed an increase in viability compared to capsaicin (agonist), as well as CBD, suggesting that the death that was observed after CBD and capsaicin treatment was due to the activation of the TRPV1 receptor. In the MDA-MB-231 and MCF10A cell lines, concomitant treatment at all concentrations of the antagonist (curcumin) showed decreased viability compared to capsaicin, as well as CBD treatment. This suggested that the cell death that was observed after capsaicin and CBD treatment was not due to the activation of the TRPV1 receptor in these cell lines. As discussed previously,

CBD was hypothesized to induce cell death via TRPV1 activation in the MCF7 cell line, but not in the MDA-MB-231 cell line, due to differences in the localization of the receptor between the cell lines. The receptor is mostly expressed on the plasma membrane in the MCF7 cell line and in the ER and Golgi apparatus in the MDA-MB-231 cell line (Lozano *et al.*, 2018).

Although it has been hypothesized that the cell death observed after capsaicin treatment in the MDA-MB-231 and MCF10A cell lines was not due to TRPV1 activation, capsaicin (agonist) treatment in both these cell lines significantly decreased viability. Although capsaicin is generally considered a TRPV1 agonist, other TRPV channels have been studied as possible receptors for capsaicin. Other than TRPV1, the most commonly documented TRPV receptor activated by capsaicin is TRPV6 (Chow *et al.*, 2007, Lau *et al.*, 2014). Capsaicin has also been documented to induce cancer cell death through various mechanisms including p53 phosphorylation, as well as acetylation via the down-regulation of sirtuin-1, activation of a pro-apoptotic gene NSAID-activated gene-1, AMP-activated protein kinase, and fatty acid synthase (Clark and Lee, 2016). This means that capsaicin can result in apoptosis through many different pathways, which may explain why cell death was observed in the MDA-MB-231 and MCF10A cell lines, despite the theory that cell death does not occur via the TRPV1 receptor after capsaicin treatment in these cell lines.

In conclusion, the MCF7 cell line was the only cell line that displayed an increase in viability after concomitant treatment with the curcumin (TRPV1 antagonist) compared to capsaicin (TRPV1 agonist) and CBD treatment. This suggested that the cell death observed with the concomitant treatment of curcumin and capsaicin, as well as CBD was, in part, due to the activation of the TRPV1 receptor. None of the other cell lines tested showed an increase in viability after concomitant treatment with the TRPV1 antagonist, suggesting that the cell death induced in these cell lines after treatment was not due to the activation of the TRPV1 receptor.

4.3.8. Differential activation of branches of the UPR

To better understand the mechanism of ER stress induction and UPR activation with CBD treatment in the MCF7 cell line, the differential activation of branches of the UPR was investigated (**Figure 65**).

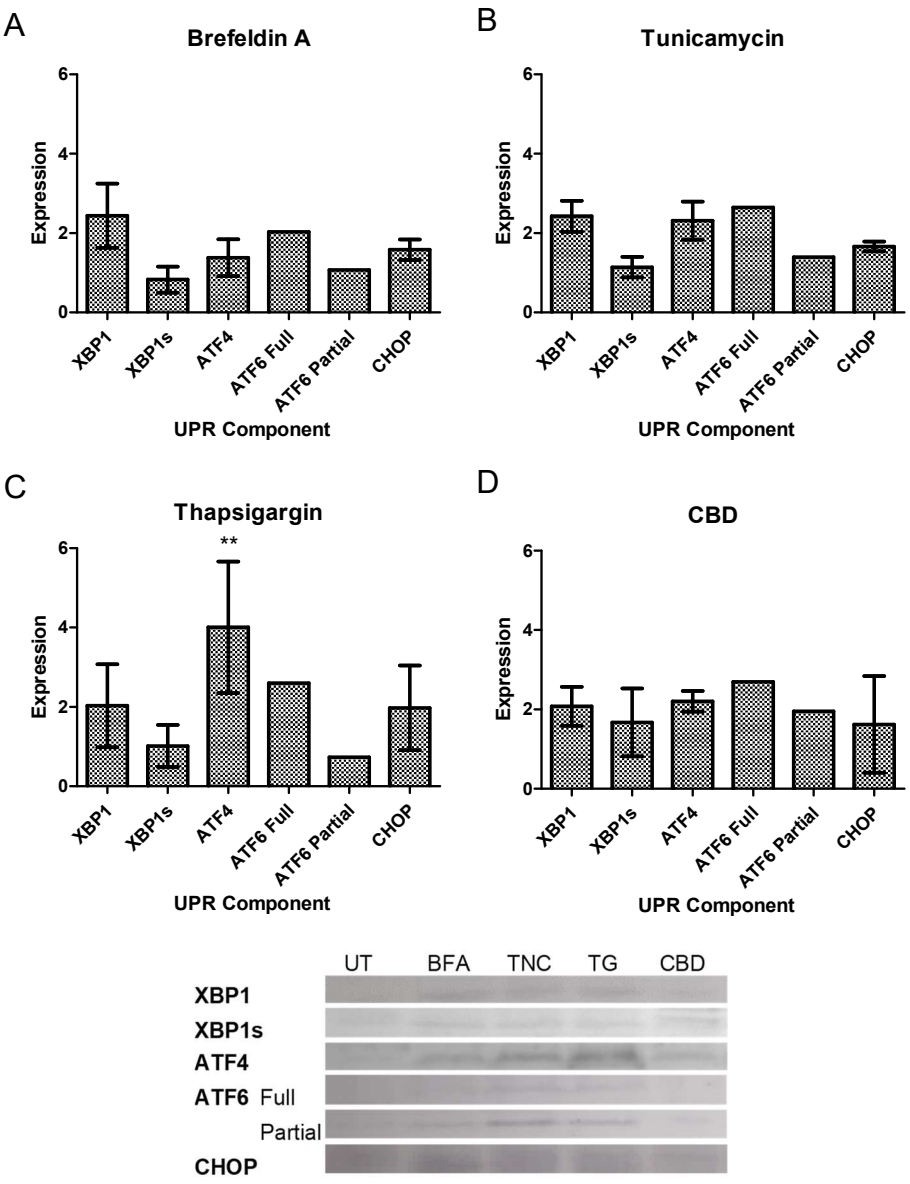

Figure 65: Effect of CBD treatment on the differential activation of the UPR in the MCF7 cell line.

Fold change in the expression of XBP1, ATF4, ATF6 and CHOP to show differential activation of the various branches of the UPR and the initiation of ER stress-induced apoptosis in the MCF7 cell line after treatment with (A) brefeldin A, (B) tunicamycin, (C) thapsigargin and (D) CBD. Fold change in expression is calculated using the normalized density relative to the untreated control. Therefore, the untreated control is represented by an arbitrary unit of 1.

XBP1 – x-box binding protein 1, XBP1s – spliced XBP1, ATF4 – activating transcription factor 4, ATF6 – activating transcription factor 6, CHOP – C/EBP homologous protein, UT – untreated, BFA – Brefeldin A, TNC – tunicamycin, TG – thapsigargin CBD – cannabidiol.

*(n=3, * - significant to untreated control, * - $p < 0.05$, ** - $p < 0.01$, *** - $p < 0.001$), ATF6 – n=1.*

Western blotting analysis for XBP1 was used to measure the activation of the IRE-1 branch of the UPR. All positive controls, as well as treatment with CBD, showed an increase in expression of XBP1, with the greatest increase in cells treated with BFA. Treatment with BFA, TNC and TG did not show a large increase in the expression of XBP1s. However, treatment with CBD resulted in a minimal increase in XBP1s expression. IRE-1 initiates various signalling pathways of the UPR, either via splicing of XBP1 or via post-transcriptional modification through regulated IRE-1-dependent decay (RIDD) of multiple substrates (Chen and Brandizzi, 2013). During the adaptive response of the UPR, IRE-1 increases the protein folding capacity of the ER by splicing XBP1 to induce the transcription of ER quality control components. IRE-1 also decreases the protein folding load by conducting RIDD on mRNAs that encode ER-translocating proteins. If homeostasis is not restored and ER stress is irreversible, XBP1 splicing terminates and IRE-1 suppresses the adaptive responses and activates apoptosis through RIDD. During this transition from the adaptive to apoptotic response, RIDD increases the intensity of ER stress through the degradation of specific UPR genes, including GRP78 (Chen and Brandizzi, 2013, Han *et al.*, 2009). RIDD also induces apoptosis through the suppression of anti-apoptotic pre-microRNAs. Caspase-2 (CASP2) is a pro-apoptotic protease that is essential for the initiation of apoptosis and is upregulated through the decay of anti-CASP2 pre-microRNAs that results from IRE-1 activation (Han *et al.*, 2009, Upton *et al.*, 2012). This suggests that IRE-1 is a molecular switch and an executioner of apoptosis during ER stress. Previously, it was believed that decreasing IRE-1 activity allowed cells to initiate apoptosis, however, the identification of the IRE-1-Casp2 pathway led to the generally accepted hypothesis that IRE-1-XBP1 is active during the adaptive phase and attenuated in the apoptotic phase, where the IRE-1-Casp2 phase initiates cell death (Chen and Brandizzi, 2013). No increase in the expression of XBP1s after treatment with the positive controls could indicate that either IRE-1 is not activated by these positive controls, or that the ER stress that was induced was irreversible and XBP1 splicing had ceased, with increased activation of the IRE-1-Casp2 pathway. No XBP1s would be detected as it has a very short half-life (~ 22 minutes) (He *et al.*, 2010). The latter is more likely as the increase in misfolded proteins after treatment with the positive controls would have titrated GRP78 away from all sensors, activating the IRE-1, PERK and ATF6 pathways. The ER stress-inducing controls would have

resulted in severe ER stress after 48 hours of exposure and may have resulted in the switch from the pro-survival to the pro-apoptotic mechanism of the IRE-1 pathway. The increased expression of XBP1s in CBD treated cells suggested that XBP1 mRNA is actively being spliced and that this branch of the UPR may still be activating the pro-survival pathway of IRE-1.

Western blotting for ATF4 was used to show the activation of the PERK branch of the UPR. All positive controls showed an increase in the activation of this branch, with the greatest activation in cells treated with TG. The PERK branch of the UPR consists of two integrated pathways (Verfaillie *et al.*, 2013). PERK has two substrates, namely eIF2α and Nrf2 (Schröder and Kaufman, 2005, Verfaillie *et al.*, 2013). Upon activation, PERK phosphorylates the α-subunit of eIF2α, inhibiting cap-dependent translation and decreasing the protein load in the ER. Phosphorylation of eIF2α favours cap-independent translation, resulting in the selective translation of ATF4, which regulates the expression of several genes, including chaperones, antioxidant stress response genes and apoptosis-associated genes. When PERK's second substrate, Nrf2, is phosphorylated it separates from its cytosolic repressor, translocates to the nucleus and upregulates the expression of genes involved in the antioxidant stress response (Verfaillie *et al.*, 2013). Treatment with TG resulted in the greatest increase in ATF4 expression. As mentioned previously, TG inhibits SERCA, which transports Ca^{2+} from the cytosol into the ER. This inhibition in SERCA would result in an increase in the cytosolic Ca^{2+} since Ca^{2+} would still be entering the cytosol from outside the cell and from the ER but would be unable to enter the ER. This would result in increased cytosolic Ca^{2+} and subsequent uptake into the mitochondria, increasing the activity of Ca^{2+}-dependent enzymes and increasing the production of ROS. This mechanism also correlated with the large increase in the PERK branch of the UPR, because of its association with the antioxidant response. CBD treatment also resulted in an increase in ATF4 expression. As discussed previously, CBD treatment in the MCF7s resulted in a significant induction of ROS via TRPV1-mediated influx of Ca^{2+}; therefore, an increase in the activation of the PERK signalling branch of the UPR would be an attempt to counteract the ROS that disrupted protein folding and resulted in the induction of ER stress.

Western blotting for ATF6 was used to show the activation of this branch of the UPR. All positive controls and CBD treatment showed an increase in full length ATF6. None of the treatments showed a large increase in partial ATF6, with the largest increase resulting from CBD treatment.

None of the treatments showed a significant increase in CHOP expression; however, they did show a slight increase which suggested the induction of ER stress-induced apoptosis, although it was not significant.

Chapter 5 – Conclusions and future recommendations

This study aimed to (i) optimize a high-throughput method for the detection and quantification of ER stress, (ii) demonstrate the effect of four cannabinoids on cell viability, mitochondrial function, the induction of ER stress and the activation of the UPR and finally (iii) investigate the possible molecular mechanism(s) through which ER stress was induced by the various cannabinoids in breast cancer cell lines.

To address the first aim of the study, ER stress was induced using three compounds known to induce ER stress via different mechanisms. Three cell lines (two breast cancer and one non-tumourigenic breast cell line) were treated for various time intervals and stained with ThT, a non-conventional fluorescent dye that binds to protein aggregates (**Figure 7**). The use of ThT to stain cells treated with various ER stress-inducing controls showed an increased fluorescence with treatment with increasing exposure time (**Figure 15, 21 & 23**). The 3D overlay also showed that ThT binding was localized around the nucleus in all cell lines, suggesting that it was binding to misfolded proteins within the ER lumen. In order to confirm localization within the ER, further studies should be completed in which treated cells are co-stained with ThT and ER Tracker in order to investigate the colocalization of these stains. Due to the changes that occur in the nucleus in cells undergoing apoptosis, namely chromatin condensation, cell number obtained using DAPI staining could not be used to accurately normalize the ThT fluorescence; however, the cell number obtained using SRB (**Figure 19**) was more consistent with the changes in viability measured using the xCelligence RTCA (**Figure 14**) and was subsequently used to normalize the ThT fluorescence. Overall, ThT staining correlated with UPR activation in that, when GRP78 expression was increased during early ER stress, a decrease in the ThT per cell was observed (**Figure 20, 27 & 28**), suggesting that there was a decrease in the misfolded proteins within the ER lumen. This was because increased levels of GRP78 would assist with folding the accumulated misfolded proteins in an attempt to re-establish ER homeostasis. With increasing exposure time, there was an increase in the ThT per cell that correlated with both an increase in GRP78 expression and a decrease in viability. This suggested that ThT can be used to detect and quantify early ER stress induced via different mechanisms. The use of ThT for ER stress detection provides several advantages over currently used methods. It provides a method which

can easily be used as a high-throughput method, once optimized for a specific cell line, and has the potential to be used to screen compounds for their potential to induce ER stress across a wide range of cell lines, once the exact state of ER stress has been determined. This is advantageous due to the increasing research that shows the importance of ER stress in the progression and treatment of many diseases. It is also a more direct method of detecting ER stress as opposed to measuring the activation of the UPR, which is a downstream response of ER stress induction, as it directly measures the accumulation of misfolded proteins. This means that the use of ThT could also indicate when ER homeostasis had been restored, as the misfolded protein level in the ER would have been restored to normal levels. This is not evident with currently used methods that measure UPR components, as these components would still be upregulated even if homeostasis had been restored. However, this characteristic of this method may also present a disadvantage in that, if ThT was used to detect ER stress, the measurement of ER stress using ThT may occur during a period in which homeostasis had been restored, even if it was temporary. Therefore, it is recommended that the use of ThT to detect ER stress should involve measurements at multiple time points to confirm ER stress induction. The use of ThT in combination with measuring changes in viability, as well as western blotting analysis for UPR components can also provide insights into the nature of the treatment, as well as the response of the cell line, with regards to ER stress induction and UPR activation.

To address the second aim of the study (to demonstrate the effect of cannabinoids on cell viability, mitochondrial function, the induction of ER stress and the activation of the UPR), each cell line was treated with a wide concentration range of THC, CBD, CBG and CBN, and viability was measured using the MTT viability assay. Only CBD at the highest concentration tested showed a significant decrease in viability in both cancer cell lines, without a significant decrease in the non-tumourigenic cell line (**Figure 32**). None of the cannabinoids resulted in the significant activation of inflammatory pathways, which may be associated with UPR activation (Davis, 2000, Hu *et al.*, 2006), based on the lack of significant nitric oxide production after treatment (**Figure 37**). However, CBD treatment in the MCF7 cell line resulted in the greatest production of NO (**Figure 37A**), suggesting that treatment with this cannabinoid may have resulted in the slight activation of inflammatory pathways, which may have occurred via the integration of the ER stress and inflammatory pathways.

ThT staining showed that, after treatment with the various cannabinoids, the general trend that was observed was an increase in ThT binding in all cell lines after treatment with THC and CBD. A decrease in bound ThT was observed after treatment with CBG and CBN, except for CBG treatment in the MDA-MB-231 cell line, which showed an increase in the bound ThT per cell (**Figure 39**). This suggested that treatment with CBD and THC resulted in an increase in the accumulation of misfolded proteins, while CBG and CBN decreased the accumulation of misfolded proteins, due to the decreased protein folding load in the ER. Western blot analyses for GRP78 was performed to measure the activation of the UPR. The only treatment in the MCF7 cell line that showed the most consistent upregulation of GRP78 expression was CBD (**Figure 40**). THC, CBG and CBN showed slight increases in GRP78 expression in this cell line. It was concluded that the consistent increase in GRP78 expression (**Figure 40**) and in the bound ThT per cell (**Figure 39**), coupled with the increase in NO production (**Figure 37**) and significant decrease in cell viability (**Figure 36C**) suggested that treatment with CBD in the MCF7 cell line was the only treatment that resulted in ER stress that was severe enough to activate the UPR and possibly result in subsequent ER stress-induced cell death. CBD treatment in the MDA-MB-231 cell line slightly increased GRP78 expression (**Figure 41**), which correlated with the slight increase in the ThT per cell (**Figure 39**). There was an increase in the ThT per cell in this cell line, but a lack of GRP78 upregulation after treatment with THC and CBG which suggested that the accumulation of misfolded proteins induced by these cannabinoids was not severe enough to elicit the activation of the UPR, as the cells were most likely able to overcome the increase in misfolded proteins without additional GRP78 expression. No increases in GRP78 expression were measured in the MCF10A cell line after treatment with any of the cannabinoids (**Figure 42**), and it was concluded that cannabinoid treatment in these cell lines did not result in the induction of ER stress and/or UPR activation under the conditions tested.

Due to the crosstalk between the ER and mitochondria, mitochondrial dysfunction triggers ER stress (Lee *et al.*, 2010, Lim *et al.*, 2009) and *vice versa* (Schönthal, 2012). To distinguish between “true” ER stress induction and mitochondrial dysfunction, Biolog redox dyes were used to measure changes in mitochondrial function (**Figure 43**). The positive control (FCCP), an uncoupler of oxidative phosphorylation, increased the reduction of the dye in the MCF7 and MCF10A cell lines but decreased in the

MDA-MB-231 cell line. It was concluded that this difference may have been due to differences in the energy metabolism of cell lines. The MCF7 and MCF10A cell lines are more dependent on oxidative phosphorylation and would be more susceptible to decreases in ATP production as a result of uncoupling. This would result in increased electron flow in these cell lines when treated with an uncoupler in an attempt to compensate for the decrease in ATP levels. Similar to FCCP treatment, treatment with THC, CBN and CBG resulted in a significant increase in the reduction of the redox dye in the MCF10A cell line, with significant increases after THC and CBG treatment. The increase in activity in the ETC in the MCF10A cell line after treatment may also have been due to uncoupling of oxidative phosphorylation. THC has been documented to uncouple oxidative phosphorylation (Sarafian *et al.*, 2003); however, further research is required to investigate if this is also caused by treatment with CBG and CBN, as it has not been documented. This can be completed by measuring the oxygen consumption rate (OCR), which would increase as a result of uncoupling, as well as measuring ATP production, which would decrease, after treatment with the respective cannabinoids.

In the cancerous cell lines, only CBN treatment in the MCF7 cell line showed a significant decrease in the activity of the ETC. Due to the significant decrease in the reduction of the dye at 24 hours (**Figure 43**), but the lack of a significant decrease in viability measured after 48 hours (**Figure 36**), it was thought that the cells were proliferating despite inhibition of the ETC due to extra-physiological levels of pyruvate that would allow for the regeneration of NAD^+ through increased LDH activity and ATP production via glycolysis (King and Attardi, 1989). However, no decreases in SDH (citric acid cycle and ETC) or increases in LDH activity were found (**Figure 45**). Therefore, the effect of CBN treatment on viability at 24 hours was measured, and it was found that there was a decrease in viability (**Figure 46**) and that the cells may have recovered by 48 hours of exposure. The mechanism of cell death induction by CBN in the MCF7 cell line was then investigated using various fluorescent stains and confocal microscopy, as it had been shown that CBN treatment in the MCF7 cell line had not induced UPR activation; therefore, the decrease in viability was most likely not ER stress-induced. The morphological features that were observed after CBN treatment were extensive vacuolization that appeared to originate from the ER (**Figure 50 & 51**), a loss of mitochondrial structure (**Figure 52**), no formation of lysosomes

(**Figure 48**), and a decrease in the number, but increase in size of lipid droplets (**Figure 49**). An overlay of the ER and lipid stains also showed that the large lipid droplets appeared to co-localize with areas of increased staining with the ER stain (**Figure 53**). Based on the morphological changes that were observed, it was concluded that CBN treatment resulted in the induction of paraptosis, a caspase-independent mechanism of programmed cell death that is characterized by cytoplasmic vacuolization that arises from the ER and mitochondria (Wang *et al.*, 2019). It was concluded that CBN treatment may only result in the induction of paraptosis in the MCF7 cell line due to differences in the expression of the IGF1R, as paraptosis has been found to be induced in cells that overexpress this receptor (Sperandio *et al.*, 2000), which is the case in the MCF7 cell line (Akekawatchai *et al.*, 2006).

To address the third aim of this study (to investigate the possible molecular mechanism(s) through which ER stress was induced), each cell line was treated with the four cannabinoids and the subsequent effect on ROS production was measured. This was completed in order to investigate one of the proposed mechanisms of ER stress induction, which involved the activation of the TRPV1 receptor, causing an influx of calcium and subsequent ROS production (Ligresti *et al.*, 2006), which would affect protein folding and result in the induction of ER stress and the activation of the UPR. It was found that only CBD treatment in the MCF7 cell line significantly increased ROS production, while THC, CBG and CBN decreased ROS production in the MCF10A cell line below basal levels (**Figure 55**). Treatment with these cannabinoids in the MCF10A cell line had also resulted in an increase in the reduction of the redox dye (**Figure 43F**) and it was concluded that this may have been a result of uncoupling in the ETC. The measured decrease in ROS production further suggested that these cannabinoids may be causing uncoupling, as it would result in an increased OCR and therefore decrease the production of ROS. However, further investigation is required to confirm this hypothesis, including investigation into the oxygen consumption rate (OCR) and ATP production. CBD was the only cannabinoid that showed a significant increase in ROS production (**Figure 55A**), therefore all subsequent experiments investigating this proposed mechanism of ER stress induction were only performed on cells treated with CBD. The MCF7 cell line showed a concentration-dependent increase in ROS, with a significant increase detected at the highest concentration (**Figure 56**). It was

concluded that this may have either been due to the inherent antioxidant mechanisms within the cell (Marengo *et al.*, 2016) or the direct antioxidant properties of CBD (Hampson *et al.*, 2000) that were able to overcome the production of ROS at the lower CBD concentrations. Despite the direct antioxidant properties of CBD, it was not surprising that a significant increase in ROS was detected at the highest concentrations, as the proposed mechanism of ROS induction is an indirect method via the influx of calcium, which is taken into the mitochondria and results in increased ROS production.

The measured influx of calcium into the cell in the MCF7 cell line after CBD treatment (**Figure 57**) correlated with the increase in ROS production where a significant increase was only detected after treatment with the highest concentration. This suggested that at the lower concentrations of CBD, the cells were able to counteract the influx of calcium through uptake into the mitochondria or ER to maintain homeostatic calcium levels, but were unable to counteract the influx at the highest concentration, resulting in the significant increase in ROS production. CBD treatment in the MDA-MB-231 cell line showed a concentration-dependent increase in intracellular calcium; however, at the lower concentrations of CBD, the measured calcium was below basal levels until the highest concentration tested, which only showed a slight increase. The MCF10A cell line showed a concentration-dependent increase in calcium, with a significant increase detected at the highest concentration. It was concluded that the differences in calcium influx that was observed between cell lines after CBD treatment was due to differences in the expression and localization of the TRPV1 receptor. The MCF7 and MCF10A cell lines display the classical distribution of the receptor, where it is localized on the outer cell membrane (Lozano *et al.*, 2018), with increased expression in the cancerous MCF7 cell line when compared to non-cancerous cells. The activation of the TRPV1 receptor would, therefore, result in an influx of calcium, with a more significant influx in the MCF7 cell line. The MDA-MB-231 cells display the non-classical distribution of the receptor, in which it is predominantly expressed in the ER and Golgi (Lozano *et al.*, 2018). This indicated that activation of the TRPV1 receptor would result in uptake of calcium into the ER and Golgi, decreasing the cytosolic calcium, which was observed (**Figure 57B**). The significant increase in calcium (**Figure 57C**), but lack of significant ROS production (**Figure 55C**) measured in the MCF10A cell lines suggested that the influx

of calcium was not sufficient to induce ROS production in the mitochondria. It was concluded that this was most likely due to decreased expression levels of TRPV1 in this non-tumourigenic cell line, as the influx of calcium would most likely have been counteracted by SERCA and PMCA in the ER, as they have higher affinities for calcium than the mitochondrial transporter (Bagur and Hajnóczky, 2017), which would have required greater calcium concentrations for activation and subsequent Ca^{2+} uptake into the mitochondria.

In alignment with the proposed mechanism of ER stress induction after CBD treatment (a disruption of protein folding by ROS) the cell lines were concomitantly treated with CBD and ascorbic acid (a non-enzymatic antioxidant) to determine the subsequent effect on cell viability and ER stress induction. Concomitant treatment with ascorbic acid significantly decreased ROS production in the MCF7 cell line relative to CBD treatment (**Figure 61A**), suggesting that it was able to counteract most of the ROS produced as a result of CBD treatment in the MCF7 cell line. Concomitant treatment in the MCF7 cell line significantly increased the viability of cells relative to CBD treatment (**Figure 62A**). This suggested that a significant proportion of cell death induced after CBD treatment was linked to the production of ROS; however, the viability of concomitantly treated cells was still significantly decreased compared to untreated cells, suggesting that not all cell death observed was due to the production of ROS. The MDA-MB-231 cells showed a slight, but significant increase in viability after concomitant treatment (**Figure 62B**) suggesting that some of the cell death observed after CBD treatment was due to the production of ROS. Concomitant treatment with ascorbic acid also showed a significant decrease in the bound ThT per cell in the MCF7 cell line, with no significant difference between the untreated and concomitantly treated cells (**Figure 63A**). It was concluded that the decrease in ROS decreased the accumulation of misfolded proteins in this cell line, suggesting that the increased ThT per cell that was observed after CBD treatment may have been due to the production of ROS. Concomitant treatment had no significant effect on the bound ThT per cell in the MDA-MB-231 (**Figure 63B**) and the MCF10A (**Figure 63C**) cell lines, suggesting that ROS had no effect on protein folding in these cell lines.

To confirm the activation of the TRPV1 receptor by CBD, the cell lines were concomitantly treated with a TRPV1 antagonist (curcumin) and an agonist (capsaicin)

as a control (**Figure 64**). In general, concomitant treatment with curcumin displayed a biphasic effect. Only concomitant treatment with curcumin and capsaicin, as well as CBD, in the MCF7 cell line showed an increase in viability compared to capsaicin and CBD treatment. It was concluded that the increase in viability after concomitant treatment with curcumin suggested that the cell death induced after capsaicin and CBD treatment was at least partially due to the activation of the TRPV1 receptor (**Figure 64A**), while the cell death induced in the MDA-MB-231(**Figure 64B**) and MCF10A (**Figure 64C**) cell lines was not due to TRPV1 activation.

As a final insight into the mechanism of ER stress induction and UPR activation after CBD treatment in the MCF7 cell line, the differential activation of branches of the UPR was investigated (**Figure 65**). CBD treatment showed a greater increase in the expression of XBP1s compared to the positive controls. The expression of XBP1s is associated with the adaptive signalling of the UPR, as opposed to the apoptotic signalling, in which the IRE-1-XBP1 branch is attenuated (Chen and Brandizzi, 2013). It was concluded that this meant that the positive controls had resulted in pro-apoptotic signalling of the UPR, while the ER stress that was induced by CBD treatment was less severe and resulted in the adaptive signalling of the UPR, indicated by the increased expression of XBP1s. CBD treatment also increased ATF4 expression, which is associated with the antioxidant response of the UPR (Verfaillie *et al.*, 2013). Therefore, it was concluded that activation of this branch of the UPR may have been an attempt to counteract the ROS that was hypothesized to have caused the initial ER stress response.

In conclusion, this study provided an alternative method for ER stress detection that provides several advantages over currently used methods and can be used in combination with cell viability assays and western blotting to gain insight into the nature of ER stress induction. With regards to the treatment of cancer using cannabinoids, this research added insight into a possible mechanism of cell death induced by CBN treatment that has not been previously documented – the induction of paraptosis. This requires further investigation for confirmation. Current research on the characteristics of paraptosis has mainly focused on the associated morphological changes, which were investigated, however various other factors could be investigated to confirm paraptosis induction. These include determining the effect of CBN treatment

on the MAPK/ERK and JNK pathways, as the IGF1R can regulate these pathways and it has been found that inhibition and down-regulation of these pathways can inhibit paraptosis (Sperandio *et al.*, 2004). CBN was noted to be most effective in the treatment of the non-metastatic MCF7 cell line, suggesting that it may only be efficient for the treatment of certain cancer cell types, possibly based on the expression of IGF1R. However, it did not show any death in the non-cancerous cell line, suggesting that it may lack toxicity in normal cells, which makes it promising in the treatment of cancer. When considering the results on CBD, the data collected in this study suggested that CBD resulted in the activation of the TRPV1 receptor, which may have been responsible for a large amount of cell death that was observed in the MCF7 cell line after CBD treatment, as the effects of TRPV1 activation (Ca^{2+} influx, ROS production and cell death) were observed after CBD treatment. CBD has been documented to activate the TRPV1 receptor and result in an influx of Ca^{2+} into the cell and causes subsequent increases in ROS production (Ligresti *et al.*, 2006). However, this research added an additional insight which suggested that a large proportion of the cell death that was induced after CBD treatment is due to the induction of ER stress by a disruption of protein folding caused by increased ROS production and the subsequent activation of the UPR. It also added an insight that showed that the differences in the response to CBD treatment between cell lines was largely dependent on the localization and expression levels of the TRPV1 receptor.

Currently, cannabinoids are commonly used for their palliative effects in cancer patients, including appetite stimulation, inhibition of chemotherapy-associated nausea and vomiting, pain relief, mood elevation and insomnia relief (Davis, 2016, Pacher *et al.*, 2006). However, research into their anti-cancer properties is increasing rapidly. CBD has frequently been documented to induce breast cancer cell death and decrease proliferation (Ligresti *et al.*, 2006, Massi *et al.*, 2013, McAllister *et al.*, 2007, Shrivastava *et al.*, 2011). However, the mechanism through which CBD exerts its effects (*i.e.* through TRPV1, CB2 or a receptor-independent mechanism) is still under debate. With regards to ER stress, THC is the most documented cannabinoid to induce ER stress through the induction of ceramide in glioma cells (Salazar *et al.*, 2009a); however, this was not observed under the conditions tested. This study showed that CBD and CBN are both promising in the treatment of cancer. Both these cannabinoids resulted in cell death in the cancerous cell lines, with little to no toxicity

in the non-cancerous cell line. Targeting ER stress in the treatment of cancer has several advantages, which include the ability to selectively target cancer cells and targeting multiple hallmarks of cancer simultaneously. Another advantage of CBD treatment is that it resulted in cancer cell death in both the MCF7 and MDA-MB-231 cell lines, suggesting that it may be effective in different cancer cell types. This is advantageous as the MDA-MB-231 cell line are generally less responsive to many treatments, due to a lack of expression of the oestrogen, progesterone and HER2 receptors. However, it was shown that the CBD-induced cell death in the MDA-MB-231 cell line was not due to the activation of the TRPV1 receptor and induction of ER stress. Elbaz *et al.* (2016) showed that CBD is also a TRPV2 channel agonist and that this channel is highly upregulated in triple-negative breast cancer (*i.e.* the MDA-MB-231 cell line). Therefore, this channel may be partially responsible for the cell death observed in this cell line, however, further investigation is required to confirm the possible mechanism(s) of cell death in the MDA-MB-231 cell line.

Paraptosis induction is also advantageous in the treatment of cancer, with the main advantage being that paraptosis could lead to cell death in cancer cells that are resistant to apoptosis. Another advantage is that many naturally-derived compounds have been shown to induce paraptotic cell death, which would limit side-effects to normal cells (Khalili and Radosevich, 2018).

Chapter 6 – References

AKEKAWATCHAI, C., HOLLAND, J., KOCHETKOVA, M., WALLACE, J. & MCCOLL, S. 2006. Transactivation of CXCR4 by the Insulin-like Growth Factor1 Receptor (IGF-1R) in Human MDA-MB-231 Breast Cancer Epithelial Cells. *The Journal of biological chemistry,* 280**,** 39701-8.

ALEXANDER, A., SMITH, P. F. & ROSENGREN, R. J. 2009. Cannabinoids in the treatment of cancer. *Cancer Letters,* 285**,** 6-12.

ASMELLASH, S., STEVENS, J. L. & ICHIMURA, T. 2005. Modulating the endoplasmic reticulum stress response with trans-4, 5-dihydroxy-1, 2-dithiane prevents chemically induced renal injury in vivo. *Toxicological Sciences,* 88**,** 576-584.

ATKIN, J. D., FARG, M. A., WALKER, A. K., MCLEAN, C., TOMAS, D. & HORNE, M. K. 2008. Endoplasmic reticulum stress and induction of the unfolded protein response in human sporadic amyotrophic lateral sclerosis. *Neurobiology of Disease,* 30**,** 400-407.

ATMACA, H., BOZKURT, E., KıSıM, A. & USLU, R. 2016. Comparative analysis of XTT assay and xCELLigence system by measuring cytotoxicity of resveratrol in human cancer cell lines. *Turkish Journal of Biochemistry,* 41**,** 413-421.

BABOUR, A., BICKNELL, A. A., TOURTELLOTTE, J. & NIWA, M. 2010. A surveillance pathway monitors the fitness of the endoplasmic reticulum to control its inheritance. *Cell,* 142**,** 256-269.

BAGUR, R. & HAJNÓCZKY, G. 2017. Intracellular Ca(2+) Sensing: Its Role in Calcium Homeostasis and Signaling. *Molecular cell,* 66**,** 780-788.

BERG, J. M., TYMOCZKO, J. L. & STRYER, L. 2002. Biochemistry, Fifth Edition. New York: W.H. Freeman.

BERIAULT, D. R. & WERSTUCK, G. H. 2013. Detection and quantification of endoplasmic reticulum stress in living cells using the fluorescent compound, Thioflavin T. *Biochimica Et Biophysica Acta,* 1833**,** 2293-2301.

BERRIDGE, M. J. 2002. The endoplasmic reticulum: a multifunctional signaling organelle. *Cell calcium,* 32**,** 235-249.

BESIO, R., GARIBALDI, N., LEONI, L., CIPOLLA, L., SABBIONEDA, S., BIGGIOGERA, M., MOTTES, M., AGLAN, M., OTAIFY, G. A., TEMTAMY, S. A., ROSSI, A. & FORLINO, A. 2019. Cellular stress due to impairment of collagen prolyl hydroxylation complex is rescued by the chaperone 4-phenylbutyrate. *Disease models & mechanisms,* 12**,** dmm038521.

BEUKES, N., LEVENDAL, R.-A., PRINSLOO, E. & FROST, C. 2019. Comparative detection method of early onset cytokine-induced stress in β-cells (INS-1E). *Biotechnology and Applied Biochemistry,* 66**,** 328-339.

BEUKES, N., LEVENDAL, R. A. & FROST, C. L. 2014. Selected terpenoids from medicinal plants modulate endoplasmic reticulum stress in metabolic disorders. *Journal of Pharmacy and Pharmacology,* 66**,** 1505-1525.

BIANCALANA, M. & KOIDE, S. 2010. Molecular mechanism of Thioflavin-T binding to amyloid fibrils. *Biochimica et Biophysica Acta (BBA)-Proteins and Proteomics,* 1804**,** 1405-1412.

BIRBEN, E., SAHINER, U. M., SACKESEN, C., ERZURUM, S. & KALAYCI, O. 2012. Oxidative stress and antioxidant defense. *The World Allergy Organization journal,* 5**,** 9-19.

BIRSOY, K., WANG, T., CHEN, W. W., FREINKMAN, E., ABU-REMAILEH, M. & SABATINI, D. M. 2015. An essential role of the mitochondrial electron transport chain in cell proliferation is to enable aspartate synthesis. *Cell,* 162**,** 540-551.

BISOGNO, T., HANUŠ, L., DE PETROCELLIS, L., TCHILIBON, S., PONDE, D. E., BRANDI, I., MORIELLO, A. S., DAVIS, J. B., MECHOULAM, R. & DI MARZO, V. 2001. Molecular targets for cannabidiol and its synthetic analogues: effect on vanilloid VR1 receptors and on the cellular uptake and enzymatic hydrolysis of anandamide. *British Journal of Pharmacology,* 134**,** 845-852.

BISSWANGER, H. 2019. *Practical enzymology*, John Wiley & Sons.

BLÁZQUEZ, C., GONZÁLEZ-FERIA, L., ÁLVAREZ, L., HARO, A., CASANOVA, M. L. & GUZMÁN, M. 2004. Cannabinoids Inhibit the Vascular Endothelial Growth Factor Pathway in Gliomas. *Cancer Research,* 64**,** 5617-5623.

BRADFORD, M. M. 1976. A rapid and sensitive method for the quantitation of microgram quantities of protein utilizing the principle of protein-dye binding. *Analytical Biochemistry,* 72**,** 248-254.

BRAVO, R., GUTIERREZ, T., PAREDES, F., GATICA, D., RODRIGUEZ, A. E., PEDROZO, Z., CHIONG, M., PARRA, V., QUEST, A. F. & ROTHERMEL, B. A. 2012. Endoplasmic reticulum:

ER stress regulates mitochondrial bioenergetics. *The International Journal of Biochemistry & Cell Biology,* 44**,** 16-20.

BRAVO, R., VICENCIO, J. M., PARRA, V., TRONCOSO, R., MUNOZ, J. P., BUI, M., QUIROGA, C., RODRIGUEZ, A. E., VERDEJO, H. E. & FERREIRA, J. 2011. Increased ER–mitochondrial coupling promotes mitochondrial respiration and bioenergetics during early phases of ER stress. *Journal of Cell Science,* 124**,** 2143-2152.

BRUNELLE, J. K. & LETAI, A. 2009. Control of mitochondrial apoptosis by the Bcl-2 family. *Journal of cell science,* 122**,** 437-441.

BRYAN, N. S. & GRISHAM, M. B. 2007. Methods to detect nitric oxide and its metabolites in biological samples. *Free Radical Biology & Medicine,* 43**,** 645-657.

CARRACEDO, A., GIRONELLA, M., LORENTE, M., GARCIA, S., GUZMÁN, M., VELASCO, G. & IOVANNA, J. L. 2006a. Cannabinoids induce apoptosis of pancreatic tumor cells via endoplasmic reticulum stress–related genes. *Cancer Research,* 66**,** 6748-6755.

CARRACEDO, A., LORENTE, M., EGIA, A., BLÁZQUEZ, C., GARCÍA, S., GIROUX, V., MALICET, C., VILLUENDAS, R., GIRONELLA, M. & GONZÁLEZ-FERIA, L. 2006b. The stress-regulated protein p8 mediates cannabinoid-induced apoptosis of tumor cells. *Cancer Cell,* 9**,** 301-312.

CHAKRAVARTI, B., RAVI, J. & GANJU, R. K. 2014. Cannabinoids as therapeutic agents in cancer: current status and future implications. *Oncotarget,* 5**,** 5852-5872.

CHARDIN, P. & MCCORMICK, F. 1999. Brefeldin A: The advantage of being uncompetitive. *Cell,* 97**,** 153-155.

CHEN, X., KARNOVSKY, A., SANS, M. D., ANDREWS, P. C. & WILLIAMS, J. A. 2010. Molecular characterization of the endoplasmic reticulum: insights from proteomic studies. *Proteomics,* 10**,** 4040-4052.

CHEN, Y. & BRANDIZZI, F. 2013. IRE1: ER stress sensor and cell fate executor. *Trends in Cell Biology,* 23**,** 547-555.

CHEUNG, H. H., KELLY, N. L., LISTON, P. & KORNELUK, R. G. 2006. Involvement of caspase-2 and caspase-9 in endoplasmic reticulum stress-induced apoptosis: a role for the IAPs. *Experimental Cell Research,* 312**,** 2347-2357.

CHOW, J., NORNG, M., ZHANG, J. & CHAI, J. 2007. TRPV6 mediates capsaicin-induced apoptosis in gastric cancer cells—Mechanisms behind a possible new "hot" cancer treatment. *Biochimica et Biophysica Acta (BBA) - Molecular Cell Research,* 1773**,** 565-576.

CLARK, R. & LEE, S.-H. 2016. Anticancer properties of capsaicin against human cancer. *Anticancer research,* 36**,** 837-843.

CLARKE, R., COOK, K. L., HU, R., FACEY, C. O. B., TAVASSOLY, I., SCHWARTZ, J. L., BAUMANN, W. T., TYSON, J. J., XUAN, J., WANG, Y., WÄRRI, A. & SHAJAHAN, A. N. 2012. Endoplasmic Reticulum Stress, the Unfolded Protein Response, Autophagy, and the Integrated Regulation of Breast Cancer Cell Fate. *Cancer Research,* 72**,** 1321-1331.

CNOP, M., WELSH, N., JONAS, J.-C., JÖRNS, A., LENZEN, S. & EIZIRIK, D. L. 2005. Mechanisms of pancreatic β-cell death in type 1 and type 2 diabetes. *Many Differences, Few Similarities,* 54**,** S97-S107.

CORAZZARI, M., GAGLIARDI, M., FIMIA, G. M. & PIACENTINI, M. 2017. Endoplasmic reticulum stress, unfolded protein response, and cancer cell fate. *Frontiers in Oncology,* 7.

CROMPTON, M. 1999. The mitochondrial permeability transition pore and its role in cell death. *Biochemical Journal,* 341**,** 233-249.

CYBULSKY, A. V., TAKANO, T., PAPILLON, J. & BIJIAN, K. 2005. Role of the endoplasmic reticulum unfolded protein response in glomerular epithelial cell injury. *Journal of Biological Chemistry,* 280**,** 24396-24403.

DAHMER, M. K. 2005. Caspases-2, -3, and -7 are involved in thapsigargin-induced apoptosis of SH-SY5Y neuroblastoma cells. *Journal of Neuroscience Research,* 80**,** 576-583.

DAVIS, M. 2016. Cannabinoids for symptom management and cancer therapy: the evidence. *Journal of the National Comprehensive Cancer Network,* 14**,** 915-922.

DAVIS, R. J. 2000. Signal transduction by the JNK group of MAP kinases. *Cell,* 103**,** 239-252.

DEVANE, W. A., DYSARZ, F. R., JOHNSON, M. R., MELVIN, L. S. & HOWLETT, A. C. 1988. Determination and characterization of a cannabinoid receptor in rat brain. *Molecular Pharmacology,* 34**,** 605-613.

DEVRIES-SEIMON, T., LI, Y., YAO, P. M., STONE, E., WANG, Y., DAVIS, R. J., FLAVELL, R. & TABAS, I. 2005. Cholesterol-induced macrophage apoptosis requires ER stress pathways and engagement of the type A scavenger receptor. *Journal of Cell Biology* 171**,** 61-73.

DI SANO, F., FERRARO, E., TUFI, R., ACHSEL, T., PIACENTINI, M. & CECCONI, F. 2006. Endoplasmic reticulum stress induces apoptosis by an apoptosome-dependent but caspase 12-independent mechanism. *Journal of Biological Chemistry,* 281**,** 2693-2700.

DIKALOV, S., GRIENDLING, K. K. & HARRISON, D. G. 2007. Measurement of reactive oxygen species in cardiovascular studies. *Hypertension,* 49**,** 717-727.

DIMMELER, S. & ZEIHER, A. M. 1997. Nitric oxide and apoptosis: another paradigm for the double-edged role of nitric oxide. *Nitric Oxide,* 1**,** 275-281.

DONALDSON, J. G., CASSEL, D., KAHN, R. A. & KLAUSNER, R. D. 1992. ADP-ribosylation factor, a small GTP-binding protein, is required for binding of the coatomer protein beta-COP to Golgi membranes. *Proceedings of the National Academy of Sciences,* 89**,** 6408-6412.

DONG, D., NI, M., LI, J., XIONG, S., YE, W., VIRREY, J. J., MAO, C., YE, R., WANG, M., PEN, L., DUBEAU, L., GROSHEN, S., HOFMAN, F. M. & LEE, A. S. 2008. Critical role of the stress chaperone GRP78/BiP in tumor proliferation, survival, and tumor angiogenesis in transgene-induced mammary tumor development. *Cancer Research,* 68**,** 498-505.

DONG, Z., SAIKUMAR, P., WEINBERG, J. & VENKATACHALAM, M. 2006. Calcium in cell injury and death. *Annual review of pathology,* 1**,** 405-34.

ELBAZ, M., AHIRWAR, D., XIAOLI, Z., ZHOU, X., LUSTBERG, M., NASSER, M. W., SHILO, K. & GANJU, R. K. 2016. TRPV2 is a novel biomarker and therapeutic target in triple negative breast cancer. *Oncotarget,* 9**,** 33459-33470.

ENGLISH, A. R., ZUREK, N. & VOELTZ, G. K. 2009. Peripheral ER structure and function. *Current Opinion In Cell Biology,* 21**,** 596-602.

FENG, B., YAO, P. M., LI, Y., DEVLIN, C. M., ZHANG, D., HARDING, H. P., SWEENEY, M., RONG, J. X., KURIAKOSE, G. & FISHER, E. A. 2003. The endoplasmic reticulum is the site of cholesterol-induced cytotoxicity in macrophages. *Nature Cell Biology,* 5**,** 781.

GALVE-ROPERH, I., SÁNCHEZ, C., CORTÉS, M. L., DEL PULGAR, T. G., IZQUIERDO, M. & GUZMÁN, M. 2000. Anti-tumoral action of cannabinoids: involvement of sustained ceramide accumulation and extracellular signal-regulated kinase activation. *Nature Medicine,* 6**,** 313.

GARG, A. D., MAES, H., VAN VLIET, A. R. & AGOSTINIS, P. 2015. Targeting the hallmarks of cancer with therapy-induced endoplasmic reticulum (ER) stress. *Molecular & Cellular Oncology,* 2**,** e975089.

GATENBY, R. A. & GILLIES, R. J. 2004. Why do cancers have high aerobic glycolysis? *Nature Reviews Cancer,* 4**,** 891.

GIAMPIETRI, C., PETRUNGARO, S., CONTI, S., FACCHIANO, A., FILIPPINI, A. & ZIPARO, E. 2015. Cancer microenvironment and endoplasmic reticulum stress response. *Mediators of Inflammation,* 2015**,** 11.

GIORGI, C., DE STEFANI, D., BONONI, A., RIZZUTO, R. & PINTON, P. 2009. Structural and functional link between the mitochondrial network and the endoplasmic reticulum. *The International Journal of Biochemistry & Cell Biology,* 41**,** 1817-1827.

GÓMEZ DEL PULGAR, T., VELASCO, G., SÁNCHEZ, C., HARO, A. & GUZMÁN, M. 2002. *De novo*-synthesized ceramide is involved in cannabinoid-induced apoptosis. *Biochemical Journal,* 363**,** 183-188.

GÖRLACH, A., BERTRAM, K., HUDECOVA, S. & KRIZANOVA, O. 2015. Calcium and ROS: A mutual interplay. *Redox Biology,* 6**,** 260-271.

GOTOH, T. & MORI, M. 2006. Nitric oxide and endoplasmic reticulum stress. *Arteriosclerosis, Thrombosis, And Vascular Biology,* 26**,** 1439-1446.

GREGOR, M. F. & HOTAMISLIGIL, G. S. 2007. Thematic review series: Adipocyte biology. Adipocyte stress: The endoplasmic reticulum and metabolic disease. *Journal of Lipid Research,* 48**,** 1905-1914.

GRIESS, P. 1879. Bemerkungen zu der Abhandlung der HH. Weselsky und Benedikt „Ueber einige Azoverbindungen". *Berichte der deutschen chemischen Gesellschaft,* 12**,** 426-428.

GUINDON, J. & HOHMANN, A. G. 2011. The endocannabinoid system and cancer: therapeutic implication. *British Journal of Pharmacology,* 163**,** 1447-1463.

HAMIDI, H., LILJA, J. & IVASKA, J. 2017. Using xCELLigence RTCA instrument to measure cell adhesion. *Bio-protocol,* 7**,** e2646.

HAMPSON, A. J., GRIMALDI, M., LOLIC, M., WINK, D., ROSENTHAL, R. & AXELROD, J. 2000. Neuroprotective antioxidants from marijuana. *Annals-New York Academy Of Sciences,* 899**,** 274-282.

HAN, D., LERNER, A. G., VANDE WALLE, L., UPTON, J.-P., XU, W., HAGEN, A., BACKES, B. J., OAKES, S. A. & PAPA, F. R. 2009. IRE1-alpha kinase activation modes control alternate endoribonuclease outputs to determine divergent cell fates. *Cell,* 138**,** 562-575.

HAN, S., LIANG, C.-P., DEVRIES-SEIMON, T., RANALLETTA, M., WELCH, C. L., COLLINS-FLETCHER, K., ACCILI, D., TABAS, I. & TALL, A. R. 2006. Macrophage insulin receptor deficiency increases ER stress-induced apoptosis and necrotic core formation in advanced atherosclerotic lesions. *Cell Metabolism,* 3**,** 257-266.

HANAHAN, D. & WEINBERG, R. A. 2011. Hallmarks of cancer: the next generation. *cell,* 144**,** 646-674.

HÄRRI, E., LOEFFLER, W., SIGG, H. P., STÄHELIN, H. & TAMM, C. 1963. Über die Isolierung neuer Stoffwechselprodukte aus Penicillium brefeldianum DODGE. *Helvetica Chimica Acta,* 46**,** 1235-1243.

HARRIS, M. 1980. Pyruvate blocks expression of sensitivity to antimycin A and chloramphenicol. *Somatic Cell Genetics,* 6**,** 699-708.

HE, Y., SUN, S., SHA, H., LIU, Z., YANG, L., XUE, Z., CHEN, H. & QI, L. 2010. Emerging roles for XBP1, a sUPeR transcription factor. *Gene Expression,* 15**,** 13-25.

HEALY, D. G., ABOU-SLEIMAN, P. M. & WOOD, N. W. 2004. PINK, PANK, or PARK? A clinicians' guide to familial parkinsonism. *The Lancet Neurology,* 3**,** 652-662.

HEALY, S. J., GORMAN, A. M., MOUSAVI-SHAFAEI, P., GUPTA, S. & SAMALI, A. 2009. Targeting the endoplasmic reticulum-stress response as an anticancer strategy. *European Journal of Pharmacology,* 625**,** 234-246.

HERSCHKOWITZ, J. I., SIMIN, K., WEIGMAN, V. J., MIKAELIAN, I., USARY, J., HU, Z., RASMUSSEN, K. E., JONES, L. P., ASSEFNIA, S., CHANDRASEKHARAN, S., BACKLUND, M. G., YIN, Y., KHRAMTSOV, A. I., BASTEIN, R., QUACKENBUSH, J., GLAZER, R. I., BROWN, P. H., GREEN, J. E., KOPELOVICH, L., FURTH, P. A., PALAZZO, J. P., OLOPADE, O. I., BERNARD, P. S., CHURCHILL, G. A., VAN DYKE, T. & PEROU, C. M. 2007. Identification of conserved gene expression features between murine mammary carcinoma models and human breast tumors. *Genome Biology,* 8**,** R76-R76.

HITOMI, J., KATAYAMA, T., EGUCHI, Y., KUDO, T., TANIGUCHI, M., KOYAMA, Y., MANABE, T., YAMAGISHI, S., BANDO, Y., IMAIZUMI, K., TSUJIMOTO, Y. & TOHYAMA, M. 2004. Involvement of caspase-4 in endoplasmic reticulum stress-induced apoptosis and Abeta-induced cell death. *The Journal of Cell Biology,* 165**,** 347-356.

HOLLIDAY, D. L. & SPEIRS, V. 2011. Choosing the right cell line for breast cancer research. *Breast Cancer Research,* 13**,** 215-215.

HOOZEMANS, J. J. M., VEERHUIS, R., VAN HAASTERT, E. S., ROZEMULLER, J. M., BAAS, F., EIKELENBOOM, P. & SCHEPER, W. 2005. The unfolded protein response is activated in Alzheimer's disease. *Acta Neuropathologica,* 110**,** 165-172.

HOWLETT, A., BARTH, F., BONNER, T., CABRAL, G., CASELLAS, P., DEVANE, W., FELDER, C., HERKENHAM, M., MACKIE, K. & MARTIN, B. 2002. International Union of Pharmacology. XXVII. Classification of cannabinoid receptors. *Pharmacological reviews,* 54**,** 161-202.

HU, P., HAN, Z., COUVILLON, A. D., KAUFMAN, R. J. & EXTON, J. H. 2006. Autocrine tumor necrosis factor alpha links endoplasmic reticulum stress to the membrane death receptor pathway through ire1α-mediated NF-κb activation and down-regulation of TRAF2 expression. *Molecular and Cellular Biology,* 26**,** 3071-3084.

HUITING, L. N., SAMAHA, Y., ZHANG, G. L., RODERICK, J. E., LI, B., ANDERSON, N. M., WANG, Y. W., WANG, L., LAROCHE, F., CHOI, J. W., LIU, C. T., KELLIHER, M. A. & FENG, H. 2018. UFD1 contributes to MYC-mediated leukemia aggressiveness through suppression of the proapoptotic unfolded protein response. *Leukemia,* 32**,** 2339-2351.

INAGI, R., NANGAKU, M., ONOGI, H., UEYAMA, H., KITAO, Y., NAKAZATO, K., OGAWA, S., KUROKAWA, K., COUSER, W. G. & MIYATA, T. 2005. Involvement of endoplasmic reticulum (ER) stress in podocyte injury induced by excessive protein accumulation. *Kidney International,* 68**,** 2639-2650.

ITTNER, L. M. & GÖTZ, J. 2010. Amyloid-β and tau — a toxic pas de deux in Alzheimer's disease. *Nature Reviews Neuroscience,* 12**,** 67.

JAMORA, C., DENNERT, G. & LEE, A. S. 1996. Inhibition of tumor progression by suppression of stress protein GRP78/BiP induction in fibrosarcoma B/C10ME. *Proceedings of the National Academy of Sciences of the United States of America,* 93**,** 7690-7694.

JHAVERI, M. S., RAIT, A. S., CHUNG, K.-N., TREPEL, J. B. & CHANG, E. H. 2004. Antisense oligonucleotides targeted to the human α folate receptor inhibit breast cancer cell growth and sensitize the cells to doxorubicin treatment. *Molecular Cancer Therapeutics,* 3**,** 1505-1512.

JI, C. & KAPLOWITZ, N. 2003. Betaine decreases hyperhomocysteinemia, endoplasmic reticulum stress, and liver injury in alcohol-fed mice. *Gastroenterology,* 124**,** 1488-1499.

JI, C. & KAPLOWITZ, N. 2004. Hyperhomocysteinemia, endoplasmic reticulum stress, and alcoholic liver injury. *World Journal Of Gastroenterology,* 10**,** 1699-1708.

JI, C. & KAPLOWITZ, N. 2006. ER stress: Can the liver cope? *Journal of Hepatology,* 45**,** 321-333.

JI, C., MEHRIAN-SHAI, R., CHAN, C., HSU, Y.-H. & KAPLOWITZ, N. 2005. Role of CHOP in hepatic apoptosis in the murine model of intragastric ethanol feeding. *Alcoholism, Clinical And Experimental Research,* 29**,** 1496-1503.

KAMMOUN, H. L., CHABANON, H., HAINAULT, I., LUQUET, S., MAGNAN, C., KOIKE, T., FERRÉ, P. & FOUFELLE, F. 2009. GRP78 expression inhibits insulin and ER stress-induced SREBP-1c activation and reduces hepatic steatosis in mice. *The Journal Of Clinical Investigation,* 119**,** 1201-1215.

KANO, M., OHNO-SHOSAKU, T., HASHIMOTODANI, Y., UCHIGASHIMA, M. & WATANABE, M. 2009. Endocannabinoid-mediated control of synaptic transmission. *Physiological Reviews,* 89**,** 309-380.

KAPUSCINSKI, J. 1995. DAPI: A DNA-specific fluorescent probe. *Biotechnic & Histochemistry,* 70**,** 220-233.

KHALILI, M. & RADOSEVICH, J. A. 2018. Paraptosis. *Apoptosis and Beyond.*

KHO, D., MACDONALD, C., JOHNSON, R., UNSWORTH, C., O'CARROLL, S., DU MEZ, E., ANGEL, C. & GRAHAM, E. 2015a. Application of xCELLigence RTCA biosensor technology for revealing the profile and window of drug responsiveness in real time. *Biosensors,* 5**,** 199-222.

KHO, D., MACDONALD, C., JOHNSON, R., UNSWORTH, C. P., #039, CARROLL, S. J., MEZ, E. D., ANGEL, C. E. & GRAHAM, E. S. 2015b. Application of xCELLigence RTCA Biosensor Technology for Revealing the Profile and Window of Drug Responsiveness in Real Time. *Biosensors,* 5**,** 199-222.

KING, A. P., MARKER, S. C., SWANDA, R. V., WOODS, J. J., QIAN, S.-B. & WILSON, J. J. 2019. A rhenium isonitrile complex induces unfolded protein response-mediated apoptosis in cancer cells. *Chemistry – A European Journal,* 25**,** 9206-9210.

KING, M. & ATTARDI, G. 1989. Human cells lacking mtDNA: repopulation with exogenous mitochondria by complementation. *Science,* 246**,** 500-503.

KLAUSNER, R. D., DONALDSON, J. G. & LIPPINCOTT-SCHWARTZ, J. 1992. Brefeldin A: insights into the control of membrane traffic and organelle structure. *The Journal of Cell Biology,* 116**,** 1071-1080.

KORITZINSKY, M., LEVITIN, F., VAN DEN BEUCKEN, T., RUMANTIR, R. A., HARDING, N. J., CHU, K. C., BOUTROS, P. C., BRAAKMAN, I. & WOUTERS, B. G. 2013. Two phases of disulfide bond formation have differing requirements for oxygen. *The Journal of Cell Biology,* 203**,** 615-627.

KORNMANN, B., CURRIE, E., COLLINS, S. R., SCHULDINER, M., NUNNARI, J., WEISSMAN, J. S. & WALTER, P. 2009. An ER-mitochondria tethering complex revealed by a synthetic biology screen. *Science,* 325**,** 477-481.

KOŞAR, P. A., NAZıROĞLU, M., ÖVEY, İ. S. & ÇIĞ, B. 2016. Synergic effects of doxorubicin and melatonin on apoptosis and mitochondrial oxidative stress in MCF-7 breast cancer cells: Involvement of TRPV1 channels. *The Journal of Membrane Biology,* 249**,** 129-140.

KOSTOVA, Z. & WOLF, D. H. 2003. For whom the bell tolls: protein quality control of the endoplasmic reticulum and the ubiquitin-proteasome connection. *The EMBO journal,* 22**,** 2309-2317.

KURUVILLA, S., QUALLS, C. W., JR., TYLER, R. D., WITHERSPOON, S. M., BENAVIDES, G. R., YOON, L. W., DOLD, K., BROWN, R. H., SANGIAH, S. & MORGAN, K. T. 2003. Effects of minimally toxic levels of carbonyl cyanide p-(trifluoromethoxy) phenylhydrazone (fccp), elucidated through differential gene expression with biochemical and morphological correlations. *Toxicological Sciences,* 73**,** 348-361.

LAI, E., TEODORO, T. & VOLCHUK, A. 2007. Endoplasmic reticulum stress: signaling the unfolded protein response. *Physiology,* 22**,** 193-201.

LAU, J. K., BROWN, K. C., DOM, A. M., WITTE, T. R., THORNHILL, B. A., CRABTREE, C. M., PERRY, H. E., BROWN, J. M., BALL, J. G., CREEL, R. G., DAMRON, C. L., ROLLYSON, W. D., STEVENSON, C. D., HARDMAN, W. E., VALENTOVIC, M. A., CARPENTER, A. B. & DASGUPTA, P. 2014. Capsaicin induces apoptosis in human small cell lung cancer via the TRPV6 receptor and the calpain pathway. *Apoptosis,* 19**,** 1190-1201.

LAWRENCE DE KONING, A. B., WERSTUCK, G. H., ZHOU, J. & AUSTIN, R. C. 2003. Hyperhomocysteinemia and its role in the development of atherosclerosis. *Clinical Biochemistry,* 36**,** 431-441.

LEE, J. W., KIM, W. H., YEO, J. & JUNG, M. H. 2010. ER stress is implicated in mitochondrial dysfunction-induced apoptosis of pancreatic beta cells. *Molecules and Cells,* 30**,** 545-549.

LI, Y., ZHU, D., HOU, L., HU, B., XU, M. & MENG, X. 2018. TRB3 reverses chemotherapy resistance and mediates crosstalk between endoplasmic reticulum stress and AKT signaling pathways in MHCC97H human hepatocellular carcinoma cells. *Oncology Letters,* 15**,** 1343-1349.

LIGRESTI, A., MORIELLO, A. S., STAROWICZ, K., MATIAS, I., PISANTI, S., DE PETROCELLIS, L., LAEZZA, C., PORTELLA, G., BIFULCO, M. & DI MARZO, V. 2006. Antitumor activity of plant cannabinoids with emphasis on the effect of cannabidiol on human breast carcinoma. *Journal of Pharmacology and Experimental Therapeutics,* 318**,** 1375-1387.

LIM, J. H., LEE, H. J., HO JUNG, M. & SONG, J. 2009. Coupling mitochondrial dysfunction to endoplasmic reticulum stress response: A molecular mechanism leading to hepatic insulin resistance. *Cellular Signalling,* 21**,** 169-177.

LIMIA, C. M., SAUZAY, C., URRA, H., HETZ, C., CHEVET, E. & AVRIL, T. 2019. Emerging roles of the endoplasmic reticulum associated unfolded protein response in cancer cell migration and invasion. *Cancers,* 11**,** 631.

LIU, Q.-R., PAN, C.-H., HISHIMOTO, A., LI, C.-Y., XI, Z.-X., LLORENTE-BERZAL, A., VIVEROS, M.-P., ISHIGURO, H., ARINAMI, T., ONAIVI, E. S. & UHL, G. R. 2009. Species differences in cannabinoid receptor 2 (CNR2 gene): identification of novel human and rodent CB2 isoforms, differential tissue expression and regulation by cannabinoid receptor ligands. *Genes, Brain and Behavior,* 8**,** 519-530.

LORZ, C., JUSTO, P., SANZ, A., SUBIRÁ, D., EGIDO, J. & ORTIZ, A. 2004. Paracetamol-induced renal tubular injury: a role for ER stress. *Journal of the American Society of Nephrology,* 15**,** 380-389.

LOZANO, C., CÓRDOVA, C., MARCHANT, I., ZÚÑIGA, R., OCHOVA, P., RAMÍREZ-BARRANTES, R., GONZÁLEZ-ARRIAGADA, W. A., RODRIGUEZ, B. & OLIVERO, P. 2018. Intracellular aggregated TRPV1 is associated with lower survival in breast cancer patients. *Breast cancer (Dove Medical Press),* 10**,** 161-168.

MA, Y. & HENDERSHOT, L. M. 2004. The role of the unfolded protein response in tumour development: friend or foe? *Nature Reviews Cancer,* 4**,** 966.

MACCARRONE, M., LORENZON, T., BARI, M., MELINO, G. & FINAZZI-AGRÒ, A. 2000. Anandamide induces apoptosis in human cells via vanilloid receptors Evidence for a protective role of cannabinoid receptors. *Journal of Biological Chemistry,* 275**,** 31938-31945.

MACKIE, K. 2005. Distribution of cannabinoid receptors in the central and peripheral nervous system. *Cannabinoids.* Springer.

MALHOTRA, J. D. & KAUFMAN, R. J. 2007. The endoplasmic reticulum and the unfolded protein response. *Seminars In Cell & Developmental Biology,* 18**,** 716-731.

MALHOTRA, J. D. & KAUFMAN, R. J. 2011. ER stress and its functional link to mitochondria: role in cell survival and death. *Cold Spring Harbor Perspectives In Biology,* 3**,** a004424-a004424.

MAMROSH, J. L., LEE, J. M., WAGNER, M., STAMBROOK, P. J., WHITBY, R. J., SIFERS, R. N., WU, S.-P., TSAI, M.-J., DEMAYO, F. J. & MOORE, D. D. 2014. Nuclear receptor LRH-1/NR5A2 is required and targetable for liver endoplasmic reticulum stress resolution. *eLife,* 3**,** e01694-e01694.

MARADA, S., STEWART, D. P., BODEEN, W. J., HAN, Y.-G. & OGDEN, S. K. 2013. The unfolded protein response selectively targets active smoothened mutants. *Molecular And Cellular Biology,* 33**,** 2375-2387.

MARENGO, B., NITTI, M., FURFARO, A. L., COLLA, R., CIUCIS, C. D., MARINARI, U. M., PRONZATO, M. A., TRAVERSO, N. & DOMENICOTTI, C. 2016. Redox homeostasis and cellular antioxidant systems: Crucial players in cancer growth and therapy. *Oxidative Medicine and Cellular Longevity,* 2016**,** 16.

MARKGRAF, D. F., KLEMM, R. W., JUNKER, M., HANNIBAL-BACH, H. K., EJSING, C. S. & RAPOPORT, T. A. 2014. An ER protein functionally couples neutral lipid metabolism on lipid droplets to membrane lipid synthesis in the ER. *Cell reports,* 6**,** 44-55.

MARTINDALE, J. J., FERNANDEZ, R., THUERAUF, D., WHITTAKER, R., GUDE, N., SUSSMAN, M. A. & GLEMBOTSKI, C. C. 2006. Endoplasmic reticulum stress gene induction and protection from ischemia/reperfusion injury in the hearts of transgenic mice with a tamoxifen-regulated form of ATF6. *Circulation Research,* 98**,** 1186-1193.

MASSI, P., SOLINAS, M., CINQUINA, V. & PAROLARO, D. 2013. Cannabidiol as potential anticancer drug. *British journal of clinical pharmacology,* 75**,** 303-312.

MATSUDA, L. A., LOLAIT, S. J., BROWNSTEIN, M. J., YOUNG, A. C. & BONNER, T. I. 1990. Structure of a cannabinoid receptor and functional expression of the cloned cDNA. *Nature,* 346**,** 561.

MATTSON, M. P. 2008. Hormesis defined. *Ageing Research Reviews,* 7**,** 1-7.

MCALLISTER, S. D., CHRISTIAN, R. T., HOROWITZ, M. P., GARCIA, A. & DESPREZ, P.-Y. 2007. Cannabidiol as a novel inhibitor of Id-1 gene expression in aggressive breast cancer cells. *Molecular cancer therapeutics,* 6**,** 2921-2927.

MEIER, R., HENNING, T. D., BODDINGTON, S., TAVRI, S., ARORA, S., PIONTEK, G., RUDELIUS, M., COROT, C. & DALDRUP-LINK, H. E. 2010. Breast Cancers: MR Imaging of Folate-Receptor Expression with the Folate-Specific Nanoparticle P1133. *Radiology,* 255**,** 527-535.

MERKSAMER, P. I. & PAPA, F. R. 2010. The UPR and cell fate at a glance. *Journal of Cell Science,* 123**,** 1003-1006.

MERKSAMER, P. I., TRUSINA, A. & PAPA, F. R. 2008. Real-time redox measurements during endoplasmic reticulum stress reveal interlinked protein folding functions. *Cell,* 135**,** 933-947.

MIYATA, T., INAGI, R., SUGIYAMA, S. & USUDA, N. 2005. Serpinopathy and endoplasmic reticulum stress. *Medical Molecular Morphology,* 38**,** 73-78.

MOLLEREAU, B., MANIÉ, S. & NAPOLETANO, F. 2014. Getting the better of ER stress. *Journal Of Cell Communication And Signaling,* 8**,** 311-321.

MOORE, C. E., OMIKOREDE, O., GOMEZ, E., WILLARS, G. B. & HERBERT, T. P. 2011. PERK activation at low glucose concentration is mediated by SERCA pump inhibition and confers preemptive cytoprotection to pancreatic β-cells. *Molecular Endocrinology (Baltimore, Md.),* 25**,** 315-326.

MORENO-GONZALEZ, I. & SOTO, C. Misfolded protein aggregates: mechanisms, structures and potential for disease transmission. Seminars In Cell & Developmental Biology, 2011. Elsevier, 482-487.

MOSMANN, T. 1983. Rapid colorimetric assay for cellular growth and survival: application to proliferation and cytotoxicity assays. *Journal Of Immunological Methods,* 65**,** 55-63.

MUNRO, S., THOMAS, K. L. & ABU-SHAAR, M. 1993. Molecular characterization of a peripheral receptor for cannabinoids. *Nature,* 365**,** 61.

MUNSON, A., HARRIS, L., FRIEDMAN, M., DEWEY, W. & CARCHMAN, R. 1975. Antineoplastic activity of cannabinoids. *Journal of the National Cancer Institute,* 55**,** 597-602.

MUNUJOS, P., COLLCANTI, J., GONZALEZSASTRE, F. & GELLA, F. J. 1993. Assay of succinate dehydrogenase activity by a colorimetric-continuous method using iodonitrotetrazolium chloride as electron acceptor. *Analytical biochemistry,* 212**,** 506-509.

NAKAGAWA, T. & YUAN, J. 2000. Cross-talk between two cysteine protease families. Activation of caspase-12 by calpain in apoptosis. *The Journal Of Cell Biology,* 150**,** 887-894.

NAVID, F. & COLBERT, R. A. 2017. Causes and consequences of endoplasmic reticulum stress in rheumatic disease. *Nature Reviews Rheumatology,* 13**,** 25.

NAZıROĞLU, M., ÇIĞ, B., BLUM, W., VIZLER, C., BUHALA, A., MARTON, A., KATONA, R., JÓSVAY, K., SCHWALLER, B., OLÁH, Z. & PECZE, L. 2017. Targeting breast cancer cells by MRS1477, a positive allosteric modulator of TRPV1 channels. *PloS ONE,* 12**,** e0179950-e0179950.

NELSON, R. & EISENBERG, D. 2006. Recent atomic models of amyloid fibril structure. *Current Opinion In Structural Biology,* 16**,** 260-265.

NOËL, S., CADET, S., GRAS, E. & HUREAU, C. 2013. The benzazole scaffold: a SWAT to combat Alzheimer's disease. *Chemical Society Reviews,* 42**,** 7747-7762.

NUR, G., NAZıROĞLU, M. & DEVECI, H. A. 2017. Synergic prooxidant, apoptotic and TRPV1 channel activator effects of alpha-lipoic acid and cisplatin in MCF-7 breast cancer cells. *Journal of Receptors and Signal Transduction,* 37**,** 569-577.

OHOKA, N., YOSHII, S., HATTORI, T., ONOZAKI, K. & HAYASHI, H. 2005. TRB3, a novel ER stress-inducible gene, is induced via ATF4–CHOP pathway and is involved in cell death. *The EMBO Journal,* 24**,** 1243-1255.

OKADA, K.-I., MINAMINO, T., TSUKAMOTO, Y., LIAO, Y., TSUKAMOTO, O., TAKASHIMA, S., HIRATA, A., FUJITA, M., NAGAMACHI, Y. & NAKATANI, T. 2004. Prolonged endoplasmic reticulum stress in hypertrophic and failing heart after aortic constriction: possible contribution of endoplasmic reticulum stress to cardiac myocyte apoptosis. *Circulation,* 110**,** 705-712.

OSLOWSKI, C. M. & URANO, F. 2011. Measuring ER stress and the unfolded protein response using mammalian tissue culture system. *Methods In Enzymology,* 490**,** 71-92.

OUTINEN, P. A., SOOD, S. K., LIAW, P. C., SARGE, K. D., MAEDA, N., HIRSH, J., RIBAU, J., PODOR, T. J., WEITZ, J. I. & AUSTIN, R. C. 1998. Characterization of the stress-inducing effects of homocysteine. *The Biochemical Journal,* 332 (Pt 1)**,** 213-221.

OZCAN, L. & TABAS, I. 2012. Role of endoplasmic reticulum stress in metabolic disease and other disorders. *Annual review of medicine,* 63**,** 317-328.

PACHER, P., BÁTKAI, S. & KUNOS, G. 2006. The endocannabinoid system as an emerging target of pharmacotherapy. *Pharmacological Reviews,* 58**,** 389-462.

PALADE, G. E. & PORTER, K. R. 1954. Studies on the endoplasmic reticulum. I. Its identification in cells *in situ*. *The Journal Of Experimental Medicine,* 100**,** 641-656.

PARAFATI, M., KIRBY, R. J., KHORASANIZADEH, S., RASTINEJAD, F. & MALANY, S. 2018. A nonalcoholic fatty liver disease model in human induced pluripotent stem cell-derived hepatocytes, created by endoplasmic reticulum stress-induced steatosis. *Disease Models & Mechanisms,* 11**,** dmm033530.

PECZE, L., JÓSVAY, K., BLUM, W., PETROVICS, G., VIZLER, C., OLÁH, Z. & SCHWALLER, B. 2016. Activation of endogenous TRPV1 fails to induce overstimulation-based cytotoxicity in breast and prostate cancer cells but not in pain-sensing neurons. *Biochimica et Biophysica Acta (BBA) - Molecular Cell Research,* 1863**,** 2054-2064.

PHYPERS, B. & PIERCE, J. T. 2006. Lactate physiology in health and disease. *BJA Education,* 6**,** 128-132.

POROWSKA, H., PASZKIEWICZ-GADEK, A., LEMANCEWICZ, D., BIELAWSKI, T. & WO, S. C. 2008. Effect of brefeldin A on membrane localization of MUC1 mucin and adhesive properties of cancer cells. *Neoplasma,* 55**,** 305-311.

PORTER, K. R., CLAUDE, A. & FULLAM, E. F. 1945. A study of tissue culture cells by electron microscopy : Methods and preliminary observations. *The Journal of experimental medicine,* 81**,** 233-246.

PRAT, A., PARKER, J. S., KARGINOVA, O., FAN, C., LIVASY, C., HERSCHKOWITZ, J. I., HE, X. & PEROU, C. M. 2010. Phenotypic and molecular characterization of the claudin-low intrinsic subtype of breast cancer. *Breast Cancer Research* 12**,** R68-R68.

PYSZNIAK, M., TABARKIEWICZ, J. & ŁUSZCZKI, J. J. 2016. Endocannabinoid system as a regulator of tumor cell malignancy–biological pathways and clinical significance. *OncoTargets and therapy,* 9**,** 4323.

QU, Y., HAN, B., YU, Y., YAO, W., BOSE, S., KARLAN, B. Y., GIULIANO, A. E. & CUI, X. 2015. Evaluation of MCF10A as a reliable model for normal human mammary epithelial cells. *PLOS ONE,* 10**,** e0131285.

RAO, R. V., ELLERBY, H. & BREDESEN, D. E. 2004. Coupling endoplasmic reticulum stress to the cell death program. *Cell Death And Differentiation,* 11**,** 372.

RISS, T. L., MORAVEC, R. A., NILES, A. L., DUELLMAN, S., BENINK, H. A., WORZELLA, T. J. & MINOR, L. 2016. *Assay guidance manual*.

RON, D. & WALTER, P. 2007. Signal integration in the endoplasmic reticulum unfolded protein response. *Nature Reviews Molecular Cell Biology,* 8**,** 519.

RUDDOCK, L. W. & MOLINARI, M. 2006. N-glycan processing in ER quality control. *Journal Of Cell Science,* 119**,** 4373-4380.

RUTKOWSKI, D. T., ARNOLD, S. M., MILLER, C. N., WU, J., LI, J., GUNNISON, K. M., MORI, K., SADIGHI AKHA, A. A., RADEN, D. & KAUFMAN, R. J. 2006. Adaptation to ER stress is mediated by differential stabilities of pro-survival and pro-apoptotic mRNAs and proteins. *PLoS Biology,* 4**,** e374-e374.

RYBERG, E., VU, H. K., LARSSON, N., GROBLEWSKI, T., HJORTH, S., ELEBRING, T., SJÖGREN, S. & GREASLEY, P. J. 2005. Identification and characterisation of a novel splice variant of the human CB1 receptor. *FEBS Letters,* 579**,** 259-264.

SALAZAR, M., CARRACEDO, A., SALANUEVA, Í. J., HERNÁNDEZ-TIEDRA, S., EGIA, A., LORENTE, M., VÁZQUEZ, P., TORRES, S., IOVANNA, J. L. & GUZMÁN, M. 2009a. TRB3 links ER stress to autophagy in cannabinoid antitumoral action. *Autophagy,* 5**,** 1048-1049.

SALAZAR, M., CARRACEDO, A., SALANUEVA, Í. J., HERNÁNDEZ-TIEDRA, S., LORENTE, M., EGIA, A., VÁZQUEZ, P., BLÁZQUEZ, C., TORRES, S. & GARCÍA, S. 2009b. Cannabinoid action induces autophagy-mediated cell death through stimulation of ER stress in human glioma cells. *The Journal Of Clinical Investigation,* 119**,** 1359-1372.

SALLABERRY, C. A. & ASTERN, L. 2018. The Endocannabinoid System, Our Universal Regulator. *Journal of Young Investigators,* 34.

SÁNCHEZ, C., DE CEBALLOS, M. L., DEL PULGAR, T. G., RUEDA, D., CORBACHO, C., VELASCO, G., GALVE-ROPERH, I., HUFFMAN, J. W., RAMÓN Y CAJAL, S. & GUZMÁN, M. 2001. Inhibition of Glioma Growth in Vivo by Selective Activation of the CB2 Cannabinoid Receptor. *Cancer Research,* 61**,** 5784-5789.

SANO, R. & REED, J. C. 2013. ER stress-induced cell death mechanisms. *Biochimica et biophysica acta,* 1833**,** 10.1016/j.bbamcr.2013.06.028.

SARAFIAN, T. A., KOUYOUMJIAN, S., KHOSHAGHIDEH, F., TASHKIN, D. P. & ROTH, M. D. 2003. Δ9-Tetrahydrocannabinol disrupts mitochondrial function and cell energetics. *American Journal of Physiology-Lung Cellular and Molecular Physiology,* 284**,** L298-L306.

SCHONTHAL, A. H. 2011. Targeting endoplasmic reticulum stress for cancer therapy. *Frontiers In Bioscience (Scholar Edition),* 4**,** 412-431.

SCHÖNTHAL, A. H. 2012. Endoplasmic reticulum stress: its role in disease and novel prospects for therapy. *Scientifica,* 2012.

SCHRÖDER, M. 2008. Endoplasmic reticulum stress responses. *Cellular And Molecular Life Sciences,* 65**,** 862-894.

SCHRÖDER, M. & KAUFMAN, R. J. 2005. ER stress and the unfolded protein response. *Mutation Research/Fundamental and Molecular Mechanisms of Mutagenesis,* 569**,** 29-63.

SCHWARZ, D. S. & BLOWER, M. D. 2016. The endoplasmic reticulum: structure, function and response to cellular signaling. *Cellular and Molecular Life Sciences,* 73**,** 79-94.

SEHGAL, P., SZALAI, P., OLESEN, C., PRAETORIUS, H. A., NISSEN, P., CHRISTENSEN, S. B., ENGEDAL, N. & MØLLER, J. V. 2017. Inhibition of the sarco/endoplasmic reticulum (ER) Ca2+-ATPase by thapsigargin analogs induces cell death via ER Ca^{2+} depletion and the unfolded protein response. *Journal of Biological Chemistry*.

SHIRE, D., CARILLON, C., KAGHAD, M., CALANDRA, B., RINALDI-CARMONA, M., LE FUR, G., CAPUT, D. & FERRARA, P. 1995. An amino-terminal variant of the central cannabinoid receptor resulting from alternative splicing. *Journal of Biological Chemistry,* 270**,** 3726-3731.

SHRIVASTAVA, A., KUZONTKOSKI, P. M., GROOPMAN, J. E. & PRASAD, A. 2011. Cannabidiol induces programmed cell death in breast cancer cells by coordinating the cross-talk between apoptosis and autophagy. *Molecular Cancer Therapeutics,* 10**,** 1161-1172.

SITIA, R. & BRAAKMAN, I. 2004. Quality control in the endoplasmic reticulum protein factory. 426**,** 891-4.

SKEHAN, P., STORENG, R., SCUDIERO, D., MONKS, A., MCMAHON, J., VISTICA, D., WARREN, J. T., BOKESCH, H., KENNEY, S. & BOYD, M. R. 1990. New colorimetric cytotoxicity assay for anticancer-drug screening. *JNCI: Journal of the National Cancer Institute,* 82**,** 1107-1112.

ŚLEDZIŃSKI, P., NOWAK, A., ZEYLAND, J. & SŁOMSKI, R. 2016. Endocannabinoid system and anticancer properties of cannabinoids. *Folia Biologica et Oecologica,* 12**,** 11-25.

SØRLIE, T., PEROU, C. M., TIBSHIRANI, R., AAS, T., GEISLER, S., JOHNSEN, H., HASTIE, T., EISEN, M. B., VAN DE RIJN, M., JEFFREY, S. S., THORSEN, T., QUIST, H., MATESE, J. C., BROWN, P. O., BOTSTEIN, D., LØNNING, P. E. & BØRRESEN-DALE, A. L. 2001. Gene expression patterns of breast carcinomas distinguish tumor subclasses with clinical implications. *Proceedings of the National Academy of Sciences of the United States of America,* 98**,** 10869-10874.

SOULE, H. D., MALONEY, T. M., WOLMAN, S. R., PETERSON, W. D., BRENZ, R., MCGRATH, C. M., RUSSO, J., PAULEY, R. J., JONES, R. F. & BROOKS, S. 1990. Isolation and characterization of a spontaneously immortalized human breast epithelial cell line, MCF-10. *Cancer Research,* 50**,** 6075-6086.

SPERANDIO, S., DE BELLE, I. & BREDESEN, D. E. 2000. An alternative, nonapoptotic form of programmed cell death. *Proceedings of the National Academy of Sciences of the United States of America,* 97**,** 14376-14381.

SPERANDIO, S., POKSAY, K., DE BELLE, I., LAFUENTE, M. J., LIU, B., NASIR, J. & BREDESEN, D. E. 2004. Paraptosis: mediation by MAP kinases and inhibition by AIP-1/Alix. *Cell Death & Differentiation,* 11**,** 1066-1075.

SUBIK, K., LEE, J.-F., BAXTER, L., STRZEPEK, T., COSTELLO, D., CROWLEY, P., XING, L., HUNG, M.-C., BONFIGLIO, T., HICKS, D. G. & TANG, P. 2010. The expression patterns of ER, PR, HER2, CK5/6, EGFR, KI-67 and AR by immunohistochemical analysis in breast cancer cell lines. *Breast Cancer : Basic And Clinical Research,* 4**,** 35-41.

SZABADKAI, G., BIANCHI, K., VÁRNAI, P., DE STEFANI, D., WIECKOWSKI, M. R., CAVAGNA, D., NAGY, A. I., BALLA, T. & RIZZUTO, R. 2006. Chaperone-mediated coupling of endoplasmic reticulum and mitochondrial Ca^{2+} channels. *The Journal of cell biology,* 175**,** 901-911.

TABAS, I. 2009. Macrophage apoptosis in atherosclerosis: consequences on plaque progression and the role of endoplasmic reticulum stress. *Antioxidants & Redox Signaling,* 11**,** 2333-2339.

TAKATSUKI, A., ARIMA, K. & TAMURA, G. 1971. Tunicamycin, a new antibiotic. I. *The Journal of antibiotics,* 24**,** 215-223.

TAM, J., TREMBOVLER, V., MARZO, V. D., PETROSINO, S., LEO, G., ALEXANDROVICH, A., REGEV, E., CASAP, N., SHTEYER, A., LEDENT, C., KARSAK, M., ZIMMER, A., MECHOULAM, R., YIRMIYA, R., SHOHAMI, E. & BAB, I. 2008. The cannabinoid CB1 receptor regulates bone formation by modulating adrenergic signaling. *The FASEB Journal,* 22**,** 285-294.

TARASOV, A. I., GRIFFITHS, E. J. & RUTTER, G. A. 2012. Regulation of ATP production by mitochondrial Ca($^{2+}$). *Cell calcium,* 52**,** 28-35.

THEODOSSIOU, T. A., ALI, M., GRIGALAVICIUS, M., GRALLERT, B., DILLARD, P., SCHINK, K. O., OLSEN, C. E., WÄLCHLI, S., INDERBERG, E. M., KUBIN, A., PENG, Q. & BERG, K. 2019. Simultaneous defeat of MCF7 and MDA-MB-231 resistances by a hypericin PDT-tamoxifen hybrid therapy. *NPJ Breast Cancer,* 5**,** 13-13.

THIAM, A. R. & BELLER, M. 2017. The why, when and how of lipid droplet diversity. *Journal of Cell Science,* 130**,** 315-324.

THIAM, A. R. & FORÊT, L. 2016. The physics of lipid droplet nucleation, growth and budding. *Biochimica Et Biophysica Acta (BBA)-Molecular and Cell Biology of Lipids,* 1861**,** 715-722.

THOMAS, D., TOVEY, S., COLLINS, T., BOOTMAN, M., BERRIDGE, M. & LIPP, P. 2000. A comparison of fluorescent Ca^{2+} indicator properties and their use in measuring elementary and global Ca^{2+} signals. *Cell calcium,* 28**,** 213-223.

TONÉ, S., SUGIMOTO, K., TANDA, K., SUDA, T., UEHIRA, K., KANOUCHI, H., SAMEJIMA, K., MINATOGAWA, Y. & EARNSHAW, W. C. 2007. Three distinct stages of apoptotic nuclear condensation revealed by time-lapse imaging, biochemical and electron microscopy analysis of cell-free apoptosis. *Experimental Cell Research,* 313**,** 3635-3644.

TRAVERS, K. J., PATIL, C. K., WODICKA, L., LOCKHART, D. J., WEISSMAN, J. S. & WALTER, P. 2000. Functional and Genomic Analyses Reveal an Essential Coordination between the Unfolded Protein Response and ER-Associated Degradation. *Cell,* 101**,** 249-258.

TSAI, B., YE, Y. & RAPOPORT, T. 2002. *Retro-translocation of proteins from endoplasmic reticulum into the cytosol*.

TSIKAS, D. 2007. Analysis of nitrite and nitrate in biological fluids by assays based on the Griess reaction: Appraisal of the Griess reaction in the l-arginine/nitric oxide area of research. *Journal of Chromatography B,* 851**,** 51-70.

UPTON, J.-P., WANG, L., HAN, D., WANG, E. S., HUSKEY, N. E., LIM, L., TRUITT, M., MCMANUS, M. T., RUGGERO, D., GOGA, A., PAPA, F. R. & OAKES, S. A. 2012. IRE1α cleaves select microRNAs during ER stress to derepress translation of proapoptotic Caspase-2. *Science (New York, N.Y.),* 338**,** 818-822.

URRA, H., DUFEY, E., AVRIL, T., CHEVET, E. & HETZ, C. 2016. Endoplasmic reticulum stress and the hallmarks of cancer. *Trends In Cancer,* 2**,** 252-262.

URSINI, F., DAVIES, K. J. A., MAIORINO, M., PARASASSI, T. & SEVANIAN, A. 2002. Atherosclerosis: another protein misfolding disease? *Trends in Molecular Medicine,* 8**,** 370-374.

VAN ANKEN, E. & SITIA, R. 2016. The Endoplasmic Reticulum. *Encyclopedia of Cell Biology.* Academic Press.

VANCE, J. E. 1990. Phospholipid synthesis in a membrane fraction associated with mitochondria. *Journal of Biological Chemistry,* 265**,** 7248-7256.

VASSAR, P. S. & CULLING, C. 1959. Fluorescent stains, with special reference to amyloid and connective tissues. *Archives of Pathology,* 68**,** 487-498.

VELASCO, G., HERNÁNDEZ-TIEDRA, S., DÁVILA, D. & LORENTE, M. 2016a. The use of cannabinoids as anticancer agents. *Progress in Neuro-Psychopharmacology and Biological Psychiatry,* 64**,** 259-266.

VELASCO, G., SÁNCHEZ, C. & GUZMÁN, M. 2012. Towards the use of cannabinoids as antitumour agents. *Nature Reviews Cancer,* 12**,** 436.

VELASCO, G., SÁNCHEZ, C. & GUZMÁN, M. 2016b. Anticancer mechanisms of cannabinoids. *Current Oncology,* 23**,** S23.

VERFAILLIE, T., GARG, A. D. & AGOSTINIS, P. 2013. Targeting ER stress induced apoptosis and inflammation in cancer. *Cancer Letters,* 332**,** 249-264.

VOELTZ, G. K., ROLLS, M. M. & RAPOPORT, T. A. 2002. Structural organization of the endoplasmic reticulum. *EMBO reports,* 3**,** 944-950.

WANG, G., YANG, Z.-Q. & ZHANG, K. 2010. Endoplasmic reticulum stress response in cancer: molecular mechanism and therapeutic potential. *American Journal of Translational Research,* 2**,** 65-74.

WANG, M. & KAUFMAN, R. J. 2014. The impact of the endoplasmic reticulum protein-folding environment on cancer development. *Nature Reviews Cancer,* 14**,** 581.

WANG, W.-A., GROENENDYK, J. & MICHALAK, M. 2014. Endoplasmic reticulum stress associated responses in cancer. *Biochimica et Biophysica Acta. Molecular Cell Research,* 1843**,** 2143-2149.

WANG, Y., VISCARRA, J., KIM, S.-J. & SUL, H. S. 2015. Transcriptional regulation of hepatic lipogenesis. *Nature Reviews. Molecular Cell Biology,* 16**,** 678-689.

WANG, Y., WEN, X., ZHANG, N., WANG, L., HAO, D., JIANG, X. & HE, G. 2019. Small-molecule compounds target paraptosis to improve cancer therapy. *Biomedicine & Pharmacotherapy,* 118**,** 109203.

WEBER, L. V., AL-REFAE, K., WÖLK, G., BONATZ, G., ALTMÜLLER, J., BECKER, C., GISSELMANN, G. & HATT, H. 2016. Expression and functionality of TRPV1 in breast cancer cells. *Breast Cancer (Dove Medical Press),* 8**,** 243-252.

WILKINS, H. M., CARL, S. M. & SWERDLOW, R. H. 2014. Cytoplasmic hybrid (cybrid) cell lines as a practical model for mitochondriopathies. *Redox Biology,* 2**,** 619-631.

WU, J., CHEN, S., LIU, H., ZHANG, Z., NI, Z., CHEN, J., YANG, Z., NIE, Y. & FAN, D. 2018. Tunicamycin specifically aggravates ER stress and overcomes chemoresistance in multidrug-resistant gastric cancer cells by inhibiting N-glycosylation. *Journal of Experimental & Clinical Cancer Research,* 37**,** 272-272.

XU, C., BAILLY-MAITRE, B. & REED, J. C. 2005. Endoplasmic reticulum stress: cell life and death decisions. *The Journal Of Clinical Investigation,* 115**,** 2656-2664.

XUE, C., LIN, T. Y., CHANG, D. & GUO, Z. 2017. Thioflavin T as an amyloid dye: Fibril quantification, optimal concentration and effect on aggregation. *Royal Society Open Science,* 4**,** 160696-160696.

YOO, J., MASHALIDIS, E. H., KUK, A. C. Y., YAMAMOTO, K., KAESER, B., ICHIKAWA, S. & LEE, S.-Y. 2018. GlcNAc-1-P-transferase-tunicamycin complex structure reveals basis for inhibition of N-glycosylation. *Nature Structural & Molecular Biology,* 25**,** 217-224.

YOSHIDA, H. 2007. ER stress and diseases. *The FEBS Journal,* 274**,** 630-658.

YOSHIDA, H., MATSUI, T., YAMAMOTO, A., OKADA, T. & MORI, K. 2001. XBP1 mRNA Is Induced by ATF6 and Spliced by IRE1 in Response to ER Stress to Produce a Highly Active Transcription Factor. *Cell,* 107**,** 881-891.

ZHANG, K. & KAUFMAN, R. J. 2008. From endoplasmic-reticulum stress to the inflammatory response. *Nature,* 454**,** 455.

ZONG, W.-X., LI, C., HATZIVASSILIOU, G., LINDSTEN, T., YU, Q.-C., YUAN, J. & THOMPSON, C. B. 2003. Bax and Bak can localize to the endoplasmic reticulum to initiate apoptosis. *The Journal Of Cell Biology,* 162**,** 59-69.

ZOU, S. & KUMAR, U. 2018. Cannabinoid receptors and the endocannabinoid system: signaling and function in the central nervous system. *International Journal of Molecular Sciences,* 19**,** 833.

Appendices

i. Appendix i – Reagents and consumables

Table 3: Manufacturer details of antibodies used in this study

Antibody (Catalogue number)	**Company**
ATF4 (D4B8)	Cell signalling technology
ATF6 (NBP1-40256SS)	Novus Biologicals
CHOP (NB600-1335)	Novus Biologicals
GRP78 (sc-13539)	Santa Cruz Biotechnology
Histone H3	Novis
XBP1 (M-186)	Santa Cruz Biotechnology
β-Actin	Santa Cruz Biotechnology

Table 4: Manufacturer details of reagents and consumables used in this study

Reagent/Consumable	**Company**
6 well tissue culture plates	Whitehead scientific
96 well E-plate for xCelligence	Roche
96 well plates	Whitehead scientific
Acetic acid	Merck
Acetone	Merck
Acrylamide	Sigma
Ammonium persulphate (APS)	Merck
Ascorbic acid	Merck
Bovine serum albumin (BSA)	Roche
Bradford reagent	Biorad
Brefeldin A	Sigma
Bromophenol Blue	Merck
Calcium Green	Thermofisher scientific
Cannabidiol (CBD)	LGC
Cannabigerol (CBG)	LGC
Cannabinol (CBN)	LGC
Cell culture dishes	Whitehead scientific
Coomassie R250	Merck
DAPI	Thermofisher scientific
Dichlorofluorescein-Diacetate (DCFH-DA)	Sigma
Diethyl ether	Merck
Di-sodium hydrogen orthophosphate (Na_2HPO_4)	Merck
DMEM	Biowest
DMSO	Merck
Donor horse serum	Biowest
Epidermal growth factor (EGF)	Thermofisher scientific
ER Tracker™ Red	Thermofisher
Ethylenediaminetetra-acetic acid (EDTA)	Merck
F12	Biowest

FCCP	Sigma
Fetal Bovine Serum (FBS)	Biowest
Gentamycin	Highveld biological
Glycerol	Merck
Glycine	Merck
Griess reagent	Sigma
Hexane	Merck
Hydrochloric acid	Merck
Hydrocortisone	Sigma
Insulin solution, human	Sigma
Isopropanol	Merck
Leibovitz 15 (L15)	Sigma
LipidTOX™ Green	Thermofisher
Low fat milk powder	Spar
LysoTracker™ Green	Thermofisher
Methanol	Merck
Mitochondrial staining kit - Cytopainter	Abcam
Non-sterile 96 well plates	Whitehead scientific
Page-ruler pre-stained molecular weight marker	Thermofisher scientific
Polyvinylfluoridine (PVDF) membrane	Roche
Potassium chloride (KCl)	Merck
Potassium dihydrogen orthophosphate (KH_2PO_4)	Merck
Redox dye	Anatech
Sodium Chloride (NaCl)	Merck
Sodium dodecyl sulphate (SDS)	Biorad
Sulphorhodamine B (SRB)	Sigma
Thapsigargin	Sigma
Thioflavin T (ThT)	Sigma
Tissue culture flasks	Whitehead scientific
Tissue culture petri dishes (10 cm)	Whitehead scientific
Tris	Merck
Triton X-100	Sigma
Trypan blue	Lonza
Trypsin	Sigma
Tunicamycin	Sigma
Tween20 20	Sigma
β-Mercaptoethanol	Fluka
Δ^9-tetrahydrocannabinol (THC)	Leico
µ-Slide angiogenesis ibiTreat for confocal microscopy	ibidi

ii. Appendix ii – Buffer components

Cell culture:

PBS

137mM NaCl
1.5 mM KH_2PO_4
20mM Na_2HPO_4
0.7 mM KCl

PBS-EDTA

137mM NaCl
1.5 mM KH_2PO_4
20mM Na_2HPO_4
0.7 mM KCl
0.5 mM EDTA

Lysis buffer

50 mM TRIS-HCl (pH 7.4)
2 mM EDTA.$2H_20$
1% (v/v) Triton X-100

Binding buffer (10x)

0.1 M HEPES (pH 7.4)
1.4 M NaCl
25 mM $CaCl_2$

SDS-PAGE and Western blotting:

Stacking Gel (4%)

0.125 M Tris (pH 6.8)
4% Acrylamide/Bis-acrylamide (37.5:1)
3.5 mM SDS
3.5mM APS
0.2% (v/v) TEMED

Resolving Gel (10%)

0,375 M Tris (pH 8.8)
10% Acrylamide/Bis-acrylamide (37.5:1)
3.5 mM SDS
3.5mM APS
0.2% (v/v) TEMED

Electrode buffer (pH 8.3)

25mM Tris
192mM Glycine
3.5 mM SDS

Sample buffer

62.5 mM Tris (pH 6.8)
40% (v/v) Glycerol
0.01% (m/v) Bromophenol Blue
69.4 mM SDS
5% (v/v) β-Mercaptoethanol

Transfer buffer

2.5 mM Tris
192mM Glycine
20% (v/v) methanol

TBS-Tween2020 (pH 7.4)

50 mM Tris
150 mM NaCl
0.1% Tween20 20

Blocking Buffer

5% (m/v) Skim milk powder in TBS-Tween20

Destain solution

40% (v/v) Methanol
10% (v/v) Acetic Acid
in ddH_20

iii. Appendix iii – Equipment and software information

Table 5: Manufacturer details of equipment used in this study

Equipment	**Manufacturer**
Cell culture hood	BioFlow II Labotec
Cell culture incubator	Thermofisher
Confocal microscope	Zeiss
Electrophoresis power pack HC	Biorad
Epoch2 microplate reader	Biotek
Fluorescent inverted microscope	Zeiss
Haemocytometer	Beckman
Inverted microscope for cell culture	Zeiss
MiniSpin benchtop centrifuge	Eppendorf
Purelab option reverse osmosis water purifier	PureLab Option
Simplicity UV deioniser	Millipore Merck
SynergyMX fluorimeter	Biotek
xCelligence RTCA	Roche

Table 6: Information of software used in this study

Software	**Version**
AxioVision	4.8.2.0
BioRender	Online tool
ImageJ	1.52a
RTCA	1.2.1
Zen 2 (Blue edition)	Lite

iv. Appendix iv – Supplementary data

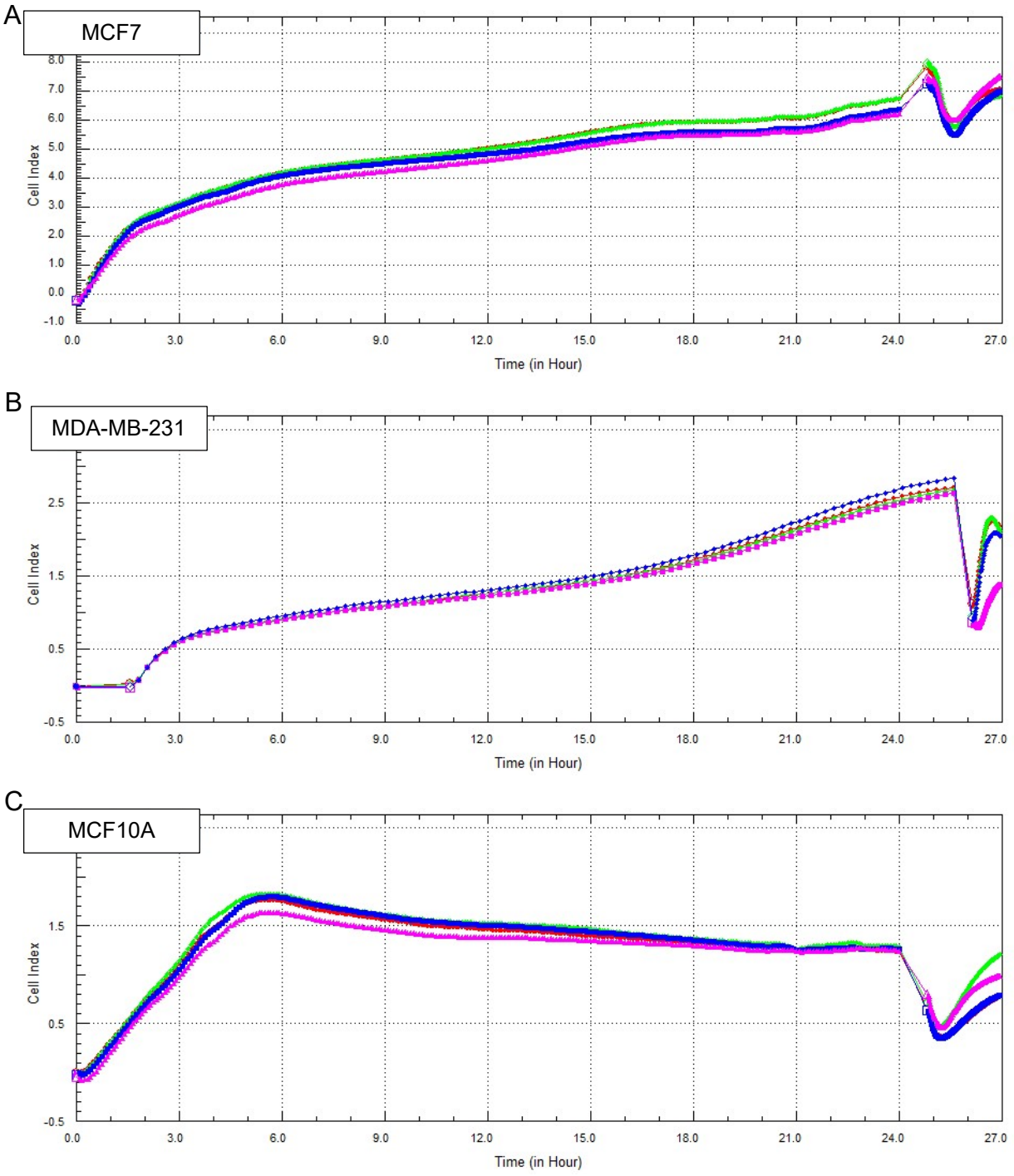

Figure 66: xCelligence curves showing real-time changes in the cell index over 24 hours showing attachment of various cell lines.
(A) MCF7, (B) MDA-MB-231 and (C) MCF10A cell lines, n=3.

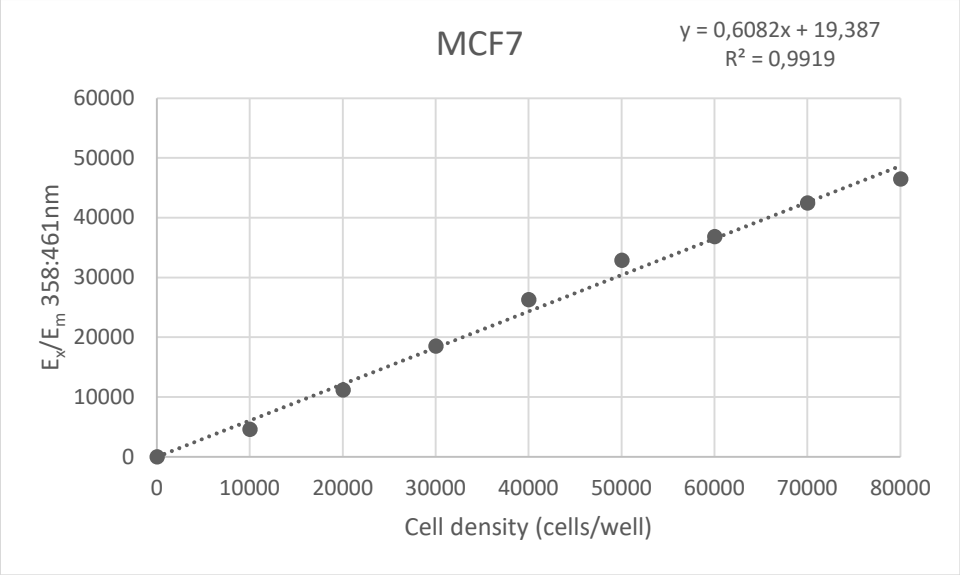

Figure 67: Cell density standard curve of the MCF7 cell line (0 – 80 000 cells/well) obtained using DAPI staining, n=1.

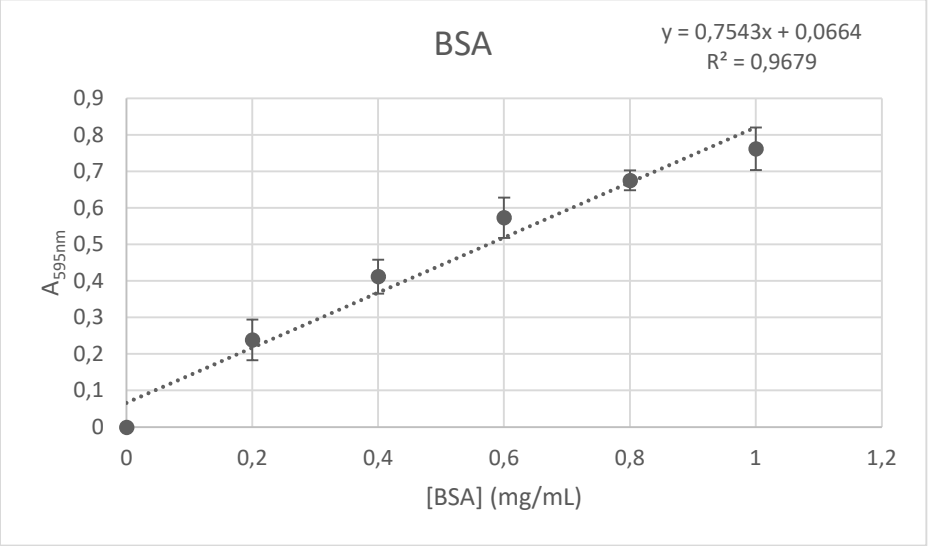

Figure 68: Protein standard curve (0-1mg/mL) obtained using BSA as a reference protein and the Bradford Reagent, n=3.

$$Normalized\ density = Target\ protein \times \frac{Untreated\ loading\ control}{Target\ loading\ control}$$

$$Fold\ difference = \frac{Normalized\ density\ (treatment)}{Normalized\ density\ (control)}$$

Equation 1: Equation used for the normalisation of western blot data

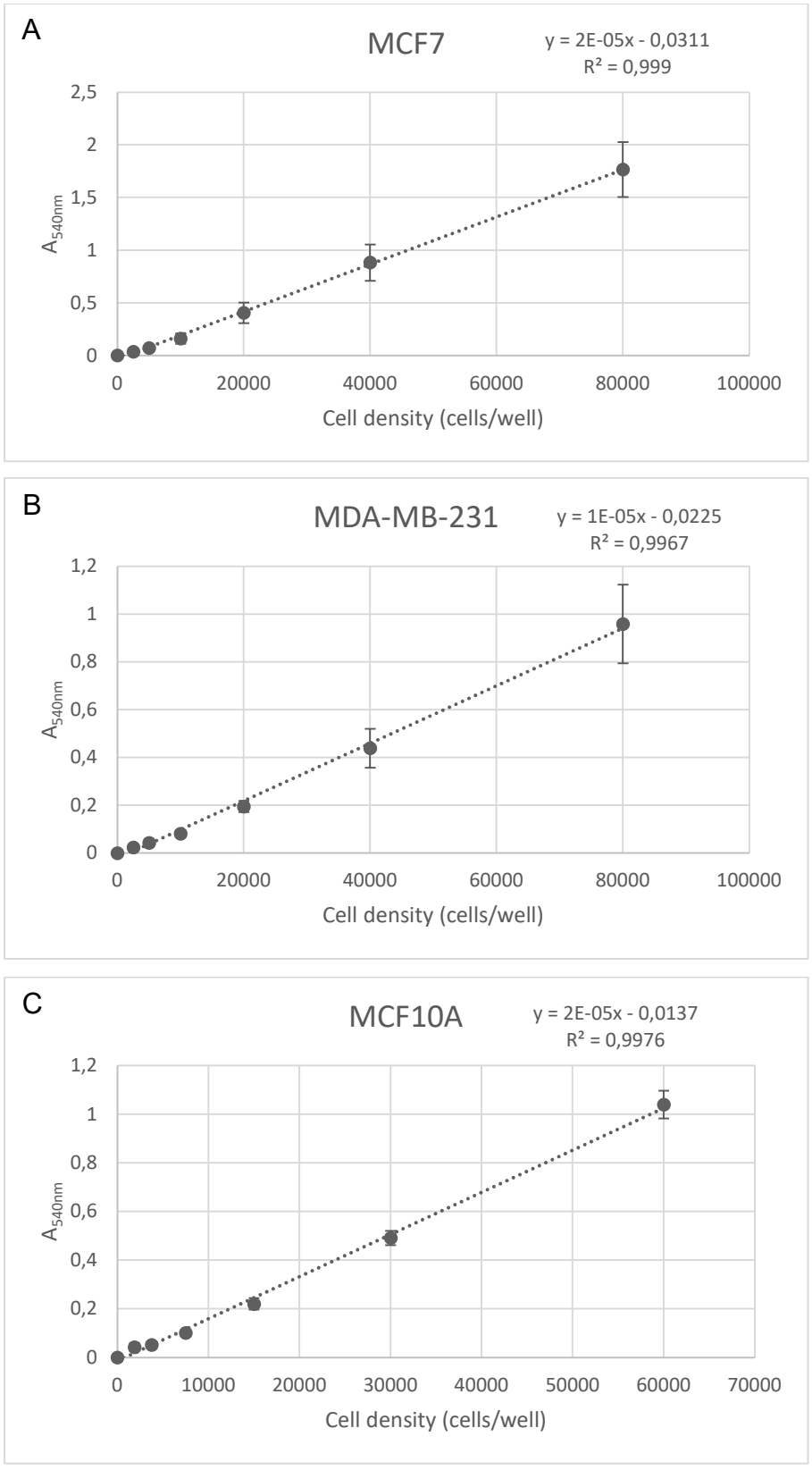

Figure 69: Cell density standard curves of various cell lines (0 – 80 000 cells/well), obtained using the SRB cell viability assay.
(A) MCF7, (B) MDA-MB-231 and (C) MCF10A cell lines, n=3.

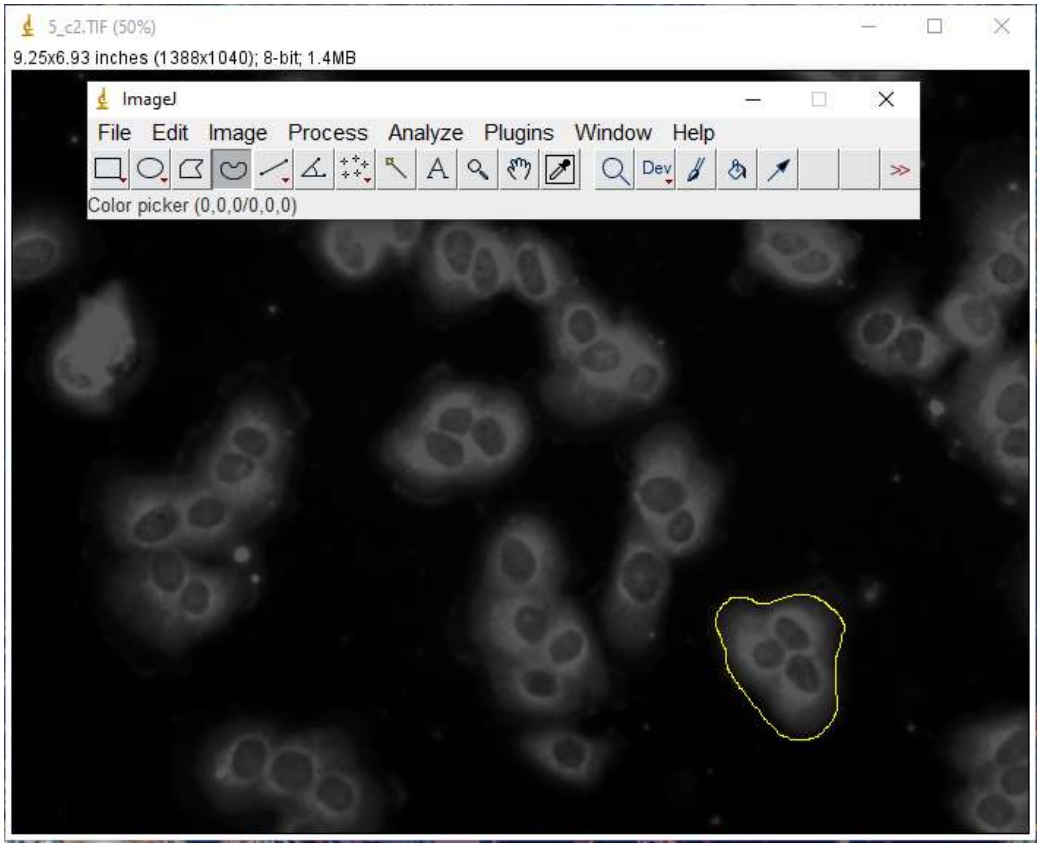

Figure 70: Screenshot of ImageJ software showing the outline of a region of interest (ROI) to generate 3D overlay of individual cells.

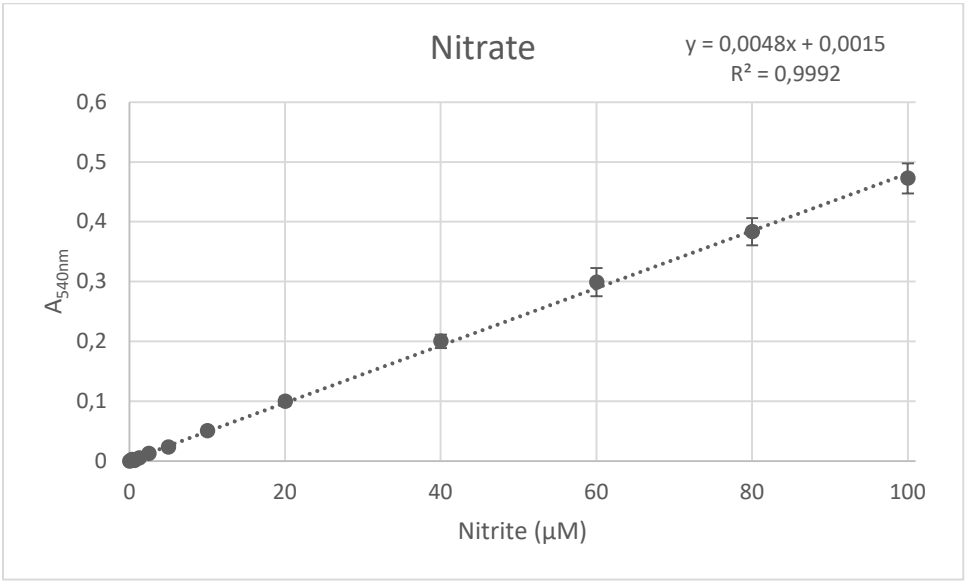

Figure 71: Nitrate standard curve (0 – 100 µM) obtained using a nitrate standard and the Griess reagent, n=3.

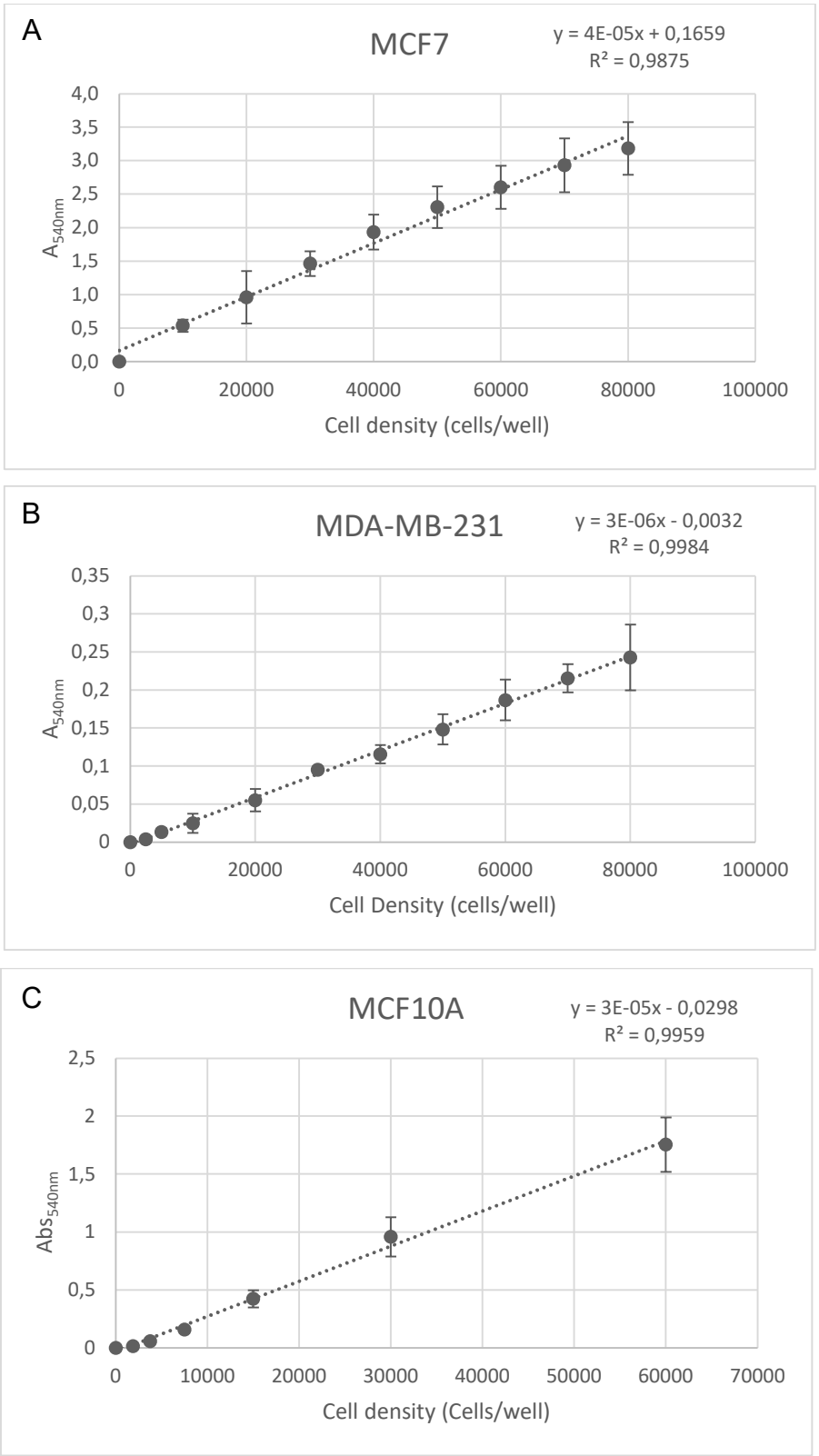

Figure 72: Cell density standard curves of various cell lines (0 – 80 000 cells/well), obtained using the MTT cell viability assay
(A) MCF7, (B) MDA-MB-231 and (C) MCF10A cell lines, n=3.

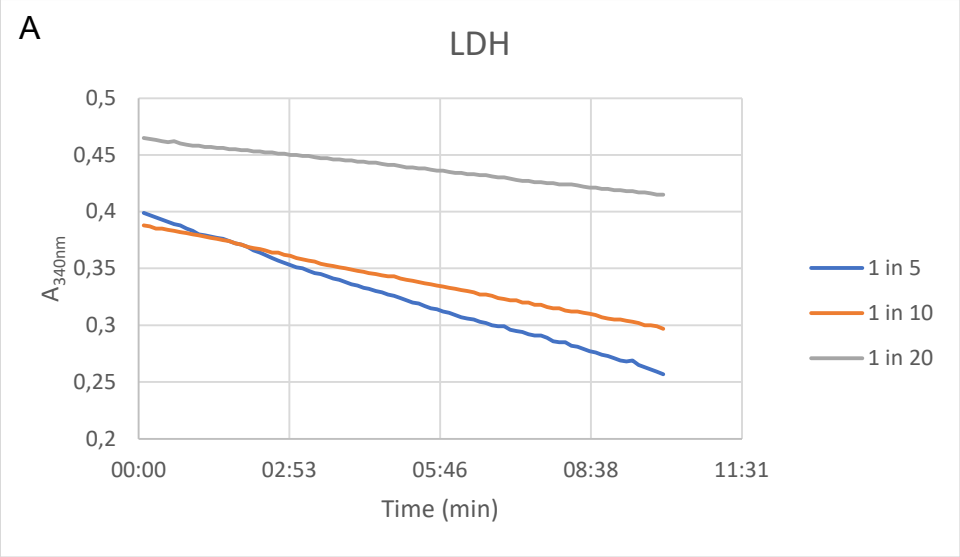

Dilution	1 in 5	1 in 10	1 in 20
Slope	-20,1	-13,2	-7,1

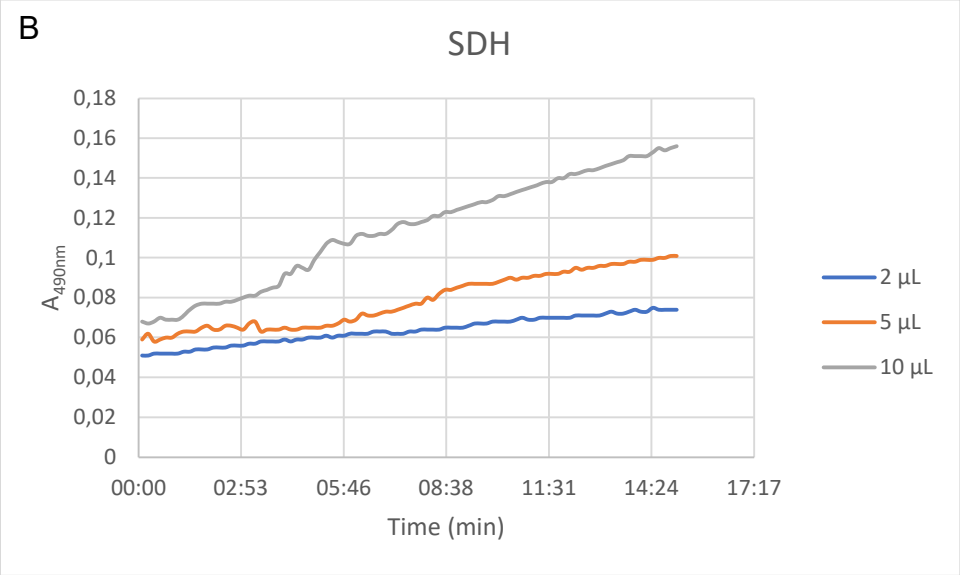

Volume	2 µL	5 µL	10 µL
Slope	2,2	4,4	9,0

Figure 73: A typical set of progress curves illustrating concentration-dependence of (A) LDH and (B) SDH enzyme assays in the MCF7 cell line and the corresponding slopes.
LDH – lactate dehydrogenase; SDH – succinate dehydrogenase

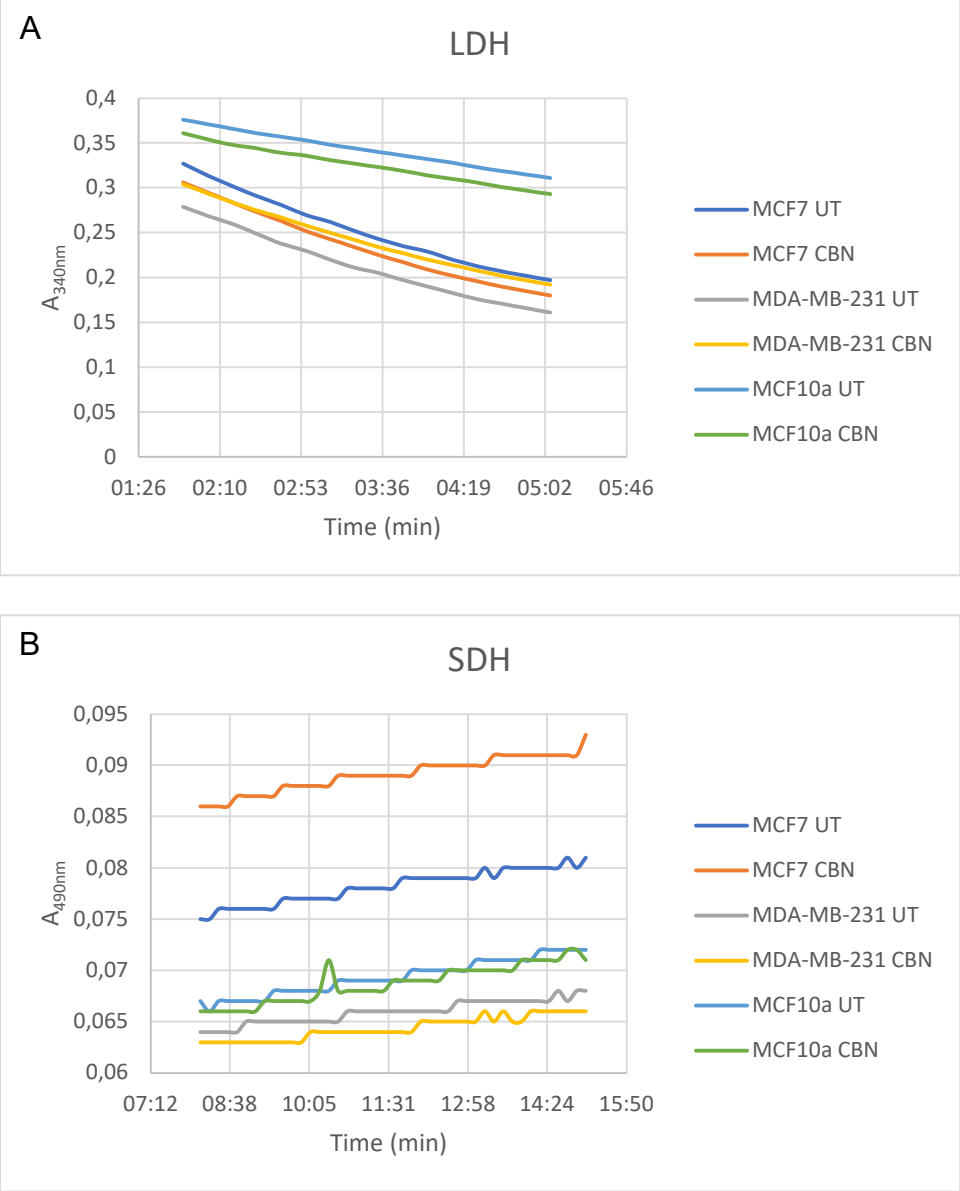

Figure 74: Representative progress curves of (A) LDH and (B) SDH activity for the various treatments in the MCF7, MDA-MB-231 and MCF10A cell lines
LDH – lactate dehydrogenase; SDH – succinate dehydrogenase; UT – untreated; CBN – cannabinol, n=3

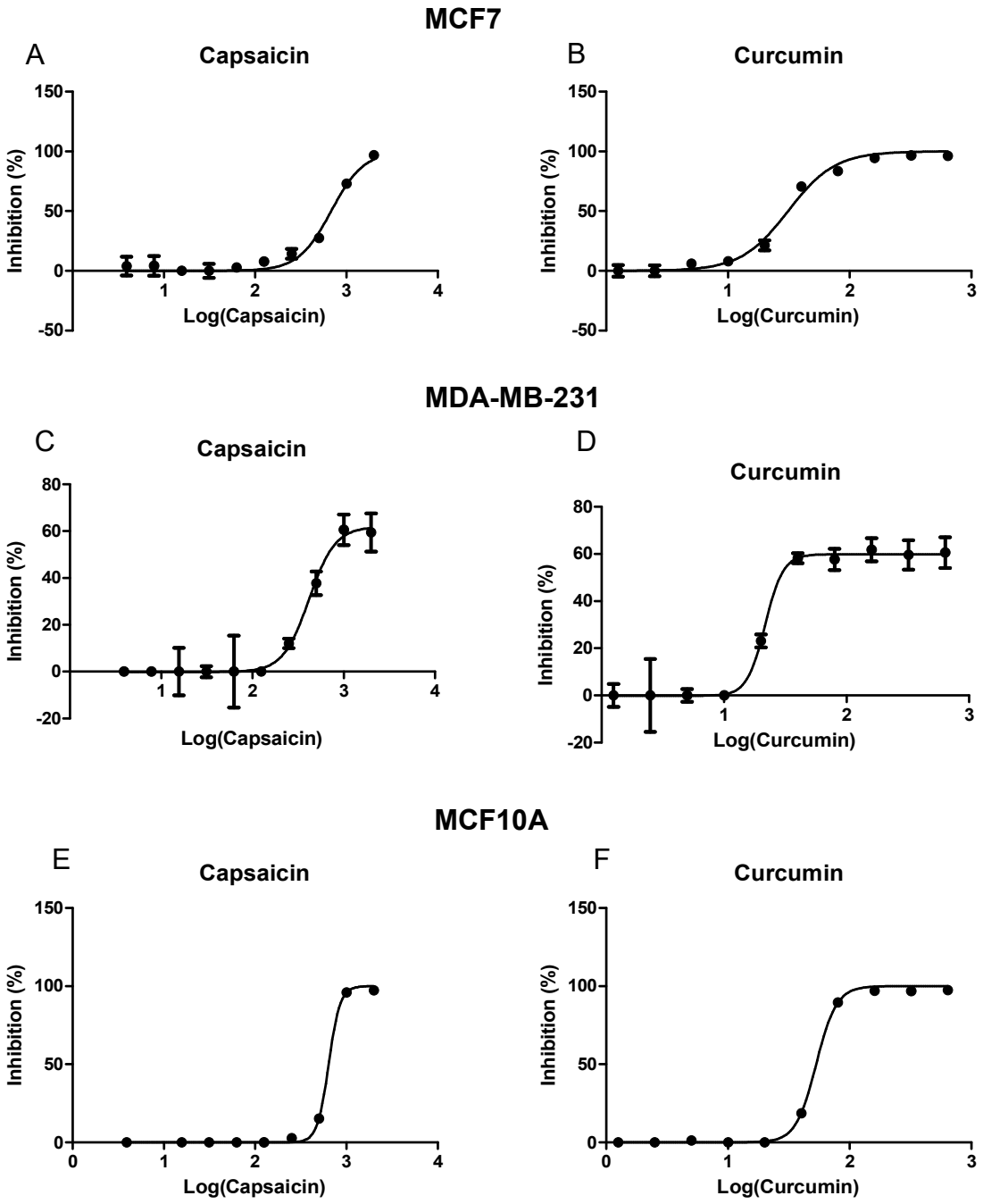

Figure 75: IC_{50} curves of capsaicin and curcumin in (A & B) MCF7, (C & D) MDA-MB-231 and (E & F) MCF10A cell lines after treatment for 48h, n=3

Table 7: IC_{50} values of capsaicin and curcumin in the MCF7, MDA-MB-231 and MCF10A cell lines.

	Capsaicin (µM)	Curcumin (µM)
MCF7	680	31
MDA-MB-231	959	104
MCF10A	639	53